DOE/ER/60707--3

DOE/ER/60707--3

DE91 006306

A Comprehensive Report Submitted to the

U.S. Department of Energy

by the

Texas A & M Research Foundation
P.O. Box 3578
College Station, Texas 77843

for a project entitled

"Considerations of Beta and Electron Transport in Internal Dose Calculations"

Prepared by

Wesley E. Bolch
John W. Poston, Sr.
Department of Nuclear Engineering
Texas A&M University
College Station, Texas 77843

December 1990

TABLE OF CONTENTS

INTRODUCTION

Ionizing radiation has broad uses in modern science and medicine. These uses often require the calculation of energy deposition in the irradiated media and, usually, the medium of interest is the human body. Energy deposition from radioactive sources within the human body and the effects of such deposition are considered in the field of internal dosimetry.

Internal dosimetry is usually defined as a process of measurement and calculation which results in an estimate of the absorbed dose to tissues of the body due to an intake of radioactive material. Internal dose calculations are a two-step process as defined in the schema of the Medical Internal Radiation Dose (MIRD) Committee of the Society of Nuclear Medicine. The first step is to model the kinetics of the radionuclide in the body. Here the parameter of interest is the rate at which the radionuclide moves from one organ to another until the nuclide is eliminated from the body or until its residence time in the body exceeds the mean life of the nuclide. Organs of the body are considered to be compartments into which nuclides move in and out. The net movement of the nuclide (including radioactive decay) from a compartment is described by a system of first-order differential equations. The solutions to these equations include constants that depend upon biochemical properties of the organs.

The second part of the internal dose calculation considers the movement (or transport) of radiation from nuclei undergoing radioactive decay to the surrounding tissue. Radiation emitted in these nuclear transformations can be alpha, beta, or gamma radiation. These radiations travel varying distances from the site of their creation before an interaction takes place. The result of an interaction can be a total or partial deposition of the radiation energy. The exact mechanisms of interaction, transport, and energy deposition are described by well-understood physical parameters.

Recent Developments Sponsored by DOE

In July of 1988, a three-year research project was initiated by the Nuclear Engineering Department at Texas A&M University under the sponsorship of the U. S. Department of Energy. The main thrust of the research was to consider, for the first time, the detailed spatial transport of electron and beta particles in the estimation of average organ doses under the MIRD schema. In the MIRD schema, these particles are classified as "non-penetrating" radiations. As a result, their absorbed fraction of energy is considered to equal unity if their production or emission occurs within the target organ of interest; otherwise, the absorbed fraction of energy is zero. As was shown in the initial research

proposal, transport calculations show that absorbed fractions can vary significantly from unity in many situations. This is particularly true for higher energy beta and electron sources within organs with a small mass and a large surface area.

Consequently, a systematic compilation of absorbed fractions for both beta particles and photons (which produce electrons) was initiated. The reference heterogeneous phantom described in MIRD Pamphlet 5 Revised (Snyder 1978) was implemented as a geometry scoring routine within the electron transport code EGS4 (Rogers 1984). This Monte Carlo transport code thus allowed the explicit treatment of electron collisional and radiative energy loss, as well as multiple scattering, in internal dose estimates. An extensive database of electron and revised photon absorbed fractions was compiled for 21 combinations of source-target regions (Akabani and Poston 1990a). Next, this database was used to reevaluate tabulations of S-values for 80 radionuclides of interest in diagnostic and therapeutic nuclear medicine procedures (Akabani and Poston 1990b). Reports for both electron absorbed fractions and the revised S-values are contained in the Comprehensive Report which accompanies this renewal proposal.

In conjunction with this work, revisions were also made to the head and neck region, the gall bladder (Patel et. al 1991a), and the kidney (Patel et. al 1991b) of the MIRD phantom . In the revised kidney model, three subregions were included: the papillae, the medulla, and the cortex. Reports for both the kidney and gall bladder can be found in the Comprehensive Report.

With the capabilities of the EGS4 code, an revised dosimetry model for the circulatory system was initiated within the second year of research. Absorbed fractions of energy were calculated for monoenergetic photons and electrons within infinite cylinders of radius 0.02 to 1.0 cm. The division between the source region (blood) and the target region (blood vessel) were varied so as to simulate the full range of vessels found within the circulatory system. Estimates of the average absorbed dose to blood and the maximum absorbed dose to the vessel walls were made for selected radionuclides and for all vessel sizes (Akabani and Poston 1990c). This effort has been identified by the MIRD Committee as being extremely important to the assessment of dose in nuclear medicine procedures. A report of this work is also included in the Comprehensive Report.

At the present time (December of 1990), research activities are continuing within five areas. Several are new initiatives begun within the second or third year of the current contract period. They include: (1) development of small-scale dosimetry; (2) development of a differential volume phantom; (3) development of a dosimetric bone model; (4) assessment of the new ICRP lung model; and (5) studies into the mechanisms of DNA damage. A progress report is given for each of these tasks within the Comprehensive

Report. In each case, preliminary results are very encouraging and plans for further research are detailed within this document.

Throughout the current contract period (July 1, 1988 - June 30, 1991), direct support has been requested for only one to two graduate students. Nevertheless, the activities performed at Texas A&M under DOE support have been a simulating source of research topics for both master's theses and doctoral dissertations. At present, a total of 13 graduate students have been either directly or indirectly involved in the dosimetry research sponsored by DOE. Six of these students have graduated (5 MS and 1 PhD), two are currently nearing graduation (2 MS), and 5 are currently pursuing their research (2 MS and 3 PhD). Three of the completed master's theses involved tasks related to, but not directly proposed under, the current DOE contract. These studies involved research into: (1) hot particle dosimetry; (2) cavity theory as it relates to TLD design; and (3) nearest-neighbor distributions of free radicals produced within electron and alpha particle tracks. For completeness, a summary of each study is contained in the Comprehensive Report. A list of all students participating in DOE-sponsored research is given below.

List of Participating Graduate Students

Graduated

T. Edmond Hui, "A Preliminary Model of the Circulating Blood for use in Radiation Dose Calculations, " Thesis, Texas A&M University, 1986.

Jyoti S. Patel, "A Revised Model of the Kidney for the Calculation of Absorbed Fraction of Various Photon Energies," Thesis, Texas A&M University, 1988.

Donna M. Busche, "A New Approach to Hot Particle Dosimetry Using a Monte Carlo Transport Code, " Thesis, Texas A&M University, 1989.

Mark D. Weyland, "A Look at General Cavity Theory through a Code Incorporating Monte Carlo Techniques," Thesis, Texas A&M University, 1989.

M. Clay Smith, "Nearest-Neighbor Distributions of Free Radicals Produced within Charged Particle Tracks in Liquid Water," Thesis, Texas A&M University, 1990.

Gamal Akabani, "Internal Dose Calculations for Electrons and Beta Particles," Dissertation, Texas A&M University, 1990.

Completing Research

Joseph Liu, "Internal Beta Dose Calculations Using a Point Kernel Algorithm," Thesis, Texas A&M University, 1991.

Todd A. Shearer, "Assessment of the Dose to Bone Using a Monte Carlo Transport Code," Thesis, Texas A&M University, 1991.

Beginning Research

Oscar Hernandez (MS)
Research Interest: Assessment of New ICRP Lung Model

Judy Hutchings (MS)
Research Interest: Development of a New Brain Model for Internal Dosimetry

How Mooi Lau (PhD)
Research Interest: Mechanisms of DNA Damage

Eun-Hee Kim (PhD)
Research Interest: Microdosimetry of Internal Beta Emitters

Carmine Plott (PhD)
Research Interest: Experiment Determination of Organ Doses from Internal Emitters

List of Research Publications

Akabani, G., J. W. Poston, Sr., and W. E. Bolch, "Estimates of Absorbed Fractions in Small Volumes for Selected Radionuclides", *Journal of Nuclear Medicine* (submitted), 1990a.

Akabani, G. and J. W. Poston, Sr., "Reevaluation of S-Values Considering Electron Transport," *Journal of Nuclear Medicine* (submitted), 1990b.

Akabani, G. and J. W. Poston, Sr., "Absorbed Dose Calculations to Blood and Blood Vessels for Internally Deposited Radionuclides," *Journal of Nuclear Medicine* (submitted), 1990c.

Bolch, W. E., J. E. Turner, H. Yoshida, K. B. Jacobson, and R. N. Hamm, "Calculations for the Irradiation of Glycylglycine in Oxygen-Free Solutions I. Microsecond Product Yields", *Radiat. Res.* (submitted), 1990a.

Bolch, W. E., J. E. Turner, H. Yoshida, K. B. Jacobson, R. N. Hamm, and H. A. Wright,
"Monte Carlo Simulation of Free Radical Attack to Biomolecules Irradiated in Aqueous Solution", *Radiat. Prot. Dosim.* **31**, 43-46 (1990b).

Busche, D. M. , G. Akabani, and J. W. Poston, Sr., "An Approach to Hot Particle Dosimetry using a Monte Carlo Transport Code," *Radiation Protection Management* (submitted), 1990.

Hui, T. E., and J. W. Poston, Sr., "A Preliminary Model of the Circulating Blood for use in Absorbed Fraction Calculations," *MIRD Monograph on Absorbed Fractions* (in preparation), 1991.

Patel, J. S., J. W. Poston, Sr., and T. E. Hui, "A Revised Model of the Gall Bladder for Absorbed Fraction Calculations," *MIRD Monograph on Absorbed Fractions* (in preparation), 1991a.

Patel, J. S., J. W. Poston, Sr., and T. E. Hui, "A Revised Model of the Kidneys for the Calculation of Absorbed Fraction of Various Photon Energies," *MIRD Monograph on Absorbed Fractions* (in preparation), 1991b.

Turner, J. E., W. E. Bolch, O. H. Crawford, H. Yoshida, K. B. Jacobson, and R. N. Hamm, "Calculations for the Irradiation of Glycylglycine in Oxygen-Free Solutions II. Final Product Yields and Comparison with Experiment" *Radiat. Res.* (submitted), 1990a.

Turner, J. E., W. E. Bolch, H. Yoshida, K. B. Jacobson, H. A. Wright, R. N. Hamm, R. H. Ritchie, and C. E. Klots, "Radiation Damage to a Biomolecule: New Physical Model Successfully Traces Molecular Events", *Int. J. Radiat. Applic. Instr.* (in press), 1990b.

Weyland, M. D., G. Akabani, and J. W. Poston, Sr., "A Look at General Cavity Theory Through a Code Incorporating Monte Carlo Techniques," *Medical Physics* (submitted), 1990.

Yoshida, H., W. E. Bolch, J. E. Turner, K. B. Jacobson, and W. M. Garrison, "Measurement of Products from X-irradiated Glycylglycine in Oxygen-Free Aqueous Solutions", *Radiat. Res.* (submitted), 1990a.

Yoshida, H., W. E. Bolch, J. E. Turner, and K. Bruce Jacobson, "The Radiation Chemistry of Glycylglycine in Aqueous Solutions", *Radiat. Prot. Dosim.* **31**, 67-70 (1990b).

References

Akabani, G., J. W. Poston, Sr., and W. E. Bolch, "Estimates of Absorbed Fractions in Small Volumes for Selected Radionuclides", *Journal of Nuclear Medicine* (submitted), 1990a.

Akabani, G. and J. W. Poston, Sr., "Reevaluation of S-Values Considering Electron Transport," *Journal of Nuclear Medicine* (submitted), 1990b.

Akabani, G. and J. W. Poston, Sr., "Absorbed Dose Calculations to Blood and Blood Vessels for Internally Deposited Radionuclides," *Journal of Nuclear Medicine* (submitted), 1990c.

Patel, J. S., J. W. Poston, Sr., and T. E. Hui, "A Revised Model of the Gall Bladder for Absorbed Fraction Calculations," *MIRD Monograph on Absorbed Fractions* (in preparation), 1991a.

Patel, J. S., J. W. Poston, Sr., and T. E. Hui, "A Revised Model of the Kidneys for the Calculation of Absorbed Fraction of Various Photon Energies," *MIRD Monograph on Absorbed Fractions* (in preparation), 1991b.

Rogers, W. O., "Low Energy Electron Transport with EGS," *Nucl. Instru. and Meth. in Res.* 227, 535-548 (1984).

Snyder, W. S., M. R. Ford, G. G. Warner, "Estimates of Specific Absorbed Fractions for Photon Sources Uniformly Distributed in Various Organs of a Heterogeneous Phantom," MIRD Pamphlet No. 5 Revised, 1978.

REEVALUATION OF S-VALUES CONSIDERING ELECTRON TRANSPORT

In 1964 the Society of Nuclear Medicine formed the Medical Internal Radiation Dose Committee (MIRD) to fulfill the needs of the nuclear medicine community to determine the radiation absorbed dose to patients who are administered radiopharmaceuticals. The MIRD objectives were to provide the best possible estimates of the absorbed dose to patients resulting from the diagnostic or therapeutic use of internally administered radiopharmaceuticals. Data required to achieve those objectives were:

1) radiological parameters,

2) anatomical and physiological data for patients of various ages and physiognomies, and

3) metabolic distribution data for radiopharmaceuticals.

Uncertainties associated with these data will be propagated in absorbed dose calculations. Although, relevant radiological transformation characteristics of radionuclides are well known, uncertainties in physiological aspects, such as variance in organ morphology and metabolic aspects, e.g., variance in organ uptakes, contribute the greatest sources of errors.

In 1978 a reference heterogeneous phantom was described in MIRD Pamphlet 5 Revised *(1)*. This mathematical phantom was used as a model upon which internal absorbed dose calculations were based. The phantom provided an approximately correct anatomical representation of the human body based on ICRP Publication 23 *(2)* which describes a Reference Man. The organs in the phantom are described geometrically by mathematical equations.

Specific absorbed fraction of energy (Φ) is defined as the ratio between the radiant energy deposited per unit mass in target organ and the total radiant energy released by a source organ. The MIRD phantom was used to calculate specific absorbed fractions for monoenergetic photon sources distributed in the organs. Monte Carlo techniques were used to transport only photons throughout the different regions of the phantom. Transport of

electrons produced by either photon interactions or radioactive emissions was not considered; however, under the MIRD methodology, conservative assumptions were used to evaluate the contribution of electron energy deposition. It was assumed that the electron ranges were small compared with the mean radius of most organs; therefore, the absorbed dose will not change drastically. The specific absorbed fraction for electrons produced by radioactive transformations is assumed to be the inverse of the mass of the source organ if the source equals the target organ, and zero otherwise. For those organs with walls, the specific absorbed fraction for electrons is assumed to be one-half the specific absorbed fraction for the contents.

MIRD Pamphlet No. 11 (3) presented absorbed doses to different target organs and regions per unit cumulated activity for various source organs and for specific radionuclides used in nuclear medicine. These values are referred to as S-values. The assumptions used by the MIRD methodology overestimate the dose to source organs and underestimate the dose to adjacent organs. Furthermore, they are not valid at the boundary of the source organs where composition and density changes occur, nor are they valid for small organs with high surface to volume ratios, such as the thyroid.

With the advent of electron transport Monte Carlo codes, such as EGS4 (4), it is possible to evaluate the contribution of electrons to the total energy deposition within any region.

METHODOLOGY

For the S-values published in MIRD Pamphlet No. 11 (3), Monte Carlo techniques were used to calculate specific absorbed fractions for photons. In addition, very conservative assumptions were used for specific absorbed fractions for electrons and beta radiation. On the other hand, using the Electron Gamma Shower (EGS4) *(4)* code, electron absorbed fractions were calculated for organs and regions in which S-values were considered, in the past, to be either overestimated or underestimated. Regions to which

this applies are those which have walls such as the stomach, small regions with high surface to volume ratios such as the thyroid gland, and regions at interfaces or in which there is a change of density, i.e., the lung.

The code EGS4 was chosen for use in this work because of its versatility and easy manipulation of three dimensional regions. This transport code allows the calculation of electron absorbed fractions for regions or organs. Furthermore, the EGS4 code can be used to evaluate to the fullest extend the net contribution of energy deposition due to electrons in complex arrangements or geometries. Lower energy cutoffs for photons and electrons of 1 keV and 10 keV, respectively, were established to allow transport of bremsstrahlung radiation generated by electron interactions. Electrons and photons with energies below their respective lower cutoff energies will deposit their energy locally.

The EGS4 code was merged with the mathematical phantom and absorbed fractions for monoenergetic electrons were calculated for the selected source regions. Moreover, specific absorbed fractions for monoenergetic photons presented by Pamphlet No. 5 Revised were compared with those obtained using the EGS4 system code to assess the differences between transport and non-transport of electrons.

Absorbed fractions for monoenergetic electrons are used in the same manner in which photon absorbed fractions are used for calculating internal doses. Together, these absorbed fractions provide a complete data base on which absorbed doses can be calculated without the need of severe conservative assumptions. As a result, a new set of revised S-values were calculated to improve internal dose assessment for several source-target combinations for a variety of radionuclides commonly used in nuclear medicine.

COMPARISON OF EGS4 AND ALGAM COMPUTER CODES

ALGAM is a computer code which has been used to calculate the specific absorbed fraction (Φ) of energy for photons in a Reference Man (5). This code was widely used by the MIRD Committee to calculate specific absorbed fractions for different source-target organ combinations. Both ALGAM and EGS4 codes used the same mathematical phantom. Due to the fact that ALGAM does not consider electron transport, to compare the two codes the energy cutoff for electrons in EGS4 was set equal to the energy of the photons being transported. In this way, electrons generated by photon interactions were not transported and, for each electron produced by a photon interaction, the energy was assumed to be deposited at the point of interaction. The source and target region of the mathematical phantom selected for comparison of the two codes was the thyroid. Figures 1 shows a comparison of specific absorbed fractions for photons for ALGAM and EGS4 in which no electron transport was considered; Figure 1 shows that the two Monte Carlo codes produce the same results when electron transport is not considered. On the other hand, Figure 2 shows a comparison between the two codes when electron transport is considered in EGS4. Lower values of specific absorbed fractions were obtained by using the EGS4 code because electrons generated by photon interactions escaped the thyroid gland and deposited energy outside of the region. Figure 3 shows the percent differences of the specific absorbed fraction of energy for the thyroid between electron and non-electron transport modalities.

Based on the above results, in the calculation of revised S-values, the ALGAM data for photon specific absorbed fractions were combined with the results obtained from the EGS4 code for monoenergetic electrons. As can be seen from Figure 3, this procedure is appropriate for photon energies below 1 MeV, the region of interest in diagnostic nuclear medicine. Above 1 MeV, the errors associated with ignoring electron transport are minimal except at a photon energy of 4 MeV.

The reader is reminded that electrons generated by radioactive decay of a radionuclide in the source regions of the body are of great importance in the dose calculation and are included in the calculation of S-values. These improved calculations take into consideration the transport of electrons across interfaces between organs. Thus, the revised S-values provide better estimates of the absorbed dose to both the source organs and to organs lying in the near vicinity of the source organ. The procedure described above ignores only a very small portion of the total photon absorbed energy.

ABSORBED FRACTIONS FOR ELECTRONS

Several regions were considered for the calculation of the absorbed fractions of energy for electrons. These source-target combinations are given in Table 1. Electrons were generated homogeneously in the source regions. The kinetic energies used for the calculation of absorbed fractions for electrons ranged from 0.25 to 4 MeV. The value of the absorbed fraction (ϕ) for a zero kinetic energy is taken as the limit of the absorbed fraction as the energy tends to zero; therefore, ϕ is equal to unity when the source equal the target and zero otherwise. As an example, Figure 4 and 5 give the absorbed fractions of energy as a function of electron kinetic energy calculated for the thyroid gland and the bladder contents as source regions, respectively. If the thyroid is considered as a source organ, the MIRD methodology assumes that the absorbed fraction of energy for electrons for the thyroid as a target region is equal to unity. However, Figure 4 shows a decrease of the absorbed fraction as the kinetic energy of the electron increases. Similarly, Figure 5 shows absorbed fractions of energy for the bladder contents and the bladder wall. As can be seen in Figure 5, the absorbed fraction in the bladder contents decreases as the electron energy increases. Note, that the absorbed fraction in the bladder wall never approaches the value of 0.5, the usual assumption for such cases.

EVALUATION OF S-VALUES

S-values can be calculated by using the following equation:

$$S(r_k \leftarrow r_h) = C\sum_i E_i Y_i \Phi_i(r_k \leftarrow r_h)$$

where m_k is the mass of the target organ or tissue r_k; E_i is the mean energy of radiation type i; Y_i is the yield of radiation type i per transformation; $\Phi_i(r_k \rightarrow r_h)$ is the specific absorbed fraction of energy of radiation type i for the target-source combination; and C is a constant, the value of which depends on the units of the included quantities. The MIRD methodology considered the specific absorbed fraction for electrons to be zero if the source is not equal the target, and $1/m_k$ if source is also the target. For organs with walls, the specific absorbed fraction for the wall was considered to be one half the specific absorbed of the contents ($1/[2\ m_h]$).

Now using the capabilities of the EGS4 code, it was possible to override the MIRD assumptions and calculate directly specific absorbed fractions for electrons. As equation (1) specifies, the specific absorbed fraction for a beta-emitting radionuclide will be that calculated using the mean energy of its spectrum. To calculate S-values, The specific absorbed fractions for photons were obtained from MIRD Pamphlet No. 5 Revised and combined with absorbed fractions for electrons calculated as part of this work. A linear interpolation method was used to estimate absorbed fractions for both photons and electrons given their average energy.

Estimates of S-values, using electron absorbed fractions, were calculated for 80 radionuclides commonly used in nuclear medicine. The decay data for each radionuclide were obtained by using the computer code RADLST (6). The code RADLST can be used to obtain data on a specific radionuclide which includes the atomic radiations arising from the radioactive decay, the average and maximum energies, the yields, and the radiation equilibrium doses in tissue.

As an example, Tables 2 and 3 give S-values for the thyroid and bladder wall, respectively. These Tables give a comparison between the S-values calculated using the standard MIRD methodology and S-values obtained using the absorbed fractions of electrons calculated with the EGS4 code. The percent difference column given in Tables 2 and 3 can be used to assess the difference between the two methodologies. Appendix A gives a complete set of tables of S-values for the different source-target combinations used in this research.

CONCLUSIONS

The reevaluated S-values obtained using specific absorbed fractions for monoenergetic electrons supersede those obtained previously using the MIRD methodology and should be used to calculate absorbed doses in nuclear medicine procedures. However, the S-values given in this work were calculated using the average energy of the different types of radiations. For the case of beta radiation, the average energy of the beta spectra was used to calculate the specific absorbed fraction (Φ). This procedure is still an approximation because it does not consider the actual spectrum to estimate the specific absorbed fraction. The results show large differences between both methodologies for regions with walls, such as the bladder and the stomach, and regions which have subdivisions, such as the kidney.

REFERENCES

1. Snyder, W. S.; Ford M. R.; Warner, G. G. Estimates of specific absorbed fractions for photon sources uniformly distributed in various organs of a heterogeneous phantom. MIRD Pamphlet No. 5, Revised. New York: Society of Nuclear Medicine; 1978.

2. International Commission of Radiological Protection. Report of the task group on reference man. Oxford: Pergamon Press; ICRP Publication 23; 1975.

3. Snyder, W. S.; Ford M. R.; Warner, G. G. Watson, S. B. "S," Absorbed dose per unit cumulated activity for selected radionuclides and organs . MIRD Pamphlet No. 11. New York: Society of Nuclear Medicine; 1975.

4. Nelson, W. R.; Hirayama; H., Rogers; D. W. O. The EGS4 code system. Stanford Linear Accelerator Center, Report 265; 1985.

5. Warner, G. G.; Craig, A. M. Jr. ALGAM, A computer program for estimating internal dose from gamma-ray sources in a man phantom. ORNL-TM-2250, Oak Ridge Natl. Lab: 1968.

6. Burrows T. W. The program RADLST. Brookhaven National Laboratory, New York, Information Analysis center report, BNl-NCS-52142; 1988.

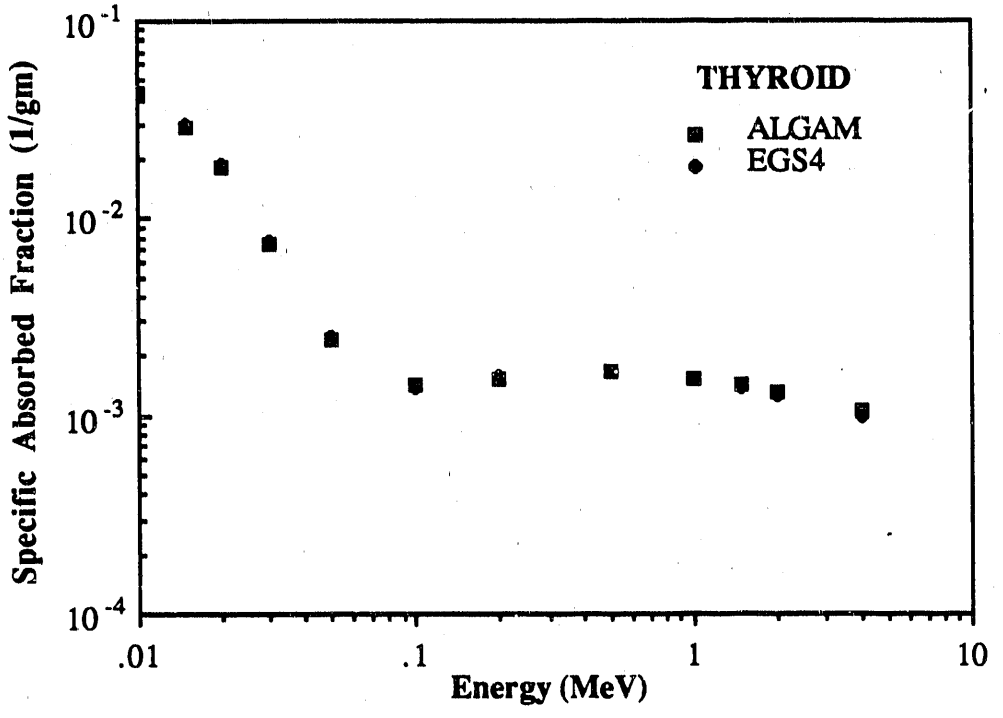

FIGURE 1. Specific absorbed fraction of photon energy in the thyroid gland. Comparison of ALGAM and EGS4 codes for the thyroid as a source and target organ. There was no electron transport in EGS4.

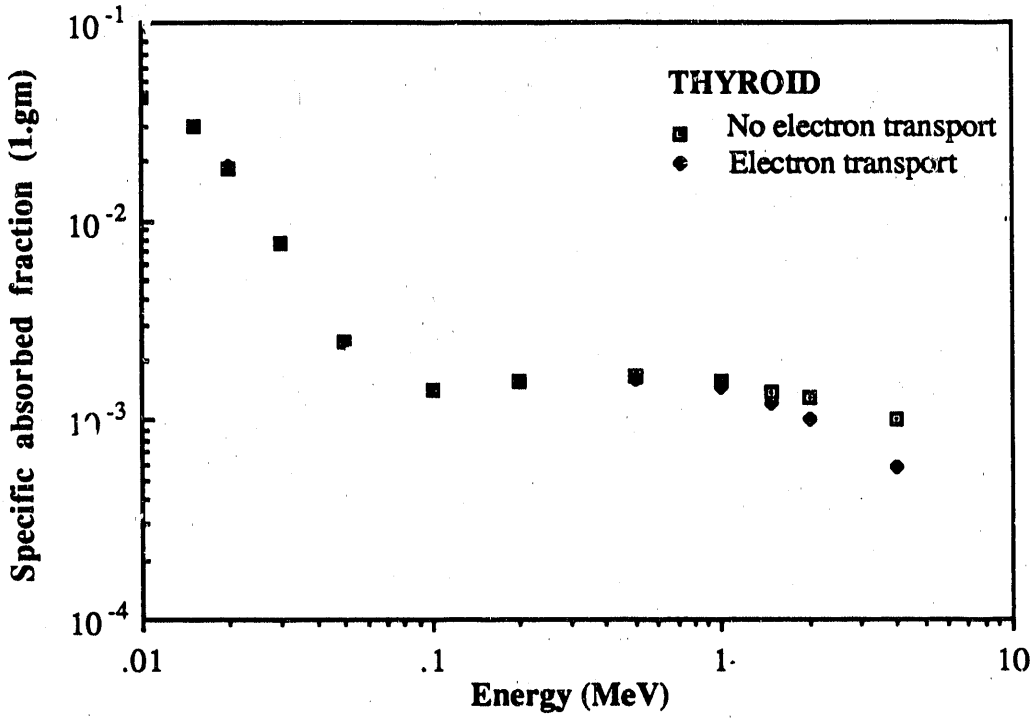

FIGUR E 2. Comparison between Specific Absorbed Fraction (SAF) with and without electron transport using the EGS4 code. The thyroid is the source and target organ. For high energy photons there is a lower SAF than that calculated without electron transport due to electrons are escaping from the thyroid.

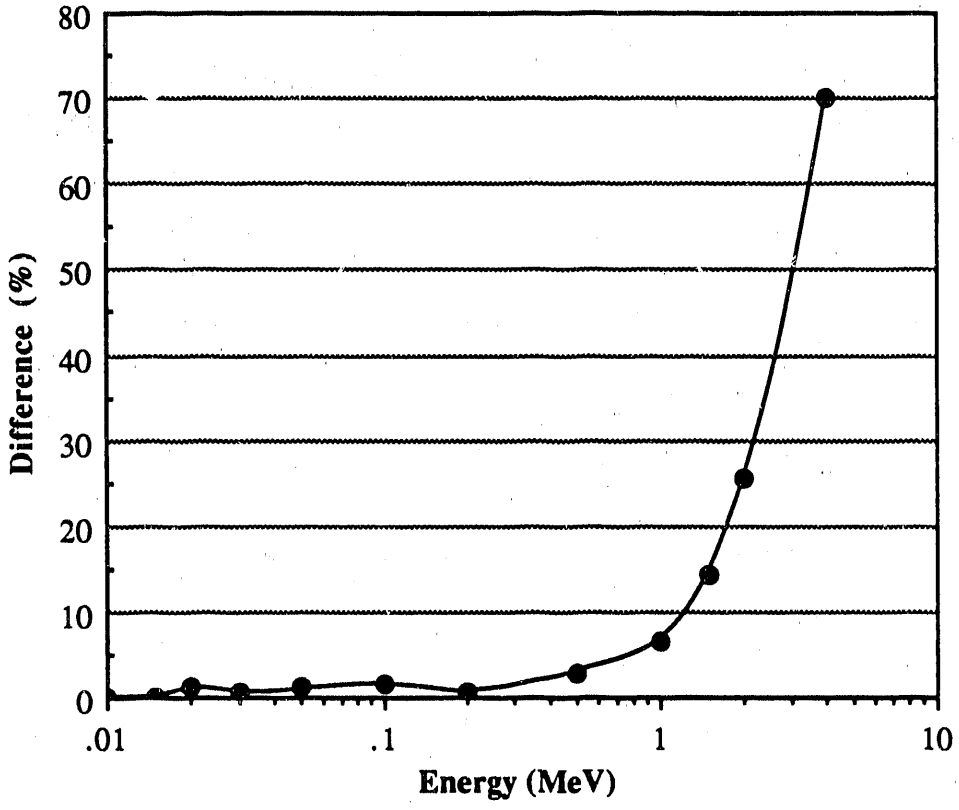

FIGURE 3. Percent differences of the specific absorbed fraction of energy between electron and non-electron modalities of EGS4 transport of electrons produced by photon interactions in the thyroid.

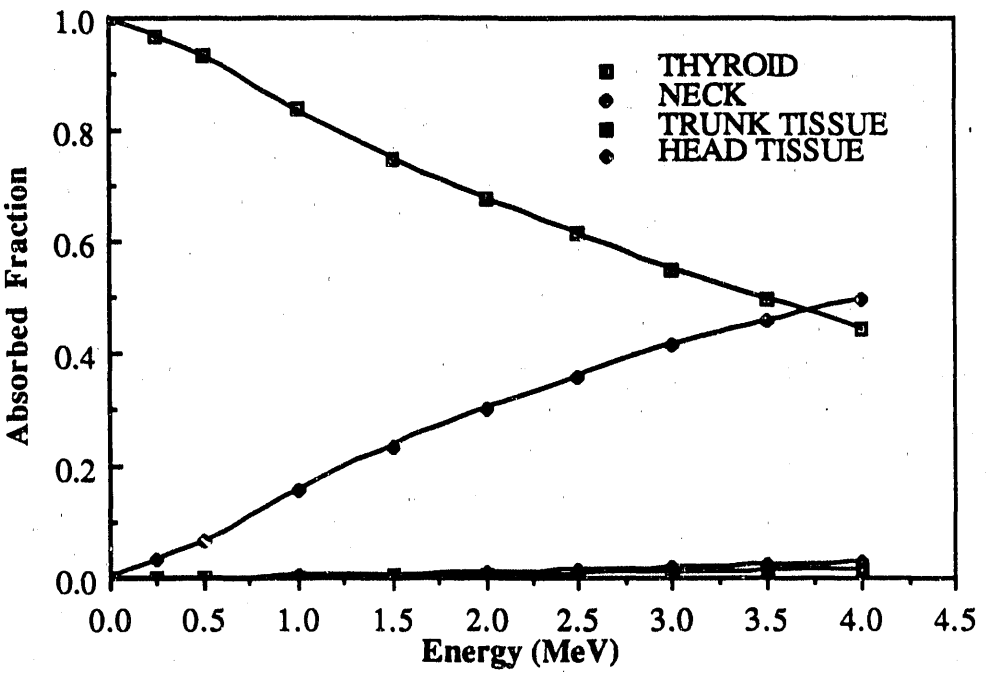

FIGURE 4. Absorbed fractions for electrons for different regions. Source organ is thyroid gland.

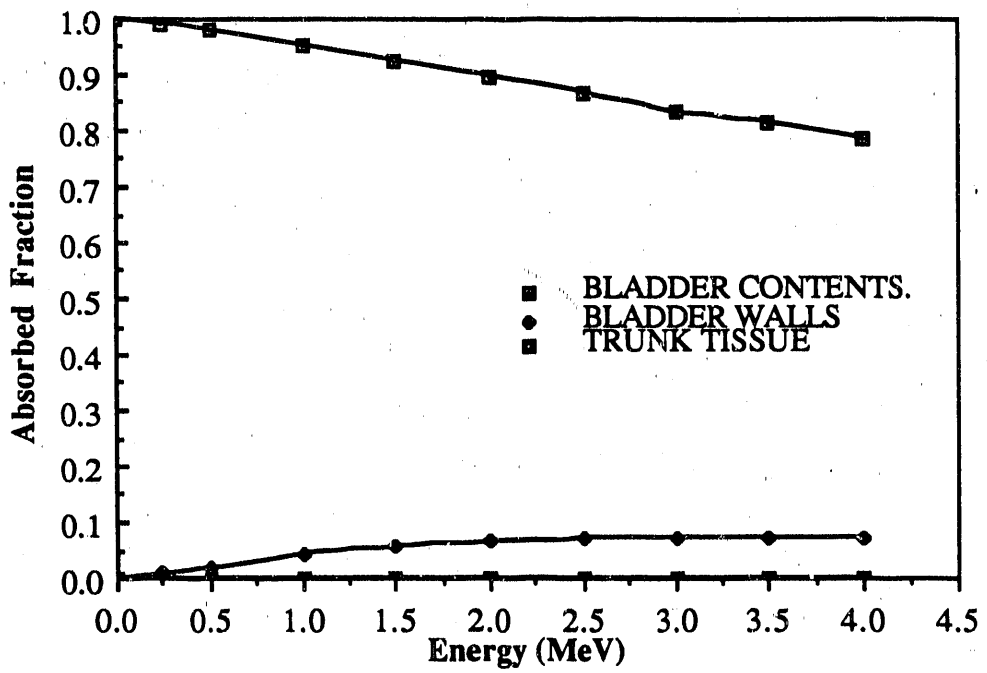

FIGURE 5. Absorbed fractions for electrons for different regions. Source organ is bladder contents.

TABLE 1

Source-Target Combinations Used in This Study

	SOURCE	TARGET
1	Bladder cont.	Bladder wall
2	Upper large intestine cont.	Upper large intestine wall
3	Gallbladder cont.	Gallbladder wall
4	Heart cont.	Heart wall
5	Lower large intestine cont.	Lower large intestine wall
6	Lungs	Lungs
7	Ovaries	Ovaries
8	Pancreas	Pancreas
9	Spleen	Spleen
10	Stomach cont.	Stomach wall
11	Testes	Testes
12	Thyroid	Thyroid
13	Kidney cortex	Kidney cortex
14	Kidney cortex	Kidney medulla
15	Kidney cortex	Kidney papillary
16	Kidney medulla	Kidney cortex
17	Kidney medulla	Kidney medulla
18	Kidney medulla	Kidney papillary
19	Kidney papillary	kidney cortex
20	Kidney papillary	Kidney medulla
21	Kidney papillary	Kidney papillary

TABLE 2

S-values for the Thyroid as a Source and Target Region

Radionuclide	MIRD	EGS4	DIFF(%)	Radionuclide	MIRD	EGS4	DIFF(%)
C-11	4.55E-02	4.33E-02	4.78%	Y-90m	7.25E-03	6.97E-03	3.94%
C-14	5.39E-03	5.35E-03	0.67%	Y-90	1.02E-01	8.64E-02	15.13%
N-13	5.70E-02	5.35E-02	6.21%	Tc-99m	2.08E-03	2.06E-03	1.15%
O-15	8.36E-02	7.45E-02	10.79%	Ru-97	3.86E-03	3.83E-03	0.88%
F-18	3.08E-02	2.99E-02	2.97%	In-111	5.50E-03	5.43E-03	1.36%
Na-22	2.84E-02	2.78E-02	2.15%	In-113m	1.56E-02	1.49E-02	4.58%
Na-24	7.17E-02	6.70E-02	6.53%	In-111m	8.70E-03	8.21E-03	5.55%
P-32	7.57E-02	6.77E-02	10.50%	In-114m	1.62E-02	1.58E-02	2.23%
S-35	5.29E-03	5.26E-03	0.64%	I-123	3.88E-03	3.84E-03	1.06%
K-42	1.56E-01	1.18E-01	24.46%	I-124	2.51E-02	2.23E-02	11.21%
K-43	3.75E-02	3.59E-02	4.20%	I-125	2.68E-03	2.68E-03	0.15%
Ca-45	8.41E-03	8.32E-03	1.05%	I-126	1.74E-02	1.67E-02	4.05%
Ca-49	1.03E-01	8.90E-02	13.18%	I-129	4.49E-03	4.46E-03	0.53%
Sc-47	1.81E-02	1.77E-02	2.20%	I-130	3.84E-02	3.71E-02	3.44%
Sc-49	8.90E-02	7.75E-02	12.87%	I-131	2.21E-02	2.15E-02	2.41%
Cr-51	6.24E-04	6.24E-04	0.00%	Xe-120	6.65E-03	6.57E-03	1.19%
Mn-52m	1 31E-01	1.07E-01	18.22%	Xe-121	6.60E-02	5.41E-02	18.02%
Fe-52	2.37E-02	2.28E-02	4.01%	Xe-122	1.39E-03	1.39E-03	0.36%
Fe-52m	2.30E-01	1.59E-01	30.64%	Xe-123	2.25E-02	2.08E-02	7.51%
Fe-55	6.16E-04	6.16E-04	0.00%	Xe-125	4.86E-03	4.81E-03	1.09%
Fe-59	1.66E-02	1.64E-02	1.37%	Xe-127	4.63E-03	4.57E-03	1.25%
Co-57	2.14E-03	2.13E-03	0.37%	Cs-129	2.95E-03	2.93E-03	0.68%
Co-58	7.18E-03	7.09E-03	1.25%	Dy-157	1.65E-03	1.63E-03	0.85%
Co-58m	2.49E-03	2.48E-03	0.20%	Yb-169	1.37E-02	1.35E-02	1.07%
Co-60	1.84E-02	1.83E-02	0.73%	W-178	6.87E-04	6.87E-04	0.00%
Co-60m	7.37E-03	7.31E-03	0.83%	Ir-192	2.61E-02	2.54E-02	2.45%
Cu-62	1.43E-01	1.12E-01	21.31%	Au-195	5.49E-03	5.46E-03	0.47%
Cu-64	1.41E-02	1.37E-02	2.83%	Au-195m	1.30E-02	1.28E-02	1.57%
Cu-67	1.72E-02	1.69E-02	1.86%	Au-198	3.70E-02	3.55E-02	4.09%
Ga-66	1.15E-01	8.21E-02	28.39%	Hg-195	6.94E-03	6.89E-03	0.75%
Ga-67	4.33E-03	4.30E-03	0.72%	Hg-197	7.19E-03	7.14E-03	0.71%
Ga-68	8.40E-02	7.33E-02	12.63%	Hg-197m	2.34E-02	2.30E-02	1.71%
Ga-72	6.28E-02	5.60E-02	10.87%	Hg-203	1.16E-02	1.14E-02	1.54%
Se-73	4.67E-02	4.35E-02	6.96%	Tl-201m	6.95E-03	6.73E-03	3.18%
Se-75	3.30E-03	3.29E-03	0.42%	Tl-201	5.10E-03	5.06E-03	0.80%
Kr-81m	6.84E-03	6.69E-03	2.14%	Te-123m	1.17E-02	1.16E-02	1.05%
Rb-82m	2.05E-02	1.98E-02	3.37%	Pt-195m	1.94E-02	1.92E-02	1.14%
Rb-82	1.57E-01	1.19E-01	24.24%	Pb-203m1	1.93E-02	1.73E-02	10.18%
Sr-90	2.13E-02	2.08E-02	2.64%	Pb-203m	2.96E-02	2.87E-02	3.01%
Y-87	2.88E-03	2.88E-03	0.31%	Pb-203	5.41E-03	5.32E-03	1.77%

TABLE 3

S-values for the Bladder Contents as a Source Region and Bladder Wall as a Target Region

Radionuclide	MIRD	EGS4	DIFF(%)	Radionuclide	MIRD	EGS4	DIFF(%)
C-11	2.61E-03	7.95E-04	69.51%	Y-90m	5.90E-04	3.77E-04	36.10%
C-14	2.64E-04	4.00E-06	98.48%	Y-90	4.99E-03	1.74E-03	65.06%
N-13	3.18E-03	9.62E-04	69.70%	Tc-99m	1.52E-04	7.40E-05	51.32%
O-15	4.47E-03	1.58E-03	64.66%	Ru-97	2.88E-04	1.71E-04	40.63%
F-18	1.89E-03	6.47E-04	65.75%	In-111	4.45E-04	2.75E-04	38.20%
Na-22	2.12E-03	1.14E-03	45.98%	In-113m	8.67E-04	2.33E-04	73.13%
Na-24	4.64E-03	2.22E-03	52.09%	In-111m	6.02E-04	3.15E-04	47.67%
P-32	3.71E-03	9.04E-04	75.61%	In-114m	8.41E-04	1.12E-04	86.68%
S-35	2.59E-04	3.00E-06	98.84%	I-123	2.91E-04	1.54E-04	47.08%
K-42	7.73E-03	3.81E-03	50.74%	I-124	1.62E-03	8.92E-04	44.80%
K-43	2.18E-03	6.76E-04	69.03%	I-125	2.09E-04	1.22E-04	41.63%
Ca-45	4.12E-04	9.00E-06	97.82%	I-126	1.03E-03	3.33E-04	67.61%
Ca-49	5.81E-03	2.70E-03	53.51%	I-129	2.23E-04	7.00E-06	96.86%
Sc-47	9.26E-04	9.70E-05	89.52%	I-130	2.63E-03	1.25E-03	52.43%
Sc-49	4.36E-03	1.30E-03	70.19%	I-131	1.22E-03	2.60E-04	78.76%
Cr-51	8.90E-05	7.00E-05	21.35%	Xe-120	5.30E-04	3.14E-04	40.75%
Mn-52m	7.22E-03	3.71E-03	48.66%	Xe-121	3.82E-03	2.09E-03	45.29%
Fe-52	1.47E-03	5.42E-04	63.15%	Xe-122	1.29E-04	9.10E-05	29.46%
Fe-52m	1.24E-02	7.89E-03	36.60%	Xe-123	1.35E-03	5.50E-04	59.14%
Fe-55	1.00E-04	7.90E-05	21.00%	Xe-125	3.81E-04	2.16E-04	43.31%
Fe-59	1.18E-03	5.72E-04	51.32%	Xe-127	3.70E-04	2.16E-04	41.62%
Co-57	3.05E-04	2.43E-04	20.33%	Cs-129	2.98E-04	2.26E-04	24.16%
Co-58	7.56E-04	5.84E-04	22.75%	Dy-157	1.99E-04	1.72E-04	13.57%
Co-58m	2.00E-04	8.90E-05	55.50%	Yb-169	9.77E-04	4.02E-04	58.85%
Co-60	1.66E-03	1.16E-03	29.99%	W-178	1.15E-04	9.40E-05	18.26%
Co-60m	4.54E-04	1.12E-04	75.33%	Ir-192	1.60E-03	5.28E-04	67.02%
Cu-62	7.38E-03	3.64E-03	50.67%	Au-195	5.41E-04	3.20E-04	40.85%
Cu-64	8.15E-04	2.02E-04	75.21%	Au-195m	8.57E-04	2.90E-04	66.16%
Cu-67	9.11E-04	1.21E-04	86.72%	Au-198	1.97E-03	3.84E-04	80.48%
Ga-66	6.40E-03	4.02E-03	37.17%	Hg-195	6.27E-04	3.53E-04	43.70%
Ga-67	4.73E-04	3.15E-04	33.40%	Hg-197	5.93E-04	2.85E-04	51.94%
Ga-68	4.48E-03	1.73E-03	61.29%	Hg-197m	1.38E-03	3.17E-04	77.08%
Ga-72	3.90E-03	1.94E-03	50.24%	Hg-203	6.55E-04	1.47E-04	77.56%
Se-73	2.71E-03	1.00E-03	62.99%	Tl-201m	6.37E-04	4.61E-04	27.63%
Se-75	2.92E-04	2.20E-04	24.66%	Tl-201	5.18E-04	3.18E-04	38.61%
Kr-81m	3.80E-04	8.80E-05	76.84%	Te-123m	6.57E-04	1.32E-04	79.91%
Rb-82m	1.97E-03	1.54E-03	21.70%	Pt-195m	1.28E-03	4.01E-04	68.70%
Rb-82	8.12E-03	4.29E-03	47.10%	Pb-203m1	1.18E-03	5.69E-04	51.66%
Sr-90	1.05E-03	5.60E-05	94.64%	Pb-203m	2.09E-03	1.08E-03	48.47%
Y-87	3.06E-04	2.72E-04	11.11%	Pb-203	3.82E-04	1.96E-04	48.69%

APPENDIX A

REVISED S-VALUES

Table 1. S-values for the bladder contents as a source region and bladder wall as a target region.

Radionuclide	MIRD	EGS4	DIFF(%)	Radionuclide	MIRD	EGS4	DIFF(%)
C-11	2.61E-03	7.95E-04	69.51%	Y-90m	5.90E-04	3.77E-04	36.10%
C-14	2.64E-04	4.00E-06	98.48%	Y-90	4.99E-03	1.74E-03	65.06%
N-13	3.18E-03	9.62E-04	69.70%	Tc-99m	1.52E-04	7.40E-05	51.32%
O-15	4.47E-03	1.58E-03	64.66%	Ru-97	2.88E-04	1.71E-04	40.63%
F-18	1.89E-03	6.47E-04	65.75%	In-111	4.45E-04	2.75E-04	38.20%
Na-22	2.12E-03	1.14E-03	45.98%	In-113m	8.67E-04	2.33E-04	73.13%
Na-24	4.64E-03	2.22E-03	52.09%	In-111m	6.02E-04	3.15E-04	47.67%
P-32	3.71E-03	9.04E-04	75.61%	In-114m	8.41E-04	1.12E-04	86.68%
S-35	2.59E-04	3.00E-06	98.84%	I-123	2.91E-04	1.54E-04	47.08%
K-42	7.73E-03	3.81E-03	50.74%	I-124	1.62E-03	8.92E-04	44.80%
K-43	2.18E-03	6.76E-04	69.03%	I-125	2.09E-04	1.22E-04	41.63%
Ca-45	4.12E-04	9.00E-06	97.82%	I-126	1.03E-03	3.33E-04	67.61%
Ca-49	5.81E-03	2.70E-03	53.51%	I-129	2.23E-04	7.00E-06	96.86%
Sc-47	9.26E-04	9.70E-05	89.52%	I-130	2.63E-03	1.25E-03	52.43%
Sc-49	4.36E-03	1.30E-03	70.19%	I-131	1.22E-03	2.60E-04	78.76%
Cr-51	8.90E-05	7.00E-05	21.35%	Xe-120	5.30E-04	3.14E-04	40.75%
Mn-52m	7.22E-03	3.71E-03	48.66%	Xe-121	3.82E-03	2.09E-03	45.29%
Fe-52	1.47E-03	5.42E-04	63.15%	Xe-122	1.29E-04	9.10E-05	29.46%
Fe-52m	1.24E-02	7.89E-03	36.60%	Xe-123	1.35E-03	5.50E-04	59.14%
Fe-55	1.00E-04	7.90E-05	21.00%	Xe-125	3.81E-04	2.16E-04	43.31%
Fe-59	1.18E-03	5.72E-04	51.32%	Xe-127	3.70E-04	2.16E-04	41.62%
Co-57	3.05E-04	2.43E-04	20.33%	Cs-129	2.98E-04	2.26E-04	24.16%
Co-58	7.56E-04	5.84E-04	22.75%	Dy-157	1.99E-04	1.72E-04	13.57%
Co-58m	2.00E-04	8.90E-05	55.50%	Yb-169	9.77E-04	4.02E-04	58.85%
Co-60	1.66E-03	1.16E-03	29.99%	W-178	1.15E-04	9.40E-05	18.26%
Co-60m	4.54E-04	1.12E-04	75.33%	Ir-192	1.60E-03	5.28E-04	67.02%
Cu-62	7.38E-03	3.64E-03	50.67%	Au-195	5.41E-04	3.20E-04	40.85%
Cu-64	8.15E-04	2.02E-04	75.21%	Au-195m	8.57E-04	2.90E-04	66.16%
Cu-67	9.11E-04	1.21E-04	86.72%	Au-198	1.97E-03	3.84E-04	80.48%
Ga-66	6.40E-03	4.02E-03	37.17%	Hg-195	6.27E-04	3.53E-04	43.70%
Ga-67	4.73E-04	3.15E-04	33.40%	Hg-197	5.93E-04	2.85E-04	51.94%
Ga-68	4.48E-03	1.73E-03	61.29%	Hg-197m	1.38E-03	3.17E-04	77.08%
Ga-72	3.90E-03	1.94E-03	50.24%	Hg-203	6.55E-04	1.47E-04	77.56%
Se-73	2.71E-03	1.00E-03	62.99%	Tl-201m	6.37E-04	4.61E-04	27.63%
Se-75	2.92E-04	2.20E-04	24.66%	Tl-201	5.18E-04	3.18E-04	38.61%
Kr-81m	3.80E-04	8.80E-05	76.84%	Te-123m	6.57E-04	1.32E-04	79.91%
Rb-82m	1.97E-03	1.54E-03	21.70%	Pt-195m	1.28E-03	4.01E-04	68.70%
Rb-82	8.12E-03	4.29E-03	47.10%	Pb-203m1	1.18E-03	5.69E-04	51.66%
Sr-90	1.05E-03	5.60E-05	94.64%	Pb-203m	2.09E-03	1.08E-03	48.47%
Y-87	3.06E-04	2.72E-04	11.11%	Pb-203	3.82E-04	1.96E-04	48.69%

Table 2. S-values for the upper large intestines as a source region and upper large intestines wall as a target region.

Radionuclide	MIRD	EGS4	DIFF(%)	Radionuclide	MIRD	EGS4	DIFF(%)
C-11	2.18E-03	4.01E-04	81.65%	Y-90m	4.23E-04	2.12E-04	49.91%
C-14	2.40E-04	9.17E-07	99.62%	Y-90	4.53E-03	6.27E-04	86.18%
N-13	2.70E-03	4.70E-04	82.61%	Tc-99m	1.15E-04	4.33E-05	62.34%
O-15	3.88E-03	6.91E-04	82.18%	Ru-97	2.07E-04	9.81E-05	52.55%
F-18	1.53E-03	3.43E-04	77.59%	In-111	3.16E-04	1.57E-04	50.39%
Na-22	1.58E-03	6.59E-04	58.35%	In-113m	7.37E-04	1.15E-04	84.39%
Na-24	3.70E-03	1.21E-03	67.25%	In-111m	4.61E-04	1.70E-04	63.09%
P-32	3.37E-03	3.29E-04	90.24%	In-114m	7.37E-04	5.13E-05	93.04%
S-35	2.36E-04	8.86E-07	99.62%	I-123	2.10E-04	8.31E-05	60.43%
K-42	6.98E-03	1.72E-03	75.38%	I-124	1.28E-03	4.47E-04	65.11%
K-43	1.82E-03	3.50E-04	80.75%	I-125	1.40E-04	6.01E-05	56.99%
Ca-45	3.74E-04	2.23E-06	99.40%	I-126	8.48E-04	1.72E-04	79.70%
Ca-49	4.92E-03	1.25E-03	74.56%	I-129	2.01E-04	3.30E-06	98.36%
Sc-47	8.24E-04	4.47E-05	94.58%	I-130	2.04E-03	7.00E-04	65.68%
Sc-49	3.96E-03	4.70E-04	88.15%	I-131	1.05E-03	1.35E-04	87.12%
Cr-51	3.91E-05	2.15E-05	44.82%	Xe-120	3.74E-04	1.72E-04	53.87%
Mn-52m	6.19E-03	1.69E-03	72.70%	Xe-121	3.19E-03	1.01E-03	68.40%
Fe-52	1.18E-03	2.75E-04	76.71%	Xe-122	8.12E-05	4.63E-05	43.03%
Fe-52m	1.08E-02	4.18E-03	61.21%	Xe-123	1.10E-03	2.74E-04	75.13%
Fe-55	3.64E-05	1.70E-05	53.31%	Xe-125	2.71E-04	1.17E-04	56.87%
Fe-59	9.08E-04	3.45E-04	62.03%	Xe-127	2.62E-04	1.18E-04	55.06%
Co-57	1.35E-04	7.86E-05	41.73%	Cs-129	1.89E-04	1.21E-04	35.62%
Co-58	4.78E-04	3.16E-04	33.77%	Dy-157	1.24E-04	9.90E-05	20.44%
Co-58m	1.21E-04	1.92E-05	84.13%	Yb-169	6.99E-04	1.66E-04	76.21%
Co-60	1.17E-03	7.06E-04	39.47%	W-178	4.42E-05	2.51E-05	43.35%
Co-60m	3.41E-04	2.55E-05	92.53%	Ir-192	1.29E-03	2.78E-04	78.50%
Cu-62	6.52E-03	1.60E-03	75.42%	Au-195	2.95E-04	9.25E-05	68.62%
Cu-64	6.65E-04	8.27E-05	87.56%	Au-195m	6.33E-04	1.04E-04	83.52%
Cu-67	7.90E-04	5.11E-05	93.54%	Au-198	1.71E-03	1.77E-04	89.65%
Ga-66	5.43E-03	2.08E-03	61.68%	Hg-195	3.72E-04	1.20E-04	67.87%
Ga-67	2.45E-04	9.89E-05	59.65%	Hg-197	3.64E-04	8.05E-05	77.86%
Ga-68	3.89E-03	7.33E-04	81.14%	Hg-197m	1.09E-03	9.08E-05	91.64%
Ga-72	3.17E-03	1.01E-03	68.04%	Hg-203	5.54E-04	8.07E-05	85.42%
Se-73	2.26E-03	5.02E-04	77.77%	Tl-201m	4.37E-04	2.63E-04	39.78%
Se-75	1.94E-04	1.28E-04	34.06%	Tl-201	2.78E-04	9.32E-05	66.43%
Kr-81m	3.22E-04	4.69E-05	85.40%	Te-123m	5.53E-04	6.80E-05	87.70%
Rb-82m	1.33E-03	9.02E-04	32.26%	Pt-195m	9.21E-04	1.07E-04	88.39%
Rb-82	7.18E-03	1.98E-03	72.43%	Pb-203m1	9.59E-04	2.84E-04	70.36%
Sr-90	9.50E-04	1.44E-05	98.49%	Pb-203m	1.60E-03	6.24E-04	61.06%
Y-87	1.87E-04	1.55E-04	17.05%	Pb-203	2.86E-04	1.11E-04	61.13%

Table 3. S-values for different radionuclides for the gallbladder contents as a source region and gallbladder wall as a target region.

Radionuclide	MIRD	EGS4	DIFF(%)	Radionuclide	MIRD	EGS4	DIFF(%)
C-11	8.30E-03	2.66E-03	68.01%	Y-90m	1.46E-03	8.16E-04	43.92%
C-14	9.48E-04	2.10E-05	97.78%	Y-90	1.79E-02	9.54E-03	46.70%
N-13	1.03E-02	4.04E-03	60.95%	Tc-99m	4.06E-04	1.34E-04	67.00%
O-15	1.50E-02	7.17E-03	52.21%	Ru-97	7.12E-04	2.99E-04	58.01%
F-18	5.72E-03	1.47E-03	74.39%	In-111	1.11E-03	5.14E-04	53.57%
Na-22	5.54E-03	2.18E-03	60.58%	In-113m	2.83E-03	8.21E-04	70.96%
Na-24	1.33E-02	6.55E-03	50.83%	In-111m	1.67E-03	8.58E-04	48.62%
P-32	1.33E-02	5.66E-03	57.49%	In-114m	2.90E-03	3.59E-04	87.60%
S-35	9.32E-04	2.00E-05	97.85%	I-123	8.05E-04	3.23E-04	59.88%
K-42	2.75E-02	1.64E-02	40.40%	I-124	4.74E-03	2.81E-03	40.76%
K-43	6.87E-03	1.96E-03	71.47%	I-125	5.98E-04	2.85E-04	52.34%
Ca-45	1.48E-03	5.10E-05	96.55%	I-126	3.22E-03	9.79E-04	69.63%
Ca-49	1.85E-02	1.03E-02	44.06%	I-129	7.92E-04	2.30E-05	97.10%
Sc-47	3.22E-03	3.28E-04	89.80%	I-130	7.35E-03	2.84E-03	61.38%
Sc-49	1.57E-02	7.52E-03	51.95%	I-131	4.00E-03	6.63E-04	83.43%
Cr-51	3.25E-04	2.56E-04	21.23%	Xe-120	1.40E-03	6.51E-04	53.47%
Mn-52m	2.37E-02	1.45E-02	38.84%	Xe-121	1.21E-02	7.31E-03	39.45%
Fe-52	4.54E-03	1.53E-03	66.17%	Xe-122	3.37E-04	2.02E-04	40.06%
Fe-52m	4.13E-02	2.71E-02	34.37%	Xe-123	4.19E-03	1.87E-03	55.41%
Fe-55	4.14E-04	3.38E-04	18.36%	Xe-125	1.03E-03	4.46E-04	56.66%
Fe-59	3.18E-03	1.07E-03	66.40%	Xe-127	9.81E-04	4.40E-04	55.15%
Co-57	1.08E-03	8.62E-04	20.26%	Cs-129	7.14E-04	4.60E-04	35.57%
Co-58	1.83E-03	1.24E-03	32.50%	Dy-157	3.99E-04	3.06E-04	23.31%
Co-58m	7.81E-04	3.82E-04	51.09%	Yb-169	3.23E-03	1.19E-03	63.02%
Co-60	3.78E-03	2.03E-03	46.42%	W-178	4.46E-04	3.70E-04	17.04%
Co-60m	1.70E-03	4.84E-04	71.51%	Ir-192	4.93E-03	1.23E-03	75.09%
Cu-62	2.55E-02	1.53E-02	39.74%	Au-195	2.00E-03	1.22E-03	39.26%
Cu-64	2.77E-03	6.71E-04	75.78%	Au-195m	2.98E-03	9.92E-04	66.73%
Cu-67	3.17E-03	4.04E-04	87.26%	Au-198	6.65E-03	1.46E-03	78.04%
Ga-66	2.09E-02	1.37E-02	34.75%	Hg-195	2.20E-03	1.23E-03	44.10%
Ga-67	1.70E-03	1.14E-03	32.98%	Hg-197	2.20E-03	1.10E-03	49.77%
Ga-68	1.51E-02	7.84E-03	48.13%	Hg-197m	5.02E-03	1.28E-03	74.46%
Ga-72	1.16E-02	5.78E-03	50.23%	Hg-203	2.10E-03	3.19E-04	84.82%
Se-73	8.53E-03	3.68E-03	56.88%	Tl-201m	1.45E-03	9.09E-04	37.40%
Se-75	6.11E-04	3.57E-04	41.57%	Tl-201	1.91E-03	1.20E-03	37.08%
Kr-81m	1.22E-03	2.01E-04	83.47%	Te-123m	2.17E-03	3.18E-04	85.37%
Rb-82m	4.27E-03	2.93E-03	31.36%	Pt-195m	4.73E-03	1.62E-03	65.79%
Rb-82	2.80E-02	1.72E-02	38.50%	Pb-203m1	3.61E-03	1.97E-03	45.57%
Sr-90	3.75E-03	3.26E-04	91.31%	Pb-203m	5.64E-03	2.21E-03	60.88%
Y-87	5.61E-04	4.42E-04	21.21%	Pb-203	1.00E-03	3.59E-04	64.21%

Table 4. S-values for the heart contents as a source region and heart walls as a target region.

Radionuclide	MIRD	EGS4	DIFF(%)	Radionuclide	MIRD	EGS4	DIFF(%)
C-11	1.24E-03	3.25E-04	73.74%	Y-90m	2.92E-04	1.84E-04	37.01%
C-14	1.22E-04	5.19E-07	99.58%	Y-90	2.31E-03	2.98E-04	87.10%
N-13	1.50E-03	3.56E-04	76.28%	Tc-99m	7.49E-05	3.83E-05	48.84%
O-15	2.10E-03	4.62E-04	78.05%	Ru-97	1.36E-04	8.04E-05	40.81%
F-18	9.04E-04	2.99E-04	66.96%	In-111	2.15E-04	1.33E-04	37.81%
Na-22	1.05E-03	5.82E-04	44.73%	In-113m	4.08E-04	9.06E-05	77.81%
Na-24	2.25E-03	9.70E-04	56.84%	In-111m	2.92E-04	1.42E-04	51.16%
P-32	1.72E-03	1.56E-04	90.93%	In-114m	3.90E-04	4.00E-05	89.73%
S-35	1.20E-04	5.02E-07	99.58%	I-123	1.35E-04	7.01E-05	48.02%
K-42	3.59E-03	7.68E-04	78.62%	I-124	7.76E-04	3.46E-04	55.38%
K-43	1.04E-03	2.92E-04	71.95%	I-125	8.73E-05	4.66E-05	46.55%
Ca-45	1.91E-04	1.26E-06	99.34%	I-126	4.87E-04	1.42E-04	70.85%
Ca-49	2.75E-03	8.57E-04	68.80%	I-129	1.04E-04	2.65E-06	97.44%
Sc-47	4.34E-04	3.69E-05	91.50%	I-130	1.29E-03	6.07E-04	52.99%
Sc-49	2.02E-03	2.23E-04	88.96%	I-131	5.80E-04	1.16E-04	80.05%
Cr-51	2.60E-05	1.71E-05	34.38%	Xe-120	2.50E-04	1.47E-04	41.17%
Mn-52m	3.42E-03	1.07E-03	68.80%	Xe-121	1.82E-03	6.67E-04	63.26%
Fe-52	6.94E-04	2.31E-04	66.63%	Xe-122	5.60E-05	3.82E-05	31.84%
Fe-52m	5.90E-03	2.22E-03	62.33%	Xe-123	6.38E-04	2.13E-04	66.68%
Fe-55	2.18E-05	1.19E-05	45.47%	Xe-125	1.79E-04	1.00E-04	43.97%
Fe-59	5.91E-04	3.04E-04	48.54%	Xe-127	1.75E-04	1.01E-04	42.04%
Co-57	9.14E-05	6.27E-05	31.42%	Cs-129	1.39E-04	1.05E-04	24.62%
Co-58	3.60E-04	2.78E-04	22.83%	Dy-157	1.01E-04	8.83E-05	12.80%
Co-58m	6.53E-05	1.34E-05	79.49%	Yb-169	4.14E-04	1.42E-04	65.71%
Co-60	8.61E-04	6.26E-04	27.29%	W-178	2.89E-05	1.91E-05	33.83%
Co-60m	1.79E-04	1.78E-05	90.03%	Ir-192	7.60E-04	2.42E-04	68.14%
Cu-62	3.45E-03	8.47E-04	75.45%	Au-195	1.76E-04	7.24E-05	58.75%
Cu-64	3.65E-04	6.76E-05	81.45%	Au-195m	3.55E-04	8.51E-05	76.01%
Cu-67	4.19E-04	4.22E-05	89.94%	Au-198	9.23E-04	1.39E-04	84.89%
Ga-66	3.01E-03	1.16E-03	61.57%	Hg-195	2.26E-04	9.69E-05	57.07%
Ga-67	1.53E-04	7.88E-05	48.61%	Hg-197	2.07E-04	6.25E-05	69.81%
Ga-68	2.10E-03	4.73E-04	77.47%	Hg-197m	5.76E-04	6.89E-05	88.04%
Ga-72	1.88E-03	7.70E-04	59.15%	Hg-203	3.12E-04	7.07E-05	77.33%
Se-73	1.29E-03	3.90E-04	69.79%	Tl-201m	3.20E-04	2.31E-04	27.78%
Se-75	1.47E-04	1.13E-04	22.98%	Tl-201	1.67E-04	7.32E-05	56.25%
Kr-81m	1.80E-04	3.99E-05	77.80%	Te-123m	3.05E-04	5.74E-05	81.17%
Rb-82m	1.01E-03	7.90E-04	21.79%	Pt-195m	4.96E-04	8.06E-05	83.75%
Rb-82	3.80E-03	1.00E-03	73.56%	Pb-203m1	5.66E-04	2.19E-04	61.34%
Sr-90	4.85E-04	8.13E-06	98.32%	Pb-203m	1.04E-03	5.44E-04	47.90%
Y-87	1.50E-04	1.34E-04	10.87%	Pb-203	1.88E-04	9.83E-05	47.58%

Table 5. S-values for lower large intestines as a source region and lower large intestine wall as a target region.

Radionuclide	MIRD	EGS4	DIFF(%)	Radionuclide	MIRD	EGS4	DIFF(%)
C-11	3.39E-03	5.02E-04	85.18%	Y-90m	5.99E-04	2.57E-04	57.09%
C-14	3.86E-04	1.41E-06	99.64%	Y-90	7.29E-03	9.46E-04	87.02%
N-13	4.21E-03	5.95E-04	85.87%	Tc-99m	1.67E-04	5.13E-05	69.24%
O-15	6.11E-03	9.35E-04	84.70%	Ru-97	2.96E-04	1.21E-04	59.02%
F-18	2.33E-03	4.22E-04	81.93%	In-111	4.47E-04	1.91E-04	57.32%
Na-22	2.28E-03	7.96E-04	65.13%	In-113m	1.15E-03	1.45E-04	87.37%
Na-24	5.52E-03	1.48E-03	73.17%	In-111m	6.81E-04	2.09E-04	69.26%
P-32	5.42E-03	4.83E-04	91.09%	In-114m	1.17E-03	6.62E-05	94.35%
S-35	3.79E-04	1.36E-06	99.64%	I-123	3.06E-04	1.02E-04	66.68%
K-42	1.12E-02	2.41E-03	78.50%	I-124	1.93E-03	5.73E-04	70.27%
K-43	2.80E-03	4.34E-04	84.54%	I-125	2.05E-04	7.72E-05	62.39%
Ca-45	6.02E-04	3.43E-06	99.43%	I-126	1.31E-03	2.14E-04	83.63%
Ca-49	7.60E-03	1.64E-03	78.36%	I-129	3.22E-04	4.26E-06	98.68%
Sc-47	1.31E-03	5.61E-05	95.72%	I-130	3.01E-03	8.48E-04	71.84%
Sc-49	6.38E-03	7.01E-04	89.00%	I-131	1.63E-03	1.66E-04	89.84%
Cr-51	5.52E-05	2.70E-05	51.03%	Xe-120	5.35E-04	2.11E-04	60.64%
Mn-52m	9.68E-03	2.30E-03	76.22%	Xe-121	4.93E-03	1.33E-03	72.97%
Fe-52	1.80E-03	3.39E-04	81.19%	Xe-122	1.14E-04	5.79E-05	49.27%
Fe-52m	1.69E-02	5.54E-03	67.17%	Xe-123	1.69E-03	3.48E-04	79.41%
Fe-55	5.34E-05	2.22E-05	58.44%	Xe-125	3.91E-04	1.43E-04	63.45%
Fe-59	1.32E-03	4.10E-04	68.85%	Xe-127	3.75E-04	1.43E-04	61.81%
Co-57	1.88E-04	9.74E-05	48.18%	Cs-129	2.57E-04	1.49E-04	42.12%
Co-58	6.37E-04	3.78E-04	40.73%	Dy-157	1.59E-04	1.18E-04	25.70%
Co-58m	1.89E-04	2.51E-05	86.70%	Yb-169	1.06E-03	2.00E-04	81.11%
Co-60	1.58E-03	8.43E-04	46.80%	W-178	6.23E-05	3.15E-05	49.49%
Co-60m	5.41E-04	3.34E-05	93.82%	Ir-192	1.98E-03	3.39E-04	82.83%
Cu-62	1.04E-02	2.23E-03	78.45%	Au-195	4.40E-04	1.15E-04	73.88%
Cu-64	1.04E-03	1.04E-04	89.98%	Au-195m	9.81E-04	1.30E-04	86.78%
Cu-67	1.25E-03	6.37E-05	94.92%	Au-198	2.70E-03	2.26E-04	91.64%
Ga-66	8.46E-03	2.74E-03	67.59%	Hg-195	5.53E-04	1.47E-04	73.42%
Ga-67	3.58E-04	1.23E-04	65.63%	Hg-197	5.56E-04	1.01E-04	81.90%
Ga-68	6.14E-03	1.01E-03	83.52%	Hg-197m	1.72E-03	1.16E-04	93.23%
Ga-72	4.78E-03	1.27E-03	73.39%	Hg-203	8.59E-04	9.77E-05	88.63%
Se-73	3.48E-03	6.33E-04	81.80%	Tl-201m	5.98E-04	3.17E-04	47.00%
Se-75	2.60E-04	1.53E-04	40.94%	Tl-201	4.13E-04	1.16E-04	71.91%
Kr-81m	5.00E-04	5.76E-05	88.48%	Te-123m	8.63E-04	8.34E-05	90.34%
Rb-82m	1.78E-03	1.08E-03	39.08%	Pt-195m	1.45E-03	1.36E-04	90.59%
Rb-82	1.14E-02	2.73E-03	76.12%	Pb-203m1	1.46E-03	3.60E-04	75.26%
Sr-90	1.53E-03	2.20E-05	98.56%	Pb-203m	2.33E-03	7.48E-04	67.85%
Y-87	2.42E-04	1.90E-04	21.27%	Pb-203	4.15E-04	1.33E-04	67.92%

Table 6. S-values for lungs as a source region and lungs as a target region.

Radionuclide	MIRD	EGS4	DIFF(%)	Radionuclide	MIRD	EGS4	DIFF(%)
C-11	9.29E-04	9.03E-04	2.81%	Y-90m	1.67E-04	1.64E-04	2.04%
C-14	1.06E-04	1.05E-04	0.43%	Y-90	1.99E-03	1.82E-03	8.73%
N-13	1.16E-03	1.11E-03	3.62%	Tc-99m	4.68E-05	4.65E-05	0.63%
O-15	1.68E-03	1.57E-03	6.16%	Ru-97	8.82E-05	8.78E-05	0.48%
F-18	6.42E-04	6.31E-04	1.78%	In-111	1.28E-04	1.27E-04	0.73%
Na-22	6.32E-04	6.24E-04	1.21%	In-113m	3.17E-04	3.08E-04	2.72%
Na-24	1.52E-03	1.47E-03	3.60%	In-111m	1.88E-04	1.83E-04	3.02%
P-32	1.48E-03	1.39E-03	6.15%	In-114m	3.22E-04	3.18E-04	1.40%
S-35	1.04E-04	1.03E-04	0.42%	I-123	8.71E-05	8.66E-05	0.59%
K-42	3.07E-03	2.62E-03	14.57%	I-124	5.32E-04	5.00E-04	6.01%
K-43	7.70E-04	7.51E-04	2.48%	I-125	6.06E-05	6.05E-05	0.08%
Ca-45	1.65E-04	1.64E-04	0.66%	I-126	3.60E-04	3.51E-04	2.38%
Ca-49	2.09E-03	1.93E-03	7.34%	I-129	8.83E-05	8.80E-05	0.35%
Sc-47	3.59E-04	3.54E-04	1.39%	I-130	8.30E-04	8.14E-04	1.93%
Sc-49	1.74E-03	1.61E-03	7.47%	I-131	4.48E-04	4.41E-04	1.48%
Cr-51	1.35E-05	1.35E-05	0.02%	Xe-120	1.51E-04	1.50E-04	0.64%
Mn-52m	2.66E-03	2.38E-03	10.30%	Xe-121	1.35E-03	1.22E-03	10.11%
Fe-52	4.94E-04	4.82E-04	2.34%	Xe-122	3.33E-05	3.33E-05	0.19%
Fe-52m	4.63E-03	3.76E-03	18.69%	Xe-123	4.67E-04	4.47E-04	4.18%
Fe-55	1.21E-05	1.21E-05	0.03%	Xe-125	1.10E-04	1.10E-04	0.60%
Fe-59	3.64E-04	3.61E-04	0.78%	Xe-127	1.06E-04	1.05E-04	0.68%
Co-57	4.76E-05	4.75E-05	0.20%	Cs-129	7.33E-05	7.30E-05	0.33%
Co-58	1.75E-04	1.74E-04	0.64%	Dy-157	4.49E-05	4.47E-05	0.41%
Co-58m	4.88E-05	4.87E-05	0.13%	Yb-169	2.86E-04	2.85E-04	0.64%
Co-60	4.41E-04	4.39E-04	0.38%	W-178	1.47E-05	1.47E-05	0.06%
Co-60m	1.45E-04	1.44E-04	0.51%	Ir-192	5.43E-04	5.35E-04	1.46%
Cu-62	2.84E-03	2.49E-03	12.37%	Au-195	1.13E-04	1.13E-04	0.29%
Cu-64	2.84E-04	2.79E-04	1.75%	Au-195m	2.64E-04	2.62E-04	0.97%
Cu-67	3.43E-04	3.39E-04	1.18%	Au-198	7.41E-04	7.22E-04	2.50%
Ga-66	2.32E-03	1.92E-03	17.09%	Hg-195	1.45E-04	1.44E-04	0.44%
Ga-67	9.14E-05	9.10E-05	0.42%	Hg-197	1.46E-04	1.45E-04	0.44%
Ga-68	1.68E-03	1.56E-03	7.17%	Hg-197m	4.63E-04	4.58E-04	1.08%
Ga-72	1.32E-03	1.24E-03	6.01%	Hg-203	2.37E-04	2.35E-04	0.93%
Se-73	9.61E-04	9.23E-04	3.95%	Tl-201m	1.67E-04	1.65E-04	1.56%
Se-75	8.08E-05	8.06E-05	0.23%	Tl-201	1.06E-04	1.05E-04	0.48%
Kr-81m	1.40E-04	1.38E-04	1.31%	Te-123m	2.38E-04	2.37E-04	0.65%
Rb-82m	5.02E-04	4.93E-04	1.62%	Pt-195m	3.86E-04	3.83E-04	0.72%
Rb-82	3.13E-03	2.68E-03	14.23%	Pb-203m1	4.01E-04	3.78E-04	5.60%
Sr-90	4.18E-04	4.11E-04	1.68%	Pb-203m	6.48E-04	6.37E-04	1.63%
Y-87	7.48E-05	7.47E-05	0.15%	Pb-203	1.20E-04	1.19E-04	1.00%

Table 7. S-values for ovaries as a source region and ovaries as a target region.

Radionuclide	MIRD	EGS4	DIFF(%)	Radionuclide	MIRD	EGS4	DIFF(%)
C-11	1.05E-01	9.91E-02	5.54%	Y-90m	1.55E-02	1.47E-02	5.19%
C-14	1.28E-02	1.27E-02	0.61%	Y-90	2.41E-01	1.97E-01	18.38%
N-13	1.32E-01	1.22E-01	7.71%	Tc-99m	4.59E-03	4.54E-03	1.11%
O-15	1.95E-01	1.69E-01	13.32%	Ru-97	8.26E-03	8.19E-03	0.88%
F-18	7.02E-02	6.82E-02	2.81%	In-111	1.17E-02	1.15E-02	1.38%
Na-22	6.15E-02	6.02E-02	2.14%	In-113m	3.62E-02	3.43E-02	5.19%
Na-24	1.61E-01	1.48E-01	8.41%	In-111m	1.93E-02	1.79E-02	7.25%
P-32	1.79E-01	1.56E-01	12.78%	In-114m	3.79E-02	3.72E-02	2.05%
S-35	1.26E-02	1.25E-02	0.60%	I-123	8.47E-03	8.38E-03	1.04%
K-42	3.69E-01	2.57E-01	30.47%	I-124	5.66E-02	4.85E-02	14.34%
K-43	8.62E-02	8.23E-02	4.59%	I-125	5.76E-03	5.75E-03	0.14%
Ca-45	1.99E-02	1.97E-02	0.94%	I-126	4.00E-02	3.82E-02	4.52%
Ca-49	2.37E-01	1.98E-01	16.40%	I-129	1.06E-02	1.06E-02	0.50%
Sc-47	4.26E-02	4.17E-02	2.02%	I-130	8.53E-02	8.19E-02	3.93%
Sc-49	2.11E-01	1.78E-01	15.65%	I-131	5.13E-02	5.01E-02	2.25%
Cr-51	1.40E-03	1.39E-03	0.03%	Xe-120	1.42E-02	1.40E-02	1.43%
Mn-52m	3.05E-01	2.36E-01	22.78%	Xe-121	1.52E-01	1.17E-01	22.79%
Fe-52	5.42E-02	5.18E-02	4.47%	Xe-122	2.87E-03	2.85E-03	0.42%
Fe-52m	5.35E-01	3.22E-01	39.88%	Xe-123	5.16E-02	4.67E-02	9.38%
Fe-55	1.46E-03	1.46E-03	0.04%	Xe-125	1.05E-02	1.04E-02	1.08%
Fe-59	3.63E-02	3.58E-02	1.37%	Xe-127	9.96E-03	9.83E-03	1.27%
Co-57	4.73E-03	4.71E-03	0.35%	Cs-129	5.90E-03	5.85E-03	0.85%
Co-58	1.44E-02	1.42E-02	1.34%	Dy-157	3.08E-03	3.05E-03	1.10%
Co-58m	5.90E-03	5.89E-03	0.19%	Yb-169	3.14E-02	3.11E-02	1.00%
Co-60	3.72E-02	3.70E-02	0.78%	W-178	1.57E-03	1.57E-03	0.09%
Co-60m	1.75E-02	1.73E-02	0.80%	Ir-192	5.96E-02	5.82E-02	2.37%
Cu-62	3.36E-01	2.47E-01	26.47%	Au-195	1.27E-02	1.26E-02	0.44%
Cu-64	3.30E-02	3.21E-02	2.71%	Au-195m	3.04E-02	2.99E-02	1.45%
Cu-67	4.05E-02	3.98E-02	1.71%	Au-198	8.66E-02	8.28E-02	4.31%
Ga-66	2.66E-01	1.68E-01	36.84%	Hg-195	1.59E-02	1.58E-02	0.76%
Ga-67	9.86E-03	9.79E-03	0.68%	Hg-197	1.68E-02	1.67E-02	0.66%
Ga-68	1.96E-01	1.66E-01	15.56%	Hg-197m	5.52E-02	5.43E-02	1.56%
Ga-72	1.43E-01	1.23E-01	13.67%	Hg-203	2.68E-02	2.64E-02	1.44%
Se-73	1.08E-01	9.82E-02	8.72%	Tl-201m	1.43E-02	1.36E-02	4.31%
Se-75	6.74E-03	6.71E-03	0.47%	Tl-201	1.18E-02	1.17E-02	0.74%
Kr-81m	1.58E-02	1.55E-02	1.98%	Te-123m	2.72E-02	2.69E-02	0.98%
Rb-82m	4.06E-02	3.87E-02	4.63%	Pt-195m	4.58E-02	4.54E-02	1.04%
Rb-82	3.70E-01	2.58E-01	30.30%	Pb-203m1	4.39E-02	3.83E-02	12.88%
Sr-90	5.05E-02	4.93E-02	2.40%	Pb-203m	6.48E-02	6.25E-02	3.53%
Y-87	5.41E-03	5.38E-03	0.47%	Pb-203	1.19E-02	1.17E-02	1.77%

Table 8. S-values for pancreas as a source region and pancreas as a target region.

Radionuclide	MIRD	EGS4	DIFF(%)	Radionuclide	MIRD	EGS4	DIFF(%)
C-11	1.52E-02	1.48E-02	2.87%	Y-90m	2.62E-03	2.55E-03	2.33%
C-14	1.75E-03	1.75E-03	0.31%	Y-90	3.31E-02	2.97E-02	10.23%
N-13	1.90E-02	1.82E-02	4.12%	Tc-99m	7.30E-04	7.26E-04	0.49%
O-15	2.76E-02	2.56E-02	7.20%	Ru-97	1.38E-03	1.38E-03	0.37%
F-18	1.04E-02	1.03E-02	1.32%	In-111	1.98E-03	1.97E-03	0.57%
Na-22	1.01E-02	9.96E-03	0.91%	In-113m	5.18E-03	5.04E-03	2.70%
Na-24	2.46E-02	2.35E-02	4.22%	In-111m	3.02E-03	2.91E-03	3.54%
P-32	2.46E-02	2.28E-02	7.12%	In-114m	5.31E-03	5.25E-03	1.02%
S-35	1.72E-03	1.72E-03	0.30%	I-123	1.36E-03	1.36E-03	0.45%
K-42	5.08E-02	4.21E-02	17.10%	I-124	8.60E-03	7.98E-03	7.21%
K-43	1.26E-02	1.23E-02	2.32%	I-125	9.46E-04	9.46E-04	0.06%
Ca-45	2.73E-03	2.72E-03	0.48%	I-126	5.86E-03	5.73E-03	2.28%
Ca-49	3.42E-02	3.12E-02	8.69%	I-129	1.46E-03	1.46E-03	0.25%
Sc-47	5.92E-03	5.86E-03	1.01%	I-130	1.33E-02	1.31E-02	1.85%
Sc-49	2.89E-02	2.64E-02	8.72%	I-131	7.33E-03	7.25E-03	1.10%
Cr-51	2.16E-04	2.16E-04	0.01%	Xe-120	2.37E-03	2.36E-03	0.63%
Mn-52m	4.36E-02	3.83E-02	12.21%	Xe-121	2.21E-02	1.94E-02	12.01%
Fe-52	8.01E-03	7.83E-03	2.23%	Xe-122	5.09E-04	5.08E-04	0.17%
Fe-52m	7.60E-02	5.91E-02	22.34%	Xe-123	7.58E-03	7.21E-03	4.87%
Fe-55	2.00E-04	2.00E-04	0.02%	Xe-125	1.72E-03	1.72E-03	0.46%
Fe-59	5.82E-03	5.79E-03	0.60%	Xe-127	1.65E-03	1.64E-03	0.54%
Co-57	7.45E-04	7.44E-04	0.15%	Cs-129	1.11E-03	1.11E-03	0.33%
Co-58	2.71E-03	2.69E-03	0.49%	Dy-157	6.60E-04	6.58E-04	0.37%
Co-58m	8.09E-04	8.08E-04	0.10%	Yb-169	4.60E-03	4.57E-03	0.48%
Co-60	6.88E-03	6.86E-03	0.29%	W-178	2.32E-04	2.32E-04	0.04%
Co-60m	2.40E-03	2.39E-03	0.42%	Ir-192	8.80E-03	8.70E-03	1.13%
Cu-62	4.69E-02	4.00E-02	14.56%	Au-195	1.83E-03	1.82E-03	0.22%
Cu-64	4.67E-03	4.60E-03	1.35%	Au-195m	4.32E-03	4.29E-03	0.71%
Cu-67	5.64E-03	5.60E-03	0.86%	Au-198	1.22E-02	1.19E-02	2.24%
Ga-66	3.81E-02	3.03E-02	20.40%	Hg-195	2.34E-03	2.33E-03	0.37%
Ga-67	1.47E-03	1.46E-03	0.32%	Hg-197	2.37E-03	2.36E-03	0.33%
Ga-68	2.77E-02	2.53E-02	8.44%	Hg-197m	7.64E-03	7.58E-03	0.78%
Ga-72	2.13E-02	1.99E-02	6.96%	Hg-203	3.86E-03	3.83E-03	0.70%
Se-73	1.57E-02	1.49E-02	4.58%	Tl-201m	2.59E-03	2.54E-03	1.80%
Se-75	1.24E-03	1.23E-03	0.18%	Tl-201	1.71E-03	1.70E-03	0.36%
Kr-81m	2.28E-03	2.26E-03	0.96%	Te-123m	3.88E-03	3.87E-03	0.48%
Rb-82m	7.76E-03	7.62E-03	1.82%	Pt-195m	6.36E-03	6.33E-03	0.52%
Rb-82	5.16E-02	4.30E-02	16.73%	Pb-203m1	6.52E-03	6.09E-03	6.63%
Sr-90	6.93E-03	6.84E-03	1.22%	Pb-203m	1.04E-02	1.02E-02	1.63%
Y-87	1.14E-03	1.14E-03	0.17%	Pb-203	1.90E-03	1.88E-03	0.78%

Table 9. S-values for the spleen as a source region and the spleen as a target region.

Radionuclide	MIRD	EGS4	DIFF(%)	Radionuclide	MIRD	EGS4	DIFF(%)
C-11	5.70E-03	5.62E-03	1.41%	Y-90m	1.17E-03	1.16E-03	0.91%
C-14	6.08E-04	6.07E-04	0.20%	Y-90	1.15E-02	1.09E-02	5.37%
N-13	7.01E-03	6.88E-03	1.93%	Tc-99m	3.08E-04	3.08E-04	0.26%
O-15	1.00E-02	9.66E-03	3.53%	Ru-97	6.04E-04	6.03E-04	0.19%
F-18	4.05E-03	4.02E-03	0.76%	In-111	8.89E-04	8.87E-04	0.28%
Na-22	4.32E-03	4.30E-03	0.48%	In-113m	1.92E-03	1.89E-03	1.36%
Na-24	9.83E-03	9.66E-03	1.83%	In-111m	1.25E-03	1.23E-03	1.48%
P-32	8.54E-03	8.24E-03	3.65%	In-114m	1.90E-03	1.88E-03	0.64%
S-35	5.98E-04	5.97E-04	0.19%	I-123	5.77E-04	5.76E-04	0.24%
K-42	1.77E-02	1.62E-02	9.28%	I-124	3.42E-03	3.31E-03	3.23%
K-43	4.76E-03	4.70E-03	1.19%	I-125	4.01E-04	4.01E-04	0.03%
Ca-45	9.49E-04	9.46E-04	0.31%	I-126	2.23E-03	2.20E-03	1.15%
Ca-49	1.28E-02	1.23E-02	4.19%	I-129	5.11E-04	5.11E-04	0.16%
Sc-47	2.10E-03	2.09E-03	0.64%	I-130	5.49E-03	5.44E-03	0.87%
Sc-49	1.00E-02	9.61E-03	4.52%	I-131	2.71E-03	2.69E-03	0.67%
Cr-51	8.84E-05	8.83E-05	0.01%	Xe-120	1.04E-03	1.04E-03	0.27%
Mn-52m	1.60E-02	1.51E-02	6.09%	Xe-121	8.34E-03	7.88E-03	5.83%
Fe-52	3.09E-03	3.06E-03	1.11%	Xe-122	2.34E-04	2.34E-04	0.08%
Fe-52m	2.78E-02	2.48E-02	12.11%	Xe-123	2.90E-03	2.83E-03	2.25%
Fe-55	6.96E-05	6.96E-05	0.01%	Xe-125	7.46E-04	7.44E-04	0.24%
Fe-59	2.45E-03	2.44E-03	0.31%	Xe-127	7.21E-04	7.19E-04	0.27%
Co-57	3.11E-04	3.11E-04	0.08%	Cs-129	5.40E-04	5.39E-04	0.13%
Co-58	1.33E-03	1.32E-03	0.23%	Dy-157	3.58E-04	3.58E-04	0.14%
Co-58m	2.81E-04	2.81E-04	0.06%	Yb-169	1.76E-03	1.75E-03	0.28%
Co-60	3.28E-03	3.27E-03	0.14%	W-178	9.06E-05	9.06E-05	0.03%
Co-60m	8.35E-04	8.33E-04	0.25%	Ir-192	3.39E-03	3.37E-03	0.64%
Cu-62	1.67E-02	1.55E-02	7.60%	Au-195	6.83E-04	6.82E-04	0.13%
Cu-64	1.70E-03	1.69E-03	0.81%	Au-195m	1.58E-03	1.58E-03	0.43%
Cu-67	2.01E-03	2.00E-03	0.54%	Au-198	4.40E-03	4.35E-03	1.23%
Ga-66	1.40E-02	1.27E-02	10.80%	Hg-195	9.00E-04	8.98E-04	0.20%
Ga-67	5.73E-04	5.72E-04	0.18%	Hg-197	8.63E-04	8.61E-04	0.20%
Ga-68	1.00E-02	9.60E-03	4.19%	Hg-197m	2.70E-03	2.68E-03	0.50%
Ga-72	8.36E-03	8.10E-03	3.21%	Hg-203	1.44E-03	1.44E-03	0.42%
Se-73	5.92E-03	5.80E-03	2.11%	Tl-201m	1.23E-03	1.23E-03	0.67%
Se-75	5.94E-04	5.94E-04	0.08%	Tl-201	6.42E-04	6.41E-04	0.21%
Kr-81m	8.47E-04	8.42E-04	0.58%	Te-123m	1.43E-03	1.43E-03	0.29%
Rb-82m	3.83E-03	3.80E-03	0.67%	Pt-195m	2.25E-03	2.24E-03	0.33%
Rb-82	1.84E-02	1.69E-02	8.86%	Pb-203m1	2.52E-03	2.45E-03	3.04%
Sr-90	2.41E-03	2.39E-03	0.79%	Pb-203m	4.36E-03	4.33E-03	0.74%
Y-87	6.00E-04	5.99E-04	0.06%	Pb-203	8.01E-04	7.98E-04	0.41%

Table 10.S-values for stomach contents as a source region and stomach walls as as target region.

Radionuclide	MIRD	EGS4	DIFF(%)	Radionuclide	MIRD	EGS4	DIFF(%)
C-11	2.05E-03	4.60E-04	77.53%	Y-90m	4.42E-04	2.53E-04	42.62%
C-14	2.14E-04	8.36E-07	99.61%	Y-90	4.04E-03	5.64E-04	86.04%
N-13	2.51E-03	5.20E-04	79.29%	Tc-99m	1.16E-04	5.24E-05	54.91%
O-15	3.56E-03	7.21E-04	79.76%	Ru-97	2.11E-04	1.14E-04	45.90%
F-18	1.47E-03	4.11E-04	72.03%	In-111	3.28E-04	1.87E-04	43.17%
Na-22	1.61E-03	7.88E-04	51.08%	In-113m	6.84E-04	1.30E-04	80.95%
Na-24	3.61E-03	1.39E-03	61.49%	In-111m	4.59E-04	2.00E-04	56.51%
P-32	3.00E-03	2.92E-04	90.26%	In-114m	6.69E-04	5.83E-05	91.29%
S-35	2.10E-04	8.07E-07	99.62%	I-123	2.13E-04	1.00E-04	52.96%
K-42	6.24E-03	1.59E-03	74.50%	I-124	1.25E-03	5.03E-04	59.59%
K-43	1.72E-03	4.08E-04	76.24%	I-125	1.43E-04	7.20E-05	49.60%
Ca-45	3.33E-04	2.03E-06	99.39%	I-126	8.03E-04	2.00E-04	75.04%
Ca-49	4.61E-03	1.34E-03	70.80%	I-129	1.80E-04	3.88E-06	97.84%
Sc-47	7.45E-04	5.14E-05	93.10%	I-130	2.02E-03	8.31E-04	58.94%
Sc 49	3.53E-03	4.20E-04	88.09%	I-131	9.70E-04	1.59E-04	83.57%
Cr-51	4.38E-05	2.82E-05	35.58%	Xe-120	3.87E-04	2.07E-04	46.37%
Mn-52m	5.73E-03	1.74E-03	69.68%	Xe-121	3.01E-03	1.07E-03	64.43%
Fe-52	1.13E-03	3.25E-04	71.26%	Xe-122	8.75E-05	5.64E-05	35.57%
Fe-52m	9.92E-03	4.12E-03	58.42%	Xe-123	1.05E-03	3.10E-04	70.45%
Fe-55	4.09E-05	2.36E-05	42.20%	Xe-125	2.79E-04	1.42E-04	49.19%
Fe-59	9.09E-04	4.08E-04	55.14%	Xe-127	2.71E-04	1.43E-04	47.35%
Co-57	1.52E-04	1.02E-04	32.93%	Cs-129	2.09E-04	1.49E-04	28.70%
Co-58	5.27E-04	3.83E-04	27.27%	Dy-157	1.43E-04	1.20E-04	15.83%
Co-58m	1.17E-04	2.67E-05	77.26%	Yb-169	6.85E-04	2.10E-04	69.28%
Co-60	1.25E-03	8.39E-04	32.85%	W-178	5.09E-05	3.38E-05	33.54%
Co-60m	3.15E-04	3.44E-05	89.10%	Ir-192	1.24E-03	3.34E-04	73.02%
Cu-62	5.91E-03	1.56E-03	73.66%	Au-195	3.03E-04	1.23E-04	59.39%
Cu-64	6.18E-04	9.95E-05	83.90%	Au-195m	6.03E-04	1.32E-04	78.16%
Cu-67	7.19E-04	6.08E-05	91.54%	Au-198	1.57E-03	2.00E-04	87.25%
Ga-66	5.05E-03	2.10E-03	58.44%	Hg-195	3.79E-04	1.54E-04	59.33%
Ga-67	2.59E-04	1.29E-04	50.21%	Hg-197	3.59E-04	1.07E-04	70.16%
Ga-68	3.56E-03	7.54E-04	78.83%	Hg-197m	1.00E-03	1.16E-04	88.39%
Ga-72	3.05E-03	1.13E-03	62.88%	Hg-203	5.18E-04	9.66E-05	81.34%
Se-73	2.13E-03	5.64E-04	73.50%	Tl-201m	4.71E-04	3.16E-04	32.86%
Se-75	2.13E-04	1.54E-04	27.63%	Tl-201	2.88E-04	1.24E-04	57.07%
Kr-81m	3.00E-04	5.51E-05	81.60%	Te-123m	5.14E-04	8.18E-05	84.06%
Rb-82m	1.46E-03	1.07E-03	26.28%	Pt-195m	8.67E-04	1.42E-04	83.65%
Rb-82	6.51E-03	1.91E-03	70.62%	Pb-203m1	9.17E-04	3.17E-04	65.49%
Sr-90	8.46E-04	1.31E-05	98.45%	Pb-203m	1.61E-03	7.39E-04	54.11%
Y-87	2.14E-04	1.85E-04	13.30%	Pb-203	2.90E-04	1.34E-04	53.70%

Table 11. S-values for testes as a source region and testes as a target region.

Radionuclide	MIRD	EGS4	DIFF(%)	Radionuclide	MIRD	EGS4	DIFF(%)
C-11	2.48E-02	2.41E-02	2.75%	Y-90m	4.32E-03	4.22E-03	2.22%
C-14	2.85E-03	2.84E-03	0.28%	Y-90	5.38E-02	4.86E-02	9.62%
N-13	3.09E-02	2.97E-02	3.97%	Tc-99m	1.20E-03	1.19E-03	0.42%
O-15	4.49E-02	4.19E-02	6.81%	Ru-97	2.30E-03	2.29E-03	0.35%
F-18	1.71E-02	1.68E-02	1.23%	In-111	3.29E-03	3.27E-03	0.52%
Na-22	1.65E-02	1.64E-02	0.85%	In-113m	8.45E-03	8.24E-03	2.58%
Na-24	4.03E-02	3.86E-02	4.02%	In-111m	4.96E-03	4.79E-03	3.39%
P-32	4.00E-02	3.73E-02	6.76%	In-114m	8.65E-03	8.57E-03	0.95%
S-35	2.80E-03	2.79E-03	0.29%	I-123	2.24E-03	2.24E-03	0.40%
K-42	8.26E-02	6.95E-02	15.90%	I-124	1.41E-02	1.31E-02	6.75%
K-43	2.05E-02	2.01E-02	2.20%	I-125	1.57E-03	1.57E-03	0.06%
Ca-45	4.44E-03	4.42E-03	0.45%	I-126	9.58E-03	9.37E-03	2.17%
Ca-49	5.58E-02	5.13E-02	8.15%	I-129	2.38E-03	2.37E-03	0.25%
Sc-47	9.63E-03	9.54E-03	0.94%	I-130	2.19E-02	2.15E-02	1.75%
Sc-49	4.70E-02	4.32E-02	8.23%	I-131	1.20E-02	1.18E-02	1.03%
Cr-51	3.54E-04	3.54E-04	0.00%	Xe-120	3.92E-03	3.90E-03	0.61%
Mn-52m	7.10E-02	6.29E-02	11.43%	Xe-121	3.61E-02	3.21E-02	11.21%
Fe-52	1.31E-02	1.28E-02	2.12%	Xe-122	8.45E-04	8.44E-04	0.12%
Fe-52m	1.24E-01	9.94E-02	19.86%	Xe-123	1.24E-02	1.18E-02	4.61%
Fe-55	3.26E-04	3.26E-04	0.00%	Xe-125	2.85E-03	2.83E-03	0.46%
Fe-59	9.57E-03	9.52E-03	0.55%	Xe-127	2.72E-03	2.71E-03	0.48%
Co-57	1.22E-03	1.22E-03	0.16%	Cs-129	1.84E-03	1.84E-03	0.33%
Co-58	4.51E-03	4.49E-03	0.44%	Dy-157	1.11E-03	1.10E-03	0.27%
Co-58m	1.32E-03	1.31E-03	0.15%	Yb-169	7.49E-03	7.45E-03	0.45%
Co-60	1.14E-02	1.13E-02	0.27%	W-178	3.78E-04	3.77E-04	0.26%
Co-60m	3.90E-03	3.89E-03	0.41%	Ir-192	1.44E-02	1.42E-02	1.06%
Cu-62	7.63E-02	6.59E-02	13.63%	Au-195	2.97E-03	2.96E-03	0.20%
Cu-64	7.61E-03	7.51E-03	1.26%	Au-195m	7.04E-03	7.00E-03	0.65%
Cu-67	9.19E-03	9.11E-03	0.81%	Au-198	1.99E-02	1.94E-02	2.13%
Ga-66	6.21E-02	5.08E-02	18.26%	Hg-195	3.82E-03	3.81E-03	0.34%
Ga-67	2.40E-03	2.39E-03	0.29%	Hg-197	3.86E-03	3.85E-03	0.31%
Ga-68	4.51E-02	4.15E-02	7.94%	Hg-197m	1.24E-02	1.23E-02	0.73%
Ga-72	3.50E-02	3.27E-02	6.49%	Hg-203	6.31E-03	6.26E-03	0.67%
Se-73	2.56E-02	2.45E-02	4.38%	Tl-201m	4.29E-03	4.22E-03	1.70%
Se-75	2.05E-03	2.05E-03	0.15%	Tl-201	2.77E-03	2.77E-03	0.32%
Kr-81m	3.72E-03	3.69E-03	0.89%	Te-123m	6.34E-03	6.31E-03	0.44%
Rb-82m	1.29E-02	1.27E-02	1.69%	Pt-195m	1.03E-02	1.03E-02	0.49%
Rb-82	8.41E-02	7.09E-02	15.61%	Pb-203m1	1.07E-02	1.00E-02	6.24%
Sr-90	1.13E-02	1.11E-02	1.14%	Pb-203m	1.71E-02	1.68E-02	1.52%
Y-87	1.92E-03	1.91E-03	0.16%	Pb-203	3.12E-03	3.09E-03	0.74%

Table.12. S-values for thyroid as a source region and thyroid as a target region.

Radionuclide	MIRD	EGS4	DIFF(%)	Radionuclide	MIRD	EGS4	DIFF(%)
C-11	4.55E-02	4.33E-02	4.78%	Y-90m	7.25E-03	6.97E-03	3.94%
C-14	5.39E-03	5.35E-03	0.67%	Y-90	1.02E-01	8.64E-02	15.13%
N-13	5.70E-02	5.35E-02	6.21%	Tc-99m	2.08E-03	2.06E-03	1.15%
O-15	8.36E-02	7.45E-02	10.79%	Ru-97	3.86E-03	3.83E-03	0.88%
F-18	3.08E-02	2.99E-02	2.97%	In-111	5.50E-03	5.43E-03	1.36%
Na-22	2.84E-02	2.78E-02	2.15%	In-113m	1.56E-02	1.49E-02	4.58%
Na-24	7.17E-02	6.70E-02	6.53%	In-111m	8.70E-03	8.21E-03	5.55%
P-32	7.57E-02	6.77E-02	10.50%	In-114m	1.62E-02	1.58E-02	2.23%
S-35	5.29E-03	5.26E-03	0.64%	I-123	3.88E-03	3.84E-03	1.06%
K-42	1.56E-01	1.18E-01	24.46%	I-124	2.51E-02	2.23E-02	11.21%
K-43	3.75E-02	3.59E-02	4.20%	I-125	2.68E-03	2.68E-03	0.15%
Ca-45	8.41E-03	8.32E-03	1.05%	I-126	1.74E-02	1.67E-02	4.05%
Ca-49	1.03E-01	8.90E-02	13.18%	I-129	4.49E-03	4.46E-03	0.53%
Sc-47	1.81E-02	1.77E-02	2.20%	I-130	3.84E-02	3.71E-02	3.44%
Sc-49	8.90E-02	7.75E-02	12.87%	I-131	2.21E-02	2.15E-02	2.41%
Cr-51	6.24E-04	6.24E-04	0.00%	Xe-120	6.65E-03	6.57E-03	1.19%
Mn-52m	1.31E-01	1.07E-01	18.22%	Xe-121	6.60E-02	5.41E-02	18.02%
Fe-52	2.37E-02	2.28E-02	4.01%	Xe-122	1.39E-03	1.39E-03	0.36%
Fe-52m	2.30E-01	1.59E-01	30.64%	Xe-123	2.25E-02	2.08E-02	7.51%
Fe-55	6.16E-04	6.16E-04	0.00%	Xe-125	4.86E-03	4.81E-03	1.09%
Fe-59	1.66E-02	1.64E-02	1.37%	Xe-127	4.63E-03	4.57E-03	1.25%
Co-57	2.14E-03	2.13E-03	0.37%	Cs-129	2.95E-03	2.93E-03	0.68%
Co-58	7.18E-03	7.09E-03	1.25%	Dy-157	1.65E-03	1.63E-03	0.85%
Co-58m	2.49E-03	2.48E-03	0.20%	Yb-169	1.37E-02	1.35E-02	1.07%
Co-60	1.84E-02	1.83E-02	0.73%	W-178	6.87E-04	6.87E-04	0.00%
Co-60m	7.37E-03	7.31E-03	0.83%	Ir-192	2.61E-02	2.54E-02	2.45%
Cu-62	1.43E-01	1.12E-01	21.31%	Au-195	5.49E-03	5.46E-03	0.47%
Cu-64	1.41E-02	1.37E-02	2.83%	Au-195m	1.30E-02	1.28E-02	1.57%
Cu-67	1.72E-02	1.69E-02	1.86%	Au-198	3.70E-02	3.55E-02	4.09%
Ga-66	1.15E-01	8.21E-02	28.39%	Hg-195	6.94E-03	6.89E-03	0.75%
Ga-67	4.33E-03	4.30E-03	0.72%	Hg-197	7.19E-03	7.14E-03	0.71%
Ga-68	8.40E-02	7.33E-02	12.63%	Hg-197m	2.34E-02	2.30E-02	1.71%
Ga-72	6.28E-02	5.60E-02	10.87%	Hg-203	1.16E-02	1.14E-02	1.54%
Se-73	4.67E-02	4.35E-02	6.96%	Tl-201m	6.95E-03	6.73E-03	3.18%
Se-75	3.30E-03	3.29E-03	0.42%	Tl-201	5.10E-03	5.06E-03	0.80%
Kr-81m	6.84E-03	6.69E-03	2.14%	Te-123m	1.17E-02	1.16E-02	1.05%
Rb-82m	2.05E-02	1.98E-02	3.37%	Pt-195m	1.94E-02	1.92E-02	1.14%
Rb-82	1.57E-01	1.19E-01	24.24%	Pb-203m1	1.93E-02	1.73E-02	10.18%
Sr-90	2.13E-02	2.08E-02	2.64%	Pb-203m	2.96E-02	2.87E-02	3.01%
Y-87	2.88E-03	2.88E-03	0.31%	Pb-203	5.41E-03	5.32E-03	1.77%

Table 13. S-values for kidney cortex as a source region and kidney cortex as a target region.

Radionuclide	MIRD	EGS4	DIFF(%)	Radionuclide	MIRD	EGS4	DIFF(%)
C-11	1.01E-02	9.68E-03	4.16%	Y-90m	1.48E-03	1.42E-03	3.97%
C-14	1.23E-03	1.22E-03	0.41%	Y-90	2.32E-02	2.04E-02	13.83%
N-13	1.27E-02	1.20E-02	6.01%	Tc-99m	4.37E-04	4.34E-04	0.76%
O-15	1.88E-02	1.71E-02	9.99%	Ru-97	7.52E-04	7.48E-04	0.63%
F-18	6.74E-03	6.61E-03	1.93%	In-111	1.10E-03	1.09E-03	0.96%
Na-22	5.87E-03	5.79E-03	1.47%	In-113m	3.47E-03	3.34E-03	3.88%
Na-24	1.54E-02	1.45E-02	6.47%	In-111m	1.85E-03	1.75E-03	5.62%
P-32	1.72E-02	1.57E-02	9.64%	In-114m	3.64E-03	3.59E-03	1.40%
S-35	1.21E-03	1.20E-03	0.40%	I-123	8.04E-04	7.98E-04	0.71%
K-42	3.54E-02	2.81E-02	26.24%	I-124	5.42E-03	4.90E-03	10.65%
K-43	8.28E-03	8.01E-03	3.32%	I-125	5.39E-04	5.38E-04	0.10%
Ca-45	1.91E-03	1.90E-03	0.64%	I-126	3.84E-03	3.72E-03	3.33%
Ca-49	2.27E-02	2.02E-02	12.27%	I-129	1.02E-03	1.02E-03	0.34%
Sc-47	4.09E-03	4.03E-03	1.38%	I-130	8.18E-03	7.96E-03	2.86%
Sc-49	2.03E-02	1.81E-02	11.75%	I-131	4.93E-03	4.85E-03	1.55%
Cr-51	1.34E-04	1.34E-04	0.02%	Xe-120	1.35E-03	1.34E-03	1.04%
Mn-52m	2.93E-02	2.48E-02	17.89%	Xe-121	1.46E-02	1.24E-02	18.02%
Fe-52	5.20E-03	5.04E-03	3.29%	Xe-122	2.70E-04	2.69E-04	0.29%
Fe-52m	5.14E-02	3.65E-02	40.58%	Xe-123	4.94E-03	4.62E-03	6.96%
Fe-55	1.40E-04	1.40E-04	0.02%	Xe-125	1.00E-03	9.93E-04	0.74%
Fe-59	3.46E-03	3.43E-03	0.94%	Xe-127	9.48E-04	9.40E-04	0.88%
Co-57	4.47E-04	4.46E-04	0.24%	Cs-129	5.64E-04	5.60E-04	0.61%
Co-58	1.38E-03	1.36E-03	0.91%	Dy-157	2.93E-04	2.91E-04	0.77%
Co-58m	5.67E-04	5.66E-04	0.13%	Yb-169	3.03E-03	3.01E-03	0.68%
Co-60	3.52E-03	3.50E-03	0.53%	W-178	1.52E-04	1.52E-04	0.06%
Co-60m	1.68E-03	1.67E-03	0.55%	Ir-192	5.72E-03	5.63E-03	1.64%
Cu-62	3.23E-02	2.66E-02	21.54%	Au-195	1.23E-03	1.22E-03	0.30%
Cu-64	3.17E-03	3.11E-03	1.88%	Au-195m	2.92E-03	2.89E-03	0.99%
Cu-67	3.89E-03	3.85E-03	1.16%	Au-198	8.32E-03	8.06E-03	3.13%
Ga-66	2.56E-02	1.88E-02	35.87%	Hg-195	1.53E-03	1.52E-03	0.52%
Ga-67	9.47E-04	9.43E-04	0.46%	Hg-197	1.62E-03	1.61E-03	0.44%
Ga-68	1.89E-02	1.69E-02	11.65%	Hg-197m	5.31E-03	5.25E-03	1.06%
Ga-72	1.37E-02	1.24E-02	10.19%	Hg-203	2.57E-03	2.54E-03	0.99%
Se-73	1.03E-02	9.66E-03	6.68%	Tl-201m	1.36E-03	1.32E-03	3.22%
Se-75	5.87E-04	5.85E-04	0.35%	Tl-201	1.14E-03	1.13E-03	0.50%
Kr-81m	1.50E-03	1.48E-03	1.37%	Te-123m	2.61E-03	2.59E-03	0.67%
Rb-82m	3.83E-03	3.70E-03	3.37%	Pt-195m	4.41E-03	4.38E-03	0.70%
Rb-82	3.56E-02	2.83E-02	25.82%	Pb-203m1	4.21E-03	3.84E-03	9.62%
Sr-90	4.86E-03	4.78E-03	1.64%	Pb-203m	6.18E-03	6.03E-03	2.45%
Y-87	4.68E-04	4.67E-04	0.38%	Pb-203	1.11E-03	1.10E-03	1.26%

Table 14. S-values for kidney cortex as a source region and kidney medulla as a target region.

Radionuclide	MIRD	EGS4	DIFF(%)	Radionuclide	MIRD	EGS4	DIFF(%)
C-11	6.29E-04	6.96E-04	9.58%	Y-90m	3.90E-04	3.99E-04	2.32%
C-14	0.00E+00	8.48E-07	100.00%	Y-90	0.00E+00	4.34E-04	100.00%
N-13	6.30E-04	7.48E-04	15.84%	Tc-99m	8.04E-05	8.10E-05	0.69%
O-15	6.30E-04	8.98E-04	29.79%	Ru-97	1.77E-04	1.78E-04	0.45%
F-18	6.31E-04	6.53E-04	3.31%	In-111	2.88E-04	2.90E-04	0.61%
Na-22	1.26E-03	1.27E-03	1.14%	In-113m	1.71E-04	1.92E-04	11.16%
Na-24	2.00E-03	2.15E-03	7.04%	In-111m	2.93E-04	3.09E-04	5.20%
P-32	0.00E+00	2.39E-04	100.00%	In-114m	7.73E-05	8.58E-05	9.95%
S-35	0.00E+00	8.19E-07	100.00%	I-123	1.53E-04	1.54E-04	0.63%
K-42	1.53E-04	1.13E-03	86.41%	I-124	6.48E-04	7.28E-04	11.10%
K-43	5.79E-04	6.23E-04	7.08%	I-125	1.08E-04	1.08E-04	0.08%
Ca-45	0.00E+00	2.06E-06	100.00%	I-126	2.84E-04	3.05E-04	6.73%
Ca-49	1.40E-03	1.78E-03	21.55%	I-129	5.29E-06	5.87E-06	9.87%
Sc-47	6.56E-05	7.50E-05	12.56%	I-130	1.27E-03	1.31E-03	2.89%
Sc-49	0.00E+00	3.32E-04	100.00%	I-131	2.34E-04	2.47E-04	5.15%
Cr-51	3.24E-05	3.24E-05	0.01%	Xe-120	3.20E-04	3.23E-04	0.72%
Mn-52m	1.37E-03	2.01E-03	31.85%	Xe-121	9.90E-04	1.30E-03	24.08%
Fe-52	4.67E-04	4.94E-04	5.57%	Xe-122	8.58E-05	8.59E-05	0.16%
Fe-52m	2.07E-03	3.76E-03	44.98%	Xe-123	3.94E-04	4.45E-04	11.46%
Fe-55	1.90E-05	1.90E-05	0.03%	Xe-125	2.18E-04	2.19E-04	0.57%
Fe-59	6.50E-04	6.55E-04	0.83%	Xe-127	2.19E-04	2.21E-04	0.63%
Co-57	1.19E-04	1.19E-04	0.15%	Cs-129	2.32E-04	2.32E-04	0.25%
Co-58	5.89E-04	5.91E-04	0.36%	Dy-157	1.90E-04	1.90E-04	0.20%
Co-58m	2.14E-05	2.15E-05	0.57%	Yb-169	2.86E-04	2.89E-04	1.20%
Co-60	1.36E-03	1.37E-03	0.23%	W-178	3.46E-05	3.46E-05	0.05%
Co-60m	2.79E-05	2.94E-05	5.20%	Ir-192	5.04E-04	5.19E-04	3.00%
Cu-62	6.18E-04	1.42E-03	56.32%	Au-195	1.34E-04	1.35E-04	0.46%
Cu-64	1.31E-04	1.41E-04	7.01%	Au-195m	1.63E-04	1.68E-04	2.89%
Cu-67	7.73E-05	8.49E-05	8.96%	Au-198	2.48E-04	2.90E-04	14.51%
Ga-66	1.26E-03	2.05E-03	38.48%	Hg-195	1.87E-04	1.89E-04	0.69%
Ga-67	1.49E-04	1.50E-04	0.49%	Hg-197	1.14E-04	1.15E-04	1.06%
Ga-68	5.86E-04	8.92E-04	34.27%	Hg-197m	1.17E-04	1.26E-04	7.48%
Ga-72	1.42E-03	1.61E-03	11.54%	Hg-203	1.46E-04	1.51E-04	2.83%
Se-73	7.15E-04	8.19E-04	12.73%	Tl-201m	4.96E-04	5.02E-04	1.39%
Se-75	2.43E-04	2.44E-04	0.14%	Tl-201	1.35E-04	1.36E-04	0.71%
Kr-81m	8.13E-05	8.47E-05	4.07%	Te-123m	1.20E-04	1.23E-04	2.38%
Rb-82m	1.69E-03	1.71E-03	1.15%	Pt-195m	1.40E-04	1.45E-04	3.61%
Rb-82	6.67E-04	1.64E-03	59.36%	Pb-203m1	3.85E-04	4.43E-04	13.06%
Sr-90	0.00E+00	1.33E-05	100.00%	Pb-203m	1.13E-03	1.15E-03	2.05%
Y-87	2.99E-04	2.99E-04	0.10%	Pb-203	2.10E-04	2.12E-04	1.10%

Table 15. S-values for kidney cortex as a source region and kidney papillary as a target region.

Radionuclide	MIRD	EGS4	DIFF(%)	Radionuclide	MIRD	EGS4	DIFF(%)
C-11	3.91E-04	3.91E-04	0.00%	Y-90m	2.39E-04	2.39E-04	0.00%
C-14	0.00E+00	0.00E+00	0.00%	Y-90	0.00E+00	0.00E+00	0.00%
N-13	3.91E-04	3.91E-04	0.00%	Tc-99m	5.06E-05	5.06E-05	0.00%
O-15	3.92E-04	3.92E-04	0.00%	Ru-97	1.03E-04	1.03E-04	0.00%
F-18	3.92E-04	3.92E-04	0.00%	In-111	1.79E-04	1.79E-04	0.00%
Na-22	8.00E-04	8.00E-04	0.00%	In-113m	1.07E-04	1.07E-04	0.00%
Na-24	1.19E-03	1.19E-03	0.00%	In-111m	1.83E-04	1.83E-04	0.00%
P-32	0.00E+00	0.00E+00	0.00%	In-114m	5.39E-05	5.39E-05	0.00%
S-35	0.00E+00	0.00E+00	0.00%	I-123	1.08E-04	1.08E-04	0.00%
K-42	9.74E-05	9.74E-05	0.00%	I-124	4.11E-04	4.11E-04	0.00%
K-43	3.61E-04	3.61E-04	0.00%	I-125	8.86E-05	8.86E-05	0.00%
Ca-45	0.00E+00	0.00E+00	0.00%	I-126	1.84E-04	1.84E-04	0.00%
Ca-49	8.00E-04	8.00E-04	0.00%	I-129	2.84E-06	2.84E-06	0.00%
Sc-47	4.11E-05	4.11E-05	0.00%	I-130	8.02E-04	8.02E-04	0.00%
Sc-49	0.00E+00	0.00E+00	0.00%	I-131	1.46E-04	1.46E-04	0.00%
Cr-51	9.11E-05	9.11E-05	0.00%	Xe-120	2.24E-04	2.24E-04	0.00%
Mn-52m	8.70E-04	8.70E-04	0.00%	Xe-121	6.16E-04	6.16E-04	0.00%
Fe-52	3.38E-04	3.38E-04	0.00%	Xe-122	6.76E-05	6.76E-05	0.00%
Fe-52m	1.32E-03	1.32E-03	0.00%	Xe-123	2.60E-04	2.60E-04	0.00%
Fe-55	1.17E-04	1.17E-04	0.00%	Xe-125	1.54E-04	1.54E-04	0.00%
Fe-59	4.21E-04	4.21E-04	0.00%	Xe-127	1.52E-04	1.52E-04	0.00%
Co-57	3.07E-04	3.07E-04	0.00%	Cs-129	1.66E-04	1.66E-04	0.00%
Co-58	4.83E-04	4.83E-04	0.00%	Dy-157	1.22E-04	1.22E-04	0.00%
Co-58m	1.32E-04	1.32E-04	0.00%	Yb-169	4.14E-04	4.14E-04	0.00%
Co-60	8.81E-04	8.81E-04	0.00%	W-178	1.30E-04	1.30E-04	0.00%
Co-60m	1.56E-04	1.56E-04	0.00%	Ir-192	3.45E-04	3.45E-04	0.00%
Cu-62	3.88E-04	3.88E-04	0.00%	Au-195	4.26E-04	4.26E-04	0.00%
Cu-64	1.61E-04	1.61E-04	0.00%	Au-195m	3.16E-04	3.16E-04	0.00%
Cu-67	8.36E-05	8.36E-05	0.00%	Au-198	1.61E-04	1.61E-04	0.00%
Ga-66	8.66E-04	8.66E-04	0.00%	Hg-195	4.33E-04	4.33E-04	0.00%
Ga-67	4.01E-04	4.01E-04	0.00%	Hg-197	3.80E-04	3.80E-04	0.00%
Ga-68	3.90E-04	3.90E-04	0.00%	Hg-197m	3.73E-04	3.73E-04	0.00%
Ga-72	8.68E-04	8.68E-04	0.00%	Hg-203	8.92E-05	8.92E-05	0.00%
Se-73	4.41E-04	4.41E-04	0.00%	Tl-201m	3.08E-04	3.08E-04	0.00%
Se-75	1.46E-04	1.46E-04	0.00%	Tl-201	4.19E-04	4.19E-04	0.00%
Kr-81m	4.81E-05	4.81E-05	0.00%	Te-123m	9.13E-05	9.13E-05	0.00%
Rb-82m	1.07E-03	1.07E-03	0.00%	Pt-195m	5.26E-04	5.26E-04	0.00%
Rb-82	4.15E-04	4.15E-04	0.00%	Pb-203m1	2.67E-04	2.67E-04	0.00%
Sr-90	0.00E+00	0.00E+00	0.00%	Pb-203m	7.17E-04	7.17E-04	0.00%
Y-87	1.78E-04	1.78E-04	0.00%	Pb-203	1.27E-04	1.27E-04	0.00%

Table 16. S-values for kidney medulla as a source region and kidney cortex as a target region.

Radionuclide	MIRD	EGS4	DIFF(%)	Radionuclide	MIRD	EGS4	DIFF(%)
C-11	3.48E-04	5.63E-04	38.30%	Y-90m	2.18E-04	2.48E-04	11.99%
C-14	0.00E+00	2.92E-06	100.00%	Y-90	0.00E+00	1.58E-03	100.00%
N-13	3.48E-04	7.25E-04	52.01%	Tc-99m	4.52E-05	4.72E-05	4.09%
O-15	3.48E-04	1.28E-03	72.90%	Ru-97	1.03E-04	1.05E-04	2.61%
F-18	3.48E-04	4.23E-04	17.58%	In-111	1.67E-04	1.73E-04	3.52%
Na-22	6.91E-04	7.41E-04	6.71%	In-113m	9.69E-05	1.67E-04	41.84%
Na-24	1.09E-03	1.59E-03	31.24%	In-111m	1.63E-04	2.14E-04	24.03%
P-32	0.00E+00	8.28E-04	100.00%	In-114m	4.66E-05	7.59E-05	38.65%
S-35	0.00E+00	2.82E-06	100.00%	I-123	9.23E-05	9.56E-05	3.46%
K-42	7.99E-05	4.15E-03	98.08%	I-124	3.61E-04	6.52E-04	44.57%
K-43	3.23E-04	4.70E-04	31.27%	I-125	7.14E-05	7.17E-05	0.42%
Ca-45	0.00E+00	7.10E-06	100.00%	I-126	1.62E-04	2.29E-04	29.34%
Ca-49	7.60E-04	2.15E-03	64.66%	I-129	2.98E-06	4.97E-06	40.10%
Sc-47	3.70E-05	6.94E-05	46.73%	I-130	7.10E-04	8.35E-04	14.93%
Sc-49	0.00E+00	1.18E-03	100.00%	I-131	1.32E-04	1.75E-04	24.86%
Cr-51	3.88E-05	3.88E-05	0.04%	Xe-120	1.91E-04	1.98E-04	3.82%
Mn-52m	7.40E-04	3.24E-03	77.15%	Xe-121	5.55E-04	1.81E-03	69.26%
Fe-52	2.73E-04	3.63E-04	24.85%	Xe-122	5.45E-05	5.50E-05	0.82%
Fe-52m	1.15E-03	8.77E-03	86.93%	Xe-123	2.26E-04	4.01E-04	43.67%
Fe-55	4.12E-05	4.12E-05	0.05%	Xe-125	1.31E-04	1.36E-04	3.16%
Fe-59	3.61E-04	3.80E-04	4.94%	Xe-127	1.31E-04	1.36E-04	3.51%
Co-57	1.34E-04	1.35E-04	0.46%	Cs-129	1.39E-04	1.41E-04	1.33%
Co-58	3.64E-04	3.71E-04	1.95%	Dy-157	1.09E-04	1.10E-04	1.16%
Co-58m	4.63E-05	4.67E-05	0.90%	Yb-169	2.28E-04	2.40E-04	4.96%
Co-60	7.46E-04	7.57E-04	1.44%	W-178	5.08E-05	5.08E-05	0.11%
Co-60m	5.56E-05	6.08E-05	8.59%	Ir-192	2.92E-04	3.45E-04	15.40%
Cu-62	3.42E-04	3.56E-03	90.37%	Au-195	1.74E-04	1.76E-04	1.21%
Cu-64	9.53E-05	1.29E-04	26.03%	Au-195m	1.54E-04	1.71E-04	9.73%
Cu-67	5.39E-05	8.01E-05	32.67%	Au-198	1.41E-04	2.80E-04	49.74%
Ga-66	7.29E-04	4.24E-03	82.82%	Hg-195	1.96E-04	2.01E-04	2.24%
Ga-67	1.73E-04	1.75E-04	1.44%	Hg-197	1.53E-04	1.57E-04	2.66%
Ga-68	3.31E-04	1.43E-03	76.76%	Hg-197m	1.52E-04	1.84E-04	17.60%
Ga-72	7.97E-04	1.50E-03	46.95%	Hg-203	8.28E-05	9.74E-05	14.98%
Se-73	3.97E-04	7.41E-04	46.35%	Tl-201m	2.77E-04	2.99E-04	7.56%
Se-75	1.37E-04	1.39E-04	0.87%	Tl-201	1.72E-04	1.76E-04	1.88%
Kr-81m	4.64E-05	5.83E-05	20.34%	Te-123m	7.38E-05	8.39E-05	11.99%
Rb-82m	9.43E-04	1.01E-03	6.79%	Pt-195m	2.05E-04	2.23E-04	8.07%
Rb-82	3.69E-04	4.44E-03	91.68%	Pb-203m1	2.24E-04	4.28E-04	47.56%
Sr-90	0.00E+00	4.57E-05	100.00%	Pb-203m	6.42E-04	7.26E-04	11.52%
Y-87	1.66E-04	1.67E-04	0.56%	Pb-203	1.18E-04	1.26E-04	6.32%

Table 17. S-values of kidney medulla as a source region and kidney medulla as a target region.

Radionuclide	MIRD	EGS4	DIFF(%)	Radionuclide	MIRD	EGS4	DIFF(%)
C-11	5.77E-03	5.60E-03	3.07%	Y-90m	1.38E-03	1.36E-03	1.74%
C-14	5.67E-04	5.64E-04	0.41%	Y-90	1.07E-02	9.44E-03	13.41%
N-13	6.99E-03	6.69E-03	4.49%	Tc-99m	3.46E-04	3.45E-04	0.45%
O-15	9.78E-03	9.04E-03	8.29%	Ru-97	7.40E-04	7.38E-04	0.30%
F-18	4.23E-03	4.17E-03	1.43%	In-111	1.07E-03	1.07E-03	0.46%
Na-22	4.95E-03	4.91E-03	0.81%	In-113m	1.92E-03	1.86E-03	2.98%
Na-24	1.06E-02	1.02E-02	3.89%	In-111m	1.38E-03	1.34E-03	3.06%
P-32	7.96E-03	7.30E-03	9.06%	In-114m	1.84E-03	1.82E-03	1.30%
S-35	5.57E-04	5.55E-04	0.41%	I-123	6.71E-04	6.69E-04	0.40%
K-42	1.66E-02	1.34E-02	24.40%	I-124	3.67E-03	3.44E-03	6.76%
K-43	4.86E-03	4.74E-03	2.48%	I-125	4.96E-04	4.96E-04	0.05%
Ca-45	8.85E-04	8.79E-04	0.65%	I-126	2.30E-03	2.24E-03	2.40%
Ca-49	1.29E-02	1.18E-02	9.45%	I-129	4.82E-04	4.80E-04	0.33%
Sc-47	2.00E-03	1.98E-03	1.32%	I-130	6.05E-03	5.95E-03	1.67%
Sc-49	9.37E-03	8.42E-03	11.25%	I-131	2.69E-03	2.66E-03	1.32%
Cr-51	9.63E-05	9.63E-05	0.01%	Xe-120	1.24E-03	1.23E-03	0.49%
Mn-52m	1.59E-02	1.39E-02	14.32%	Xe-121	8.49E-03	7.49E-03	13.34%
Fe-52	3.21E-03	3.14E-03	2.30%	Xe-122	3.00E-04	3.00E-04	0.12%
Fe-52m	2.74E-02	2.12E-02	29.55%	Xe-123	3.00E-03	2.86E-03	4.89%
Fe-55	6.49E-05	6.48E-05	0.02%	Xe-125	8.77E-04	8.73E-04	0.39%
Fe-59	2.77E-03	2.75E-03	0.55%	Xe-127	8.51E-04	8.47E-04	0.45%
Co-57	3.50E-04	3.49E-04	0.14%	Cs-129	6.93E-04	6.91E-04	0.22%
Co-58	1.66E-03	1.65E-03	0.35%	Dy-157	4.70E-04	4.69E-04	0.22%
Co-58m	2.62E-04	2.62E-04	0.13%	Yb-169	1.80E-03	1.79E-03	0.53%
Co-60	4.06E-03	4.05E-03	0.22%	W-178	9.39E-05	9.38E-05	0.05%
Co-60m	7.80E-04	7.76E-04	0.54%	Ir-192	3.52E-03	3.48E-03	1.22%
Cu-62	1.60E-02	1.34E-02	19.10%	Au-195	6.82E-04	6.80E-04	0.25%
Cu-64	1.67E-03	1.64E-03	1.64%	Au-195m	1.56E-03	1.55E-03	0.86%
Cu-67	1.92E-03	1.90E-03	1.10%	Au-198	4.28E-03	4.17E-03	2.67%
Ga-66	1.40E-02	1.11E-02	25.83%	Hg-195	9.30E-04	9.26E-04	0.39%
Ga-67	5.99E-04	5.97E-04	0.34%	Hg-197	8.41E-04	8.37E-04	0.40%
Ga-68	9.75E-03	8.87E-03	9.87%	Hg-197m	2.55E-03	2.53E-03	1.03%
Ga-72	8.81E-03	8.24E-03	6.84%	Hg-203	1.45E-03	1.44E-03	0.81%
Se-73	6.06E-03	5.79E-03	4.73%	Tl-201m	1.51E-03	1.50E-03	1.21%
Se-75	7.81E-04	7.80E-04	0.12%	Tl-201	6.47E-04	6.45E-04	0.41%
Kr-81m	8.63E-04	8.54E-04	1.11%	Te-123m	1.43E-03	1.42E-03	0.57%
Rb-82m	4.86E-03	4.81E-03	1.14%	Pt-195m	2.14E-03	2.12E-03	0.68%
Rb-82	1.76E-02	1.44E-02	22.65%	Pb-203m1	2.64E-03	2.48E-03	6.56%
Sr-90	2.24E-03	2.21E-03	1.66%	Pb-203m	4.95E-03	4.88E-03	1.37%
Y-87	8.31E-04	8.30E-04	0.09%	Pb-203	9.27E-04	9.21E-04	0.69%

Table 18. S-values of kidney medulla as a source region and kidney papillary as a target region.

Radionuclide	MIRD	EGS4	DIFF(%)	Radionuclide	MIRD	EGS4	DIFF(%)
C-11	9.35E-04	1.26E-03	25.81%	Y-90m	5.77E-04	6.21E-04	7.10%
C-14	0.00E+00	4.73E-06	100.00%	Y-90	0.00E+00	2.37E-03	100.00%
N-13	9.35E-04	1.49E-03	37.23%	Tc-99m	1.17E-04	1.20E-04	2.60%
O-15	9.36E-04	2.33E-03	59.87%	Ru-97	2.77E-04	2.81E-04	1.58%
F-18	9.37E-04	1.06E-03	11.41%	In-111	4.20E-04	4.30E-04	2.30%
Na-22	1.88E-03	1.96E-03	4.11%	In-113m	2.50E-04	3.55E-04	29.71%
Na-24	2.95E-03	3.69E-03	19.87%	In-111m	4.36E-04	5.11E-04	14.82%
P-32	0.00E+00	1.23E-03	100.00%	In-114m	1.15E-04	1.62E-04	29.35%
S-35	0.00E+00	4.57E-06	100.00%	I-123	1.87E-04	1.92E-04	2.80%
K-42	2.21E-04	6.38E-03	96.54%	I-124	9.38E-04	1.37E-03	31.68%
K-43	8.64E-04	1.09E-03	20.77%	I-125	9.73E-05	9.78E-05	0.50%
Ca-45	0.00E+00	1.15E-05	100.00%	I-126	4.08E-04	5.11E-04	20.15%
Ca-49	2.06E-03	4.14E-03	50.28%	I-129	2.46E-06	5.69E-06	56.84%
Sc-47	9.47E-05	1.47E-04	35.71%	I-130	1.92E-03	2.11E-03	9.07%
Sc-49	0.00E+00	1.77E-03	100.00%	I-131	3.44E-04	4.14E-04	17.01%
Cr-51	1.08E-04	1.08E-04	0.02%	Xe-120	4.29E-04	4.40E-04	2.63%
Mn-52m	2.02E-03	5.78E-03	65.05%	Xe-121	1.44E-03	3.32E-03	56.65%
Fe-52	7.30E-04	8.68E-04	15.93%	Xe-122	8.73E-05	8.80E-05	0.81%
Fe-52m	3.12E-03	1.49E-02	79.10%	Xe-123	5.48E-04	8.09E-04	32.29%
Fe-55	1.17E-04	1.17E-04	0.03%	Xe-125	2.69E-04	2.76E-04	2.52%
Fe-59	9.91E-04	1.02E-03	2.96%	Xe-127	2.77E-04	2.85E-04	2.70%
Co-57	3.70E-04	3.71E-04	0.27%	Cs-129	2.76E-04	2.79E-04	1.03%
Co-58	9.92E-04	1.00E-03	1.17%	Dy-157	2.83E-04	2.85E-04	0.71%
Co-58m	1.32E-04	1.33E-04	0.52%	Yb-169	6.19E-04	6.39E-04	3.02%
Co-60	2.05E-03	2.07E-03	0.86%	W-178	1.43E-04	1.43E-04	0.06%
Co-60m	1.58E-04	1.66E-04	4.97%	Ir-192	7.73E-04	8.59E-04	9.94%
Cu-62	9.21E-04	5.76E-03	84.02%	Au-195	4.86E-04	4.89E-04	0.71%
Cu-64	2.61E-04	3.15E-04	17.06%	Au-195m	4.22E-04	4.49E-04	6.00%
Cu-67	1.42E-04	1.85E-04	22.96%	Au-198	3.74E-04	5.90E-04	36.58%
Ga-66	1.98E-03	7.40E-03	73.26%	Hg-195	5.47E-04	5.54E-04	1.29%
Ga-67	4.79E-04	4.83E-04	0.85%	Hg-197	4.29E-04	4.35E-04	1.56%
Ga-68	8.93E-04	2.53E-03	64.71%	Hg-197m	4.24E-04	4.77E-04	11.04%
Ga-72	2.14E-03	3.21E-03	33.18%	Hg-203	2.14E-04	2.38E-04	9.91%
Se-73	1.06E-03	1.56E-03	32.48%	Tl-201m	7.37E-04	7.71E-04	4.38%
Se-75	3.48E-04	3.50E-04	0.56%	Tl-201	4.81E-04	4.87E-04	1.10%
Kr-81m	1.19E-04	1.38E-04	13.96%	Te-123m	1.61E-04	1.77E-04	9.22%
Rb-82m	2.56E-03	2.66E-03	3.90%	Pt-195m	5.74E-04	6.03E-04	4.83%
Rb-82	9.93E-04	7.14E-03	86.08%	Pb-203m1	6.09E-04	9.13E-04	33.27%
Sr-90	0.00E+00	7.41E-05	100.00%	Pb-203m	1.73E-03	1.86E-03	6.95%
Y-87	4.49E-04	4.50E-04	0.31%	Pb-203	3.02E-04	3.15E-04	4.07%

Table 19. S-values for kidney papillary as a source region and kidney cortex as a target region.

Radionuclide	MIRD	EGS4	DIFF(%)	Radionuclide	MIRD	EGS4	DIFF(%)
C-11	2.82E-04	2.82E-04	0.00%	Y-90m	1.71E-04	1.71E-04	0.00%
C-14	0.00E+00	0.00E+00	0.00%	Y-90	0.00E+00	0.00E+00	0.00%
N-13	2.82E-04	2.82E-04	0.00%	Tc-99m	3.47E-05	3.47E-05	0.00%
O-15	2.82E-04	2.82E-04	0.00%	Ru-97	6.97E-05	6.97E-05	0.00%
F-18	2.83E-04	2.83E-04	0.00%	In-111	1.20E-04	1.20E-04	0.00%
Na-22	5.53E-04	5.53E-04	0.00%	In-113m	7.44E-05	7.44E-05	0.00%
Na-24	8.43E-04	8.43E-04	0.00%	In-111m	1.31E-04	1.31E-04	0.00%
P-32	0.00E+00	0.00E+00	0.00%	In-114m	3.34E-05	3.34E-05	0.00%
S-35	0.00E+00	0.00E+00	0.00%	I-123	6.69E-05	6.69E-05	0.00%
K-42	6.71E-05	6.76E-05	0.73%	I-124	2.85E-04	2.85E-04	0.00%
K-43	2.55E-04	2.55E-04	0.00%	I-125	4.74E-05	4.74E-05	0.00%
Ca-45	0.00E+00	0.00E+00	0.00%	I-126	1.25E-04	1.25E-04	0.00%
Ca-49	5.74E-04	5.74E-04	0.00%	I-129	1.98E-06	1.98E-06	0.00%
Sc-47	2.87E-05	2.87E-05	0.00%	I-130	5.60E-04	5.60E-04	0.00%
Sc-49	0.00E+00	0.00E+00	0.00%	I-131	1.03E-04	1.03E-04	0.00%
Cr-51	3.63E-05	3.63E-05	0.00%	Xe-120	1.42E-04	1.42E-04	0.00%
Mn-52m	6.07E-04	6.07E-04	0.00%	Xe-121	4.29E-04	4.29E-04	0.00%
Fe-52	2.22E-04	2.22E-04	0.00%	Xe-122	3.89E-05	3.89E-05	0.00%
Fe-52m	9.03E-04	9.09E-04	0.65%	Xe-123	1.74E-04	1.74E-04	0.00%
Fe-55	4.12E-05	4.12E-05	0.00%	Xe-125	9.64E-05	9.64E-05	0.00%
Fe-59	2.79E-04	2.79E-04	0.00%	Xe-127	9.69E-05	9.69E-05	0.00%
Co-57	1.24E-04	1.24E-04	0.00%	Cs-129	1.05E-04	1.05E-04	0.00%
Co-58	2.90E-04	2.90E-04	0.00%	Dy-157	8.47E-05	8.47E-05	0.00%
Co-58m	4.63E-05	4.63E-05	0.00%	Yb-169	1.98E-04	1.98E-04	0.00%
Co-60	5.88E-04	5.88E-04	0.00%	W-178	4.91E-05	4.91E-05	0.00%
Co-60m	5.53E-05	5.53E-05	0.00%	Ir-192	2.32E-04	2.32E-04	0.00%
Cu-62	2.78E-04	2.78E-04	0.00%	Au-195	1.66E-04	1.66E-04	0.00%
Cu-64	8.32E-05	8.32E-05	0.00%	Au-195m	1.38E-04	1.38E-04	0.00%
Cu-67	4.47E-05	4.47E-05	0.00%	Au-198	1.12E-04	1.12E-04	0.00%
Ga-66	5.70E-04	5.72E-04	0.40%	Hg-195	1.80E-04	1.80E-04	0.00%
Ga-67	1.61E-04	1.61E-04	0.00%	Hg-197	1.46E-04	1.46E-04	0.00%
Ga-68	2.70E-04	2.70E-04	0.00%	Hg-197m	1.45E-04	1.45E-04	0.00%
Ga-72	6.06E-04	6.06E-04	0.00%	Hg-203	6.33E-05	6.33E-05	0.00%
Se-73	3.16E-04	3.16E-04	0.00%	Tl-201m	2.19E-04	2.19E-04	0.00%
Se-75	1.03E-04	1.03E-04	0.00%	Tl-201	1.64E-04	1.64E-04	0.00%
Kr-81m	3.37E-05	3.37E-05	0.00%	Te-123m	5.52E-05	5.52E-05	0.00%
Rb-82m	7.36E-04	7.36E-04	0.00%	Pt-195m	1.98E-04	1.98E-04	0.00%
Rb-82	2.98E-04	2.98E-04	0.07%	Pb-203m1	1.73E-04	1.73E-04	0.00%
Sr-90	0.00E+00	0.00E+00	0.00%	Pb-203m	4.85E-04	4.85E-04	0.00%
Y-87	1.28E-04	1.28E-04	0.00%	Pb-203	8.96E-05	8.96E-05	0.00%

Table 20. S-values of kidney papillary as a source region and kidney medulla as a target region.

Radionuclide	MIRD	EGS4	DIFF(%)	Radionuclide	MIRD	EGS4	DIFF(%)
C-11	9.94E-04	1.18E-03	15.55%	Y-90m	6.30E-04	6.55E-04	3.82%
C-14	0.00E+00	2.55E-06	100.00%	Y-90	0.00E+00	1.37E-03	100.00%
N-13	9.94E-04	1.31E-03	24.15%	Tc-99m	1.32E-04	1.34E-04	1.26%
O-15	9.95E-04	1.80E-03	44.67%	Ru-97	3.35E-04	3.37E-04	0.71%
F-18	9.96E-04	1.06E-03	6.13%	In-111	5.11E-04	5.16E-04	1.03%
Na-22	2.08E-03	2.13E-03	2.05%	In-113m	2.85E-04	3.44E-04	17.21%
Na-24	3.32E-03	3.74E-03	11.21%	In-111m	4.70E-04	5.13E-04	8.43%
P-32	0.00E+00	7.08E-04	100.00%	In-114m	1.42E-04	1.67E-04	15.35%
S-35	0.00E+00	2.47E-06	100.00%	I-123	2.70E-04	2.72E-04	1.06%
K-42	2.51E-04	3.84E-03	93.47%	I-124	1.07E-03	1.32E-03	19.04%
K-43	9.39E-04	1.07E-03	11.85%	I-125	2.13E-04	2.13E-04	0.12%
Ca-45	0.00E+00	6.22E-06	100.00%	I-126	4.75E-04	5.33E-04	10.79%
Ca-49	2.31E-03	3.51E-03	34.23%	I-129	9.42E-06	1.12E-05	15.63%
Sc-47	1.06E-04	1.34E-04	21.12%	I-130	2.09E-03	2.20E-03	4.85%
Sc-49	0.00E+00	1.02E-03	100.00%	I-131	3.80E-04	4.19E-04	9.11%
Cr-51	4.47E-05	4.47E-05	0.03%	Xe-120	5.58E-04	5.64E-04	1.14%
Mn-52m	2.23E-03	4.41E-03	49.46%	Xe-121	1.63E-03	2.73E-03	40.13%
Fe-52	7.37E-04	8.14E-04	9.47%	Xe-122	1.55E-04	1.55E-04	0.25%
Fe-52m	3.47E-03	1.02E-02	66.18%	Xe-123	6.59E-04	8.09E-04	18.53%
Fe-55	1.90E-05	1.91E-05	0.09%	Xe-125	3.78E-04	3.82E-04	0.98%
Fe-59	1.13E-03	1.15E-03	1.43%	Xe-127	3.77E-04	3.81E-04	1.09%
Co-57	1.68E-04	1.69E-04	0.32%	Cs-129	3.89E-04	3.91E-04	0.41%
Co-58	9.82E-04	9.88E-04	0.64%	Dy-157	3.09E-04	3.10E-04	0.36%
Co-58m	2.14E-05	2.17E-05	1.70%	Yb-169	4.26E-04	4.36E-04	2.39%
Co-60	2.34E-03	2.35E-03	0.41%	W-178	4.24E-05	4.25E-05	0.11%
Co-60m	2.97E-05	3.43E-05	13.24%	Ir-192	8.10E-04	8.56E-04	5.41%
Cu-62	9.76E-04	3.80E-03	74.29%	Au-195	1.72E-04	1.74E-04	1.07%
Cu-64	1.99E-04	2.28E-04	12.83%	Au-195m	2.41E-04	2.56E-04	5.69%
Cu-67	1.22E-04	1.45E-04	15.85%	Au-198	3.97E-04	5.16E-04	23.14%
Ga-66	2.08E-03	5.20E-03	59.97%	Hg-195	2.69E-04	2.73E-04	1.43%
Ga-67	2.06E-04	2.08E-04	1.06%	Hg-197	1.44E-04	1.48E-04	2.47%
Ga-68	9.26E-04	1.87E-03	50.48%	Hg-197m	1.52E-04	1.81E-04	15.72%
Ga-72	2.39E-03	3.00E-03	20.47%	Hg-203	2.40E-04	2.53E-04	5.03%
Se-73	1.14E-03	1.43E-03	20.29%	Tl-201m	8.01E-04	8.21E-04	2.33%
Se-75	4.06E-04	4.07E-04	0.26%	Tl-201	1.76E-04	1.79E-04	1.61%
Kr-81m	1.40E-04	1.51E-04	6.89%	Te-123m	2.06E-04	2.15E-04	4.09%
Rb-82m	2.85E-03	2.91E-03	2.03%	Pt-195m	1.72E-04	1.88E-04	8.37%
Rb-82	1.06E-03	4.65E-03	77.15%	Pb-203m1	6.59E-04	8.34E-04	20.98%
Sr-90	0.00E+00	4.00E-05	100.00%	Pb-203m	1.95E-03	2.02E-03	3.59%
Y-87	5.01E-04	5.02E-04	0.16%	Pb-203	3.43E-04	3.50E-04	1.98%

Table 21. S-values of kidney papillary as a source region and kidney papillary as a target region.

Radionuclide	MIRD	EGS4	DIFF(%)	Radionuclide	MIRD	EGS4	DIFF(%)
C-11	2.94E-02	2.82E-02	4.20%	Y-90m	4.64E-03	4.47E-03	3.66%
C-14	3.50E-03	3.48E-03	0.48%	Y-90	6.60E-02	5.69E-02	13.90%
N-13	3.69E-02	3.47E-02	5.85%	Tc-99m	1.35E-03	1.34E-03	0.82%
O-15	5.41E-02	4.87E-02	10.01%	Ru-97	2.49E-03	2.47E-03	0.63%
F-18	1.99E-02	1.94E-02	2.14%	In-111	3.54E-03	3.51E-03	0.98%
Na-22	1.83E-02	1.80E-02	1.55%	In-113m	1.01E-02	9.69E-03	3.96%
Na-24	4.65E-02	4.37E-02	6.13%	In-111m	5.59E-03	5.30E-03	5.28%
P-32	4.91E-02	4.43E-02	9.74%	In-114m	1.05E-02	1.03E-02	1.60%
S-35	3.44E-03	3.42E-03	0.47%	I-123	2.51E-03	2.49E-03	0.75%
K-42	1.01E-01	7.36E-02	27.28%	I-124	1.63E-02	1.46E-02	10.36%
K-43	2.42E-02	2.34E-02	3.48%	I-125	1.75E-03	1.75E-03	0.10%
Ca-45	5.45E-03	5.41E-03	0.74%	I-126	1.13E-02	1.09E-02	3.42%
Ca-49	6.64E-02	5.83E-02	12.15%	I-129	2.91E-03	2.90E-03	0.39%
Sc-47	1.17E-02	1.15E-02	1.58%	I-130	2.48E-02	2.40E-02	2.88%
Sc-49	5.78E-02	5.09E-02	11.87%	I-131	1.43E-02	1.40E-02	1.74%
Cr-51	4.02E-04	4.02E-04	0.02%	Xe-120	4.29E-03	4.25E-03	1.01%
Mn-52m	8.51E-02	7.05E-02	17.17%	Xe-121	4.28E-02	3.55E-02	17.16%
Fe-52	1.53E-02	1.48E-02	3.37%	Xe-122	9.01E-04	8.99E-04	0.28%
Fe-52m	1.49E-01	6.08E-02	59.20%	Xe-123	1.46E-02	1.36E-02	6.94%
Fe-55	4.00E-04	4.00E-04	0.03%	Xe-125	3.14E-03	3.12E-03	0.78%
Fe-59	1.08E-02	1.06E-02	1.00%	Xe-127	2.98E-03	2.96E-03	0.91%
Co-57	1.39E-03	1.38E-03	0.25%	Cs-129	1.89E-03	1.88E-03	0.57%
Co-58	4.58E-03	4.54E-03	0.90%	Dy-157	1.04E-03	1.03E-03	0.70%
Co-58m	1.62E-03	1.61E-03	0.15%	Yb-169	8.87E-03	8.80E-03	0.77%
Co-60	1.19E-02	1.19E-02	0.52%	W-178	4.48E-04	4.47E-04	0.07%
Co-60m	4.79E-03	4.76E-03	0.63%	Ir-192	1.68E-02	1.65E-02	1.80%
Cu-62	9.26E-02	7.37E-02	20.41%	Au-195	3.57E-03	3.55E-03	0.34%
Cu-64	9.15E-03	8.95E-03	2.10%	Au-195m	8.44E-03	8.35E-03	1.13%
Cu-67	1.12E-02	1.10E-02	1.34%	Au-198	2.40E-02	2.32E-02	3.33%
Ga-66	7.43E-02	3.67E-02	50.53%	Hg-195	4.50E-03	4.48E-03	0.57%
Ga-67	2.80E-03	2.78E-03	0.51%	Hg-197	4.67E-03	4.65E-03	0.51%
Ga-68	5.44E-02	4.80E-02	11.67%	Hg-197m	1.52E-02	1.50E-02	1.22%
Ga-72	4.08E-02	3.66E-02	10.10%	Hg-203	7.49E-03	7.41E-03	1.11%
Se-73	3.02E-02	2.82E-02	6.53%	Tl-201m	4.43E-03	4.30E-03	2.93%
Se-75	2.11E-03	2.10E-03	0.33%	Tl-201	3.32E-03	3.30E-03	0.57%
Kr-81m	4.43E-03	4.36E-03	1.53%	Te-123m	7.59E-03	7.54E-03	0.76%
Rb-82m	1.31E-02	1.27E-02	3.03%	Pt-195m	1.26E-02	1.25E-02	0.81%
Rb-82	1.02E-01	7.65E-02	25.10%	Pb-203m1	1.25E-02	1.13E-02	9.44%
Sr-90	1.38E-02	1.36E-02	1.89%	Pb-203m	1.91E-02	1.86E-02	2.53%
Y-87	1.82E-03	1.82E-03	0.29%	Pb-203	3.49E-03	3.45E-03	1.30%

Estimates of Absorbed Fractions in Small Tissue Volumes for Selected Radionuclides

INTRODUCTION

The importance of evaluating absorbed fractions of energy for small volumes is based on the need for better dosimetry associated with regions of the body that can be considered of special interest in nuclear medicine. These regions may be localized tumors or isolated regions which contain a known amount of radioactive material. Absorbed dose calculations for small volumes require the use of electron transport codes which are capable of evaluating their energy deposition patterns. Small volumes are considered in this paper to be regions which have a mean chord length from a fraction to several times the range of the maximum energy electron emitted by the radionuclide.

In this study, spheres of different radii were used in which a radionuclide was uniformly distributed. These spheres can be representative of many small regions and/or can be combined to provide an estimate of the absorbed dose to a specific region of the human body. The purpose of this paper is to report calculations of absorbed fractions of energy for spheres of different radii for selected radionuclides by using two methodologies. The first methodology considers the average energy of the beta spectrum to be representative of the radionuclide. The second method considers the entire beta spectrum. Given a specific radionuclide, results obtained from both methodologies are compared to assess their differences for any sphere size with a specific surface-to-volume ratio.

METHODOLOGY

Figure 1 shows a schematic representation of a tissue sphere of radius $2R_0$ subdivided into 100 concentric subregions or shells with thickness ΔR ($\Delta R = 2R_0/100$). The source region was defined analytically by a sphere of radius R_0. Monoenergetic electrons were generated uniformly and isotropically throughout the source region. Absorbed fractions for electron energies were calculated for every shell of the sphere. Six different spheres sizes were used and a complete set of electron absorbed fractions was generated for each sphere size. The radii (R_0) of the source regions of the tissue spheres were 2.0, 1.0, 0.5, 0.25, 0.125 and 0.1 cm. The kinetic energies of the monoenergetic electrons were 0.05, 0.25, 0.5, 1.0, 1.5, 2.0, and 4.0 MeV. The absorbed fractions for zero kinetic energy represent the mathematical limit of the absorbed fractions; consequently, for shells inside the source region, the limiting absorbed fraction is given by the volume fraction of the source region. For regions outside the source region, the limiting absorbed fraction is zero.

To calculate the absorbed fractions of energy, the Monte Carlo code Electron-Gamma Shower (EGS4) was used in this research *(1)*. The code is capable of simulating the

transport of electrons and photons in any element, compound or mixture. In this research, the material in which electrons and photons were transported was tissue. The elemental composition of tissue was based on the data given by MIRD Pamphlet No. 5 Revised *(2)*. The lower cutoff energies for electrons and photons were 10 keV and 1 keV, respectively. Photons or electrons with energies below these cutoffs were not transported and the remaining energy was assumed to be deposited locally.

The results obtained using the EGS4 code for monoenergetic electrons were used to calculate absorbed fractions of energy for actual spectra of various radionuclides. Information on radionuclides was obtained from the National Nuclear Data Center (Brookhaven National Laboratory) using the computer code RADLST *(3)*. The spectra are given in the form of a histograms based on "group intensities". Each group intensity is given by the average energy of the "bin" corresponding to the width of each element of the histogram.

The energy deposited in each annular region of the sphere, ε_i, is calculated directly using the following equation:

$$\varepsilon_i = \int_0^{T_{max}} T \frac{dI(T)}{dT} \phi(i,T) dT \,, \tag{1}$$

where dI(T)/dT is the differential energy probability distribution of the spectrum, T is the electron kinetic energy, and $\phi(i,T)$ is the absorbed fraction of energy in the i^{th} shell of the sphere. The above equation can be approximated by summing over energy groups:

$$\varepsilon_i \cong \sum_j^n T_j I_j \phi_i \,, \tag{2}$$

where ϕ_i is the absorbed fraction for shell index i, and I_j is the group intensity at the mean energy T_j. The sum of the energy group decay intensities I_j is normalized to unity.

The average electron energy, $\overline{T}$, for a ß-decaying radionuclide is given by:

$$\bar{T} = \int_0^{T_{max}} T \frac{dI(T)}{dT} dT \ , \tag{3}$$

where equation (3) can be approximated by

$$\bar{T} \approx \sum_j I_j T_j \ . \tag{4}$$

The absorbed fraction, ϕ_i, calculated by using the average electron energy, $\bar{T}$, is obtained by interpolating between the values of absorbed fractions for monoenergetic electrons; consequently, the absorbed fraction of the average electron energy is

$$\phi_i(\bar{T}) = \phi_i\left(\sum_j I_j T_j\right) \ , \tag{5}$$

and the value of $\phi_i(\bar{T})$ must be calculated for every shell of the sphere to obtain an absorbed fraction profile. The energy deposited in the i^{th} shell under the above assumptions can be approximated by:

$$\varepsilon_i = \bar{T}\, \phi_i(\bar{T}) \ . \tag{6}$$

However, the energy deposited from the actual beta-decay spectra in the i^{th} shell is given in equation (1). From equation (1), a *weighted absorbed fraction* for a given radionuclide can be obtained by using the average energy to calculate the actual energy deposited in the i^{th} shell. The weighted absorbed fraction, $\bar{\phi}_i$, is then obtained by weighting the individual absorbed fractions of average group energies $\phi_i(T_j)$; i.e,

$$\bar{\phi}_i = \frac{\sum_j I_j T_j \phi_i(T_j)}{\sum_j I_j T_j} \tag{7}$$

or

$$\bar{\phi}_i = \frac{\sum_j I_j T_j \phi_i(T_j)}{\bar{T}} \tag{8}$$

By comparing $\overline{\phi_i}$ and $\phi_i(\overline{T})$, it is possible to assess the differences between the two methods for absorbed dose calculations.

RESULTS

Using the absorbed fractions for monoenergetic electrons and the spectra for selected radionuclides, absorbed fractions were calculated for specific radionuclides by using equation (5) and (8) for the two methodologies, respectively. As an example, figures 2 and 3 show the absorbed fraction profiles for ^{72}Ga for source regions with radii R_0 of 2.0 cm and 0.1 cm, respectively. The spectral profile is based on equation (8) and the average energy profile is based on equation (5).

Figure 2 shows that the use of the average energy of the spectrum provides an overestimate of the actual absorbed fraction in the source region when compared with that obtained using the entire beta spectrum. Conversely, the use of the average energy provides an underestimate of the total absorbed fraction outside the source region. However, Figure 3 shows that as the radius of the source region decreases, the relation between the absorbed fractions based upon the average and spectral beta energies reverse.

The total absorbed fraction in source region, ϕ_S, was evaluated by adding the individual absorbed fractions of shells inside source region (i=1,2,...50):

$$\phi_S = \sum_{i=1}^{50} \phi_i . \qquad (9)$$

In the same manner, the total absorbed fraction in the target region, ϕ_T, was calculated for shells outside the source region (i=51,52...100):

$$\phi_T = \sum_{i=51}^{100} \phi_i . \qquad (10)$$

Table 1 presents a comparison of the total absorbed fractions for selected radionuclides in source regions of radii of 0.1 0.5, 1.0, and 2.0 cm, respectively. Here, the absorbed fraction of energy obtained by using the average energy of the spectrum (equation 5) is compared with the absorbed fraction obtained by considering the entire beta spectrum (equation 8). Table 1 indicates clearly the importance of considering the beta spectrum as

opposed to using the average beta energy in dosimetric calculations due to the differences in calculated absorbed fractions. The use of average energies generally leads to over-estimates of the absorbed fraction for the source regions; however, in cases where the source region becomes smaller, this relationship seems to reverse (for example I-124 and Na-24 in Table 1). Therefore, the absorbed fraction is dependent on the spectral shape of the beta emitter.

Figures 4 through 7 show the total absorbed fraction in the source region, based on both methods, as a function of the radionuclide's average beta energy for spheres of different sizes. In these figures, the absorbed fraction values for a particular radionuclide are connected by a vertical line. This line is intended only to identify the pairs of data points and not to indicate the errors associated with the Monte Carlo calculations. From these figures, it is possible to approximately assess, under either methodology, the absorbed fractions of any radionuclide given its average beta energy.

Figure 8 shows another result of this study in which a relation between the surface-to-volume ratio and total absorbed fraction of energy in the source region is given for several radionuclides. Using these plots, or the data given in Table 1, an interpolation procedure can be applied to calculate the actual absorbed fractions for any source region for various radionuclides by knowing the appropriate surface-to-volume ratio. The relation associated with the surface-to-volume ratio is independent of geometrical considerations with the condition that the region must be convex; therefore, such plots can be used for any geometrical configuration. In other words, if two convex regions composed of tissue material have the same surface-to-volume ratio, then these regions must have the same absorbed fraction for a given radionuclide.

SUMMARY OF RESULTS

For volumes with radii on the order of several times the maximum electron range, the use of average electron energy of the beta spectrum gives is a good approximation to the absorbed fraction when compared to results obtained using the emission spectrum of the radionuclide. When the volume of the source region becomes on the order of the range of the most energetic beta particle, the average energy electron absorbed fraction provides a conservative over-estimation of the actual absorbed fraction of energy. However, when the volume of the source region is a fraction of the range of the most energetic beta particle, the use of average electron energy can over-estimate or under-estimate the actual absorbed fraction depending on the softness or hardness of the emission spectrum of the radionuclide (for example ^{15}O, ^{24}Na, ^{32}P given in Table 1). The factors associated with the difference

between both methods are the spectral shape and maximum electron energy of the radionuclide.

As stated above, Figure 8 shows absorbed fractions in the source region for various radionuclides as a function of surface-to-volume ratio. This plot can be used to obtain estimates of absorbed fractions in the source region for any convex geometrical arrangement with a specific surface-to-volume ratio containing a specific radionuclide. The only restriction associated with this plot is that the region must be convex and the radioactive material must be uniformly distributed in the source region.

REFERENCES

1. Nelson, W. R.; Hirayama; H., Rogers; D. W. O. The EGS4 code system. Stanford Linear Accelerator Center, Report 265; 1985.

2. Snyder, W. S.; Ford M. R.; Warner, G. G. Estimates of specific absorbed fractions for photon sources uniformly distributed in various organs of a heterogeneous phantom. MIRD Pamphlet No. 5, Revised. New York: Society of Nuclear Medicine; 1978.

3. Burrows T. W. The program RADLST. Brookhaven National Laboratory, New York,Information Analysis center report, BNl-NCS-52142; 1988.

TABLE 1

Total Absorbed Fraction in the Source Region for Different Sphere Sizes Using Either the Emission Spectrum and Average Energy for Selected Radionuclides

	Sphere Size									
	0.1 cm		0.25 cm		0.5 cm		1.0 cm		2.0 cm	
Radionuclide	a	b	a	b	a	b	a	b	a	b
Xe-133	0.68	0.85	0.85	0.93	0.92	0.97	0.96	0.98	0.98	0.99
Mo-99	0.14	0.13	0.32	0.47	0.55	0.71	0.74	0.85	0.87	0.92
In-111	0.53	0.81	0.76	0.92	0.87	0.96	0.94	0.98	0.97	0.99
In-114	0.05	0.00	0.15	0.10	0.31	0.37	0.54	0.64	0.74	0.81
C-11	0.15	0.14	0.37	0.50	0.62	0.72	0.80	0.86	0.89	0.93
Xe-120	0.15	0.13	0.39	0.47	0.63	0.71	0.80	0.85	0.90	0.92
Xe-121	0.03	0.03	0.09	0.08	0.19	0.17	0.38	0.42	0.62	0.68
Xe-123	0.06	0.02	0.18	0.15	0.39	0.45	0.63	0.70	0.80	0.84
I-124	0.04	0.01	0.13	0.09	0.29	0.31	0.49	0.58	0.71	0.78
Xe-125	0.61	0.98	0.80	0.99	0.89	1.00	0.95	1.00	0.97	1.00
I-126	0.20	0.22	0.42	0.60	0.64	0.79	0.80	0.89	0.90	0.94
I-129	0.91	0.95	0.96	0.98	0.98	0.99	0.99	1.00	1.00	1.00
I-130	0.22	0.25	0.45	0.63	0.66	0.81	0.82	0.90	0.90	0.95
I-131	0.37	0.58	0.64	0.81	0.80	0.90	0.90	0.95	0.95	0.98
N-13	0.10	0.10	0.27	0.31	0.51	0.59	0.72	0.79	0.85	0.89
C-14	0.90	0.94	0.96	0.98	0.98	0.99	0.99	0.99	1.00	1.00
F-18	0.29	0.33	0.58	0.69	0.76	0.84	0.88	0.92	0.94	0.96
O-15	0.05	0.01	0.16	0.12	0.34	0.41	0.58	0.67	0.77	0.83
Na-24	0.08	0.05	0.21	0.21	0.42	0.51	0.64	0.74	0.80	0.86
P-32	0.06	0.01	0.17	0.13	0.35	0.43	0.59	0.68	0.78	0.83
S-35	0.89	0.94	0.96	0.98	0.98	0.99	0.99	0.99	0.99	1.00
Cl-38	0.03	0.03	0.07	0.07	0.14	0.13	0.24	0.30	0.43	0.58
K-42	0.03	0.03	0.08	0.07	0.16	0.15	0.30	0.35	0.53	0.62
K-43	0.20	0.21	0.43	0.58	0.65	0.78	0.81	0.89	0.90	0.94
Ca-45	0.78	0.89	0.90	0.95	0.95	0.98	0.97	0.99	0.99	0.99
Sc-47	0.43	0.64	0.69	0.84	0.84	0.92	0.92	0.96	0.96	0.98
Ca-49	0.05	0.01	0.13	0.09	0.28	0.31	0.49	0.59	0.71	0.78
Sc-49	0.05	0.01	0.13	0.09	0.27	0.30	0.48	0.58	0.70	0.78
Fe-59	0.54	0.78	0.77	0.91	0.88	0.95	0.94	0.98	0.97	0.99
Co-61	0.11	0.10	0.27	0.36	0.51	0.63	0.72	0.81	0.85	0.90
Ga-66	0.03	0.03	0.06	0.06	0.11	0.11	0.21	0.24	0.43	0.51
Ga-72	0.12	0.10	0.25	0.30	0.41	0.59	0.58	0.78	0.75	0.89
Se-73	0.08	0.06	0.23	0.23	0.46	0.53	0.69	0.75	0.83	0.87
Sr-90	0.38	0.56	0.66	0.80	0.82	0.90	0.91	0.95	0.95	0.97
Y-90	0.04	0.03	0.12	0.10	0.24	0.26	0.43	0.53	0.67	0.75
Tc-99m	0.55	0.76	0.79	0.89	0.90	0.95	0.95	0.97	0.97	0.99

a: spectral method
b: average energy method

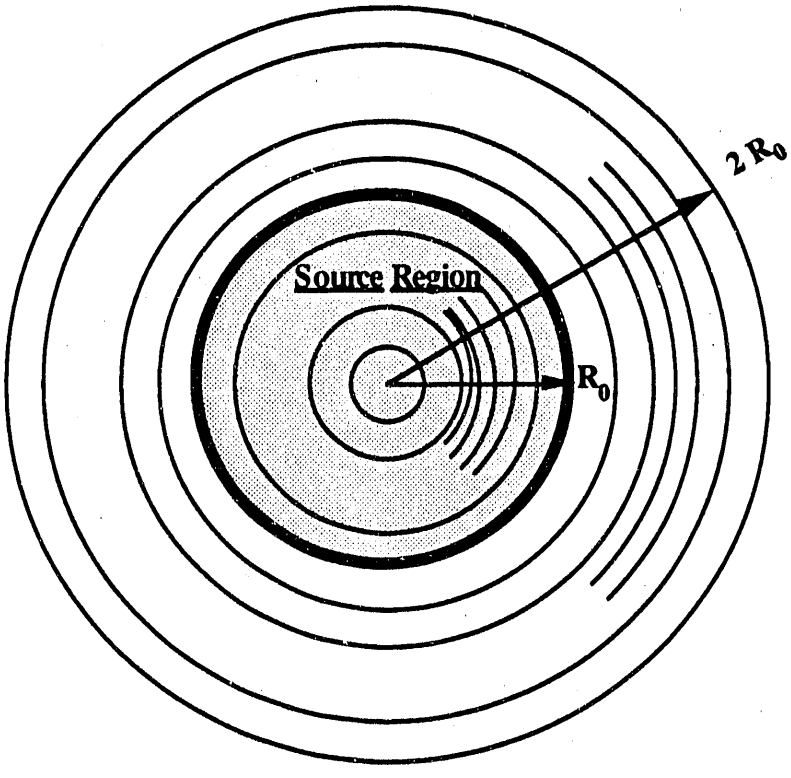

FIGURE 1. Schematic representation of the spherical geometry used for comparison of absorbed fraction calculation methodologies.

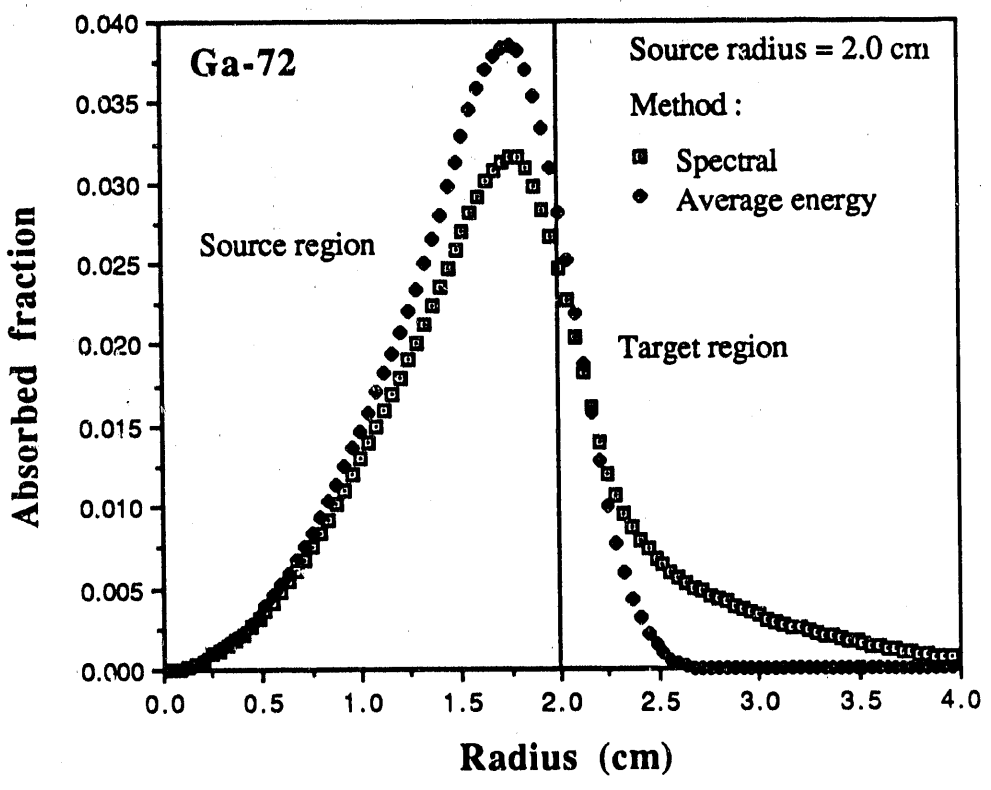

FIGURE 2. Absorbed fraction profile for Ga-72 for a source region with radius of 2.0 cm.

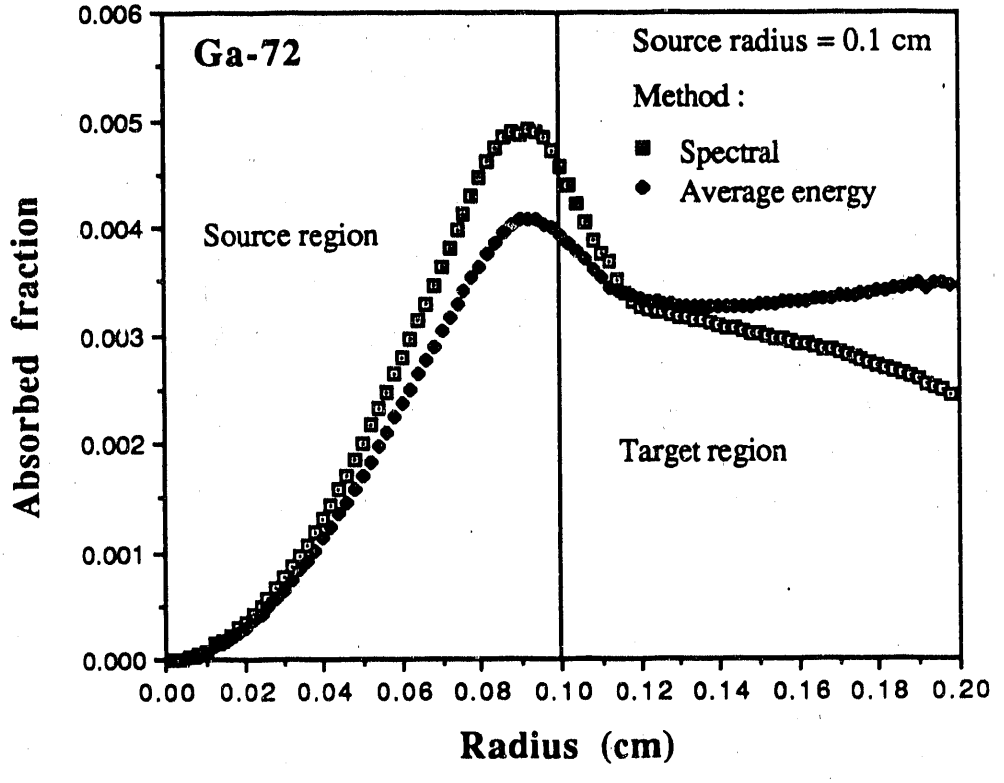

FIGURE 3. Absorbed fraction profile for Ga-72 for a source region with radius of 0.1 cm.

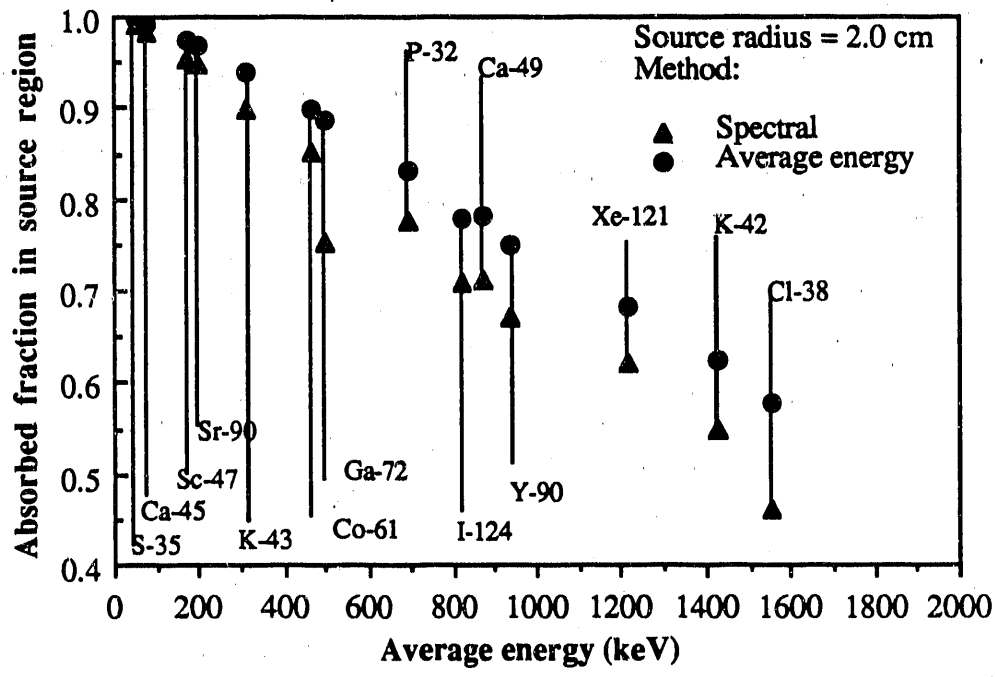

FIGURE 4. Absorbed fraction in source region of a sphere of 2.0 cm radius for different radionuclides.

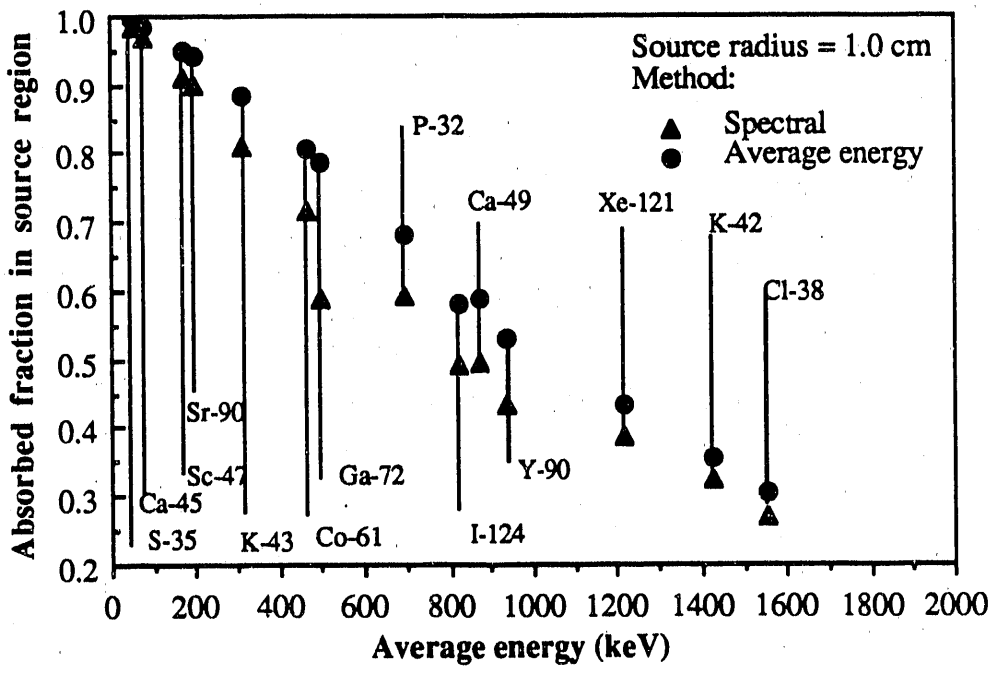

FIGURE 5. Absorbed fraction in source region of a sphere of 1.0 cm radius for different radionuclides.

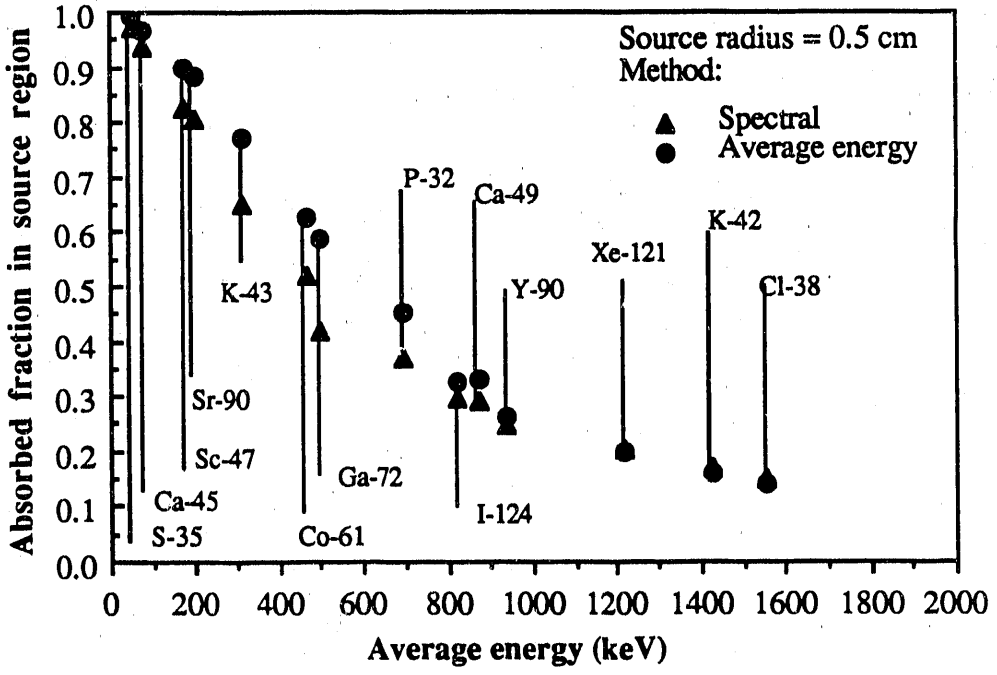

FIGURE 6. Absorbed fraction in source region of a sphere of 0.5 cm radius for different radionuclides.

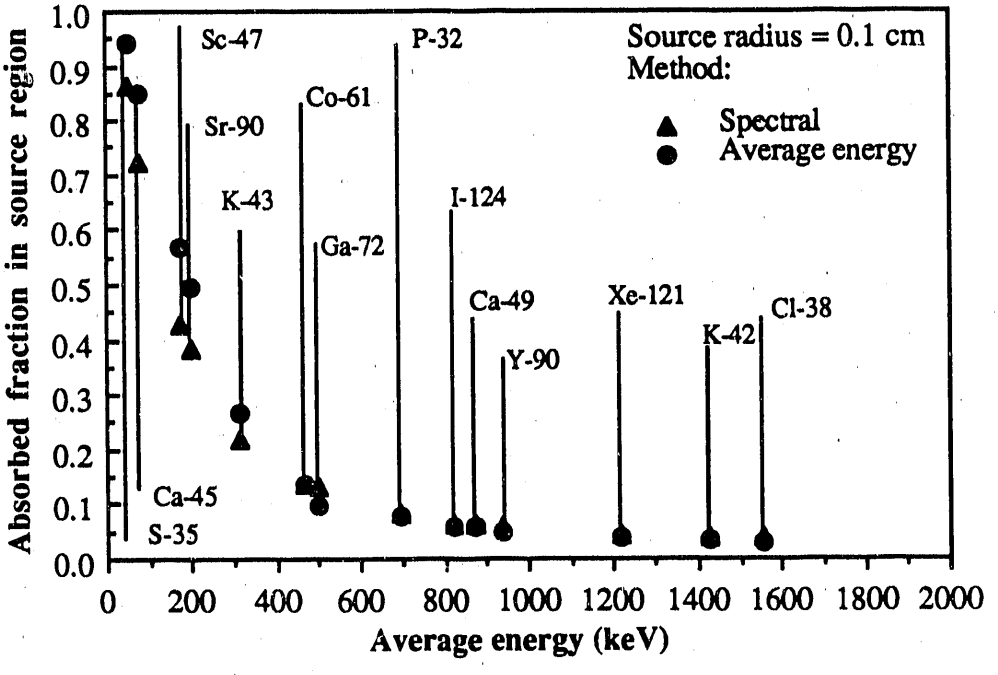

FIGURE 7. Absorbed fraction in source region of a sphere of 0.1 cm radius for different radionuclides.

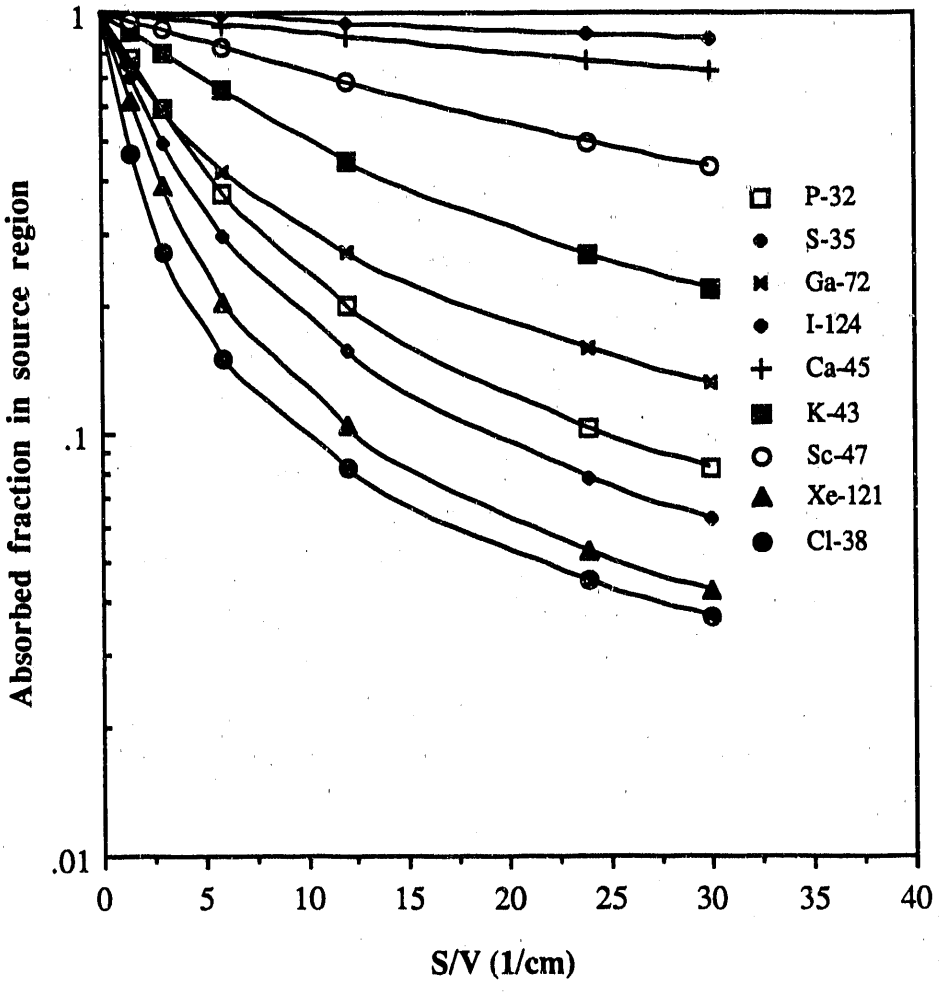

FIGURE 8. Absorbed fraction in source region as a function of surface to volume ratio for different radionuclides.

Absorbed Dose Calculations to Blood and Blood Vessels for Internally Deposited Radionuclides

A number of radionuclides are used for purposes of medical imaging, radiation therapy, and *in vivo* determination of kinetic factors for modeling. Use of these radionuclides often delivers large doses to certain regions and organs of the body. When the material is injected intravenously, there is the possibility of delivering large doses to blood vessels. There have been several simplified attempts to estimate the dose to the blood and the vessel wall. For example, Cloutier and Watson *(1)* investigated the absorbed fraction for non-penetrating radiation due to a few selected radionuclides in the blood. Hui and Poston *(2)* attempted to model the major features of the circulatory system in an adult human but focussed primarily on photon absorbed fractions. Explicit calculations of doses to the surface area of the vessel and to the blood containing the emitter are not available in the literature. The purpose of this paper is to report calculations of absorbed doses to the blood and to the surface of the blood vessel walls of the circulatory system for selected radionuclides.

The vascular system is important for the integrity and function of all tissues. Moreover, damage to the blood vessels may initiate, promote or precipitate various types of damage in many organs. The main functions of the vascular system are to supply nutrients, oxygen, and to remove metabolic products. Damage induced by irradiation of the vascular system may be expressed from several months to years after exposure. Late changes in blood vessels observed after irradiation include a reduction in number of endothelial cells, wall thickening and focal occlusion with subsequent decrease in blood flow. These changes may be important in the development of damage to other tissues.

Estimated absorbed doses to the organs of the body from radionuclides distributed in the blood depends on the assumptions used in the calculations. For non-penetrating radiations in the blood, the absorbed fraction of energy has not been examined in detail. When considering radionuclides carried in the blood stream, the absorbed fraction depends on the geometry of the circulatory system. In large blood vessels, the self-absorbed fraction for non-penetrating radiation approaches unity, and little of the energy reaches the organ through which the blood flows. The amount of energy reaching the organ depends on the distribution of the blood and the size of the blood vessels; other factors also must be taken into account. First, the radius of the vessel must be considered; second, the concentration of the radionuclide in the blood; third, the types of radiation and their spectral shapes; and fourth, the exposure time which is determined by the rate of injection, blood flow, retention time, etc.

The circulatory system comprises all structures concerned with the transportation of body fluids from one region of the body to another. The structures comprising the blood-vascular system are the heart, which by contraction forces blood through the blood vessels; arteries, which conduct blood from the heart to tissues with their smaller branches called arterioles; veins, which conduct blood from tissues toward the heart with their smaller branches called venules; and capillaries, extremely small vessels which connect arteries and veins.

Figure 1 shows the average percentage distribution of blood in a resting man *(3)*, and Table 1 presents representative dimensions of blood vessels in the circulatory system *(4)*. As Figure 1 shows, only about 5 % of the total amount of blood in the body is in the capillaries; however, this blood is exposed to a large surface area which facilitates the transfer of oxygen, carbon dioxide, nutrients and electrolytes through their walls.

METHODOLOGY

With the advent of Monte Carlo codes capable of simulating electron transport, it is possible to assess the energy deposition patterns of electrons. The code Electron Gamma Shower (EGS4) was used in this research because it is versatile and allows the manipulation of three-dimensional geometries *(5)* . The EGS4 code is a general purpose package for the simulation of electrons (+ or -) and photons in any element, compound or mixture. Data and cross sections are created by the preprocessor PEGS4 using cross sections for elements 1 through 100.

The code has shown to be acceptable for the energy range of 1 keV to 1 GeV for photons and 10 keV to 1 GeV for electrons. The code can be used to simulate closely all electron interactions in matter such as Bremsstrahlung, backscatter, and knock-on electrons, which are transported if their energies are above a certain threshold. Electron transport was simulated by assuming that electrons are moved through the material in discrete steps. The electron step size was restricted not to exceed a maximum fraction of energy loss previously established. This fraction has the variable name ESTEPE in the EGS4 system code and was set equal to 1%. The lower cutoff energies were set to 10 keV and 1 keV for electrons and photons, respectively. Blood and blood vessel walls were considered to be tissue equivalent; thus, all transport calculations were made for tissue equivalent material (4).

In general it is possible to assume that a blood vessel (arteries and veins) can be represented by a long annular cylinder, although actually the vessel nearly resembles an

elongated circular cone. In these calculations it was assumed that the inner radius of the cylinder was R_0 and the outer radius was $2R_0$. The cylinder was subdivided arbitrarily into 100 annular regions with thickness ΔR (i.e., $2R_0/100$). A cross section of the cylinder is shown in Figure 2. The inner region of the cylinder, the lumen, of radius R_0 will contain the blood stream with a uniform distribution of radioactive material. The region between R_0 and $2R_0$ represents the wall of the blood vessel. Radiations crossing the boundary at $2R_0$ were followed because interactions, such as backscatter, would allow the return of energy to the regions of interest. However, energy deposited in the region greater than $2R_0$ was calculated but was not used in these dose estimates. Absorbed fractions of energy were calculated for selected monoenergetic photons and electrons generated in the source region (blood stream) for each subregion of the cylinder as shown in Figure 3. The radii of the different blood vessels were 0.02, 0.1, 0.5 and 1.0 cm. Calculations for 100,000 histories were made from which the mean absorbed fraction of energy to each annular region was determined for both electrons and photons. Since the distance between the large blood vessels is relatively large compared to the range of beta particles, it is possible to assume that little of the energy, lost from these vessels, is absorbed by other vessels.

The dose delivered to i^{th} region of the cylinder with mass m_i is given by:

$$D_i = \frac{\varepsilon_i}{m_i} \qquad (1)$$

where ε_i is the energy deposited in i^{th} shell.

The energy deposited, ε_i, in the i^{th} shell can be calculated using the following equation:

$$\varepsilon_i = 1.602 \times 10^{-13} \pi R_0^2 \Delta X Q \sum_j \phi_{i,j} Y_j E_j \quad [J], \qquad (2)$$

where πR_0^2 is the cross sectional area of the lumen or inner cylinder in which the blood stream flows, ΔX is the length of the cylinder in which energy is deposited, Q is the number of transformations per cm^3 in the source region (blood), $\phi_{i,j}$ is the absorbed fraction for type of radiation j and the i^{th} shell of the cylinder, Y_j is the yield per transformation for radiation type j and E_j (MeV) is the energy for radiation type j. The mass of region i with length ΔX is:

$$m_i = \rho \pi (R_i^2 - R_{i-1}^2) \Delta X \quad [g]. \qquad (3)$$

where ρ is the density of the material.

The nuclear and atomic radiations associated with the radioactive decay of a radionuclide were calculated by using the computer code RADLST *(6)*, this code also gives as an option the $\beta^{\pm}$ spectrum of each radionuclide which is broken into several energy bins. Thus, the beta spectrum for a particular radionuclide was represented by a histogram rather than as a continuum and was used in equation (2). The total number of transformations in the inner radius R_0 is $\pi R_0^2 \Delta X Q$.

Consequently, the dose D_i delivered to the i^{th} shell of the cylinder is given by:

$$D_i = \frac{1.602 \times 10^{-13} \pi R_0^2 \Delta X Q \sum_j \phi_{i,j} Y_j E_j}{1.0 \times 10^{-3} \rho \pi \left(R_i^2 - R_{i-1}^2\right) \Delta X} \quad [\text{Gy}] \qquad (4)$$

eq. (4) consequently can be expressed as:

$$\frac{D_i}{Q} = \frac{1.602 \times 10^{-10} R_0^2 \sum_j \phi_{i,j} Y_j E_j}{\rho \left(R_i^2 - R_{i-1}^2\right)} \quad \left[\frac{\text{Gy cm}^3}{\text{Bq sec}}\right]. \qquad (5)$$

Equation (5) gives the dose per unit transformation per cm^3 which is representative of the radionuclide used. Therefore, the dose profile can be calculated by using equation (5) for every i^{th} shell of the cylinder.

RESULTS

Table 2 gives average absorbed doses to the blood per transformation per cm^3 for several radionuclides commonly used in medical imaging and radiation therapy for different blood vessel radii. As an example, the absorbed dose profile for ^{90}Y, ^{90}Sr, ^{11}C and ^{133}Xe are shown in Figure 4 for a blood vessel radius of 0.02 cm. Figure 5 shows a plot of the data given in Table 2 for several radionuclides on which an interpolation method can be used to assess the average dose (Gy cm^3/Bq sec) to the blood for different blood vessel radii. The absorbed dose to capillaries was obtained by extrapolation from 0.02 cm radius, using the assumption that as the radius of the blood vessel tends to zero the absorbed dose to the blood will approach zero.

Table 3 gives the absorbed dose (Gy cm^3/Bq sec) to the surface of the blood vessel wall (i.e., the surface of the inner cylinder with radius R_0). Figure 6 shows a plot of the data given in Table 3, and again an interpolation method can be used to assess the surface dose to the blood vessel wall for other radii. The surface dose is assumed to be the average of the absorbed doses obtained for the last region in the source (blood) and the first region

in the blood vessel wall. The usefulness of the data obtained for the different radionuclides varies according to the application. Individual organ doses can be assessed by defining their vascular system and the amount of blood in different blood vessel sizes.

As an example, let 3.7×10^7 Bq (1.0 mCi) of ^{90}Y be uniformly distributed in the blood of the circulatory system. Assuming no biological elimination of the material from the body (non-dynamic problem), the total number of transformations is 1.23×10^{13}. The average amount of blood in a Reference Man can be given as 5200 ml (4); assuming that the number of transformations per unit volume remains constant throughout the circulatory system, this will give a total number of transformation per cubic centimeter of 2.37×10^9 . By using an interpolation method, it is possible to calculate the dose to the blood and to the surface of the blood vessel wall for the different blood vessels of the circulatory system given in Table 1. Table 4 gives the doses to the blood in different regions of the circulatory system and Table 5 gives the doses delivered to the surface of the blood vessel walls. As can be seen in Table 4, the blood in the aorta will receive an average absorbed dose of 31.6 rad and the wall of the aorta will receive a maximum absorbed dose of 16.7 rad. The average absorbed dose to the blood will be the absorbed doses in every vessel weighted by the amount of blood contained in each. For this specific case, the average absorbed dose to the blood is 27.2 rad.

It is important to notice that the total number of transformation which occurred in the blood are dependent on the half life of the radionuclide and other physiological and metabolic parameters. So far, it has been assumed that the total number of transformations per cm^3, Q (Bq sec/cm^3), is a constant which is not dependent of the point of intake. The parameter Q in real life is dependent on time and is analogous to the retention function used in internal dosimetry calculations. It must be emphasized that a dynamic model of the circulatory system is necessary for future work in nuclear medicine.

CONCLUSIONS

The methodology described above can be applied to any radionuclide of interest in nuclear medicine and will provide estimates of the absorbed doses to the blood and blood vessels of the circulatory system for different medical procedures such as tumor therapy using radiolabeled antibodies. The results shown in figures 4 and 5 can be used in dynamic processes of blood circulation by determining the total number of transformations per unit volume in different regions of the circulatory system.

REFERENCES

1. Cloutier R.J. and Watson E.E. Radiation Dose from Radioisotopes in the Blood, In: Cloutier, Edwards and Snyder, eds. *Medical Radionuclides: Radiation Dose and Effects*; CONF-691212, 325-346, 1969.

2. Hui T.E. and Poston J.W. A Model of the Circulatory Blood for Use in Radiation Dose Calculations, Proceedings of the International Conference on Radiation Dosimetry and safety 151-168 March 1987.

3. Folkow B. and Neil E. *Circulation.* Ist Edition. New York: Oxford University Press; 1971.

4. International Commission of Radiological Protection. *Report of the task group on reference man.* Oxford: Pergamon Press; ICRP Publication 23; 1975.

5. Nelson, W. R.; Hirayama; H., Rogers; D. W. O. The EGS4 code system. Stanford Linear Accelerator Center, Report 265; 1985.

6. Burrows T. W. The program RADLST. Brookhaven National Laboratory, New York,Information Analysis center report, BNl-NCS-52142; 1988.

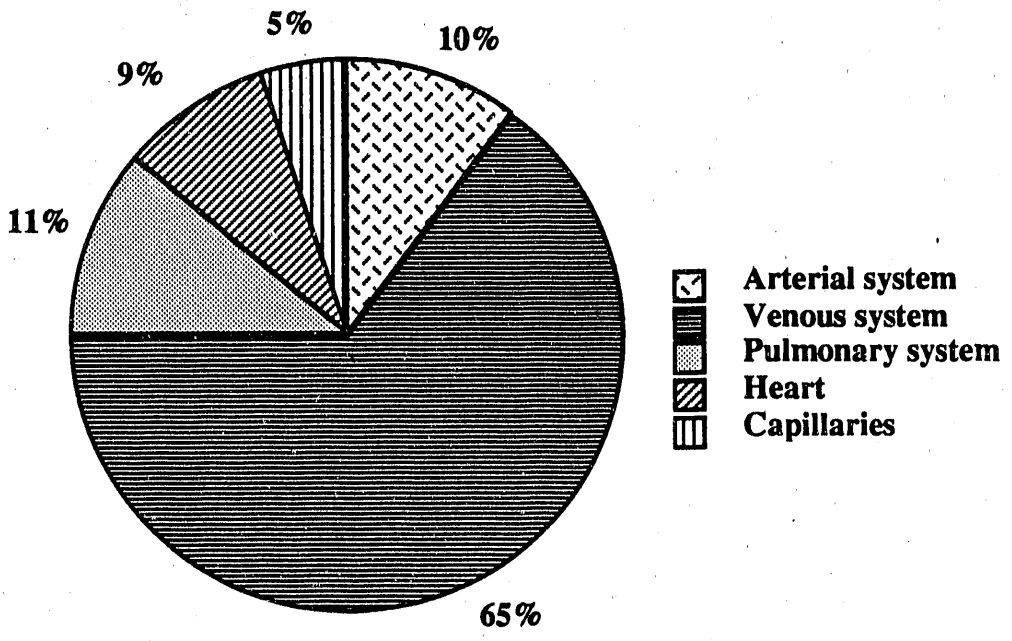

FIGURE 1. Distribution of blood volume in resting man.

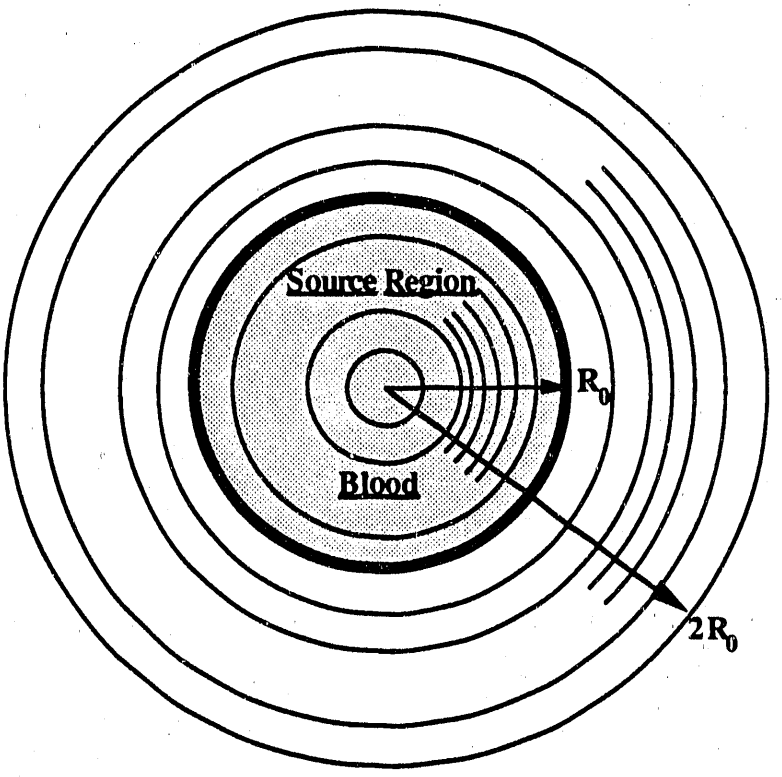

FIGURE 2. Cross section of a cylinder used to simulate a blood vessel. The inner cylinder with radius R_0 represents the source region which is the blood. The cylinder is divided into 100 inner cylinders to calculate absorbed fraction profiles throughout the source region and the wall.

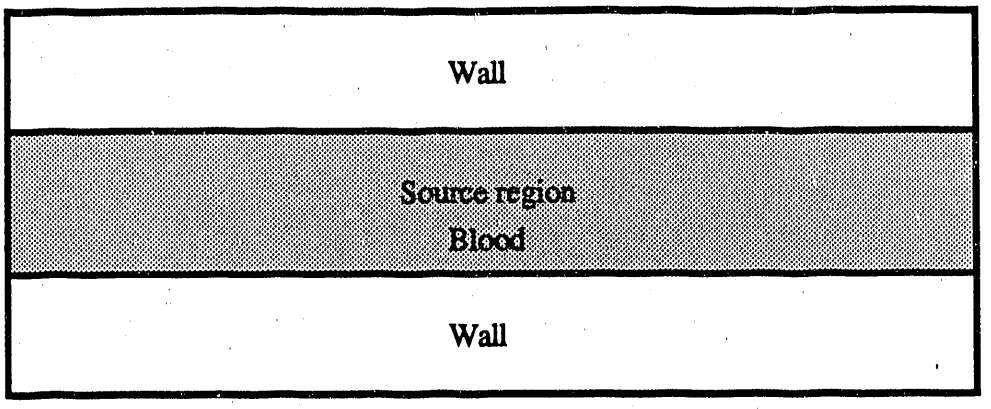

FIGURE 3. Model of a blood vessel used to obtain absorbed fraction profiles. The source region contains a uniform distribution of radioactive material.

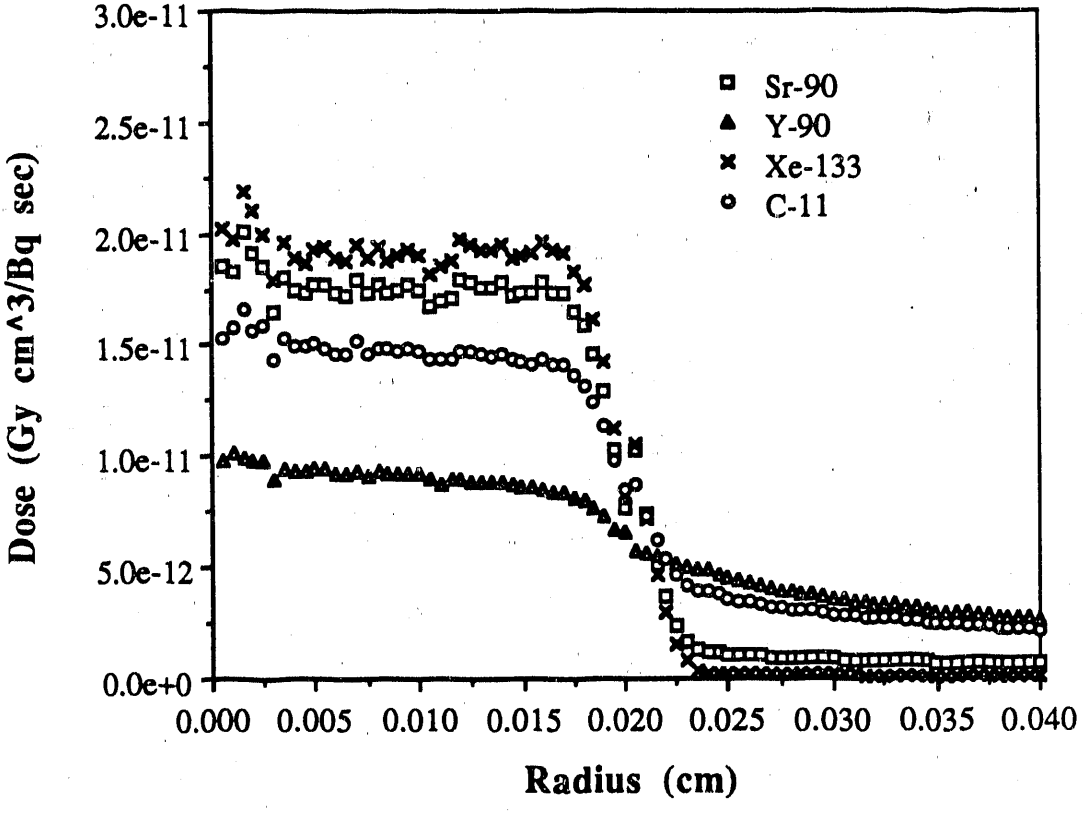

FIGURE 4. Absorbed dose profile for ^{90}Y, ^{11}C, ^{90}Sr and ^{133}Xe for a blood vessel of 0.02 cm radius.

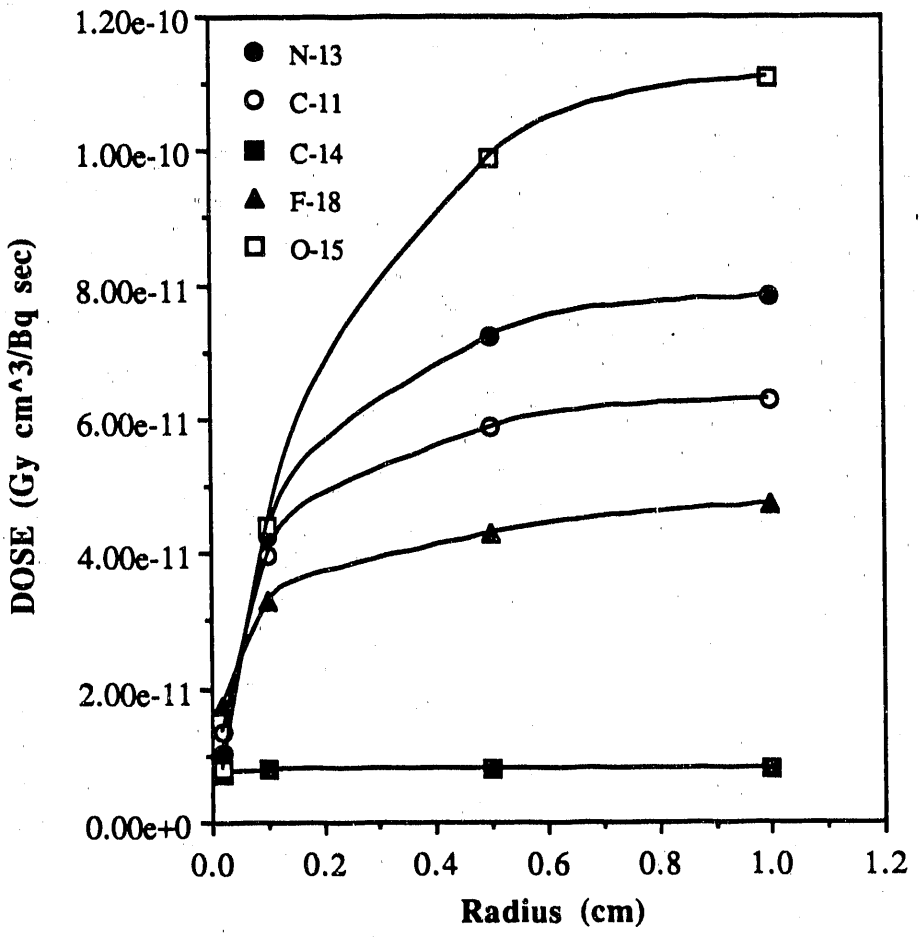

FIGURE 5. Average absorbed dose per transformation per cm^3 to blood as a function of blood vessel radius for different radionuclides.

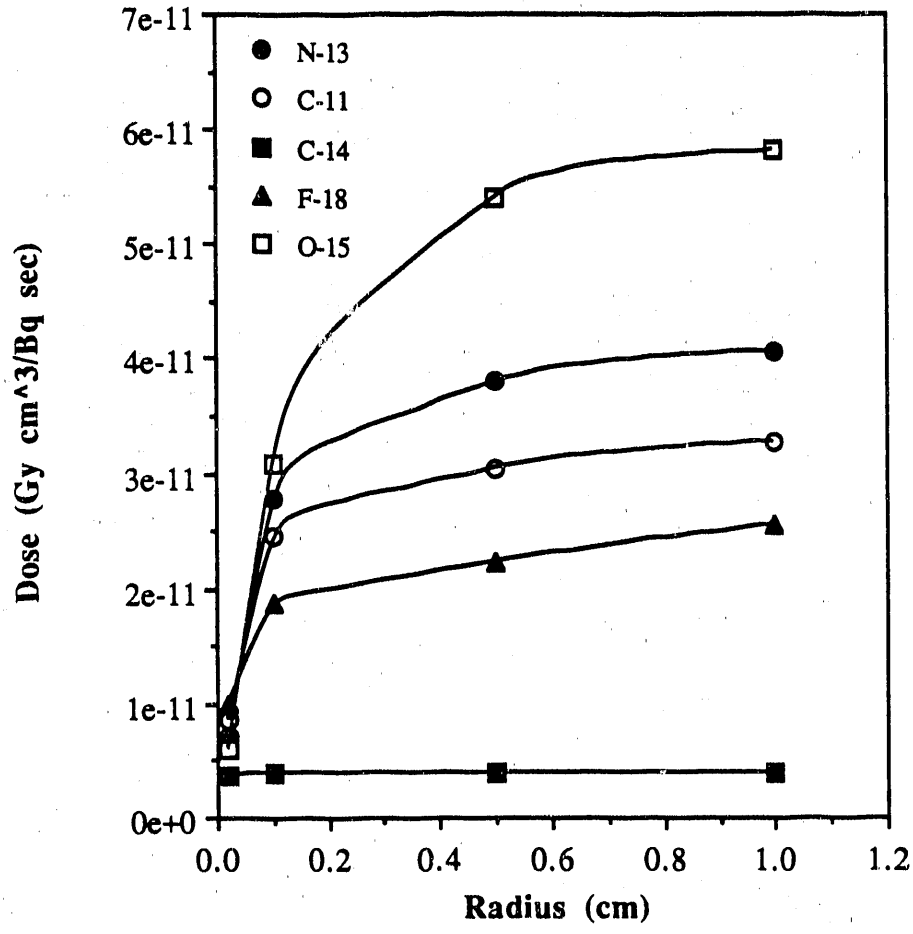

FIGURE 6. Absorbed dose per transformation per cm^3 to the surface of the blood vessel wall as a function of blood vessel radius for different radionuclides.

TABLE 1

Representative Values of Blood Vessels for the Circulatory System *(4)*

Adult Arterial System			
	Sex	Thickness of wall (mm)	Diameter of lumen (cm)
Aorta:			
Ascending	male	1.63	2.50
	female	1.48	2.50
Descending	male	1.20	2.50
	female	1.11	2.50
Abdominals	male	1.14	0.90-1.80
	female	1.08	0.90-1.80
Arteries:			
Common iliac	male	0.93	0.90-1.80
	female	0.89	0.90-1.80
Common carotid	male	0.91	0.67
	female	0.81	0.67
Small arteries	both	0.80 and lower	0.40
Arterioles:	both	20μm	16-30 μm
Capillaries:	both	1μm	8-10 μm

Adult Venous System			
	Sex	Thickness of wall (mm)	Diameter of lumen (cm)
Venae cavae:			
Superior	male	1.50	3.00
	female	1.50	3.00
Inferior	male	1.50	3.00
	female	1.50	3.00
Veins	male	0.50	0.50
	female	0.50	0.50
Venules	both	2 μm	20 μm

Adult Pulmonary System			
	Sex	Thickness of wall (mm)	Diameter of lumen (cm)
Arteries	male	1.27	2.40
	female	0.96	2.40

TABLE 2

Average Absorbed Dose to Blood for Different Sizes of Blood Vessels

Radionuclide	Average Absorbed Dose to Blood (Gy cm^3/Bq sec) Radius of Blood Vessel (cm)			
	0.02	0.10	0.50	1.00
N-13	1.05E-11	4.26E-11	7.23E-11	7.82E-11
C-11	1.36E-11	3.98E-11	5.88E-11	6.28E-11
C-14	7.29E-12	7.82E-12	7.94E-12	7.96E-12
F-18	1.75E-11	3.28E-11	4.29E-11	4.73E-11
O-15	7.84E-12	4.41E-11	9.89E-11	1.11E-10
Na-24	9.40E-12	4.29E-11	8.70E-11	1.04E-10
P-32	8.16E-12	4.29E-11	9.26E-11	1.02E-10
Fe-55	7.49E-13	8.56E-13	8.95E-13	9.00E-13
Kr-81m	6.71E-12	8.62E-12	9.64E-12	1.01E-11
Sr-90	1.62E-11	2.60E-11	3.03E-11	3.08E-11
Y-90	8.45E-12	4.22E-11	1.16E-10	1.35E-10
Tc-99m	2.07E-12	2.39E-12	2.74E-12	3.08E-12
Mo-99	1.21E-11	3.68E-11	5.81E-11	6.17E-11
I-123	3.69E-12	4.29E-12	5.04E-12	5.86E-12
I-124	2.49E-12	1.17E-11	2.96E-11	3.69E-11
I-125	2.67E-12	2.83E-12	3.39E-12	4.12E-12
I-126	6.10E-13	1.20E-12	2.46E-12	3.65E-12
I-130	1.42E-11	3.30E-11	5.07E-11	5.96E-11
I-131	1.61E-11	2.64E-11	3.22E-11	3.40E-11
In-111	4.10E-12	5.31E-12	6.98E-12	8.61E-12
In-114	8.07E-12	4.18E-11	9.88E-11	1.11E-10
Xe-127	4.00E-12	4.91E-12	6.11E-12	7.33E-12
Xe-131	1.83E-11	2.17E-11	2.28E-11	2.32E-11
Xe-133	1.77E-11	2.08E-11	2.19E-11	2.22E-11
Xe-133m	2.02E-11	2.76E-11	3.05E-11	3.11E-11
Tl-200	2.37E-12	4.72E-12	9.48E-12	1.37E-11
Tl-201	2.12E-12	4.80E-12	8.44E-12	1.14E-11
Tl-202	1.57E-12	2.83E-12	4.64E-12	6.14E-12

TABLE 3

Absorbed Dose to the Surface of the Blood Vessel Wall for Different Sizes of Blood Vessels.

Radionuclide	Absorbed Dose to the Surface of the Blood Vessel (Gy cm^3/Bq sec)			
	Radius of Blood Vessel (cm)			
	0.02	0.10	0.50	1.00
N-13	7.19E-12	2.77E-11	3.79E-11	4.06E-11
C-11	8.59E-12	2.46E-11	3.04E-11	3.27E-11
C-14	3.80E-12	3.93E-12	4.02E-12	3.96E-12
F-18	9.95E-12	1.88E-11	2.23E-11	2.55E-11
O-15	5.93E-12	3.09E-11	5.40E-11	5.81E-11
Na-24	6.64E-12	2.87E-11	4.88E-11	5.88E-11
P-32	6.03E-12	2.98E-11	5.01E-11	5.28E-11
Fe-55	3.95E-13	4.34E-13	4.51E-13	4.54E-13
Kr-81m	3.64E-12	4.52E-12	4.99E-12	5.30E-12
Sr-90	8.98E-12	1.43E-11	1.52E-11	1.58E-11
Y-90	6.13E-12	2.98E-11	6.79E-11	7.10E-11
Tc-99m	1.10E-12	1.23E-12	1.48E-12	1.73E-12
Mo-99	7.62E-12	2.32E-11	3.02E-11	3.17E-11
I-123	1.96E-12	2.22E-12	2.79E-12	3.26E-12
I-124	1.75E-12	8.06E-12	1.74E-11	2.06E-11
I-125	1.36E-12	1.45E-12	1.94E-12	2.28E-12
I-126	3.41E-13	7.30E-13	1.50E-12	2.26E-12
I-130	8.43E-12	1.99E-11	2.73E-11	3.32E-11
I-131	8.95E-12	1.47E-11	1.65E-11	1.78E-11
In-111	2.20E-12	2.84E-12	3.95E-12	4.96E-12
In-114	5.91E-12	2.94E-11	5.47E-11	5.77E-11
Xe-127	2.13E-12	2.58E-12	3.39E-12	4.15E-12
Xe-131	9.83E-12	1.11E-11	1.17E-11	1.17E-11
Xe-133	9.38E-12	1.07E-11	1.11E-11	1.12E-11
Xe-133m	1.10E-11	1.47E-11	1.54E-11	1.59E-11
Tl-200	1.33E-12	2.85E-12	5.73E-12	8.75E-12
Tl-201	1.27E-12	2.89E-12	4.86E-12	6.76E-12
Tl-202	8.75E-13	1.64E-12	2.65E-12	3.65E-12

TABLE 4

Average Absorbed Dose to Blood for Different Blood Vessels in the Circulatory System

Radionuclide: Y-90 1.23×10^{13} dis.	Blood amount (ml)	Radius (cm)	Dose (Gy cm^3/Bq sec)	Dose (Gy)
Arterial System				
Aorta	140	1.0000	1.34E-10	3.17E-01
Arteries	420	0.5000	1.22E-10	2.88E-01
Arterioles	70	0.0025	1.51E-11	3.56E-02
Capillaries	280	0.0010	6.10E-12	1.44E-02
Venous System				
Venae Cavae	300	1.5000	1.43E-10	3.37E-01
Veins	2600	0.2500	1.17E-10	2.77E-01
Venules	300	0.0020	1.21E-11	2.86E-02
Pulmonary System				
Arteries	200	1.2000	1.38E-10	3.26E-01
Veins	230	0.2500	1.17E-10	2.77E-01
Capillaries	100	0.0010	6.10E-12	1.44E-02

TABLE 5

Absorbed Dose to the Surface of the Blood Vessel Wall for Different Blood Vessels in the Circulatory System

Radionuclide: Y-90 1.23 x10^{13} dis.	Blood amount (ml)	Radius (cm)	Dose (Gy cm^3/Bq sec)	Dose (Gy)
Arterial System				
Aorta	140	1.0000	7.10E-11	1.68E-01
Arteries	420	0.5000	6.31E-11	1.49E-01
Arterioles	70	0.0025	7.68E-12	1.82E-02
Capillaries	280	0.0010	3.11E-12	7.36E-03
Venous System				
Venae Cavae	300	1.5000	7.71E-11	1.82E-01
Veins	2600	0.2500	6.01E-11	1.42E-01
Venuoles	300	0.0020	6.17E-12	1.46E-02
Pulmonary System				
Arteries	200	1.2000	7.36E-11	1.74E-01
Veins	230	0.2500	6.01E-11	1.42E-01
Capillaries	100	0.0010	3.11E-12	7.36E-03

A PRELIMINARY MODEL OF THE CIRCLULATING BLOOD FOR USE IN ABSORBED FRACTION CALCULATIONS

INTRODUCTION

In recent years, there has been an increase in the number of radiopharmaceuticals used in nuclear medicine. Radionuclides were used to label leukocytes, platelets, and erythrocytes for imaging procedures. These radionuclides are confined primarily to the blood, have short half-lives, and irradiate the body as they move through the circulatory system. Marcus et al. (*1*) reported that tens of thousands of patients have been diagnosed using newly approved indium-111 labeled leukocyte imaging procedures. The rapid growth in the number of procedures and the number of radionuclides available for such studies emphasizes the need for estimates of the absorbed doses to tissues and organs of the body as well as the doses to the "blood" itself. A Task Group has been established by the MIRD committee of the Society of Nuclear Medicine to attack this problem (*2*). No model is available at present which describ concentrations of radionuclides in different body organs, such as the "face", which are fed primarily from the blood pool.

This is not a new problem. Since 1970, estimates of the radiation dose to various body organs due to radionuclides in the circulating blood were reported (*3*). In 1974, McEwan estimated the dose to blood monoenergetic electron, beta radiation, and low energy photon sources uniformly distributed in blood (*4*). In this work, blood vessels were approximated by infinite right circular cylinders ranging in radius from 0.0004 cm (capillaries) to 1.75 cm (heart), and absorbed fractions of energy for twenty beta-emitting radionuclides were calculated by numerical integration. van Reenen et al. (*5, 6*) measured the distribution of indium-111-labeled blood platelets in normal patients by whole body counting and scintillation-camera computer-assisted imaging. Using the data, radiation absorbed dose in different body organs when indium-111 was present in blood platelets was estimated. Robertson et al. (*7*) reported dose estimates for indium-111 and indium-113m labeled blood platelets. All of these calculations were based on very simple models which considered the blood either as a "source" region or a "target" region. Prior to the research described here there has been no model available which could be used to calculate the absorbed doses to tissues and organs of the body as well as the "blood" itself.

The goal of this research has been to design a preliminary but reasonably accurate blood model that can be used to obtain absorbed dose information for body organs and "blood" itself for radionuclides in the circulatory system. Unlike other approaches, regions in the blood model have sizes and shapes similar to the human circulatory system. Only major organs that contain large amounts of blood were included in the design. This model has been incorporated into the MIRD phantom (*8*), which is widely accepted for radiation dose calculations.

DEVELOPMENT OF A BLOOD MODEL

An initial effort has been made toward the development of a very simple, static model of the circulating blood. It is assumed that, in this static model, there is always a constant amount of blood in different regions throughout the body. Also, it is assumed that rapid distribution kinetics over the first five minutes can be neglected. In actual practice, the radionuclides, after being tagged to the blood and injected to the patients, take time to circulate throughout the whole body. No attempt was made to model this and it was assumed that there was a constant concentration of radionuclides in blood throughout the body. For simplicity, only major organs which contain a large fraction of blood will be included in this preliminary model. As more necessary data are accumulated, more sophistication may be added to the model.

Initial data, on which the model was based, were selected from the Report of Reference Man (*9*) and an evaluation of available data on blood volume and distribution in the circulatory system. Preliminary parameters for the blood model was developed by the MIRD Task Group (*10*). Data were available, from several sources (*3, 4, 11, 12, 13, 14*), for a hypothetical male, weighing about 63 kg and having a total blood volume in the range 5000 to 5100 ml. A total blood volume of 5200 ml was selected as being appropriate for a 70 kg adult. This value was in agreement with the data selected for the Reference Man.

The Report on Reference Man (*9*) also presented data on the total blood volume in most organs of the body. These data were used to select those organs which should be included

explicitly in the model. In addition, these data provided important guidance on those organs or regions of the body which could be combined into a single region in the model. Organs included in the blood model were the brain, heart, kidneys, liver, lungs, and the spleen. Special regions, created in the simplified model, included the extremities, face, intestinal region, aorta and vena cava, and the "remainder". Table 1 gives the total blood volume assumed to be in each organ or region of the model.

Those organs named specifically in Table 1 were included in the MIRD adult human phantom (*8*) and described mathematically by equations in a computer code called ALGAM (*15*). The dimensions and coordinate system of the phantom are shown in Figure 1. All other regions were designed especially for use in the model of the circulating blood. A short description of each of these regions is given below. All equations will follow the coordinate system as in Figure 1. Unless otherwise stated, numerical values in all following equations are in cm.

Extremities: The extremities are right circular cylinders, 1.0 cm in diameter, located just to the inside of the existing arm and leg bones. For example, cylinders representing the arm regions lie between the existing arm bone and the ribs and run parallel to the bone region. Each arm region has a length of 69.0 cm while each leg region was 79.8 cm in length. The arm regions were moved forward 2.5 cm along the Y-axis to eliminate overlapping with the ribs.

Face Region: A region representing the "face" was created because of high blood flow through the region and data indicating that significant radioactivity was present in the region during some diagnostic procedures. The face region was assumed to be a region on the lower two-thirds of the head (i.e., $70.0 < z < 85.5$). This region was formed by a plane which cut vertically through the elliptical cylinder of the head at $y = -7.0$. Care was taken in the definition of the face region to assure that there was no overlap between this region and the skull, skin and thyroid.

Intestinal Region: The intestinal region was assumed to be located in the lower trunk constrained between $z = 0.0$ and $z = 27.0$. For simplicity, the region was assumed to be represented by an elliptical cylinder with essentially the same dimensions as the trunk. However, the skin was not

included in the region. The semi-major axis of the elliptical cylinder was assumed to be 19.8 cm and the semi-minor axis was 9.8 cm. The center of this region, a circular cylinder with the height of 11.5 cm and a radius of 2.5 cm, was removed to bring the volume in line with the design parameters. Care was taken that the intestinal region did not overlap with the aorta and vena cava region. Several organs included in the intestinal region were the bladder, ovaries, uterus, pelvis, small intestine, upper (ULI) and lower (LLI) large intestine.

Aorta and Vena Cava: This region was described by a right circular cylinder with a radius of 2.5 cm located between z = 15.5 and 44.8. Care was taken to eliminate overlapping with the liver and heart source organs. The uterus, which belongs to the intestinal region, also is excluded.

Remainder Region: The "remainder" was assumed to be the total body, minus all other organs and regions mentioned above. This region was included to account for the essentially uniform distribution of a large fraction (16.3 %) of the total blood volume in the body. Organs included in the "remainder" region are the stomach, adrenals, genitalia, skeleton, testes, thyroid, pancreas, skin and body tissue. Assuming blood is uniformly distributed throughout the remainder region and a total blood volume of 5200 ml, the fraction of the blood volume for each organ included in the remainder was calculated. The calculation shows that the fraction of total body blood per gram is 3.74×10^{-6} per gram of tissue and 2.48×10^{-6} per gram of bone. These values, for fraction of blood per gram of tissue or bone, also were used to calculate blood volumes for organs in the intestinal region.

Other organs in the model were updated with new data which were available. For instance, Coffey et al. (*16*) proposed a new model for the heart, which includes heart walls and heart chambers instead of a solid heart, and a modified lung. Equations describing these improved organs were included in this model to provide a more accurate model for the circulatory system.

The above established blood model was incorporated into the MIRD phantom (*8*). The MIRD phantom consists of three different media: lung, tissue and bone which have different compositions and properties. Some of the organs in the blood model, such as aorta and vena cava,

and the extremities, contain blood only, and were not the same as either of the three media. However, the density of blood is 1.058 g/cm^3 (*9*) which is about the same as that of the tissue, 0.987 g/cm^3. Therefore, for simplicity these regions were assumed to have similar properties as the tissue medium.

APPLICATION OF MIRD TECHNIQUE TO THE BLOOD MODEL

The widely accepted technique recommended by the Medical Internal Radiation Dose (MIRD) Committee of the Society of Nuclear Medicine was used for radiation dose calculation for radionuclides in the circulating blood. The basic equation of this technique (*17*) is:

$$D(r_k \leftarrow r_h) = \frac{\tilde{A}_h \sum_i \Delta_i \phi_i(r_k \leftarrow r_h)}{m_k} = \tilde{A}_h \sum_i \Delta_i \Phi_i(r_k \leftarrow r_h) \qquad (1)$$

where $D(r_k \leftarrow r_h)$ is the mean absorbed dose (in rad) in a target region r_k from radionuclides distributed uniformly in a source region r_h, $\tilde{A}_h$(μCi-hr) is the cumulated activity in source region r_h, Δ_i is the mean energy emitted per unit cumulated activity (in g-rad/μCi-hr) for radiation of a particular type and energy, $\phi_i(r_k \leftarrow r_h)$ is the absorbed fraction (dimensionless) for target region r_k for i^{th} radiation emitted in the source region r_h, $\Phi_i(r_k \leftarrow r_h)$ is the specific absorbed fraction (in g^{-1}) and m_k is the mass of target region.

The MIRD technique requires some modifications when applied to the blood model for radiation dose calculations. In the past, radionuclides were assumed to be distributed in a single source region and calculations were made for a large number of target regions (*8*). However, in this blood model, radionuclides were assumed to be uniformly distributed in the blood which circulates throughout the whole body. There are eleven specific source regions as well as a region called the "remainder". Only a fraction of circulating blood is in each body region, and for non-penetrating radiations, only blood in a body region would deposit energy in that particular region. Therefore, for non-penetrating radiations, the absorbed fraction for a body region when

blood is the source region is equal to fraction of blood in that particular region. In equation form:

$$\phi_i(r_k \leftarrow \text{blood}) = 1 \text{ x blood fraction in } r_k \tag{2}$$

and

$$\Phi_i(r_k \leftarrow \text{blood}) = \frac{\text{blood fraction in } r_k}{m_k} . \tag{3}$$

In this model, the circulating blood not only serves as a source region, but also as one of the target regions. To calculate the energy deposited in the blood, it is assumed that, when there is energy deposition,

$$\frac{\text{energy deposited in the blood of a region}}{\text{energy deposited in the region}} = \frac{\text{mass of blood in that region}}{\text{mass of that region}} . \tag{4}$$

For penetrating radiation, the above equations apply to every interaction in every region. For non-penetrating radiation, to apply the above assumption on the ratio of energy deposition, the absorbed fraction can be expressed as:

$$\phi_i(\text{blood in } r_k \leftarrow \text{blood}) = \phi_i(r_k \leftarrow \text{blood}) \text{ x } \frac{\text{mass of blood in } r_k}{m_k} \tag{5}$$

$$\phi_i(\text{blood} \leftarrow \text{blood}) = \Sigma_k \, \phi_i(r_k \leftarrow \text{blood}) \text{ x } \frac{\text{mass of blood in } r_k}{m_k} \tag{6}$$

whereas the specific absorbed fraction can be expressed as:

$$\Phi_i(\text{blood} \leftarrow \text{blood}) = \frac{\phi_i(\text{blood} \leftarrow \text{blood})}{\text{total blood mass}} = \Sigma_k \frac{(\text{blood fraction in } r_k)^2}{m_k} . \tag{7}$$

For penetrating radiations, the Monte-Carlo code ALGAM (*15*) was modified for use in

calculations of absorbed and specific absorbed fractions for different organs for monoenergetic photon sources. A source routine, based on the blood model, was incorporated into ALGAM to specify the radionuclide distribution. Given the source distribution and initial photon energy, a large number (100,000) of photon histories were traced in every calculation. Each photon may undergo photoelectric effect, Compton scattering or pair-production interactions in different body regions. For each interaction occurring as part of a photon history, the energy deposited in a specific body region of the MIRD phantom is calculated. The original code had no provision for calculating energy deposited in the blood nor for the specifically designed regions in the blood model. So, the existing routines in the code were expanded, based on the assumptions of equation (4), and were used to calculate, for each interaction, the amount of energy deposited in blood. When all source photon histories were compiled, the information on accumulated energy deposited in each region was used to calculate absorbed and specific absorbed fractions. Calculations were performed of absorbed and specific absorbed fractions for twelve monoenergetic photon sources ranging from 0.01 to 4.0 MeV. This interval covers the energies for photons emitted by most radionuclides of interest.

RESULTS AND DISCUSSION

Using the model described above, computer calculations of the absorbed fractions of energy were performed for twelve monoenergetic photon energies ranging from 0.01 to 4.0 MeV. In each calculation 100,000 photon histories were traced. Table 2 presents absorbed fractions for the twelve monoenergetic photon sources uniformly distributed in the circulating blood. Only data for organs of clinical importance are listed. Data for other minor organs were obtained but were not included here. The coefficients of variation of the absorbed fractions for different organs also are listed. It has been reported that a coefficient of variation greater then 20 % indicates considerable uncertainty in the estimate of absorbed fractions by the Monte Carlo technique (*8*).

It was assumed that blood has similar composition and properties as the tissue medium of

the MIRD phantom for simplicity in calculation. However, if the elemental composition of blood can be established and a cross-section set can be assembled, blood can be considered as a new medium in future work to provide a more accurate model. Moreover, the ratio of energy deposited in blood in an organ to energy deposited in an organ was assumed to be equal to the ratio of mass of blood in an organ to mass of the organ. More data on physical properties of the blood will enable one to verify or modify the assumption to improve the model to obtain more accurate results.

It must be emphasized that this blood model is a simple and preliminary model. Only major organs and a remainder region are included. It was assumed that there is a uniform distribution of blood in the remainder region. However, data of blood volume for minor organs included in the remainder region are available (*9*). Therefore, more sophistication can be added to improve the model if desired. Besides, parameters of the blood model and of organs in the blood model can be updated as more biological data become available.

Finally, the intial effort had been directed to set up a preliminary static model. It is assumed in this blood model that there is a uniform distribution of radionuclides in the blood throughout the body. It is desirable to include the consideration of metabolism of blood and to set up a time-dependent blood model to provide more accurate results.

ACKNOWLEDGEMENTS

The authors would like to acknowledge the assistance of T. F. Budinger and E. E. Watson who suggested many of the initial parameters to be used in this model. In addition, the assistance of A. Aissi and B. M. Jimba in the preliminary phases of this work is gratefully acknowledged.

REFERENCES

1. Marcus CS, Stabin MG, Watson EE and Kuperus JH. "Contribution of Contamination Indium-114m /Indium-114 to Indium-111 Oxine Blood Dosimetry," *J. Nucl. Med.* 1985; 26:1091.

2. Minutes of the MIRD Committee Meeting, July 26-27, 1984, Washington, DC.

3. Cloutier RJ and Watson EE. "Radiation Dose from Radioisotopes in the Blood", *Medical Radionuclides: Radiation Dose and Effects*, AEC Symposium Series 20, Oak Ridge, TN, 1970; 325-346.

4. McEwan AC. "Dosimetry of Radionuclides in Blood," *Brit J. Radiology* 1974; 47:652.

5. van Reenen OR, Lotter MG, Minnaar PC, Heyns A, Du P, Badenhorst P N and Pieters H. "Radiation Dose from Human Platelets Labeled with Indium-111," *Brit J. Radiology* 1980; 54:790.

6. van Reenen OR. Correspondence on "Radiation Dose from Human Platelets Labeled with Indium-111," *Brit J. Radiology* 1981; 54:1011.

7. Robertson JS, Ezekowitz MD, Dewanjee MK and Lotter MG. "Radiation Absorbed Dose Estimates for Radioindium Labeled Blood Platelets," Draft MIRD Dose Estimate Report, 1984.

8. Snyder WS, Ford MR and Warner GG. "Estimates of Specific Absorbed Fractions for Photon Sources Uniformly Distributed in Various Organs of a Heterogeneous Phantom," *MIRD Pamphlet No.*5, Revised. New York: Society of Nuclear Medicine, 1978.

9. International Commission on Radiological Protection. "Report on the Task Group on Reference Man," *ICRP Publication* 23. Oxford: Pergamon Press, 1975.

10. Minutes of the MIRD Committee Meeting, March 6-7, 1985, Washington, DC.

11. Albert SN. *Blood Model.* Springfield, IL: Charles C. Thomas, 1963.

12. Bard P. *Medical Physiology*, 11th edition. St. Louis: Mosby Co, 1961.

13. Cowles AL, Borgstedt HH and Gillies AJ. "Tissue Weights and Rates of Blood Flow in Man for the Prediction of Anesthetic Uptake and Distribution," *Anesthesiology* 1971; 35:523.

14. Smith JJ and Kampine JP. *Circulatory Physiology - The Essentials*, 2nd edition. Baltimore, MD: Williams and Wilkins, 1968.

15. Warner GG and Craig AN, Jr. *ALGAM: A Computer Program for Estimating Internal Dose in a Man Phantom*, Oak Ridge, TN: Oak Ridge National Laboratory, 1968; ORNL-TM-2250.

16. Coffey JL, Cristy M and Warner GG. "Specific Absorbed Fractions for Photon Sources Uniformly Distributed in the Heart Chambers and Heart Wall of a Heterogeneous Phantom," *MIRD Pamphlet No.*13, *J. Nucl. Med.* 1981; 22:65.

17. Snyder WS, Ford MR and Warner GG. "S. Absorbed Dose per Unit Cumulated Activity for Selected Radionuclides and Organs," *MIRD Pamphlet No.*11. New York: Society of Nuclear Medicine, 1975.

TABLE 1. BLOOD MODEL PARAMETERS

ORGAN/REGION	BLOOD VOL. (ml)	% OF TOTAL
BRAIN	260	5.0
HEART	500	9.6
KIDNEYS	70	1.3
LIVER	280	5.4
LUNGS	520	10.0
SPLEEN	90	1.7
ARMS	520	10.0
LEGS	780	15.0
FACE	220	4.2
INTESTINAL REGION	700	13.5
AORTA & VENA CAVA	410	7.9
REMAINDER	850	16.3
TOTAL IN BODY	5200	100.0

TABLE 2. ABSORBED FRACTIONS OF ENERGY FOR SELECTED ORGANS, SOURCE REGION IS BLOOD

	ENERGY (MEV)		
TARGET REGION	0.010	0.015	0.020
BRAIN	5.0E-02(1)*	4.6E-02(1)	4.2E-02(1)
UTERUS	4.0E-04(16)	6.3E-04(12)	8.2E-04(10)
KIDNEYS	1.2E-02(3)	1.1E-02(3)	7.9E-03(3)
LIVER	5.4E-02(1)	5.2E-02(1)	5.1E-02(1)
LUNGS	1.0E-01(1)	8.3E-02(1)	6.3E-02(1)
RED MARROW	6.7E-03(2)	9.3E-03(2)	1.4E-02(1)
OVARIES	5.0E-05(44)	5.1E-05(41)	1.1E-04(24)
SPLEEN	1.6E-02(3)	1.4E-02(3)	1.0E-02(3)
TESTES	1.7E-04(24)	1.6E-04(24)	9.7E-05(28)
THYROID	4.3E-04(15)	6.4E-04(12)	9.0E-04(9)
HEART WALL	1.7E-02(2)	1.8E-02(2)	1.8E-02(2)
FACE	3.7E-02(2)	3.0E-02(2)	2.2E-02(2)
BLOOD	4.1E-01(**)	3.1E-01(**)	2.2E-01(**)
TOTAL BODY	1.0E+00(**)	9.8E-01(**)	9.4E-01(**)

	ENERGY (MEV)		
TARGET REGION	0.030	0.050	0.100
BRAIN	2.7E-02(2)	1.4E-02(2)	9.3E-03(2)
UTERUS	9.7E-04(7)	7.2E-04(6)	5.3E-04(6)
KIDNEYS	5.2E-03(3)	3.2E-03(3)	2.3E-03(3)
LIVER	4.4E-02(1)	2.9E-02(1)	2.0E-02(1)
LUNGS	3.7E-02(1)	1.9E-02(1)	1.2E-02(1)
RED MARROW	2.3E-02(1)	2.5E-02(1)	1.4E-02(1)
OVARIES	9.7E-04(19)	7.2E-05(16)	5.1E-04(17)
SPLEEN	6.2E-03(3)	2.9E-03(4)	2.0E-03(4)
TESTES	1.5E-04(18)	1.1E-04(16)	6.9E-05(16)
THYROID	6.7E-04(8)	3.0E-04(9)	2.1E-04(10)
HEART WALL	1.3E-02(2)	7.4E-03(2)	4.8E-03(2)
FACE	1.1E-02(2)	4.2E-03(3)	2.6E-03(3)
BLOOD	1.3E-01(**)	6.8E-02(1)	4.5E-02(1)
TOTAL BODY	8.2E-01(**)	5.9E-01(**)	3.9E-01(**)

* -- COEFFICIENTS OF VARIATION IN PERCENT.

** - COEFFICIENTS OF VARIATION LESS THAN 0.5 %.

TABLE 2. (CONTINUED)

TARGET REGION	ENERGY (MEV) 0.200	0.500	1.000
BRAIN	9.4E-03(2)*	9.4E-03(2)	9.0E-03(3)
UTERUS	4.2E-04(8)	3.9E-04(10)	3.0E-04(13)
KIDNEYS	2.3E-03(4)	2.4E-03(4)	2.2E-03(5)
LIVER	1.9E-02(1)	1.8E-02(2)	1.8E-02(2)
LUNGS	1.1E-02(2)	1.1E-02(2)	9.7E-03(2)
RED MARROW	8.8E-03(1)	7.5E-03(1)	6.9E-03(2)
OVARIES	7.4E-05(18)	3.1E-05(33)	4.0E-05(37)
SPLEEN	1.9E-03(4)	1.9E-03(5)	1.9E-03(6)
TESTES	8.9E-05(18)	5.6E-05(27)	8.9E-05(25)
THYROID	1.4E-04(13)	2.3E-04(14)	1.8E-04(18)
HEART WALL	4.5E-03(3)	4.5E-03(3)	4.2E-03(4)
FACE	2.8E-03(3)	3.0E-03(4)	3.0E-03(4)
BLOOD	4.3E-02(1)	4.4E-02(1)	4.1E-02(1)
TOTAL BODY	3.5E-01(**)	3.5E-01(**)	3.3E-01(**)

TARGET REGION	ENERGY (MEV) 1.500	2.000	4.000
BRAIN	8.4E-03(3)	7.4E-03(3)	6.4E-03(3)
UTERUS	4.0E-04(12)	3.2E-04(14)	2.9E-04(15)
KIDNEYS	1.8E-03(6)	1.9E-03(6)	1.6E-03(7)
LIVER	1.6E-02(2)	1.4E-02(2)	1.2E-02(2)
LUNGS	9.1E-03(3)	8.2E-03(3)	6.7E-03(3)
RED MARROW	6.4E-03(2)	6.0E-03(2)	5.2E-03(2)
OVARIES	3.9E-05(38)	1.8E-05(48)	3.9E-05(40)
SPLEEN	1.7E-03(6)	1.5E-03(7)	1.1E-03(8)
TESTES	1.1E-04(22)	9.2E-05(27)	6.8E-05(31)
THYROID	1.7E-04(19)	1.6E-04(21)	1.1E-04(25)
HEART WALL	4.3E-03(4)	3.7E-03(4)	3.0E-03(5)
FACE	2.6E-03(5)	2.4E-03(5)	1.9E-03(6)
BLOOD	3.8E-02(1)	3.5E-02(1)	2.9E-02(1)
TOTAL BODY	3.1E-01(**)	2.9E-01(**)	2.4E-01(**)

* -- COEFFICIENTS OF VARIATION IN PERCENT.

** - COEFFICIENTS OF VARIATION LESS THAN 0.5 %.

A REVISED MODEL OF THE GALL BLADDER FOR ABSORBED FRACTION CALCULATIONS

INTRODUCTION

Short lived radiopharmaceuticals, that are now injected in millicurie quantities in nuclear medicine for rapid-sequence imaging of the brain, heart, and abdominal organs, are selected frequently on the basis of their rapid clearance from the bloodstream and as a rule this clearance is achieved at the expense of the urinary tract (Mc70). Therefore, there is a need to develop a more accurate dosimetric model of the gall bladder which consists of the wall and content regions, and to modify the parameters and mathematical equations to describe these regions in the existing computer code ALGAM. Such a model will be useful in producing more accurate dose estimates for those radionuclides present in the contents of the gall bladder.

The improved model of the gall bladder was incorporated into an existing computer code developed at Oak Ridge National Laboratory by Warner et al. (Wa68) which included additions by Hui (Hu85). This code featured the mathematical phantom used for previous MIRD calculations, with the addition of a model of the circulating blood as a target region. Using the Monte Carlo technique, the modified code was used to obtain absorbed fractions of energy for monoenergetic photons.

In addition, a gall bladder model was incorporated into the phantom and the appropriate dose calculations were performed. This model designed by Cristy et al. (Cr87), included both the "walls" and the "contents" of the organ. The previous version of the computer code did not include a specification for the gall bladder. The model will be discussed briefly and results of dose calculations will be presented.

THE MIRD TECHNIQUE

The widely accepted technique recommended by the Medical Internal Radiation Dose (MIRD) Committee of the Society of Nuclear Medicine was used for radiation dose calculations for radionuclides in the gall bladder. The basic equation of this technique is:

$$D(r_k \leftarrow r_h) = \frac{\tilde{A}_h \, \Sigma_i \Delta_i \phi_i(r_k \leftarrow r_h)}{m_k} = \tilde{A}_h \, \Sigma_i \Delta_i \Phi_i(r_k \leftarrow r_h) \qquad (1)$$

where $D(r_k \leftarrow r_h)$ is the mean absorbed dose (in rad) in a target region r_k from radionuclides distributed uniformly in a source region r_h, $\tilde{A}_h$(μCi-hr) is the cumulated activity in source region r_h, Δ_i is the mean energy emitted per unit cumulated activity (in g-rad/μCi-hr) for radiation of a particular type and energy, $\phi_i(r_k \leftarrow r_h)$ is the absorbed fraction of energy (dimensionless) for target region r_k for i^{th} radiation emitted in the source region r_h, m_k is the mass of target region, and $\Phi_i(r_k \leftarrow r_h)$ is called the specific absorbed fraction (in g^{-1}). The absorbed fraction has a numerical value between zero and one; while the specific absorbed fraction is bounded between zero and the reciprocal of the source region mass, m_k.

Radiations are classified into two types; penetrating and non-penetrating. Photons having energies greater than or equal to 10 keV are penetrating, whereas electrons, beta particles and photons with energies less than 10 keV are non-penetrating.

For non-penetrating radiation, it is assumed that, because of the short range of the radiation, all the energy emitted is deposited in the source region (Sn75). Then, if the source and target are the same

$$\Phi_i (r_k \leftarrow r_h) = \phi_i (r_k \leftarrow r_h) / m_k = 1/ m_k$$

and when the source and target are different,

$$\Phi_i (r_k \leftarrow r_h) = \phi_i (r_k \leftarrow r_h) / m_k = 0.$$

Exceptions to the above rules are organs with walls in which the contents are assumed to contain the source. In these estimations, the value of $\Phi_i (r_k \leftarrow r_h)$ is taken as $1 / 2 \; m_h$, where m_h is the mass of the source region (i.e., the contents).

Since for penetrating radiation, not all the emitted energy is deposited in any single organ or region of the body, the absorbed fraction of energy and the specific absorbed fraction are bounded by the following relations:

$$0 < \phi_i (r_k \leftarrow r_h) < 1.$$

The absorbed fraction for body regions for different photon source energies are computed by the Monte Carlo procedure.

MODEL FOR THE GALL BLADDER

General Description

The gall bladder is pear shaped and lies in a fossa in the inferior side of the right lobe of the liver (St59). It is about 10 cm in length, 3-5 cm in diameter and has a capacity of about 50 cubic centimeters.

The constricted portion or neck is bent and attached closely to the peritoneal covering of the organ. Its expanded portion of *fundus* is directed anteriorly and lies near the end of the 9th costal cartilage.

The *Cystic duct,* 3 to 4 cm. long, leads from the gallbladder to the hepatic duct, with which it unites to form the common bile duct. The common bile duct contains a spiral valve, a fold which serves to keep the duct open.

The gall bladder serves as a reservoir of bile and renders it more concentrated. Acute inflammation of the gall bladder obstructs the cystic duct thus preventing reflux of bile into it from the hepatic duct. Occasionally, in radioisotope tracer studies, an intrahepatic gall bladder is responsible for producing a defect in the radiocolloid image of the right hepatic lobe.

Model for the Gall Bladder and Contents

The mathematical model for the gall bladder was designed by Cristy et al. (Cr87). It is represented by the frustum of a cone capped with a hemisphere and is defined as a walled organ. The Reference Man data gives the mass of the gall bladder as 10 grams (ICRP75). The walls are specified as follows:

Hemispherical Part:

$$X_1^2 + Y_1^2 + Z_1^2 \leq 2.12 \quad \text{and}$$

$$X_1^2 + Y_1^2 + Z_1^2 > 4 \quad \text{and} \quad Z_1 < 0.$$

Conical Part:

$$X_1^2 + Y_1^2 \leq (2.12 - 0.2275\, Z_1)^2 \quad \text{and}$$

$$X_1^2 + Y_1^2 \geq (2.0 - 0.2275\, Z_1)^2 \quad \text{and} \quad 0 \leq Z_1 \leq 8.$$

The contents are specified as follows:

Hemispherical Part:

$$X_1^2 + Y_1^2 + Z_1^2 < 4 \quad \text{and} \quad Z_1 < 0.$$

Conical part:

$$X_1^2 + Y_1^2 < (2 - 0.2275\, Z_1)^2 \quad \text{and} \quad 0 \leq Z_1 \leq 8$$

The equations given above in (X_1, Y_1, Z_1)-coordinates are related to the standard Cartesion (X,Y,Z)-coordinate system by the following rotation-translation equations:

$$X_1 = 0.9615\,(X + 4.5) - 0.2748\,(Z - 30)$$

$$Y_1 = -0.574\,(X + 4.5) + 0.9779\,(Y + 3.2) - 0.2008\,(Z - 30)$$

$$Z_1 = 0.2687\,(X + 4.5) + 0.2090\,(Y + 3.2) + 0.9403\,(Z - 30).$$

Volume of the walls is taken to be 10.1 cm^3, volume of the contents is 53.6 cm^3 and total volume of the gall bladder is 63.7 cm^3.

CALCULATIONAL PROCEDURE

Initially, absorbed fractions of energy (AF) were determined by making use of an existing Monte Carlo code (Wa68). The code has been designed to take account of (1) the geometrical shape of the body and of the major internal organs, (2) the different densities and compositions of the various tissues of the body, and (3) the multiple scattering of photons in the body to provide a more

accurate estimate of the AF, or dose. It should be noted that, at the present time, the code does not take account of the secondary electrons and positrons that are produced. Generally, the electron ranges are small compared with the dimensions of most organs, and the absorbed dose will not change abruptly with distance except at a boundary between organs where composition and density change or at the boundary of the source organ. The Monte Carlo method takes account of the above factors in as much detail as possible, but excessive detail necessarily increases the time for each computer calculation. Since the technique is a sampling method, the results always involve some statistical uncertainty which varies inversely with the square root of the sample size. Calculations for estimating absorbed fractions are made typically with 100,000 photon histories and, in some cases, 500,000 histories can be worthwhile and practical. However, above such a level, further calculations are not cost efficient. For the purposes of this research, 100,000 photon histories were compiled for each source region. Source regions included the three regions of the kidney as well as the gall bladder. Calculations of the absorbed fractions of energy were performed for energies ranging from 0.01 MeV to 4.0 MeV. Organs of specific interest include stomach and liver which are closest to the gall bladder and would comparatively receive a higher dose.

RESULTS AND DISCUSSION

The model of the gall bladder was incorporated into an exsisting program and calculations were performed for photon energies ranging from 0.01 to 4.0 MeV. The liver is located next to the gall bladder and, as such, would receive the highest dose from a source in the gall bladder. Absorbed fractions for 12 photon energies are shown in Table 1 for the source in the gall bladder. In general, these data indicate that the absorbed fraction increases rapidly as the photon energy increases, then at higher energy it decreases once more. These results compare favorably with the results of Cristy et al. (Cr87). However, in the calculations reported here, the three-region kidney was used.

REFERENCES

At82 Atkins H., 1982, personal communication to J. W. Poston.

Be68 Berger M. J., 1968, "Energy Deposition in Water by Photons from Point Isotropic Sources," *MIRD Pamphlet No. 2* (New York: Society of Nuclear Medicine).

Bl78 Blau M., McAfee J. G., Rohrer R. H., Snyder W. S., and Smith E. M., 1978, "Estimated Absorbed Doses from Intravenous Administration of ^{197}Hg and ^{203}Hg labeled Chlormerodin," *MIRD Estimate Report No. 6* (New York: Society of Nuclear Medicine).

Br68 Brownell G. L., Ellett W. H., and Reddy A. R., 1968, "Absorbed Fractions for Photon Dosimetry," *MIRD Pamphlet No. 3* (New York: Society of Nuclear Medicine).

Cr87 Cristy M. and Eckerman K. F., 1987, *Specific Absorbed Fractions of Energy at Various Ages from Internal Photon Sources. I. Methods*, Oak Ridge National Laboratory, Oak Ridge, TN, 0RNL/TM-8381/V1.

Fr70 Frose F., Broedel M., and Schlossberg L., 1970, *Atlas of Human Anatomy*, (New York: Harper and Row, Publishers).

Hu85 Hui T-Y. E., 1985, " A Preliminary Model of the Circulating Blood for use in Radiation Dose Calculations, " Master of Science Thesis, Texas A&M University.

ICRP75 International Commission on Radiological Protection, 1975, "Report on the Task Group on Reference man," *ICRP PUBLICATION* 23 (Oxford: Pergamon Press).

Lo68 Loevinger R. and Berman M., 1968, "A Schema for Absorbed Dose Calculations for Biologically-Distributed Radionuclides," *MIRD Pamphlet No.1* (New York: Society of Nuclear Medicine).

Lo69 Loevinger R., 1969, "Distributed Radionuclide Sources," In *Radiation Dosimetry*, 2nd edition, Vol III, eds. F. H. Attix and E. Tochilin, pp. 51-90. (NewYork: Academic Press).

Mc70 McAfee J., 1970, "Problems in Evaluating the Radiation Dose for Radionuclides Excreted by the Kidneys," Medical Radionuclides: Radiation Dose and Effects, proceedings of a symposium held at the Oak Ridge Associated Universities available as CONF-691212 from Clearinghouse for Federal Scientific and Technical Information National Bureau of Standards, U.S. Department of Commerce, Springfield, Virginia 22151

Po87 Poston J. W., 1987, personal communication to J. S. Patel

So78 Solomon E. P. and Davis P. W., 1978, *Understanding Human Anatomy and Physiology* (New York: Mcgraw-Hill Book Company).

St59 Steen E. B. and Montagu A., 1959, *Anatomy and Physiology; Volume 2* (New York: Harper and Row Publishers).

Sn67 Snyder W. S. and Ford M. R., 1967, *A Dosimetric Study for the Administration of*

Neohydrin labeled with ^{203}*Hg and* ^{197}*Hg*, Oak Ridge National Laboratory, Oak Ridge, TN ORNL-DWG 67-1768R

Sn78 Snyder W. S., Ford M. R. and Warner G. G., 1978, " Estimates of Specific Absorbed Fractions for Photon Sources Uniformly Distributed in Various Organs of a Heterogeneous Phantom," *MIRD Pamphlet No. 5*, Revised (New York: Society of Nuclear Medicine).

Wa68 Warner G. G. and Craig A. N., Jr., 1968, *ALGAM: A Computer Program for Estimating Internal Dose in a Man Phantom*, Oak Ridge National Laboratory, Oak Ridge, TN ORNL-TM-2250.

TABLE 1. ABSORBED FRACTION OF PHOTON ENERGY

SOURCE = GALL BLADDER CONTENTS

	ENERGY (MEV)		
TARGET REGION	0.010	0.015	0.020
G. I. Stomach	0.00	0.00	4.8E-05(17)
G. I. ULI	0.00	2.3E-04(9)	3.8E-03(4)
Liver	4.8E-08(11) *	8.1E-03(2)	5.1E-02(1)
Kidneys (Pap)	0.00	0.00	1.3E-08(24)
Kidneys (Cor)	0.00	1.3E-06(37)	1.6E-04(12)
Kidneys (Med)	0.00	2.8E-09(42)	1.6E-04(13)
Kidneys	0.00	1.3E-06(26)	3.6E-04(9)
Gall Bladder	5.6E-05(9)	1.0E-02(3)	2.2E-02(2)
Total Body	9.8E-01(**)	9.8E-01(**)	9.8E-01 (**)

	ENERGY (MEV)		
TARGET REGION	0.030	0.050	0.100
G. I. Stomach	1.0E-03(6)	2.4E-03(3)	2.1E-03(3)
G. I. ULI	1.3E-02(2)	1.3E-02(1)	8.6E-03(1)
Liver	1.2E-01(1)	1.1E-01(1)	7.4E-02(1)
Kidneys (Pap)	5.1E-04(9)	8.8E-04(5)	6.9E-04(5)
Kidneys (Cor)	1.8E-03(5)	3.3E-03(3)	2.8E-03(2)
Kidneys (Med)	1.7E-03(5)	3.1E-03(3)	2.7E-03(3)
Kidneys	4.2E-03(4)	7.6E-03(1)	6.0E-03(2)
Gall Bladder	1.8E-02(1)	7.7E-03(1)	4.3E-03(2)
Total Body	0.98 (**)	7.0E-01(**)	5.3E-01(**)

* -- COEFFICIENTS OF VARIATION IN PERCENT

** - COEFFICIENTS OF VARIATION LESS THAN 0.5 % .

TABLE 1. (CONTINUED)

TARGET REGION	ENERGY (MEV) 0.200	0.500	1.000
G. I. Stomach	1.7E-03(3) *	1.7E-03(4)	1.7E-03(5)
G. I. ULI	7.5E-03(2)	6.7E-03(8)	6.3E-03(3)
Liver	6.5E-02(1)	6.2E-02(1)	5.6E-02(1)
Kidneys (Pap)	6.9E-04(6)	6.6E-04(7)	4.8E-04(9)
Kidneys (Cor)	2.4E-03(3)	2.0E-03(4)	2.0E-03(5)
Kidneys (Med)	2.3E-03(3)	2.1E-03(4)	1.9E-03(5)
Kidneys	5.4E-03(2)	4.8E-03(3)	4.5E-03(3)
Gall Bladder	4.1E-03(2)	4.3E-03(3)	3.8E-03(3)
Total Body	4.8E-01(**)	4.7E-01(**)	4.3E-01(**)

TARGET REGION	ENERGY (MEV) 1.500	2.000	4.000
G. I. Stomach	1.5E-03(6)	1.4E-03(6)	1.1E-03(8)
G. I. ULI	5.4E-03(3)	5.2E-03(3)	4.2E-03(4)
Liver	4.9E-02(1)	4.7E-02(1)	3.6E-02(1)
Kidneys (Pap)	4.8E-04(10)	5.4E-04(10)	4.2E-04(14)
Kidneys (Cor)	2.0E-03(5)	1.8E-03(5)	1.5E-03(6)
Kidneys (Med)	1.6E-03(5)	1.5E-03(6)	1.4E-03(7)
Kidneys	4.2E-03(4)	3.9E-03(4)	3.3E-03(4)
Gall Bladder	3.5E-03(4)	3.1E-03(4)	2.4E-03(5)
Total Body	4.0E-01(**)	3.8E-01(**)	3.1E-01(**)

* -- COEFFICIENTS OF VARIATION IN PERCENT

** - COEFFICIENTS OF VARIATION LESS THAN 0.5 % .

A REVISED MODEL OF THE KIDNEYS FOR THE CALCULATION OF ABSORBED FRACTION OF VARIOUS PHOTON ENERGIES

INTRODUCTION

The basic equation of the technique recommended by the Medical Internal Radiation Dose (MIRD) Committee of the Society of Nuclear Medicine for radiation dose calculation (*1*) is:

$$D(r_k \leftarrow r_h) = \frac{\tilde{A}_h \sum_i \Delta_i \phi_i(r_k \leftarrow r_h)}{m_k} = \tilde{A}_h \sum_i \Delta_i \Phi_i(r_k \leftarrow r_h) \qquad (1)$$

where $D(r_k \leftarrow r_h)$ is the mean absorbed dose (in rad) in a target region r_k from radionuclides distributed uniformly in a source region r_h, $\tilde{A}_h$(μCi-hr) is the cumulated activity in source region r_h, Δ_i is the mean energy emitted per unit cumulated activity (in g-rad/μCi-hr) for radiation of a particular type and energy, $\phi_i(r_k \leftarrow r_h)$ is the absorbed fraction (dimensionless) for target region r_k for i^{th} radiation emitted in the source region r_h, $\Phi_i(r_k \leftarrow r_h)$ is the specific absorbed fraction (in g^{-1}) and m_k is the mass of target region. For penetrating radiations, which are photons having energies greater than or equal to 10 keV, the absorbed fraction has a numerical value between zero and one.

Major organs in the human body are modeled and described mathematically in the existing MIRD phantom (*2*). The dimensions, shape and coordinate system describing this phantom are shown in Figure 1. The overall dimensions of the phantom and its major organs are based on the Reference Man (*3*). The phantom consists basically of three mediums of different compositions: skeleton, lung tissue and body tissue, having density of 1.48, 0.295 and 0.986 g/cm^3, respectivly. Based on this phantom, Synder et al. applied Monte Carlo techniques and calculated absorbed fractions of energy for photons of different energies for different organs. In these calculations, radiation dose averaged over each target organ was calculated assuming a uniform distribution of radionuclide in a source organ (2). However, in situations when the source radionuclide was not reasonably distributed uniformly in the source organ, more spatial detail was needed. Therefore, models of organs are subject to revision from time to time due to the need to specify regions within a tissue in more detail, as well as to reflect accurately the tissue distribution of a particular radionuclide within an anatomic structure. For example, the assumption of uniform distribution in

the source organ could lead to inaccuracies when calculating the kidney dose from a radionuclide deposited only in kidney cortex (2). The kidney is considered to be a relatively "radiosensitive" organ, yet the kidneys are frequently the organs receiving high level of radioactivity and, therefore, the largest radiation dose. Short lived radiopharmaceuticals, that are now injected in millicurie quantities in nuclear medicine for rapid-sequence imaging of the brain, heart, and abdominal organs, are selected frequently on the basis of their rapid clearance from the bloodstream and as a rule this clearance is achieved at the expense of the urinary tract (4). Therefore, there is a need to improve the present model of kidneys to provide better estimation of radiation dose.

The purpose of this research was to develop a more accurate dosimetric model of the kidneys which consists of important anatomical regions. In this model, the source regions were the cortex, medulla and the papillae, while the target regions were these regions as well as the other organs of the body. The parameters and mathematical equations describing these regions are incorporated into the existing MIRD phantom for absorbed fraction calculations. Such a model will be useful in producing more accurate dose estimates for those radionuclides deposited in the kidneys.

DESCRIPTION OF THE KIDNEYS

Adult human kidneys are considered as identical paired structures of reddish-brown organs lying against the posterior wall of the abdominal cavity, near the level of the last thoracic vertebrae and the first lumbar vertebrae (5). The right kidney is pressed down by the liver and, therefore is somewhat lower than the left. The kidneys, resembling a pair of lima beans turned on the flat side, are embedded in fat which helps to support them. In the middle of each kidney surface is a concave indentation, the hilum, through which blood vessels, lymph vessels, and nerves enter and from which the ureter emerges. Tough, white fibers form a capsule around the kidney. Sheets of connective tissue help to keep the kidneys in position. Since the kidneys touch the diaphragm, they necessarily move with it when the air is drawn into the lungs.

A longitudinal cut in the kidney discloses its internal structure, consisting of the outer granular portion, or the cortex, and the striated inner portion, or the medulla. The medulla consists of cone shaped pyramids. Each pair of pyramids is separated by columns (the renal columns) extending from the cortex into the medulla as far as the inner opening (the renal sinus) near the hilum. In the central portion of the renal sinus is a cavity (the renal pelvis) which is the expanded end of the ureter and includes cup-shaped tissues (calyces) that enclose the ends (papillae) of the pyramids. Microscopic examination shows each kidney to be composed of more than a million units called nephrons. Each nephron consists of a renal corpuscle (corpuscle of Malpighi) and a tubule. The corpuscle is a cluster of looped capillaries (a glomerus) enclosed by the renal capsule (Bowman's capsule); it contains two convoluted parts (between which is a loop - the loop of Henle), one of which leads into a straight collecting duct. The straight collecting ducts give the medulla of the kidney its striated appearance; the other parts of the nephron are mainly in the cortex.

The kidneys produce urine by separating water and minerals from the blood (carried along with the afferent arteries of the renal artery to the looped capillaries of the corpuscles), while leaving the blood cells in the capillaries. The fluid thus taken out the blood travels to the renal pelvis through the tubules. During the passage, 99 per cent of the lost fluid is reabsorbed into the blood surrounding the tubules, including some glucose, potassium, and calcium. About 1400 ml of urine is excreted daily, the amount varying with the diet, water ingestion and loss, and the degree of physical activity of the individual (*3*). Nerve impulses stimulating the arteries and veins to the kidneys affect the secretion of urine. Hormones in the blood influence the reabsorbing action of the tubules and affect the amount of water, salts, and other substances excreted.

A REVISED MODEL FOR THE KIDNEYS

Based on the above description, a revised model of the kidneys has been developed. The dimensions and the location of the whole kidneys are based on the existing MIRD phantom. The kidneys were assumed to be alike and equal in volume; the combined weight of the both kidneys

was 302.4 g (*6*). The model of a kidney is shown in Figure 2. Each kidney is modeled as an ellipsoid of semiaxes 4.5, 2.0 and 5 cm, with a small part truncated 2 cm from the origin of the ellipsoid perpendicular to the X-axis.

As shown in Figure 2, instead of having the whole kidney as a single source or target region, this model consists of three main regions: the cortex, the medulla and the papillae, as the source as well as the target regions. For the purpose of illustration, in Figure 2, part of the kidney is truncated along the XY plane and XZ plane to show the three regions of the kidneys. These three sections of the kidney, simulated for computational purposes, are defined as follows:

Papillae: the papillae consists of the innermost region of the kidney. It is defined by an ellipsoid of semiaxes 2.5, 0.5 and 3 cm. As mentioned before, part of the ellipsoid is truncated, as shown in Figure 2.

Medulla: the medulla consists of the layer in between the papillae and the cortex region. The thickness of the layer is 1 cm. It is defined by an ellipsoid of semiaxes 3.5, 1.5 and 4 cm., but excluding the papillae region. Similar to the pipallae region, part of the ellipsoid is truncated, as shown in Figure 2.

Cortex: the cortex contains of the outermost band of tissue of the kidney. It is defined as the region of the whole kidney, excluding both the papillae and the medulla regions.

For the purpose of dose calculation, it is assumed that these three regions of kidneys are of same composition and density, same as the body tissue of density 0.986 g/cm^3.

PROCEDURE

Calculations of absorbed fractions can be done using an existing computer code, ALGAM, developed at Oak Ridge National Laboratory by Warner et al (*7*). The MIRD phantom, which describes major human organs of clinical interest, was featured in ALGAM. The code was further expanded by Hui (*8*) by incorporating a model of the circulating blood and a model of the heart and lungs developed by Coffey et al (*9*). A source routine, based on the improved model of the

kidneys, was incorporated into the modified code to specify the radionuclide distribution. The existing routines for calculating energy depostion in the code were modified, based on the improved kidney model, to incorporate cortex, medulla and papillae as target regions. Using the Monte Carlo technique, the modified code was used to obtain absorbed fractions of energy for monoenergetic photons for different regions of kidneys as source organs.

Given the source distribution and initial photon energy, a large number (100,000) of photon histories were traced in every calculation. Each photon may undergo photoelectric effect, Compton scattering or pair-production interactions in different body regions. The code has been designed to take account of the geometrical shape of the body and of the major internal organs, the different densities and compositions of the various tissues of the body, and the multiple scattering of photons in the body to provide a more accurate estimate of the energy deposited. For each interaction occurring as part of a photon history, the energy deposited in a specific body region of the MIRD phantom is calculated. It should be noted that, at the present time, the code does not take account of the secondary electrons and positrons that are produced. Generally, the electron ranges are small compared with the diameters of most organs, and the absorbed dose will not change abruptly with distance except at a boundary between organs where composition and density change or at the boundary of the source organ.

When all source photon histories were compiled, the information on accumulated energy deposited in each region was used to calculate absorbed and specific absorbed fractions. Calculations were performed of absorbed and specific absorbed fractions for twelve monoenergetic photon sources ranging from 0.01 to 4.0 MeV. This interval covers the energies for photons emitted by most radionuclides of interest.

RESULTS AND DISCUSSION

Absorbed fractions of major organs for different photon energies are shown in Tables 1, 2 and 3, for the cortex, medulla and the papillae, respectively, as the source organ. At 0.010 MeV

essentially all the photon energy is deposited in the source organ. As energy increases the absorbed fraction decreases following roughly the attenuation coefficient relation. This is as would be expected for all three regions for the kidneys. At lower energies (0.010 MeV) the coefficient of variation, in most cases, does not exceed more than 10%. Snyder accepted any results for which the coefficient of variation was less than 20% and advised that those results with a coefficient of variation in the range of 20% to 50% be used with caution (2). For the purpose of this research a coefficient of variation not exceeding 30% was considered acceptable. Absorbed fractions with coefficient of variation greater than 30% are not listed in Tables 1, 2 and 3.

From Tables 1, 2 and 3, the absorbed fractions of the cortex, medulla and papillae varies greatly, depending whether the source region is cortex, medulla or papillae. This indicates that, for dose estimates to the kidneys, a three-region model provides more accurate results than a homogeneous kidney model. Table 4 shows the specific absorbed fractions of energy for both kidneys as the target region and for different regions of kidney as source regions. The specific absorbed fractions varies significantly, depending on whether the radionuclide is present in the cortex, medulla or papillae region. This further illustrates that more spatial information is needed when the source radionulcide was not distributed reasonably uniformly in the source region. For target organs that are far away from the kidneys, such as the the brain, absorbed fractions remain more or less the same, independent of whether the radionuclide is in the cortex, medulla or papillae. A homogeneous kidney model may be adequate for these organs.

REFERENCES

1. Snyder WS, Ford MR and Warner GG. "S. Absorbed Dose per Unit Cumulated Activity for Selected Radionuclides and Organs," *MIRD Pamphlet No.*11. New York: Society of Nuclear Medicine, 1975.

2. Snyder WS, Ford MR and Warner GG. "Estimates of Specific Absorbed Fractions for Photon Sources Uniformly Distributed in Various Organs of a Heterogeneous Phantom," *MIRD Pamphlet No.*5, Revised. New York: Society of Nuclear Medicine, 1978.

3. International Commission on Radiological Protection. "Report on the Task Group on Reference Man," *ICRP Publication* 23. Oxford: Pergamon Press, 1975.

4. McAfee J, "Problems in Evaluating the Radiation Dose for Radionuclides Excreted by the Kidneys," *Medical Radionuclides: Radiation Dose and Effects*, Oak Ridge, TN: Oak Ridge Associated Universities, 1970; CONF-691212.

5. Frose F, Broedel M, and Schlossberg L, *Atlas of Human Anatomy*. New York: Harper and Row Publishers, 1970.

6. Atkins H, Personal communication to J. W. Poston, 1982.

7. Warner GG and Craig AN, Jr. *ALGAM: A Computer Program for Estimating Internal Dose in a Man Phantom*, Oak Ridge, TN: Oak Ridge National Laboratory, 1968; ORNL-TM-2250.

8. Hui TE, "A Preliminary Model of the Circulating Blood for use in Radiation Dose Calculations," Master Thesis, Texas A&M University, 1986.

9. Coffey JL, Cristy M and Warner GG. "Specific Absorbed Fractions or Photon Sources Uniformly Distributed in the Heart Chambers and Heart Wall of a Heterogeneous Phantom," *MIRD Pamphlet No.*13, *J. Nucl. Med.* 1981; 22:65.

TABLE 1. ABSORBED FRACTIONS OF ENERGY FOR SELECTED ORGANS, SOURCE REGION IS CORTEX

	ENERGY (MEV)		
TARGET REGION	0.010	0.015	0.020
BRAIN			
UTERUS			
KIDNEYS	9.0E-01(**)	7.4E-01(**)	5.7E-01(**)
CORTEX	8.4E-01(**)	6.2E-01(**)	4.4E-01(**)
MEDULLA	5.5E-02(1)*	1.1E-01(1)	1.2E-01(1)
PAPILLAE	1.3E-03(9)	7.9E-03(3)	1.4E-02(2)
LIVER	3.4E-04(17)	3.7E-03(5)	1.2E-02(3)
LUNGS			3.9E-04(13)
RED MARROW	7.0E-05(17)	1.4E-03(5)	5.8E-03(2)
OVARIES			
SPLEEN	3.3E-04(17)	3.1E-03(5)	7.4E-03(3)
HEART WALL			1.6E-04(19)
BLOOD	2.2E-01(**)	1.9E-01(**)	1.6E-01(**)
TOTAL BODY	1.0E+00(**)	9.9E-01(**)	9.6E-01(**)

	ENERGY (MEV)		
TARGET REGION	0.030	0.050	0.100
BRAIN			4.0E-05(28)
UTERUS	7.4E-05(23)	1.2E-04(12)	2.3E-04(9)
KIDNEYS	3.2E-01(**)	1.3E-01(1)	7.3E-02(1)
CORTEX	2.1E-01(**)	7.7E-02(1)	4.2E-02(1)
MEDULLA	9.5E-02(1)	4.5E-02(1)	2.5E-02(1)
PAPILLAE	1.7E-02(2)	1.0E-02(2)	5.6E-03(2)
LIVER	2.7E-02(1)	3.4E-02(1)	2.9E-02(1)
LUNGS	1.8E-03(5)	3.2E-03(3)	3.2E-03(3)
RED MARROW	2.0E-02(1)	3.2E-02(1)	2.1E-02(1)
OVARIES		1.7E-05(28)	3.8E-05(18)
SPLEEN	1.2E-02(2)	1.0E-02(2)	7.1E-03(2)
HEART WALL	5.5E-04(8)	1.2E-03(4)	1.4E-03(4)
BLOOD	1.1E-01(**)	6.6E-02(**)	4.6E-02(**)
TOTAL BODY	8.5E-01(**)	6.3E-01(**)	4.5E-01(**)

* -- COEFFICIENTS OF VARIATION IN PERCENT.

** - COEFFICIENTS OF VARIATION LESS THAN 0.5%.

TABLE 1. (CONTINUED)

TARGET REGION	ENERGY (MEV) 0.200	0.500	1.000
BRAIN	4.4E-05(27)	9.0E-05(21)	1.1E-04(20)
UTERUS	1.8E-04(10)	1.7E-04(13)	1.9E-04(15)
KIDNEYS	7.3E-02(1)	7.7E-02(1)	7.1E-02(1)
CORTEX	4.4E-02(1)	4.6E-02(1)	4.3E-02(1)
MEDULLA	2.5E-02(1)	2.6E-02(1)	2.3E-02(2)
PAPILLAE	5.3E-03(2)	5.5E-03(3)	5.3E-03(3)
LIVER	2.7E-02(1)	2.6E-02(1)	2.5E-02(1)
LUNGS	3.1E-03(3)	3.1E-03(3)	3.2E-03(4)
RED MARROW	1.4E-02(1)	1.1E-02(1)	1.0E-02(2)
OVARIES	1.6E-05(25)	3.4E-05(29)	
SPLEEN	6.7E-03(2)	6.3E-03(3)	5.9E-03(3)
HEART WALL	1.4E-03(4)	1.5E-03(5)	1.3E-03(6)
BLOOD	4.5E-02(**)	4.6E-02(1)	4.3E-02(1)
TOTAL BODY	4.2E-01(**)	4.2E-01(**)	4.0E-01(**)

TARGET REGION	ENERGY (MEV) 1.500	2.000	4.000
BRAIN	1.2E-04(21)	1.8E-04(17)	1.8E-04(18)
UTERUS	1.9E-04(16)	2.3E-04(16)	2.3E-04(16)
KIDNEYS	6.5E-02(1)	5.9E-02(1)	4.9E-02(1)
CORTEX	3.9E-02(1)	3.5E-02(1)	3.0E-02(2)
MEDULLA	2.2E-02(2)	2.0E-02(2)	1.6E-02(2)
PAPILLAE	4.8E-03(4)	4.0E-03(4)	3.3E-03(5)
LIVER	2.2E-02(2)	2.2E-02(2)	1.8E-02(2)
LUNGS	3.3E-03(4)	3.1E-03(4)	2.7E-03(5)
RED MARROW	9.8E-03(2)	9.2E-03(2)	8.0E-03(2)
OVARIES			
SPLEEN	5.5E-03(3)	5.3E-03(3)	4.1E-03(4)
HEART WALL	1.3E-03(6)	1.3E-03(7)	1.2E-03(8)
BLOOD	4.0E-02(1)	3.8E-02(1)	3.2E-02(1)
TOTAL BODY	3.8E-01(**)	3.6E-01(**)	3.1E-01(**)

* -- COEFFICIENTS OF VARIATION IN PERCENT.

** - COEFFICIENTS OF VARIATION LESS THAN 0.5%.

TABLE 2. ABSORBED FRACTIONS OF ENERGY FOR SELECTED ORGANS, SOURCE REGION IS MEDULLA

	ENERGY (MEV)		
TARGET REGION	0.010	0.015	0.020
BRAIN			
UTERUS			
KIDNEYS	9.8E-01(**)	8.8E-01(**)	7.2E-01(**)
CORTEX	6.9E-02(1)	1.3E-01(1)	1.5E-01(1)
MEDULLA	8.7E-01(**)	6.8E-01(**)	5.0E-01(**)
PAPILLAE	3.7E-02(2)	6.9E-02(1)	7.5E-02(1)
LIVER		1.6E-03(7)	7.7E-03(3)
LUNGS			2.9E-04(15)
RED MARROW		1.4E-03(5)	6.2E-03(2)
OVARIES			
SPLEEN		1.4E-03(8)	4.4E-03(4)
HEART WALL			1.1E-04(23)
BLOOD	2.4E-01(**)	2.2E-01(**)	1.9E-01(**)
TOTAL BODY	1.0E+00(**)	9.9E-01(**)	9.7E-01(**)

	ENERGY (MEV)		
TARGET REGION	0.030	0.050	0.100
BRAIN			2.7E-05(28)
UTERUS		1.1E-04(16)	1.8E-04(10)
KIDNEYS	4.3E-01(**)	1.7E-01(**)	9.4E-02(1)
CORTEX	1.2E-01(1)	5.6E-02(1)	3.1E-02(1)
MEDULLA	2.6E-01(**)	9.4E-02(1)	5.0E-02(1)
PAPILLAE	5.5E-02(1)	2.4E-02(1)	1.2E-02(1)
LIVER	2.1E-02(2)	3.1E-02(1)	2.7E-02(1)
LUNGS	1.3E-03(6)	2.8E-03(3)	3.1E-03(3)
RED MARROW	2.2E-02(1)	3.5E-02(1)	2.3E-02(1)
OVARIES		2.2E-05(27)	3.7E-05(19)
SPLEEN	8.1E-03(2)	8.8E-03(2)	6.0E-03(2)
HEART WALL	5.1E-04(8)	1.1E-03(5)	1.4E-03(4)
BLOOD	1.3E-01(**)	7.5E-02(**)	5.1E-02(**)
TOTAL BODY	8.6E-01(**)	6.5E-01(**)	4.7E-01(**)

* -- COEFFICIENTS OF VARIATION IN PERCENT.

** - COEFFICIENTS OF VARIATION LESS THAN 0.5%.

TABLE 2. (CONTINUED)

TARGET REGION	ENERGY (MEV) 0.200	0.500	1.000
BRAIN		8.4E-05(23)	1.3E-04(18)
UTERUS	1.9E-04(11)	1.8E-04(12)	2.2E-04(14)
KIDNEYS	9.5E-02(1)	9.9E-02(1)	9.1E-02(1)
CORTEX	3.0E-02(1)	3.1E-02(1)	2.8E-02(1)
MEDULLA	5.2E-02(1)	5.5E-02(1)	5.0E-02(1)
PAPILLAE	1.3E-02(2)	1.3E-02(2)	1.2E-02(2)
LIVER	2.5E-02(1)	2.5E-02(1)	2.3E-02(2)
LUNGS	2.9E-03(3)	3.0E-03(3)	2.9E-03(4)
RED MARROW	1.5E-02(1)	1.2E-02(1)	1.1E-02(1)
OVARIES	3.1E-05(22)	2.8E-05(30)	
SPLEEN	6.0E-03(2)	5.3E-03(3)	5.0E-03(3)
HEART WALL	1.3E-03(4)	1.3E-03(5)	1.2E-03(6)
BLOOD	4.9E-02(**)	5.0E-02(1)	4.7E-02(1)
TOTAL BODY	4.3E-01(**)	4.3E-01(**)	4.1E-01(**)

TARGET REGION	ENERGY (MEV) 1.500	2.000	4.000
BRAIN	2.2E-04(16)	1.8E-04(17)	2.3E-04(17)
UTERUS	1.9E-04(16)	2.2E-04(16)	2.7E-04(16)
KIDNEYS	8.3E-02(1)	7.7E-02(1)	6.2E-02(1)
CORTEX	2.6E-02(2)	2.5E-02(2)	1.9E-02(2)
MEDULLA	4.6E-02(1)	4.2E-02(1)	3.5E-02(1)
PAPILLAE	1.1E-02(2)	1.0E-02(3)	8.5E-03(3)
LIVER	2.2E-02(2)	2.1E-02(2)	1.7E-02(2)
LUNGS	3.0E-03(4)	3.0E-03(4)	2.6E-03(5)
RED MARROW	1.1E-02(2)	1.0E-02(2)	8.6E-03(2)
OVARIES			
SPLEEN	4.5E-03(4)	4.4E-03(4)	3.5E-03(5)
HEART WALL	1.2E-03(6)	1.3E-03(7)	1.1E-03(7)
BLOOD	4.4E-02(1)	4.1E-02(1)	3.5E-02(1)
TOTAL BODY	3.9E-01(**)	3.7E-01(**)	3.1E-01(**)

* -- COEFFICIENTS OF VARIATION IN PERCENT.

** - COEFFICIENTS OF VARIATION LESS THAN 0.5%.

TABLE 3. ABSORBED FRACTIONS OF ENERGY FOR SELECTED ORGANS, SOURCE REGION IS PAPILLAE

	ENERGY (MEV)		
TARGET REGION	0.010	0.015	0.020
BRAIN			
UTERUS			
KIDNEYS	9.6E-01(**)	8.9E-01(**)	7.5E-01(**)
CORTEX	4.7E-03(4)	3.2E-02(2)	6.1E-02(1)
MEDULLA	1.2E-01(1)	2.4E-01(1)	2.6E-01(**)
PAPILLAE	8.3E-01(**)	6.3E-01(**)	4.3E-01(**)
LIVER		8.9E-04(10)	4.1E-03(4)
LUNGS			2.5E-04(16)
RED MARROW	5.5E-05(29)	1.5E-03(5)	7.2E-03(2)
OVARIES			
SPLEEN		1.0E-03(9)	3.8E-03(4)
HEART WALL			8.6E-05(26)
BLOOD	2.4E-01(**)	2.2E-01(**)	1.9E-01(**)
TOTAL BODY	1.0E+00(**)	9.9E-01(**)	9.7E-01(**)

	ENERGY (MEV)		
TARGET REGION	0.030	0.050	0.100
BRAIN			
UTERUS		1.2E-04(14)	2.1E-04(10)
KIDNEYS	4.6E-01(**)	1.9E-01(**)	1.0E-01(**)
CORTEX	7.2E-02(1)	4.3E-02(1)	2.5E-02(1)
MEDULLA	1.9E-01(**)	8.4E-02(1)	4.5E-02(1)
PAPILLAE	2.0E-01(**)	6.2E-02(1)	3.3E-02(1)
LIVER	1.4E-02(2)	2.2E-02(1)	2.1E-02(1)
LUNGS	1.2E-03(6)	2.6E-03(3)	2.9E-03(3)
RED MARROW	2.3E-02(1)	3.9E-02(1)	2.5E-02(1)
OVARIES		1.7E-05(28)	2.2E-05(24)
SPLEEN	8.7E-03(2)	9.4E-03(2)	6.8E-03(2)
HEART WALL	5.2E-04(8)	1.2E-03(4)	1.4E-03(4)
BLOOD	1.4E-01(**)	7.8E-02(**)	5.3E-02(**)
TOTAL BODY	8.7E-01(**)	6.6E-01(**)	4.7E-01(**)

* -- COEFFICIENTS OF VARIATION IN PERCENT.

** - COEFFICIENTS OF VARIATION LESS THAN 0.5%.

TABLE 3. (CONTINUED)

TARGET REGION	ENERGY (MEV) 0.200	0.500	1.000
BRAIN	5.5E-05(27)	4.0E-05(28)	7.8E-05(23)
UTERUS	1.8E-04(10)	1.9E-04(13)	2.5E-04(13)
KIDNEYS	1.0E-01(1)	1.1E-01(1)	9.8E-02(1)
CORTEX	2.3E-02(1)	2.4E-02(1)	2.1E-02(2)
MEDULLA	4.5E-02(1)	4.6E-02(1)	4.3E-02(1)
PAPILLAE	3.5E-02(1)	3.8E-02(1)	3.4E-02(1)
LIVER	1.9E-02(1)	1.9E-02(2)	1.8E-02(2)
LUNGS	2.8E-03(3)	2.9E-03(3)	2.8E-03(4)
RED MARROW	1.7E-02(1)	1.3E-02(1)	1.2E-02(1)
OVARIES	2.9E-05(23)		
SPLEEN	6.2E-03(2)	6.1E-03(3)	5.7E-03(3)
HEART WALL	1.4E-03(4)	1.4E-03(5)	1.5E-03(6)
BLOOD	5.1E-02(**)	5.2E-02(1)	4.8E-02(1)
TOTAL BODY	4.4E-01(**)	4.4E-01(**)	4.2E-01(**)

TARGET REGION	ENERGY (MEV) 1.500	2.000	4.000
BRAIN	1.7E-04(18)	1.9E-04(18)	2.3E-04(17)
UTERUS	2.0E-04(15)	2.1E-04(15)	1.6E-04(19)
KIDNEYS	9.1E-02(1)	8.4E-02(1)	6.8E-02(1)
CORTEX	2.0E-02(2)	1.8E-02(2)	1.4E-02(2)
MEDULLA	3.9E-02(1)	3.6E-02(1)	2.9E-02(2)
PAPILLAE	3.2E-02(1)	2.9E-02(1)	2.4E-02(2)
LIVER	1.7E-02(2)	1.7E-02(2)	1.4E-02(2)
LUNGS	3.0E-03(4)	2.8E-03(4)	2.6E-03(5)
RED MARROW	1.1E-02(2)	1.1E-02(2)	9.6E-03(2)
OVARIES			
SPLEEN	5.1E-03(3)	5.2E-03(4)	3.9E-03(4)
HEART WALL	1.4E-03(6)	1.3E-03(7)	1.1E-03(7)
BLOOD	4.6E-05(1)	4.3E-02(1)	3.5E-02(1)
TOTAL BODY	3.9E-01(**)	3.7E-01(**)	3.1E-01(**)

* -- COEFFICIENTS OF VARIATION IN PERCENT.

** - COEFFICIENTS OF VARIATION LESS THAN 0.5%.

TABLE 4. COMPARISON OF SPECIFIC ABSORBED FRACTIONS OF ENERGY FOR BOTH KIDNEYS AS TARGET ORGAN.

	SOURCE REGION		
ENERGY	CORTEX	MEDULLA	PAPILLAE
0.010	2.9E-03	3.2E-03	3.2E-03
0.015	2.4E-03	2.9E-03	3.0E-03
0.020	1.9E-03	2.4E-03	2.5E-03
0.030	1.1E-03	1.4E-03	1.5E-03
0.050	4.4E-04	5.7E-04	6.3E-04
0.100	2.4E-04	3.1E-04	3.4E-04
0.200	2.4E-04	3.1E-04	3.4E-04
0.500	2.6E-04	3.3E-04	3.6E-04
1.000	2.3E-04	3.0E-04	3.2E-04
1.500	2.1E-04	2.7E-04	3.0E-04
2.000	1.9E-04	2.6E-04	2.8E-04
4.000	1.6E-04	2.1E-04	2.2E-04

An Approach to Hot Particle Dosimetry Using a Monte Carlo Transport Code

INTRODUCTION

Hot particles were first identified in the early 1960's at some of the original operating nuclear plants. However, hot particles did not gain wide attention until the 1980's. In the early 1980's, Portland General Electric's Trojan plant had a significant fuel failure caused by baffle-jetting and many small radioactive particles were discovered on workers. In October of 1985, a 433 mrad/hr particle was detected on a workers' clothing at San Onofre Nuclear Generating Station, Unit 3 (Warnock et al. 1987). Another incident in 1985 occurred at the McGuire nuclear plant where eight skin contaminations from activated cobalt particles were reported. The estimated dose received from these particles ranged from 1.06 to 10.6 rem (Bray et al. 1987).

These and other incidents have led to an increasing concern over the identification and control of hot particles (USNRC1986a, USNRC 1987). Health physics programs have been developed at essentially all facilities to minimize hot particle control problems and facilitate hot particle identification. Usually, these programs are site specific and are directed towards an extensive list of possible contaminants derived from particular operations at each facility. Emphasis has been placed on the detection of hot particles at several check points to ensure exposures are identified quickly. In addition, most facilities have taken steps to reduce the sources of hot particles.

Federal regulations regarding exposure of the skin represent one of the main areas of controversy in the hot particle issue. The Nuclear

Regulatory Commission currently limits the exposure of extremities to 18.75 rem per quarter and the skin of the whole body is limited to 7.5 rem per quarter (USNRC 1986b). Although there has been a great deal of discussion as to the regulatory definition of extremities and the skin, these limits assume that the exposure is uniform, over a reasonably large area. Hot particles, in contrast, deliver extremely high doses to a very small area of skin. Many experts feel that the above limits are too restrictive in the case of hot particles. Even though the dose from a hot particle is very high, the actual injury to an exposed individual may be negligible, and, in many cases, undetectable. Therefore, the limits specified in the federal regulations are much too restrictive when applied to the assessment of hot particle incidents.

More recently, the National Council on Radiation Protection and Measurements (NCRP) has issued their report on hot particles on the skin (NCRP 1989). The NCRP has focussed on preventing deep ulceration of the skin and has recommended a limit based upon the total number of beta particles emitted from the radionuclide(s) present in the hot particle. Exposure to the skin by a hot particle of a size less than 1 mm in diameter should be limited to 10^{10} beta particles emitted from the contaminant. If one beta particle is emitted per disintegration, this recommended limit may be expressed as a time integral of activity equal to 75 μCi h. It is interesting to note that the NCRP specifically avoided the specification of the area or depth of assessment of the dose equivalent due to hot particles (NCRP 1989).

Many variables must be evaluated to assess properly the potential

damage from hot particles. The dose delivered is dependent on the biological endpoint, the size, composition, and activity of the particle, location of the particle on the worker, and the residence time. NCRP recognized these variables and took them into account in their recommended limit. The NCRP assumed that acute deep ulceration occurred at a threshold dose of approximately 230,000 rads when the dose was evaluated at a depth of 100 μm directly under the hot particle. The NCRP-recommended 75 μCi h value was based upon this threshold, a small, unspecified area, and, apparently, a depth of 100 μm (NCRP 1989).

The purpose of our research was evaluate the current methods used in industry to assess doses from hot particles and to compare the results obtained to those obtained using an electron transport code. A Monte Carlo photon-electron transport code, which can be used to model the physical process of energy deposition by electrons in tissue, was used to determine the actual behavior of hot particle beta radiation in the skin. A comparison was made between the results from these transport calculations and those obtained using the computer code VARSKIN and Loevinger's formulation. These latter approaches represent current methods of dose assessment. In addition, our goal was to evaluate the need for changes to current methodologies for handling hot particle exposure incidents.

CODE DESCRIPTIONS

A. LOPOINT

A computer code, LOPOINT, was used to calculate the skin dose from contamination deposited on the surface of the skin. The code, written by the authors, utilized a widely accepted method derived by Loevinger for determining dose distributions due to beta radiation sources. Loevinger measured dose distributions from planar sources and derived empirical equations for point, infinite plane, and finite plane sources (Loevinger 1956, Bartlett 1987).

The code LOPOINT uses the following equation in the calculation of dose from a point source:

$$J(x) = \frac{kn}{(vx)^2}\left\{ c\left[1 - \left(\frac{vx}{c}\right) e^{1-\frac{vx}{c}} \right] + vxe^{1-\frac{vx}{c}} \right\}. \qquad (3)$$

Where: $J(x)$= beta skin dose rate at point x (rad/hr)/μCi;

x = distance from point source (g/cm^2);

k = $0.17\ v^3\ E_{ave}\ a$ (rad/hr)/mCi -- for tissue;

$$v = \frac{18.6}{(E_0 - 0.036)^{1.37}}\left(2 - \frac{E_{ave}}{E_{ave^*}}\right) \left(cm^2/g\right) \text{ of tissue};$$

c = $2.20\ e^{-0.36\ Eo}$;

a = $[3c^2 - (c^2 - 1)\ e]^{-1}$;

n = fractional abundance of beta with E_0 (per disintegration);

E_0 = maximum beta energy (MeV);

E_{ave}= average beta energy (MeV); and

E_{ave}*= average beta energy for an allowed spectrum (MeV).

Loevinger's empirical formula can be used for hot particle dose assessment by invoking the reciprocal dose theorem. The theorem states, "...the dose to a point from a circular plane source is equal to the dose to the circular plane from a point source, provided that both sources are of equal activity and inside a uniform absorbing material" (Bartlett 1987).

VARSKIN

The computer code VARSKIN also was used in this study since this code is widely used and accepted as the standard in the nuclear power industry for hot particle evaluations. VARSKIN can be used to calculate the radiation dose due to skin contamination from beta emitting radionuclides at any depth below the surface of the skin. The user may evaluate the dose from point sources, disk sources of any radius, and infinite planar sources (where the radius of the source is greater than the maximum range of the beta particle). The user selects the radionuclides comprising the source from a predetermined list, the activity of the source, the duration of the exposure, and the depth of interest (Traub et al. 1987).

In this code, the dose due to a point source is calculated at 26 locations all at depth d below the skin surface. These points extend horizontally from the axis of the source to a distance R and are spaced

with a square root distribution. The points are packed tightly in the center of the exposed basal layer. The space between the points increases with distance from the axis of the source to radius R. Figure 1 illustrates the simplest geometry, the point source. In this figure, R_m is the effective range of the beta particle in the skin and is equal to 1.8 times X_{90}, where X_{90} is the 90-percentile range for a given beta particle. Within a distance X_{90}, all particles have deposited 90% of their total energy. The radius, R, is calculated using the following formula:

$$R = (R_m^2 - d^2). \qquad (1)$$

The dose received at each of the 26 points is a function of the parameters defined above and the energy spectrum of the beta radiation.

The code accesses tabular data that were originally developed by Berger for the distribution of absorbed energy around point sources of beta emitting radionuclides in water (Berger 1971).

Next, the doses to each of the 26 points are averaged over the skin area determined by a circle with radius R at depth d. The equation is as follows:

$$\text{Average Dose} = \frac{2\pi \int_0^R \text{dose}(r)\, r\, dr}{\pi R^2} . \qquad (2)$$

The disk source geometry is illustrated in Figure 2. In this case, the exposed area of the basal layer is divided into two regions. The first

region contains the points within the range of the source radiations. The cells in this region view the source as an infinite planar source. The dose is calculated to 26 points in this region from an infinite planar source. The second region is called the "edge". The dose is calculated to 26 points in this region using the same method as for a point source. The dose to the points in both regions is averaged over the circular areas using equation 2. The limits of integration, differentiating between the two regions, are chosen in the VARSKIN program depending on the range of the particles and the radius of the disk source.

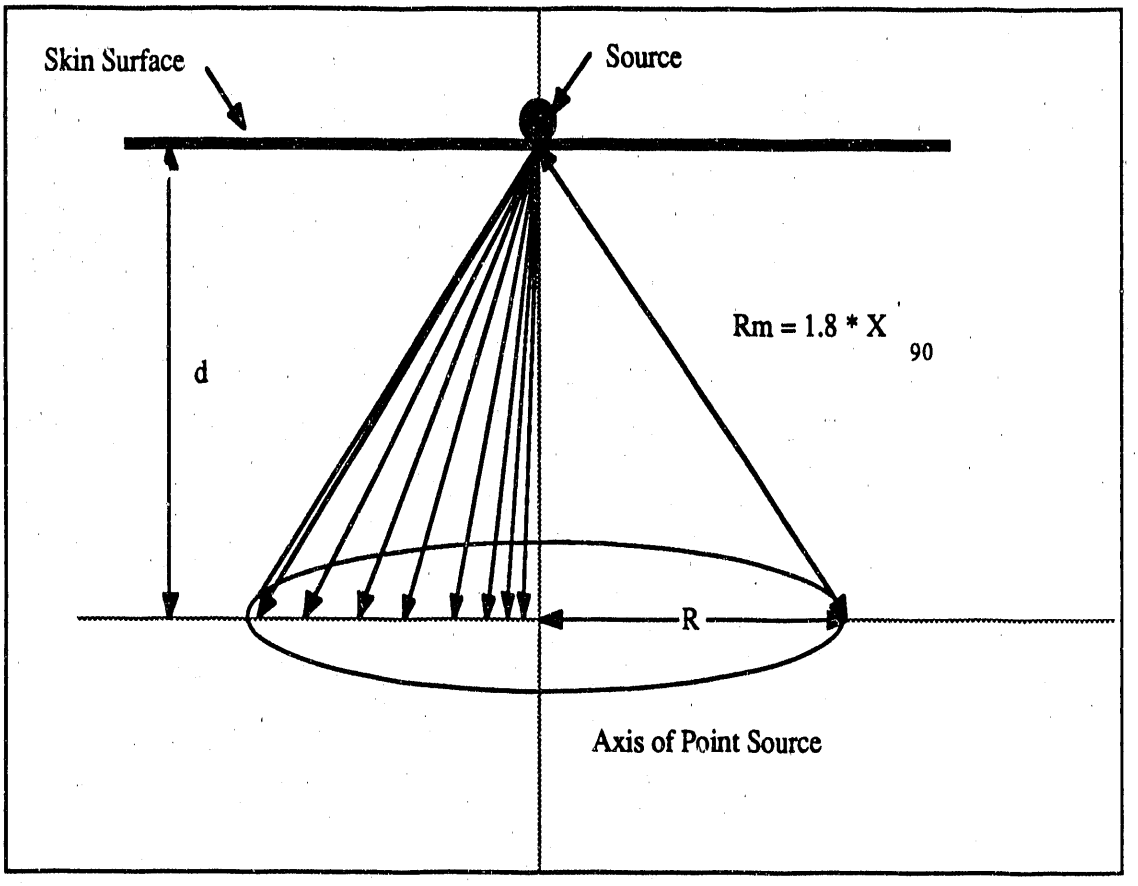

Figure 1. Point Source Geometry

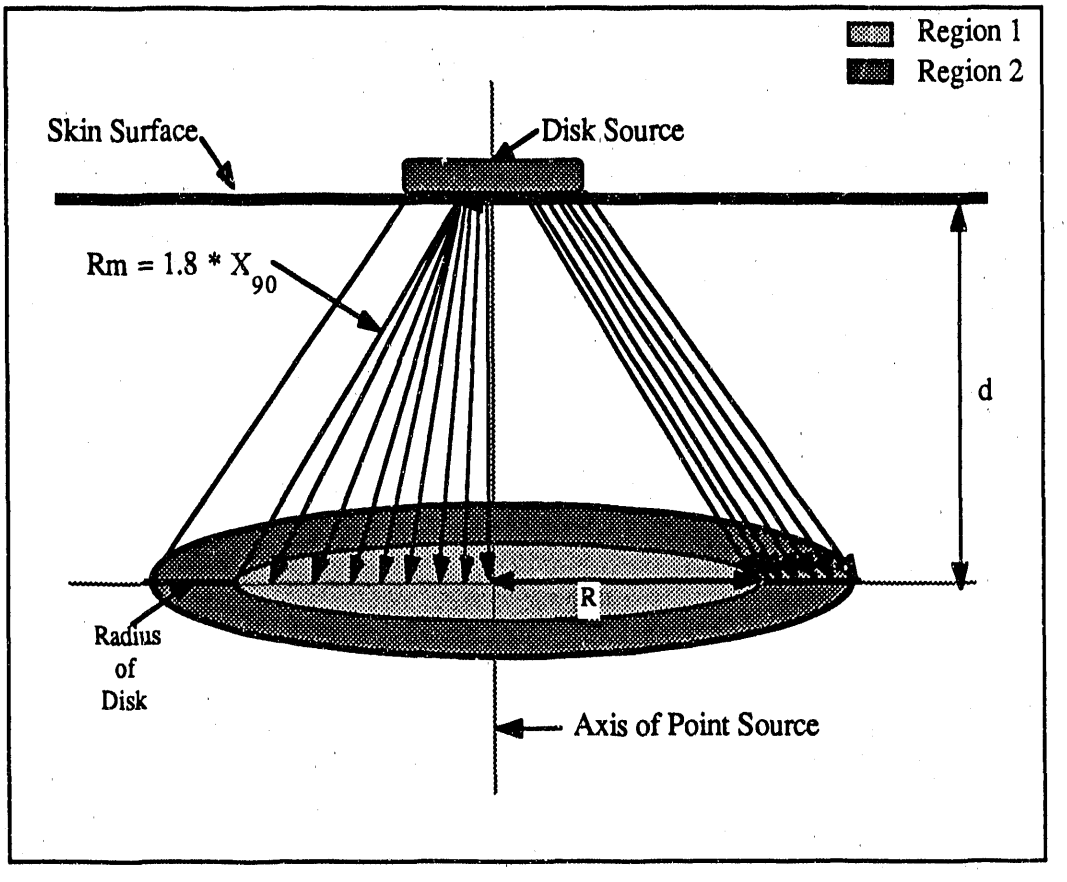

Figure 2. Disk Source Geometry

EGS4

EGS4 is a Monte Carlo code that can be used to simulate the radiation transport of electrons or photons in any element, compound, or mixture. It was used in this research to follow charged particles (beta radiation) which were transported in random steps through regions simulating the skin. As the particle is transported, several physical processes are followed; Bremsstrahlung production, positron annihilation in flight and at rest, Moliere multiple scattering, Moller (e^-e^-) and Bhabha (e^+e^-) scattering, continuous energy loss applied to charged particle tracks between discrete interactions, pair production, Compton scattering, Raleigh scattering, and the photoelectric effect.

Two user-written subroutines are incorporated: HOWFAR and AUSGAB. HOWFAR is used to establish the specific geometry for the problem. AUSGAB is used to tabulate energy losses within the geometrical regions specified in HOWFAR.

The two input files used in EGS4 are MEDIA and PATCLE. MEDIA is a fixed data file containing cross sections for tissue down to an energy of 1 keV. PATCLE is a variable input file which specifies the cut-off energies for electrons and photons, the number of electrons, energy of the electrons, the pathlength step size, and the radius of the source.

EGS4 was used to calculate the average dose at different depths below the surface of the skin for a fixed volume. The beta particles were considered to be monoenergetic electrons with an energy equivalent to the average beta energy of the radionuclide of interest. A geometry was designed for EGS4 with the following parameters, so that a comparison

could be made with the results obtained from VARSKIN and LOPOINT. The volume created for EGS4 was a cylinder with a height of 400 μm and a variable radius. There were three variations used for the radius; the radius specified by VARSKIN for all cell damage, the continuous slowing down distance as specified by Attix (Attix 1986), and 0.5642 cm which corresponds to a circular area of 1 cm^2. The cylinder was divided into 400 layers, 1 μm thick; the small volume constructed approximately represented a planar area. Figure 3 shows the geometry created for EGS4.

METHODS

To calculate the skin dose received from hot particles, the composition and activity of the source must be determined. Once the radiation characteristics have been identified, appropriate beta dose equations and computer codes can be applied to calculate the dose to the basal layer at any specified depth and over any area.

After reviewing the literature, a list of typical components of hot particles was constructed. The radionuclides, evaluated in our study, are listed in Table 1. This tabulation is not a complete list of all isotopes that have been detected in hot particles, rather it contains the most prominent components encountered in both fuel and stellite particles.

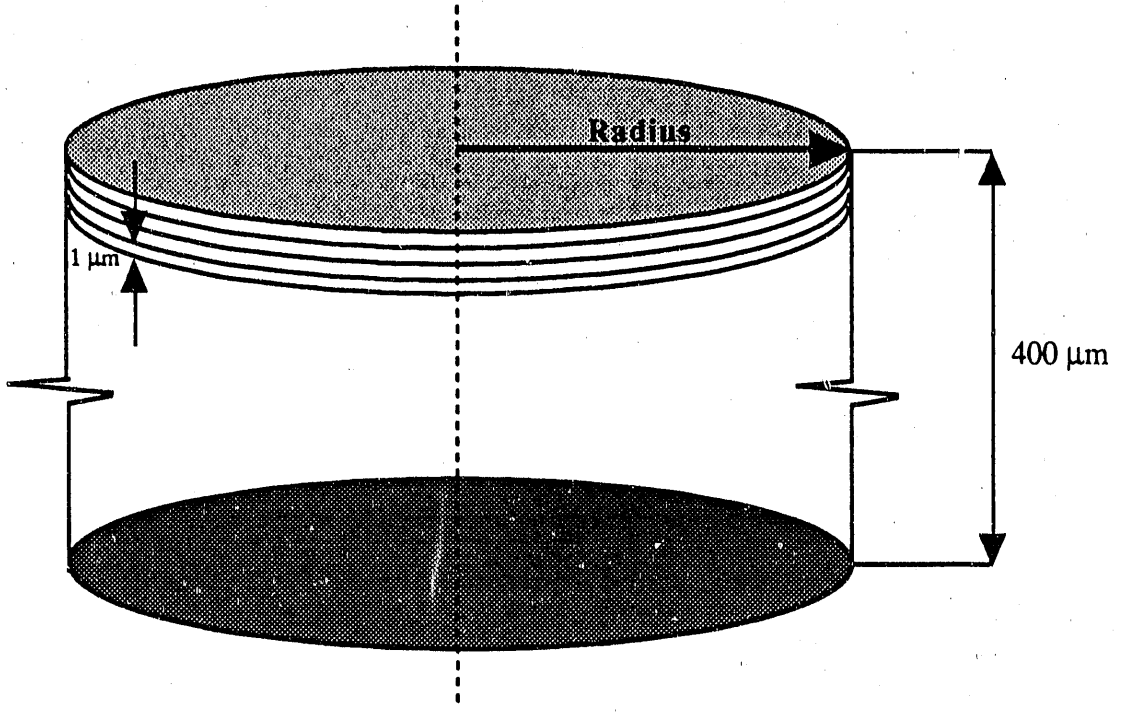

Figure 3. EGS4 Geometry

Table 1. Hot Particle Radionuclides

Radionuclide	E_{ave} (MeV)	E_{max} (MeV)
Sr-89	0.593	1.470
Sr-90	0.196	0.544
Nb-95	0.046	0.930
Ce-144	0.081	0.320
Co-60	0.094	1.478
Zr-95	0.115	1.130
Ce-141	0.144	0.580
Co-58	0.201	0.474
I-131	0.180	0.810
Ba-140	0.282	1.010
Cs-137	0.195	1.167
La-140	0.490	2.200
Y-90	0.931	2.245
Pr-144	1.225	2.984
Pm-147	0.062	2.450

The three computer codes LOPOINT, VARSKIN, and EGS4 were used to calculate the average dose at various depths below the surface of the skin. The three codes utilized different methods in the calculations. To compare the results from each code, similar geometries were constructed.

LOPOINT was used to calculate the dose rate to a point using Loevinger's empirical dose distribution equation. This code was written by the authors. The user specified the radionuclide, number of betas emitted per disintegration, maximum particle energy, average particle energy, hypothetical energy ratio (E_{ave}/E_{ave*}), and the fractional abundance. Then, LOPOINT was used to calculate the dose to individual points or a range of points.

VARSKIN was used to calculate the dose to the 26 points mentioned in the previous section. The points were determined in the program depending on the range of the beta radiation and the size of the source. The dose was computed for the 26 points using equation 2.

EGS4 can be used to calculate the dose to a volume and a cylindrical geometry was constructed for use in this code. The height of the cylinder was 400 μm and the cylinder was divided in steps of 1 μm. The radius of the cylinder was either 0.5642 cm or R_{max} cm. The resulting elemental volume was a thin layer that approximated a planar area.

A. Comparison One - LOPOINT vs. VARSKIN at Current Regulatory Specifications

For the first comparison, VARSKIN was used as a control. The code was used to dictate the geometry to be utilized by EGS4 and distances for LOPOINT. The output of VARSKIN lists the dose equivalent averaged over an area of 1 cm^2, the dose averaged over a circle with radius R, and the dose at 26 points horizontally outward from the axis of the source.

The 26 points were used to calculate the distance from the source using the Pythagorean theorem. LOPOINT was used to calculate the dose at the same distances from the source. The dose at each of the points was averaged over 1 cm^2 at a depth of 70 μm for comparison with VARSKIN. The isotopes evaluated were Co-60, Sr-89, and Pr-144 with average beta energies of 0.094 MeV, 0.593 MeV, and 1.225 MeV, respectively. These isotopes were chosen because their energies encompassed the typical energy range of hot particles. The average doses from the two codes were normalized to the results for VARSKIN because this code is the current method used by the NRC and industry to evaluate hot particles for regulatory compliance.

B. Comparison Two - VARSKIN vs. EGS4 for Various Depths

VARSKIN and EGS4 were used to calculate the average dose from a point source at the following depths; 10 μm, 50 μm, 70 μm, 100 μm, 150 μm, 200 μm, 250 μm, 300 μm, and 400 μm. The hot particle was assumed to be a point source with an integrated activity of 1 μCi-sec.

Beta particles were transported in EGS4 as monoenergetic electrons having the average energy of the radionuclide. The depths were chosen to account for fluctuations in the basal layer depth in different regions of the body (ICRP 1975). The codes were used to calculate the dose over two different areas. The first area was 1 cm^2, the depth used to demonstrate regulatory compliance. The second was an area with a radius of R_{max}, determined by the 90-percentile distance for electrons. Three isotopes were evaluated; Co-60, Sr-89, and Pr-144.

Since EGS4 is a Monte Carlo code, it was necessary to establish the number of particle histories required to reduce the calculational error to less than one percent of the energy deposited in the elemental volume. In the second comparison, the number of histories introduced into EGS4 directly corresponded to the activity of the hot particle assuming that one beta particle was emitted per disintegration. For the remaining evaluations, only 10,000 histories were required to obtain reliable results.

C. Comparison Three - Dose as a Function of Average Beta Particle Energy

The next comparison was designed to determine the dependence of the average dose on the average energy of the beta particle at various depths below the surface of the skin. EGS4 was used to calculate the average dose at the following depths; 40 μm, 50 μm, 150 μm, and 300 μm. These depths corresponded to the average depth of the basal layer determined for the head and trunk, arms and legs, dorsal hand and foot, and

voral hand and foot, respectively (Konishi and Yashizawa 1985). The depth of 70 μm also was evaluated because it is the current average depth of the basal layer recognized by the ICRP and the NRC. All isotopes listed in Table 1 were evaluated in this comparison using the average energy of the beta radiations.

After evaluating the results from this comparison, it was determined that VARSKIN could be used to calculate the dose to points outside the range of the particle. The range is approximately equal to the average path length an electron travels. For beta particles with energy greater than 10 keV, the range calculated assuming the continuous slowing down approximation (CSDA) is a useful measure of average electron penetration distance, therefore the CSDA range is a better representation of the actual particle pathlength (Turner 1986). In this comparison the average dose at the different depths was calculated over 1 cm^2 and $\pi(CSDA)^2$ cm^2.

The input file for EGS4 was the only parameter that was changed in this comparison. The radius used in EGS4 was either the CSDA range or 0.5642 cm. Table 2 contains the CSDA path lengths of the radionuclides evaluated assuming the average beta particle energy.

D. Comparison Four - Dose as a Function of Averaging Area

This comparison investigated the dependence of the average area on the resulting dose using EGS4. Three radionuclides were investigated; Sr-89, Pr-144, and Co-60. The radius of the cylindrical geometry input into EGS4 was changed to allow evaluation of the dose over several areas.

The following areas were investigated; 0.25 cm^2, 1 cm^2, 2 cm^2, $\pi(R_{max})^2$ cm^2, and $\pi(CSDA)^2$ cm^2. Currently, the Federal regulations require the dose be determined to an area of 1 cm^2 at a depth of 70 μm.

Table 2. CSDA Mean Path Length

Radionuclide	CSDA Range (cm)
Sr-90	2.174E-01
Sr-89	4.224E-02
Nb-95	3.609E-03
Ce-144	1.011E-02
Co-60	1.250E-02
Zr-95	1.767E-02
Ce-141	2.563E-02
Co-58	4.396E-02
I-131	3.685E-02
Ba-140	7.471E-02
Cs-137	4.191E-02
La-140	1.673E-01
Y-90	3.911E-01
Pr-144	5.382E-01
Pm-147	6.099E-03

E. Comparison Five - Dose as a Function of Disk Size

The final relationship studied was the effect of disk size on the average dose at the following depths; 40 μm, 50 μm, 70 μm, 150 μm, and 300 μm. The following disk radii were evaluated; 0.0001 cm, 0.0005 cm, 0.001 cm, 0.005 cm, 0.01 cm, 0.05 cm, 0.1 cm, and 1.0 cm, for the same radionuclides, i.e., Sr-89, Pr-144, and Co-60.

RESULTS

To facilitate a comparison in terms of the absorbed dose per unit activity, i.e., rad/μCi, for all the investigations in this research, the total number of disintegrations introduced into the computer codes was assumed to be equivalent to a 1 μCi source on the skin for a period of one second. The dose estimate for higher activity sources is a simple multiple of the normalized absorbed dose per unit activity (rad/μCi) and the exposure period in seconds, and, since the quality factor for beta radiation is unity, the results can be interpreted in units of rem/μCi.

A. Comparison One - LOPOINT vs. VARSKIN at Current Regulatory Specifications

Industry currently uses Loevinger's beta dose rate equations or the computer code VARSKIN to calculate the dose from hot particles. First, a comparison was made between LOPOINT and VARSKIN at a depth of 70 μm and an area of 1 cm^2. A point source was chosen for the comparison with an activity of 1 μCi (i.e., 3.7 x 10^4 dps). The results from both computer codes were normalized to the output from VARSKIN because

it is the code utilized by the NRC for such assessments. Since the assumed exposure corresponded to 1 μCi-sec, all dose estimates were small. For example, for a 1 μCi point source of ^{60}Co, the VARSKIN estimate was 0.002 rem, while the LOPOINT estimate was 0.004 rem. For ^{89}Sr, the estimates were 0.005 rem and 0.009 rem, and for ^{144}Pr, the estimates were 0.005 rem and 0.008 rem, respectively. These results agree with a similar investigation using Loevinger equations and VARSKIN to assess the dose delivered from fuel fragments (Bray et al. 1987). For cases in which the distances of interest are beyond one-half the range of the beta radiation, it has been reported that the differences reach more than a factor of ten (NCRP 1989).

B. Comparison Two - VARSKIN vs. EGS4 for Various Depths

In the second comparison, VARSKIN and EGS4 were used to calculate the average doses for two areas, 1 cm^2 and $\pi(R_{max})^2$ cm^2, at various depths. The $\pi(R_{max})^2$ areas were 0.0099 cm^2 , 0.93 cm^2 , and 4.58 cm^2 for Co-60, Sr-89, and Pr-144, respectively. Figures 4 through 9 compare the absorbed doses as a function of depth for these three isotopes. In these figures, the dose decreases with increasing depth for both areas over which the dose was averaged. Close to the skin surface, the doses obtained with VARSKIN tended to be higher than those from EGS4. At depths of 70 μm, the two codes were in agreement within ±35%. For depths greater than 100 μm, the difference decreased to ±15%.

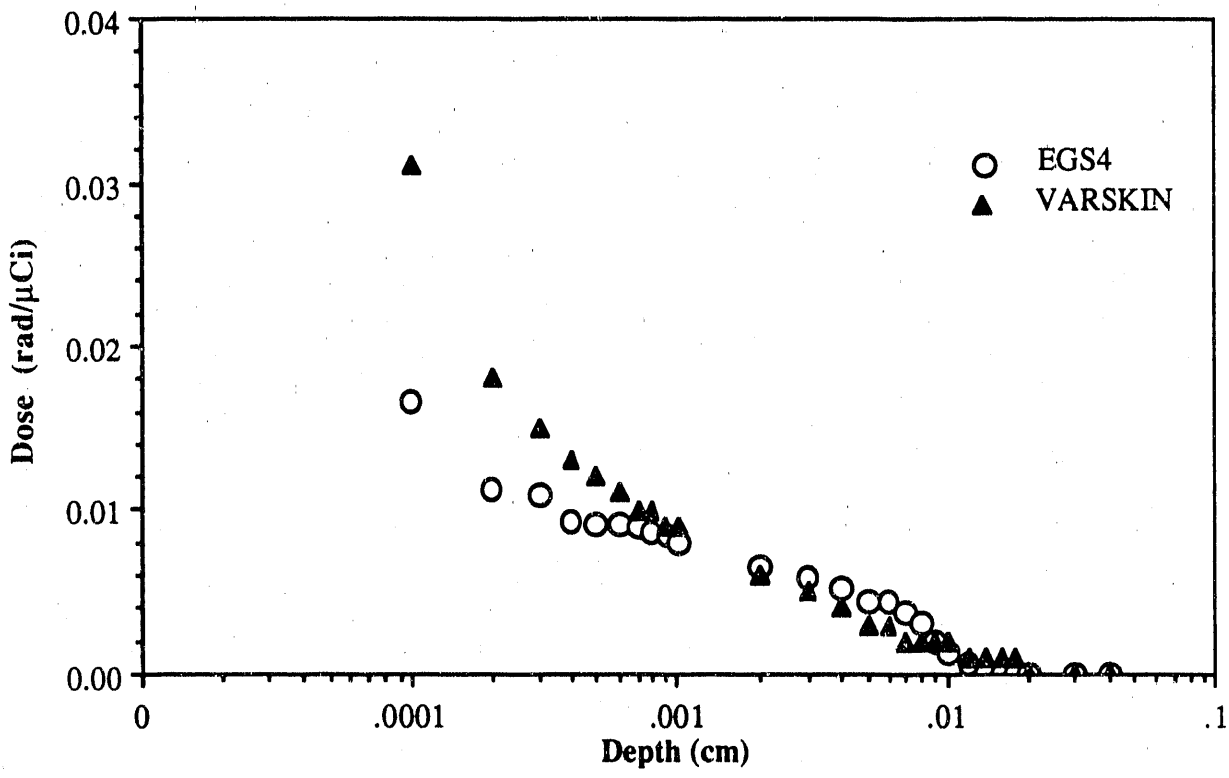

Figure 4. Comparison of VARSKIN and EGS4 for Dose from 1 μCi Co-60 Point Source Averaged Over 1 cm^2.

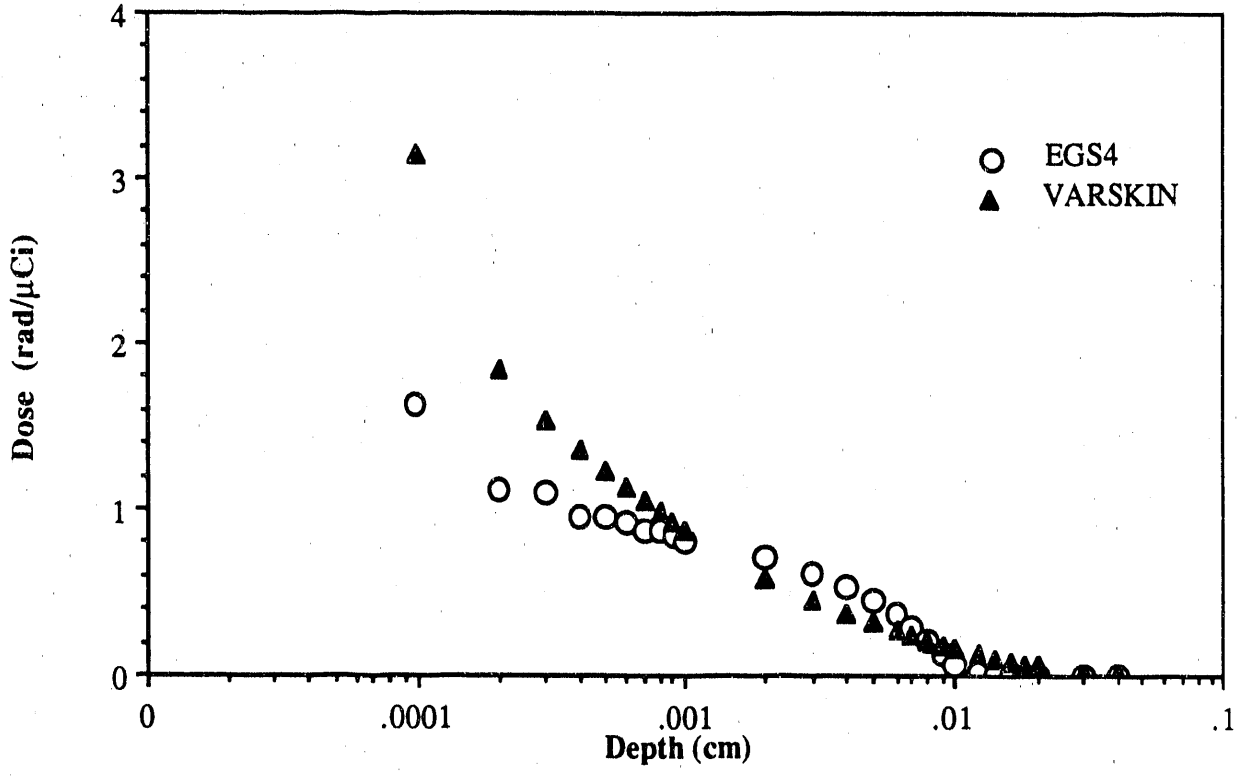

Figure 5. Comparison of VARSKIN and EGS4 for Dose from 1 μCi Co-60 Point Source Averaged Over $\pi(R_{max})^2$ cm^2.

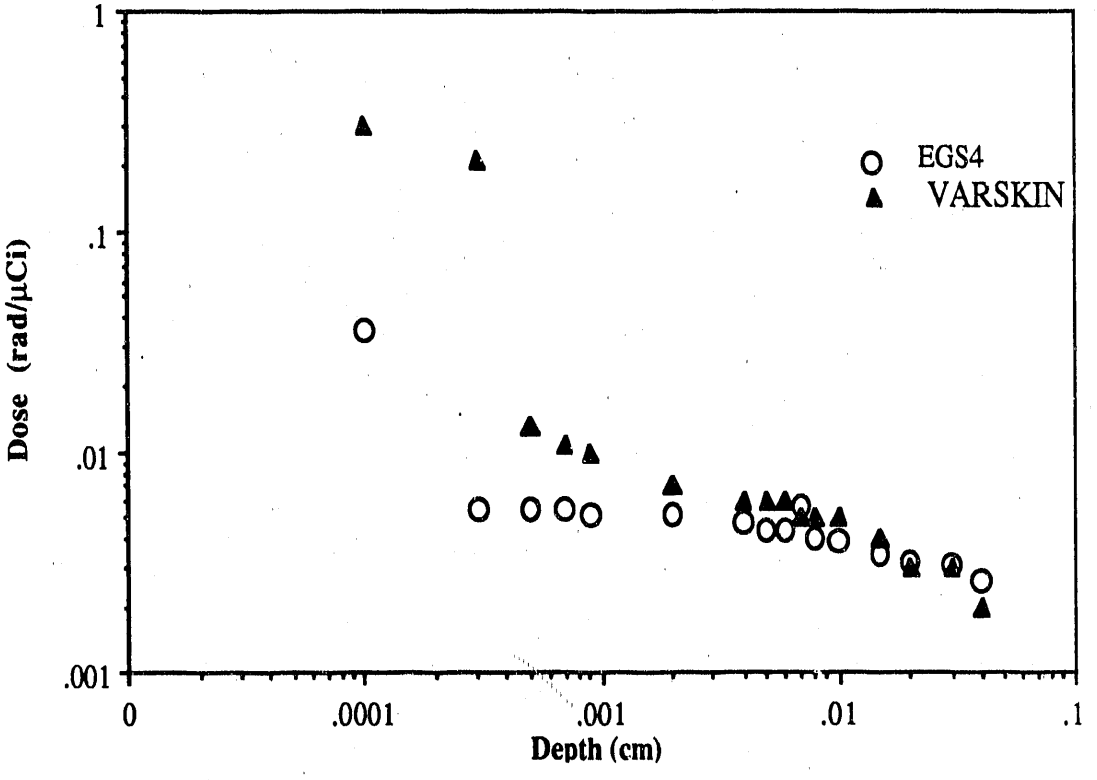

Figure 6. Comparison of VARSKIN and EGS4 for Dose from 1 μCi Sr-89 Point Source Averaged Over 1 cm^2.

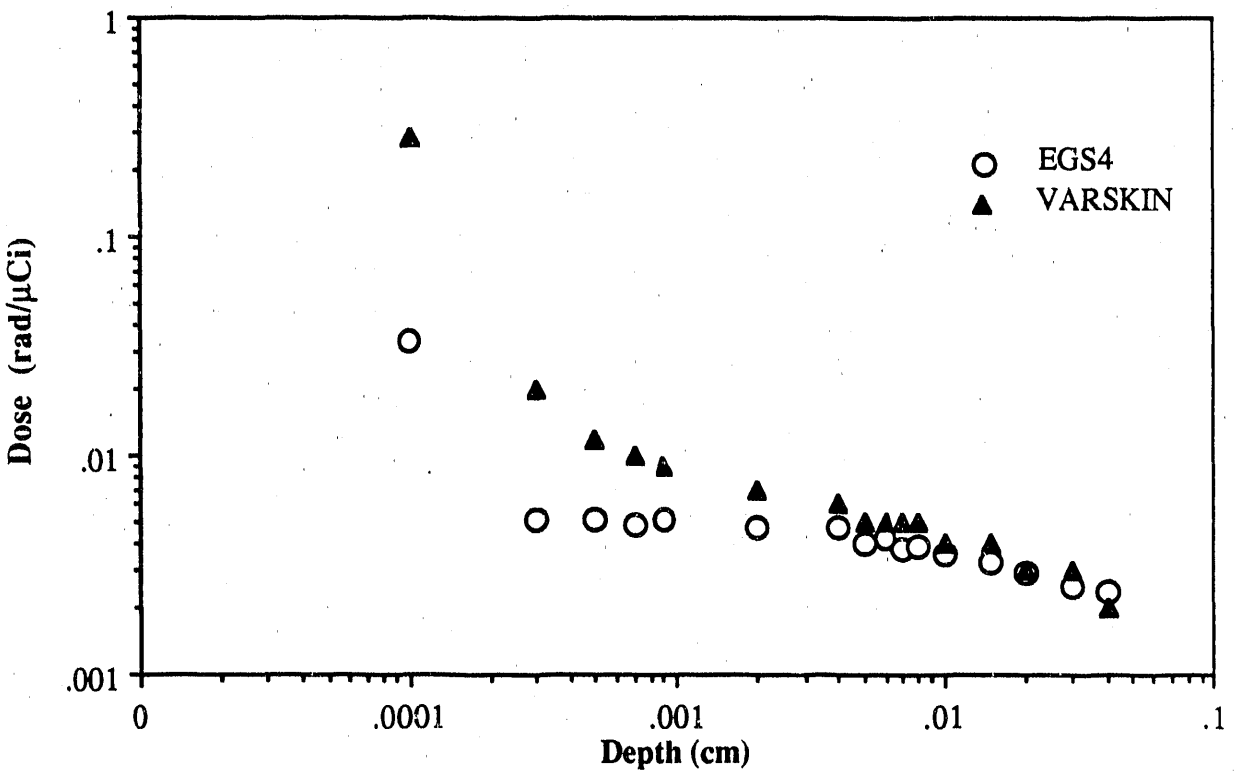

Figure 7. Comparison of VARSKIN and EGS4 for Dose from 1 μCi Sr-89 Point Source Averaged Over $\pi(R_{max})^2$ cm^2.

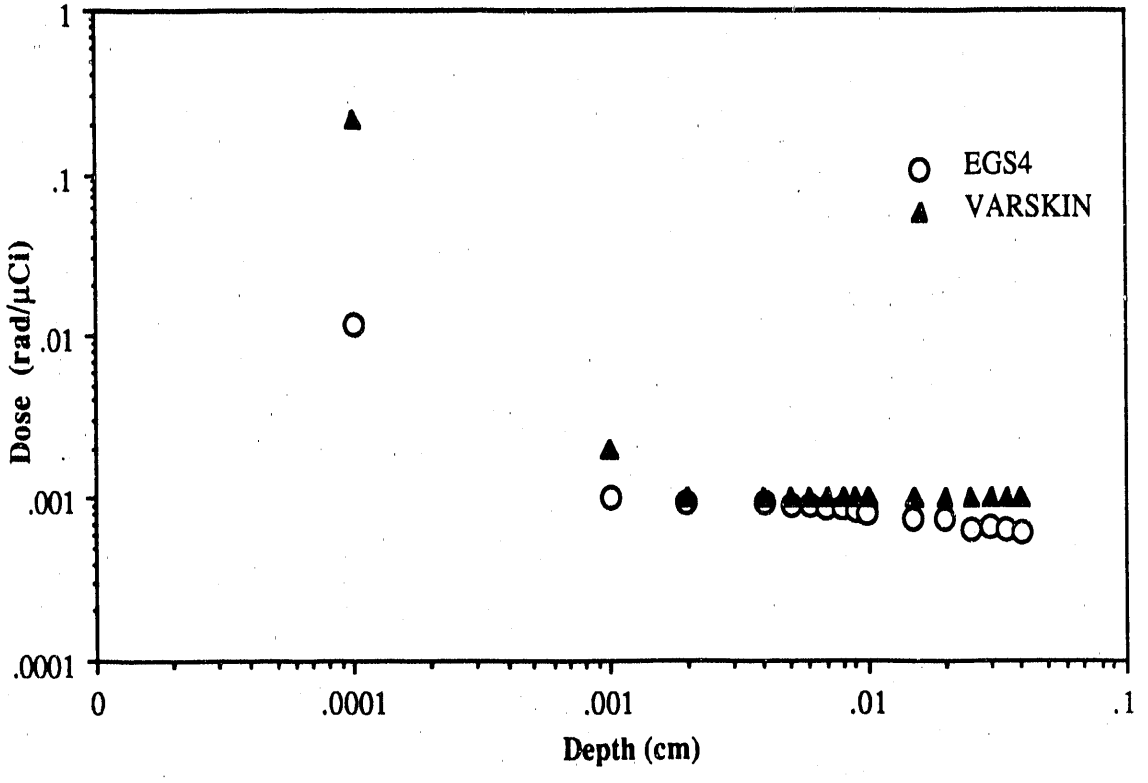

Figure 8. Comparison of VARSKIN and EGS4 for Dose from 1 μCi Pr-144 Point Source Averaged Over 1 cm^2.

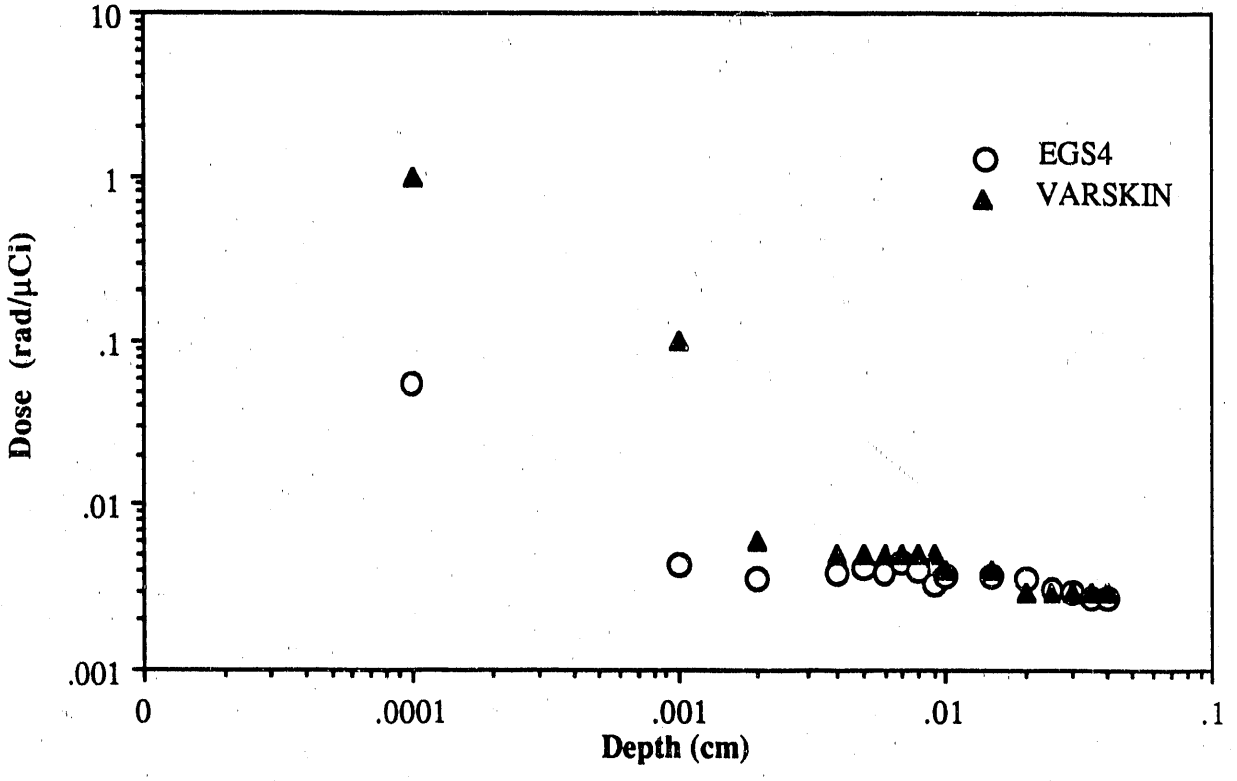

Figure 9. Comparison of VARSKIN and EGS4 for Dose from 1 μCi Pr-144 Point Source Averaged Over $\pi(R_{max})^2$ cm^2.

C. Comparison Three - Dose as a Function of Average Beta Particle Energy

The next comparison studied the dependence of the average dose at various depths on the average energy of the beta particle. EGS4 was used to calculate the dose averaged over areas of 1 cm^2 and $\pi(CSDA)^2$ cm^2. Figure 10 illustrates the dose averaged over 1 cm^2 and $\pi(CSDA)^2$ cm^2 at a depth of 70 μm as a function of particle energy. The dose per unit activity decreased as the energy of particle increased for an area of 1 cm^2. The dose averaged over the CSDA range remained constant for energies greater than 100 keV because the CSDA range (see Table 2) also increased with particle energy. The curves for other depths in tissue had similar shapes, these data are tabulated in Table 3.

D. Comparison Four - Dose as a Function of Averaging Area

The fourth comparison investigated the effect of the area over which the dose was averaged on the dose at several depths. Figures 11 through 13 show the relationship between the area over which the dose is averaged and the dose for Co-60, Sr-89, and Pr-144 at the average

depths of the basal layer. The dose decreased for all three radionuclides evaluated with increasing area over which the dose was averaged, at each specified depth.

Table 3. Dose as a Function of Average Basal Layer Depth

		Area=π(CSDA)^2 cm^2, Dose (rad/μCi)				
Nuclide	**E_{ave} (Mev)**	**40 μm**	**50μm**	**70μm**	**150μm**	**300 μm**
Nb-95	0.046	0.000	0.000	0.000	0.000	0.000
Pm-147	0.062	20.180	5.470	0.000	0.000	0.000
Ce-144	0.081	13.840	6.570	5.310	0.000	0.000
Co-60	0.097	8.494	7.500	4.536	0.000	0.000
Zr-95	0.115	4.150	3.680	2.960	0.152	0.000
Ce-141	0.144	2.990	2.810	2.370	0.999	0.000
I-131	0.180	0.840	0.800	0.740	0.469	0.031
Cs-137	0.195	0.810	0.760	0.710	0.486	0.094
Sr-90	0.200	0.800	0.750	0.700	0.520	0.121
Co-58	0.201	0.800	0.750	0.700	0.527	0.127
Ba-140	0.282	0.230	0.210	0.200	0.150	0.101
La-140	0.490	0.050	0.040	0.040	0.032	0.030
Sr-89	0.583	0.030	0.030	0.030	0.021	0.019
Y-90	0.931	0.008	0.009	0.007	0.006	0.007
Pr-144	1.225	0.004	0.004	0.005	0.004	0.004

Nuclide	Area=1 cm^2, Dose (rad/μCi) E_{ave} (Mev)	40 μm	50 μm	70 μm	150 μm	300 μm
Nb-95	0.046	0.000	0.000	0.000	0.000	0.000
Pm-147	0.062	0.002	0.001	0.000	0.000	0.000
Ce-144	0.081	0.005	0.004	0.001	0.000	0.000
Co-60	0.097	0.005	0.004	0.003	0.000	0.000
Zr-95	0.115	0.005	0.005	0.004	0.002	0.000
Ce-141	0.144	0.005	0.004	0.004	0.001	0.000
I-131	0.180	0.005	0.005	0.004	0.003	0.000
Cs-137	0.195	0.005	0.005	0.004	0.003	0.000
Sr-90	0.200	0.005	0.005	0.004	0.003	0.001
Co-58	0.201	0.005	0.004	0.004	0.003	0.001
Ba-140	0.282	0.004	0.004	0.004	0.003	0.002
La-140	0.490	0.005	0.004	0.004	0.003	0.003
Sr-89	0.583	0.005	0.004	0.004	0.003	0.003
Y-90	0.931	0.005	0.004	0.004	0.004	0.004
Pr-144	1.225	0.004	0.004	0.005	0.004	0.004

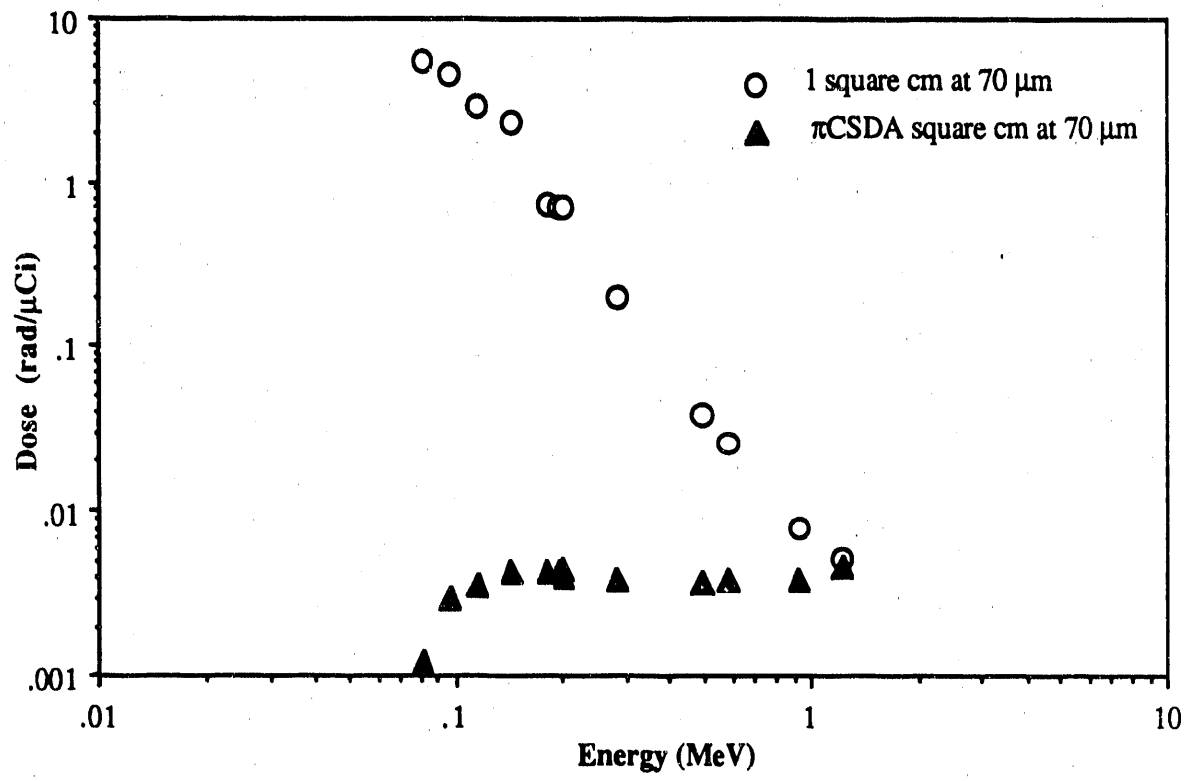

Figure 10. Average Dose as a Function of Energy at a Depth of 70 μm

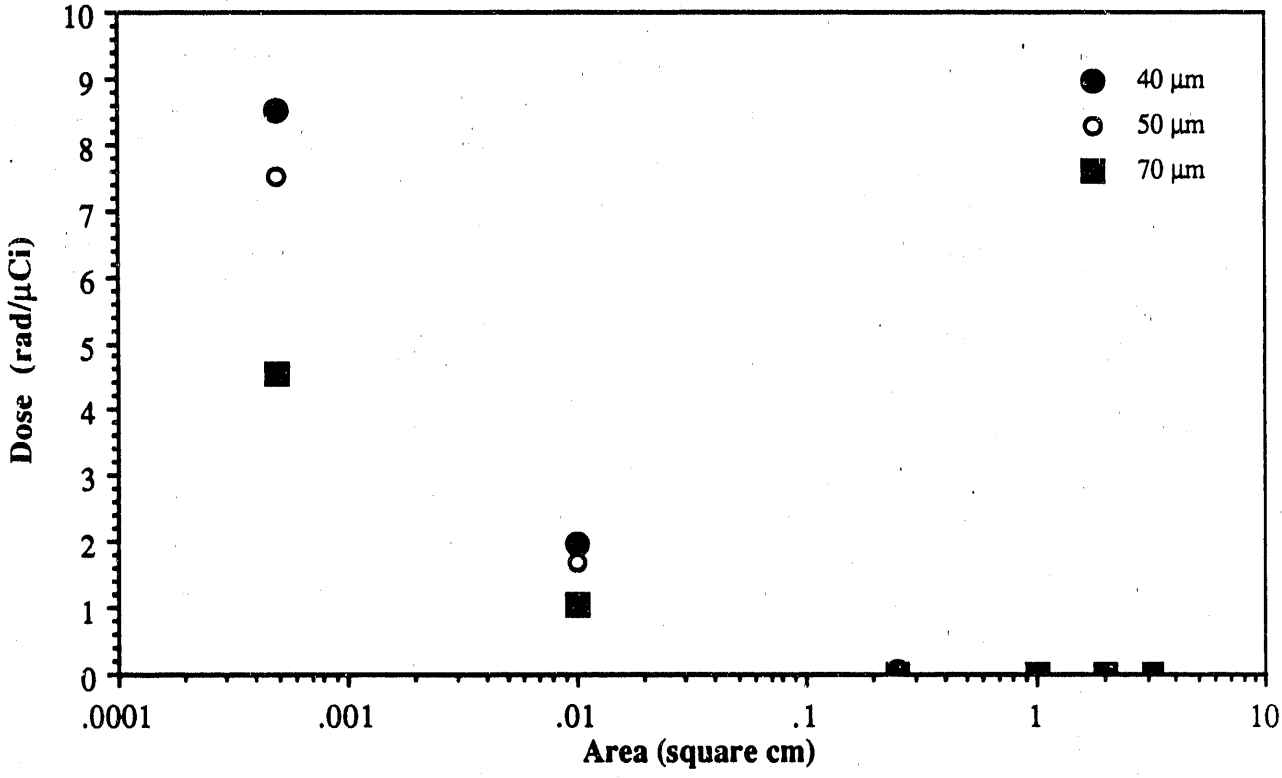

Figure 11. Dose as a Function of Area for Co-60

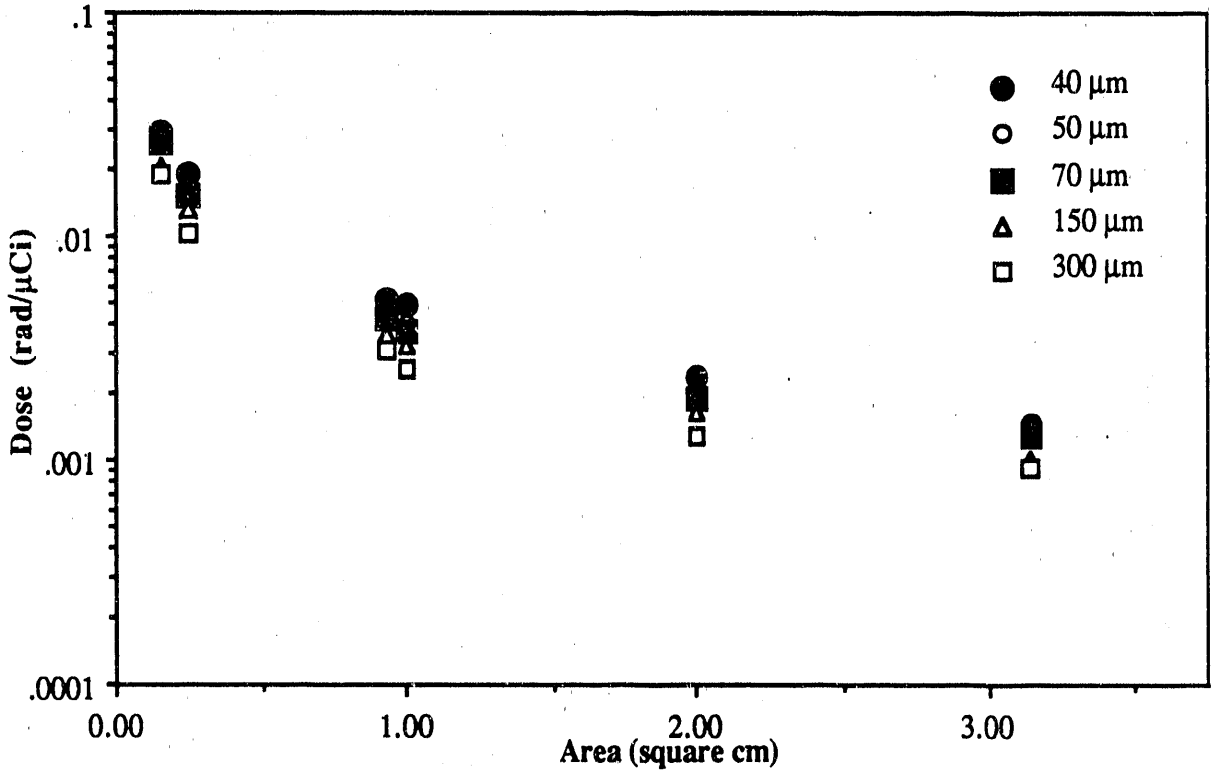

Figure 12. Dose as a Function of Area for Sr-89

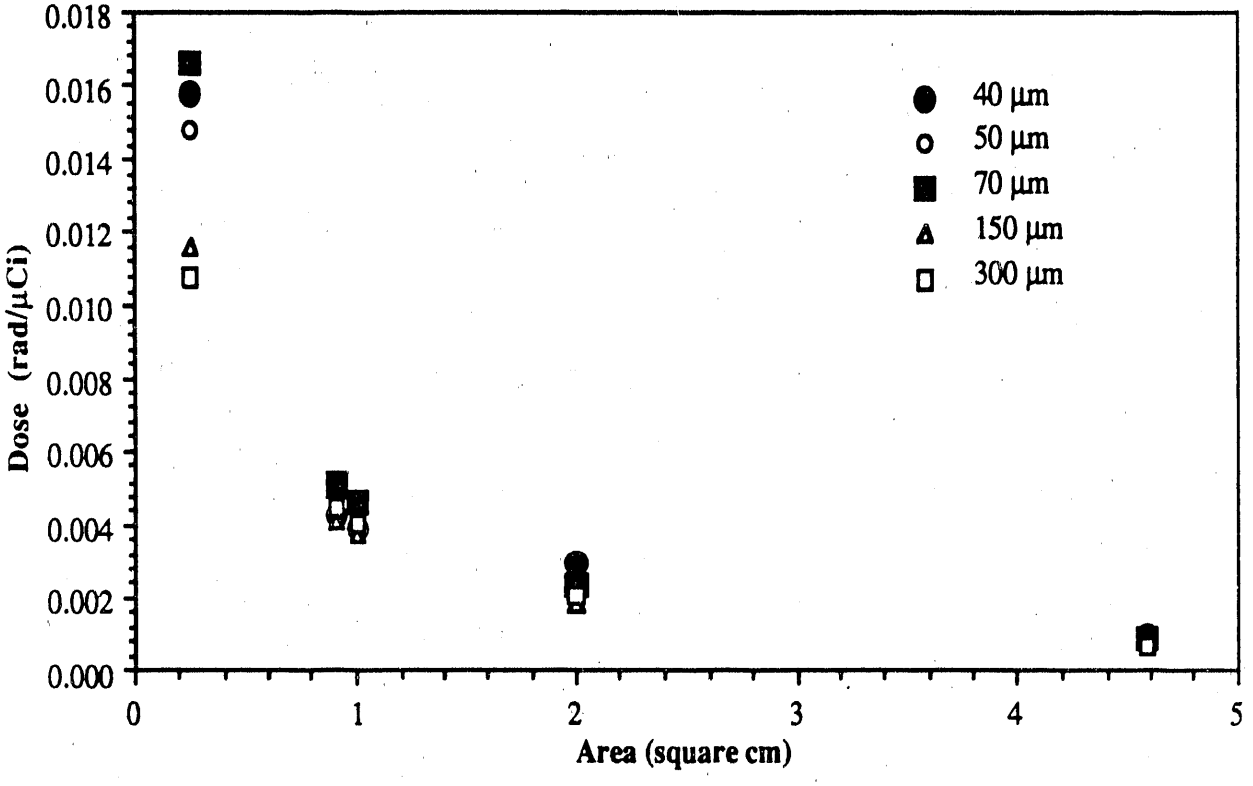

Figure 13. Dose as a Function of Area for Pr-144

CONCLUSIONS

The two most prominent methods utilized to determine the dose received from hot particles are Loevinger's equation and the computer code VARSKIN. Results obtained with VARSKIN currently are accepted by the NRC for hot particle exposure assessments. Comparison of LOPOINT and VARSKIN revealed that the delivered dose obtained with LOPOINT is greater than the VARSKIN estimate by a factor of 1.5 to 2.2. The lowest energy isotope evaluated, Co-60 (0.097 MeV), showed the greatest increase of a factor of 2.2 and the highest energy isotope, Pr-144 (1.225 MeV), showed an increase over VARSKIN of a factor of 1.6. These results are not inconsistent with those reported previously (Bray 1987, NCRP 1989). Base on these results, it is recommended that Loevinger's equation should be used only as a rough approximation of the dose delivered by a hot particle.

To model more realistically the actual behavior of beta particles in tissue, EGS4 was used to calculate the dose at several different depths and areas. Figures 4 through 9 show that the VARSKIN results are higher than those obtained with EGS4 at very shallow depths, but as the depth increases there is good agreement between the two codes.

The next comparison investigated the average dose as a function of incident particle energy. The dose was averaged over two areas with the following radii; 0.5642 cm (area = 1 cm^2) and CSDA-range cm (area = $\pi(CSDA)^2$ cm^2). Figure 10 shows the relationship obtained in this comparison. For the area representing a 1 cm^2 area, it can be seen that

as the particle energy increases, the average dose decreases at a specified depth. After evaluating the data, it can be concluded that the average dose to a 1 cm^2 area increases with increasing particle energy and increasing depth. For the area representing $\pi(CSDA)^2$ cm^2, it should be noticed that as the particle energy increases the CSDA-range also increases. Therefore, the average dose approaches a constant value of the dose which depends on the particle energy and the depth of investigation.

The fourth part of this research evaluated the dependence of dose on the area over which the dose was averaged. Dose is defined as energy deposited per unit mass (or unit volume). From this simple relationship, it can be concluded that if the energy deposited is constant, and the volume increases, then the average dose must decrease. Figure 11 through 13 demonstrate this relationship.

The final comparison investigated the effect of disk size on the average dose to the exposed basal layer. Hot particles deliver a high dose to a small area. As the disk size increases the exposure becomes more uniform and more closely represents an infinite planar source. Figures 14 through 16 demonstrate this relationship. As the disk size was increased, the dose averaged over 1 cm^2 decreased.

The method recommended by the NRC, VARSKIN, provides estimates of the absorbed dose which are higher than those obtained using the EGS4 code. In this research, EGS4 was used to simulate the actual behavior of beta particles interacting in the skin, to provide a more realistic dose delivered the basal layer of the skin. After comparing the two computer codes, it was concluded that VARSKIN is not only convenient and quick in

assessing doses, but the dose estimates obtained from VARSKIN are very applicable to current industry needs. With the many variables that are

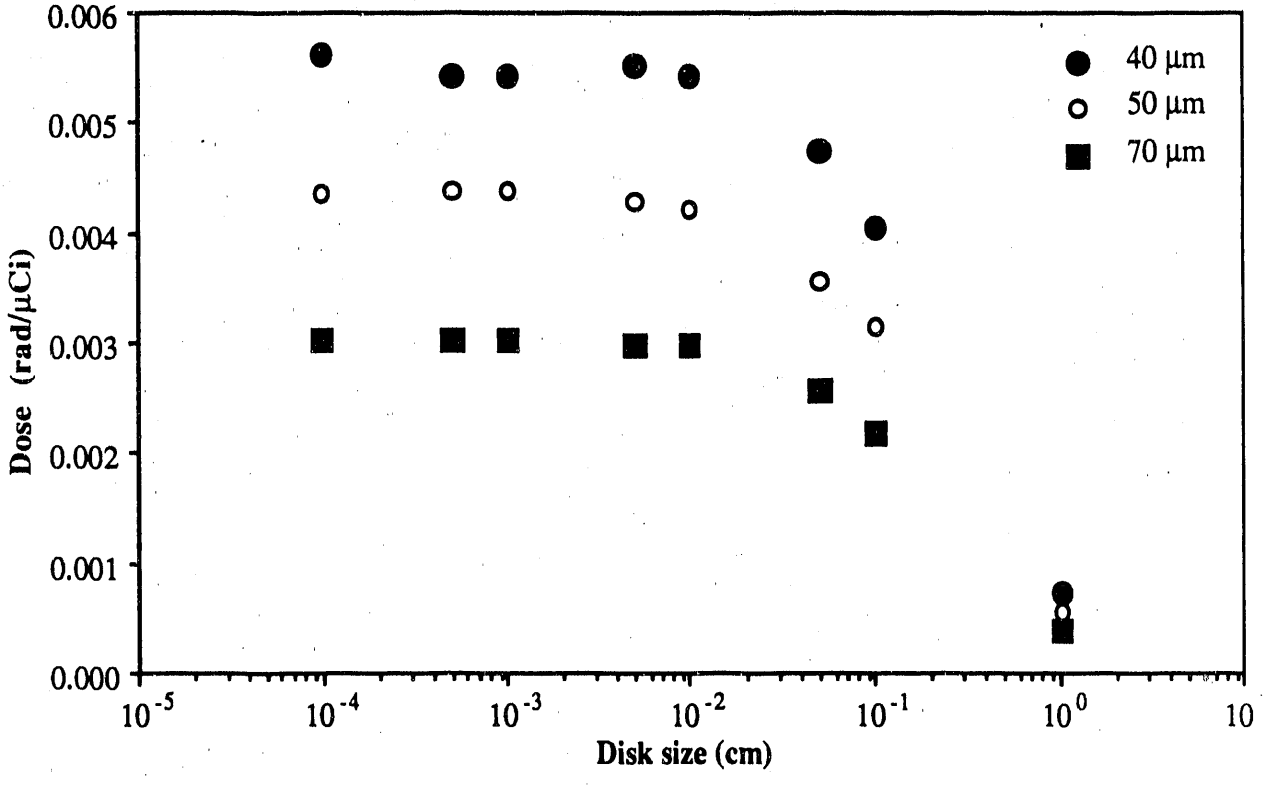

Figure 14. Dose Averaged over 1 cm^2 as a Function of Disk Size for Co-60

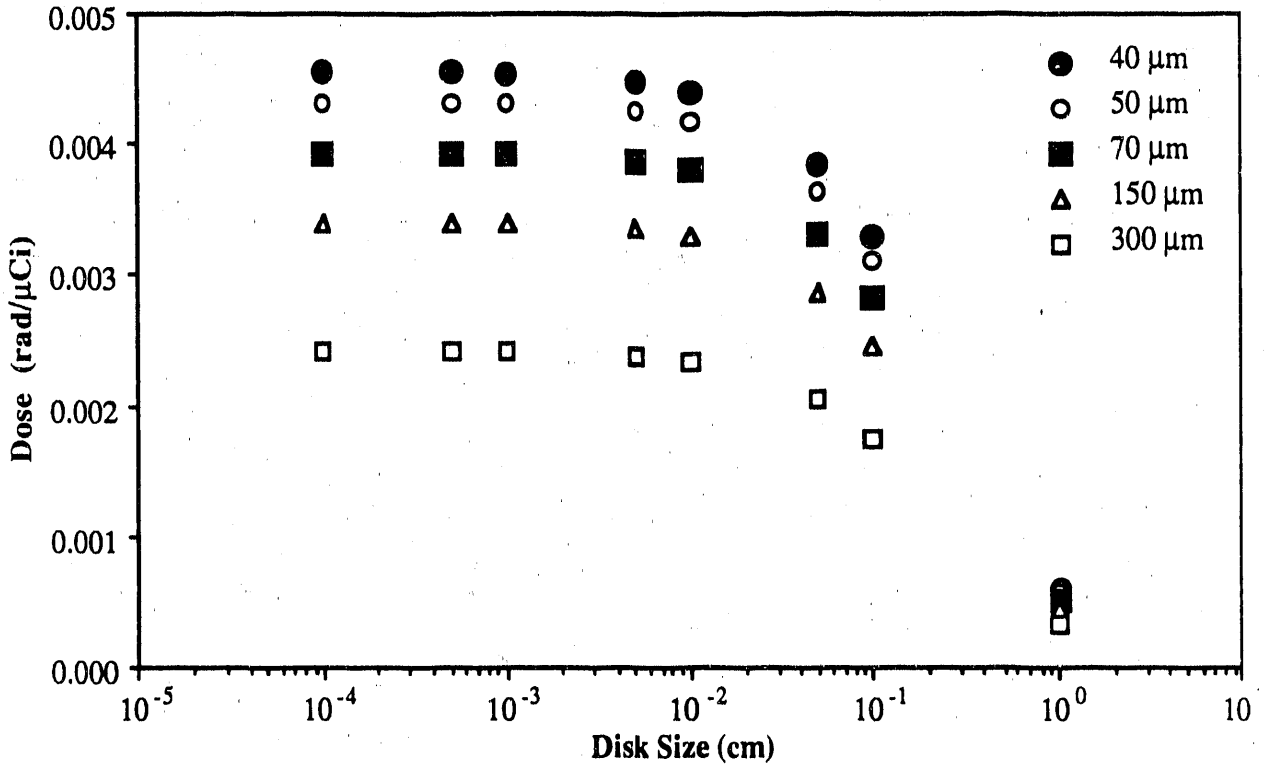

Figure 15. Dose Averaged over 1 cm^2 as a Function of Disk Size for Sr-89

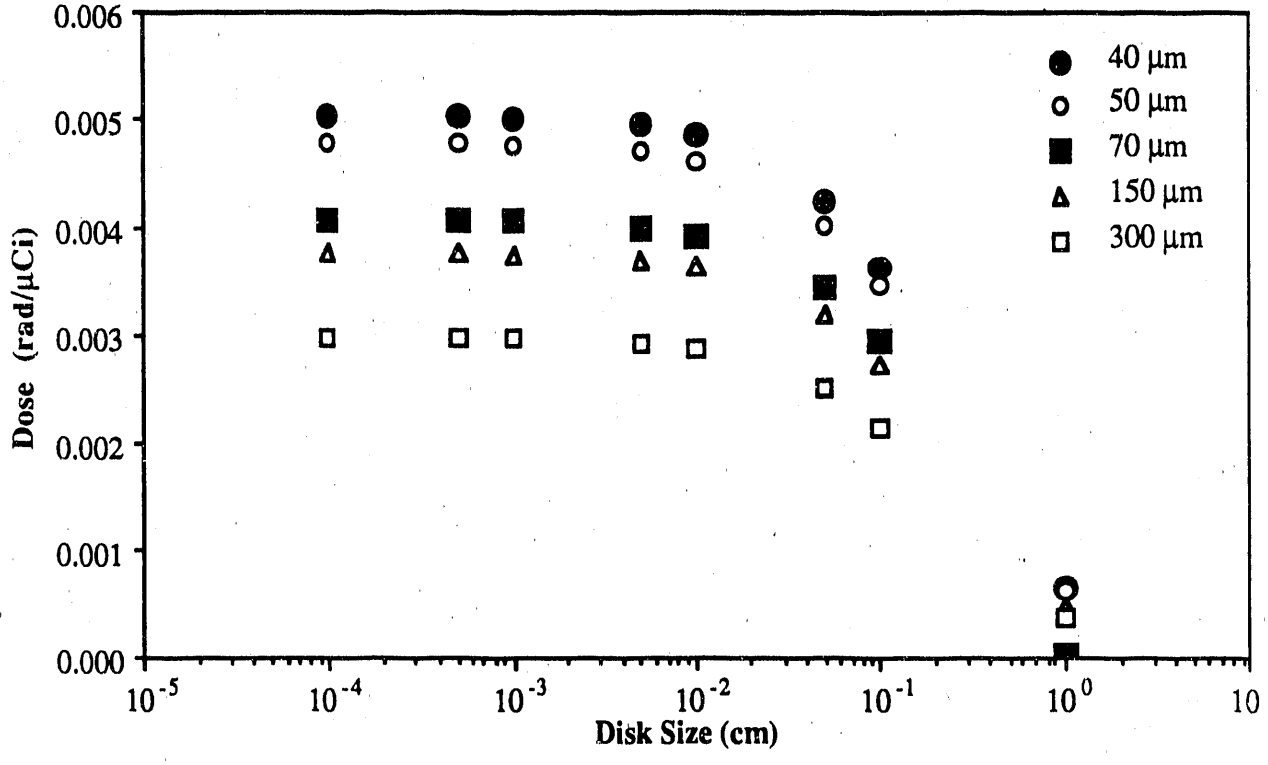

Figure 16. Dose Averaged over 1 cm^2 as a Function of Disk Size for Pr-144

present in a skin dose calculation, the accuracy of the estimate ranges from ±25 to ±50%. At this time, these differences in dose estimations do not warrant alterations in the current regulations and methodologies.

References

Attix, Frank H. Introduction to Radiological Physics and Radiation Dosimetry. New York; John Wiley & Sons; 1986.

Bartlett, T. W. Calculation of Skin Dose from Small Area Beta Sources. Radiation Protection Management. Vol. 4, No. 4, pp. 31-38, 1987.

Berger, M. J. Distribution of Absorbed Dose Around Point Sources of Electrons and Beta Particles in Water and Other Media. Journal of Nuclear Medicine. Vol.12, Supplement No. 5--Nuclear Medicine No. 7, 1971.

Bray, L. G.; Cooper, T. L.; Goldwin, E. M.; Warnock, R.V. Skin Dose Calculations for Fuel Particles. Radiation Protection Management. Vol. 4, No. 5, pp. 25-30; September/October 1987.

International Commission on Radiological Protection. Report of the Task Group on Reference Man. ICRP Publication 23; Oxford: Pergamon Press; 1975.

International Commission on Radiological Protection. Recommendations of the ICRP. ICRP Publication 26; Oxford: Pergamon Press; 1977.

Konishi, E.; Yoshizawa, Y. Estimation of Depth of Basal Cell Layer of Skin for Radiation Protection. Radiation Protection Dosimetry. Vol. 11, No. 1, pp. 29-33, 1985.

Loevinger, R. L.; Japha, E. M.; and Brownell, G. L. Discrete Radioisotope Sources. Radiation Dosimetry. New York: Academic Press; 1956.

National Council on Radiation Protection and Measurements (NCRP). Limit for Exposure to "Hot Particles" on the Skin. NCRP Report No. 106, Bethesda, MD, March 7, 1988.

Traub, R. J.; Reece, W. D.; Scherpelz, R. I.; Sigalla, L. A. Dose Calculation for Contamination of the Skin Using the Computer Code VARSKIN, PNL-5610, NUREG/CR-4418. Battelle Northwest Laboratory; August 1987.

Turner, James E. Atoms, Radiation, and Radiation Protection. New York: Pergamon Press; 1986.

U. S. Nuclear Regulatory Commission. Excessive Skin Exposures Due to Contamination with Hot Particles. I. E. Notice No. 86-23, Washington, DC,1986a.

U. S. Nuclear Regulatory Commission. Standards for Protection against Radiation. U. S. Government Printing Office; Title 10, Chapter 1, Code of Federal Regulations, Part 20, Washington, DC, January 1986b.

U. S. Nuclear Regulatory Commission. Control of Hot Particles Contamination at Nuclear Power Plants. I. E. Notice No. 87-39, Washington, DC, 1987.

Warnock, R. V.; Rigby, W. F.; Goldwin, E. M. Health Physics Problems Resulting from Power Reactor Operations with Failed Fuel. Proceedings of the Health Physics Society 21st midyear topical meeting; 13-17 December 1987; Bal Harbour, Florida.

A LOOK AT GENERAL CAVITY THEORY THROUGH A CODE INCORPORATING MONTE CARLO TECHNIQUES

INTRODUCTION

Measurement of the absorbed dose in a medium exposed to ionizing radiation requires the introduction of a radiation sensitive device into that medium (Burlin, 1968). Usually, this device is composed of a material different from the medium in terms of atomic number and density and is referred to as a "cavity". Because of differences between the two materials, patterns of energy deposition in the medium will differ from those in the cavity. Cavity theory is used to relate the absorbed dose in a cavity to that in the surrounding medium.

A dosimeter responds to the absorbed dose inside its sensitive volume. Usually, the sensitive volume is surrounded by a container of some sort which protects it from the outside elements, including light. When the primary radiation field is composed mostly of indirectly ionizing radiation, this wall also serves as the medium in which the radiation may interact to create the secondary charged particles which reach the sensitive volume. If the wall is at least as thick as the maximum secondary charged-particle range, the response of a dosimeter will be a result only from secondary charged particles originating both in the wall and in the sensitive volume itself. If the wall and the sensitive volume are of the same composition, charged particle equilibrium (CPE) may exist in the sensitive volume (Ogunleye et al., 1980). Charged particle equilibrium being defined as the state in which, for every charged particle of a given type and energy leaving the volume, there is an identical charged particle of the same energy entering (Attix, 1986). When the materials are not the same, however, the dose in the sensitive volume, or cavity, depends on the relative fluence of charged particles originating in the wall. If the dosimeter is small, with respect to the range of the secondary charged particles, the dose to the sensitive volume may be assumed to be caused solely by particles originating in the

wall, and thus the sensitive volume does not perturb the charged particle flux crossing it. The original Bragg - Gray cavity theory, along with modifications by Spencer and Attix, apply to this situation (Spencer et al., 1955). In most cases, however, current dosimeters do not meet the assumptions made in these theories. T.E. Burlin was the first to address the problem of a larger sensitive volume or cavity (Burlin, 1966; Burlin, 1968). The main difference between the Burlin theory and the Bragg et al. theories is the parameter d. This parameter is a weighting factor which eliminates the cavity size restriction and, thus, is a critical variable. This parameter is dimensionless and depends on the depth of penetration in the cavity of the electrons produced in the wall. Burlin assumed the electron attenuation to be exponential. This assumption and the weighting factor, d, were investigated and tested in this research using a Monte Carlo electron transport code.

Cavity theory is used to determine the absorbed dose in a material which differs in composition to that of the dosimeter's sensitive volume. Knowing the absorbed doses in different materials is extremely important. First, the sensitive volume of a dosimeter is not tissue, and does not match it perfectly. This alone is reason enough to test the validity of cavity theory. There are also researchers, engineers, and scientists who have the need to know the absorbed dose in other materials for their own research or applications. Since the only way at present to determine the dose in a different material is to use a dosimeter and relate the measured dose to that within the material, Monte Carlo techniques have been used to simulate the irradiation of various materials. The computer code EGS4 (Nelson et al., 1985, ORNL, 1986) uses Monte Carlo techniques to simulate the randomness of radiation interactions and can be used to transport photons and electrons with great spatial detail in any material or compound. Utilizing this code, the energy deposited, and thus the dose, may be estimated in any material or compound

without using a dosimeter. The goal of this research will be to calculate doses in selected materials including some commonly used dosimeter materials and to compare these results to values given by cavity theory.

In summary, this research will involve the application of modern computer techniques to the study of cavity theory. Although a number of modifications to the original theory have been proposed, this investigation will focus on those modifications suggested by Burlin (Burlin, 1966). The specific objectives of this research are as follows: 1) set up the appropriate geometries inside a suitable Monte Carlo radiation transport code, 2) follow a sufficient number of photon histories through selected wall materials to obtain results with a statistical significance, 3) track energy depositions throughout the cavity and wall, and 4) analyze the results and compare them to published theoretical values.

BACKGROUND

The relation between the absorbed dose deposited in two different media is not a new problem. In 1910, W.H. Bragg qualitatively discussed the problem (Bragg, 1910). However, it wasn't until 1929 that L.H. Gray made quantitative statements concerning cavity ionization theory (Gray, 1929, 1936). He proved that a gas - filled cavity did not perturb the electron spectrum if the cavity was small enough with respect to the range of the electrons. Many investigations have studied the original Bragg - Gray theory and have suggested modifications. The most important of these are those of Spencer and Attix, and Burlin (Spencer and Attix, 1955, Burlin, 1966). The following discussion focusses only on modifications to the theory suggested by Burlin.

T.E. Burlin (1966) is credited with deriving an expression which could account for larger cavity sizes. Most dosimeters are too large and do not comply with the cavity size

restrictions of the earlier theories. A theory relating absorbed dose in a wall to that of a cavity, or dosimeter, of any size allowed for more the accurate estimates of doses in any media. Attix (1986) illustrates the difference in cavity sizes in Fig. 1. In this figure, there is a homogeneous medium w with a uniform γ ray irradiation. All three cavities contain a medium g and are shown as: a) small (applicable for Bragg - Gray, and Spencer - Attix), b) intermediate, and c) large compared to the ranges of the secondary electrons present (Attix, 1986).

The absorbed dose in the small cavity is almost completely delivered by secondary electrons completely crossing the cavity such as e_1. In the intermediate sized cavity, the absorbed dose is partly due to secondary electrons such as e_1, but also from electrons which originate in the cavity and stop in the wall such as e_2, electrons which originate in

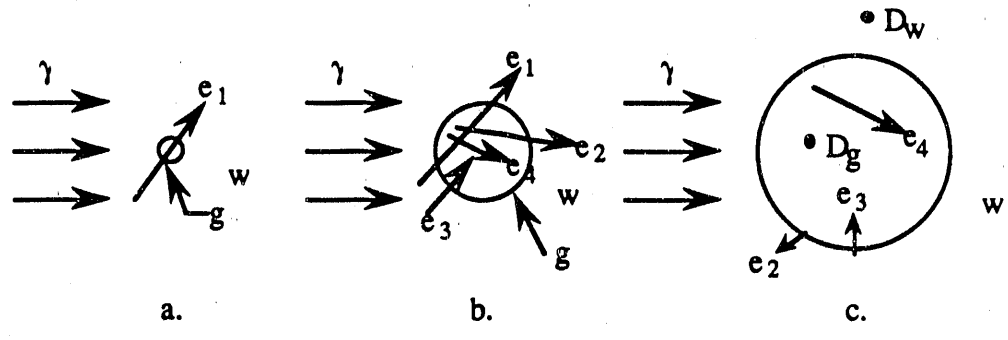

Fig. 1 The cavity - size transition in Burlin theory (Adapted from Attix, 1986).

the wall and stop in the cavity such as e_3, and from electrons which start and stop inside the cavity such as e_4. If the cavity is large, with respect to the range of the secondary electrons, it should be clear that the majority of the absorbed dose would come from

electrons such as e_4 which start and stop inside the cavity. The following list of assumptions made by Burlin in his 1966 paper were assembled by Attix (1986); these assumptions simplify the theory:

1.) The media w and g are homogeneous throughout, but are not necessarily of the same material.

2.) A homogeneous γ-ray field exists everywhere throughout w and g. (This means that no γ-ray attenuation correction is made in the theory for the presence of the cavity.)

3.) Charged-particle equilibrium (CPE) exists at all points in w and g that are farther than the maximum electron range from the cavity boundary.

4.) The equilibrium spectra of secondary electrons generated in w and g are the same.

5.) The fluence of electrons entering from the wall is attenuated exponentially as it passes through the medium g, without changing the spectral distribution.

6.) The fluence of electrons that originate in the cavity builds up to an equilibrium value exponentially as a function of distance into the cavity, according to the same attenuation coefficient β that applies to the incoming electrons.

In its simplest form, the absorbed dose ratio, according to the Burlin theory, may be written as follows:

$$f = \frac{D_g}{D_w} = d\left[\frac{{}_m\bar{S}_g}{{}_m\bar{S}_w}\right] + (1 - d)\left[\frac{(\mu_{en}/\rho)_g}{(\mu_{en}/\rho)_w}\right] \quad , \qquad \text{Eq. 2.11}$$

where:

f = ratio of absorbed dose in the cavity to that in the wall;

D_g = absorbed dose in the cavity;

D_w = absorbed dose in the wall;

d = weighting factor for different cavity sizes;

${}_mS_g$ = average mass collision stopping power for the cavity;

${}_mS_w$ = average mass collision stopping power for the wall;

$(\mu_{en}/\rho)_g$ = average mass energy - absorption coefficient for the cavity;

$(\mu_{en}/\rho)_w$ = average mass energy - absorption coefficient for the wall.

The parameter d is the critical variable in this equation because it eliminates the cavity size restriction. It can be seen that d approaches zero for large cavities and unity for smaller ones. Other studies have investigated different cavity sizes and their effects on dose and have shown limited variation in f (Kearsley, 1984, Horowitz, 1986).

One of the assumptions Burlin made was that the secondary electrons would be attenuated exponentially, and d represents this assumption. He defined d as the mean of Φ_w/Φ_w^e in the cavity as expressed in Eq. 2 (Attix, 1986):

$$d = \frac{\overline{\Phi_w}}{\Phi_w^e} = \frac{\int_0^L \Phi_w^e \, e^{-\beta l} \, dl}{\int_0^L \Phi_w^e \, dl} = \frac{1 - e^{-\beta L}}{\beta L} \quad , \qquad \text{Eq. 2.12}$$

where: l = distance of any point in cavity from wall (cm);

L = mean chord length (cm); and

β = attenuation coefficient (cm^{-1}).

The other parameters have been defined previously. The parameter L may be defined as 4 times the volume divided by its surface area, for convex cavities and diffuse (i.e., isotropic) electron fields (Attix, 1986). The attenuation coefficient, β, was defined by Burlin for air filled cavities as:

$$\beta = \frac{16\,\rho}{(T_{max} - 0.036)^{1.4}} \quad , \qquad \text{Eq. 2.13}$$

where: ρ = air density (g/cm^3);

T_{max}= maximum value of the starting β ray energies (MeV).

In a later paper, Burlin et al. defined β as (Burlin et al., 1969):

$$\exp(-\beta R) = 0.01 \quad , \qquad \text{Eq. 2.14}$$

where R is the range obtained from the continuous slowing down approximation (R_{CSDA}) in $g\text{-}cm^{-2}$. This parameter, β, was modified when detailed experiments were carried out with different materials.

This study focussed exclusively on a cavity the size of a standard TLD chip (Harshaw/Filtrol, 1988), which in Burlin's theory is considered to be a medium cavity. For such a cavity, the parameter d was calculated using the above equation as, d = 0.514. The expression obtained for LiF was (Paliwal, Almond, 1975):

$$\beta = \frac{14}{E_{max}^{1.09}} \quad (cm^2/g) \quad , \qquad \text{Eq. 2.15}$$

where E_{max} is the maximum electron energy in MeV. This expression was obtained by the method of linear regression which was applied to fit the data of E_{max}. It should be noted that even today there is controversy surrounding this parameter (Paliwal and Almond, 1975).

The Burlin theory along with the Bragg - Gray and Spencer - Attix theories all ignore electron scattering. Experiments by Ogunleye et al. (1980) seem to show that the Burlin theory comes very close to approximating the doses in various media. There have been many theories and published papers challenging the Burlin theory and its related parameters. Theories trying to match the data produced by Ogunleye et al. also have been published, but the simplicity of Burlin's theory and its seemingly close approximation of doses in different media warrant further study as to the accuracy of the actual doses.

EGS4 AND CAVITY THEORY

The Monte Carlo code used in this study is called EGS4 (Electron Gamma Shower 4). The EGS4 system of computer codes is a general purpose package for the Monte Carlo simulation of the coupled transport of electrons and photons in an arbitrary geometry for particles with energies above a few keV. The code can be used to follow detailed interactions including; Bremsstrahlung production, positron annihilation, Moliere and Bhabha scattering, continuous energy loss applied to charged particle tracks between discrete interactions, along with pair production, Compton scattering, and the photoelectric effect (ORNL, 1986). Transport of electrons or photons can be simulated

in any element, compound, or mixture. Cross sections for materials of interest are prepared using the data preparation package, PEGS4, which includes cross section tables for elements 1 through 100. The geometry for any given problem is specified by the user - written subroutine HOWFAR. The user scores and outputs information in the user - written subroutine AUSGAB. Input parameters such as cutoff energies, photon energies, and wall thicknesses are read from the main program, MAINEGS4. MAINEGS4 contains a data file called PATCLE, which also contains some user input parameters, such as photon energy, number of histories, and step size. A flow chart of EGS4 may be seen in Fig. 2.

This code was modified to include a thermoluminescent dosimetry (TLD) chip cavity and a surrounding wall as thick as the maximum range of the secondary charged particles. A monoenergetic photon field was introduced on one side of the wall and energy deposition was tracked and recorded throughout the wall and cavity. Fig. 3 shows the geometry used in the EGS4 calculations. This is a cross sectional view, actually the wall completely surrounds the TLD chip cavity shown in the middle of the configuration.

Energy deposition in these regions was divided by the mass of the wall and cavity, respectively, to obtain absorbed doses. The cavity to wall absorbed dose ratio was obtained for four different photon energies ranging from 0.5 MeV to 1.5 MeV and five different materials: aluminum, copper, carbon, lead, and a tissue equivalent (A-150) plastic.

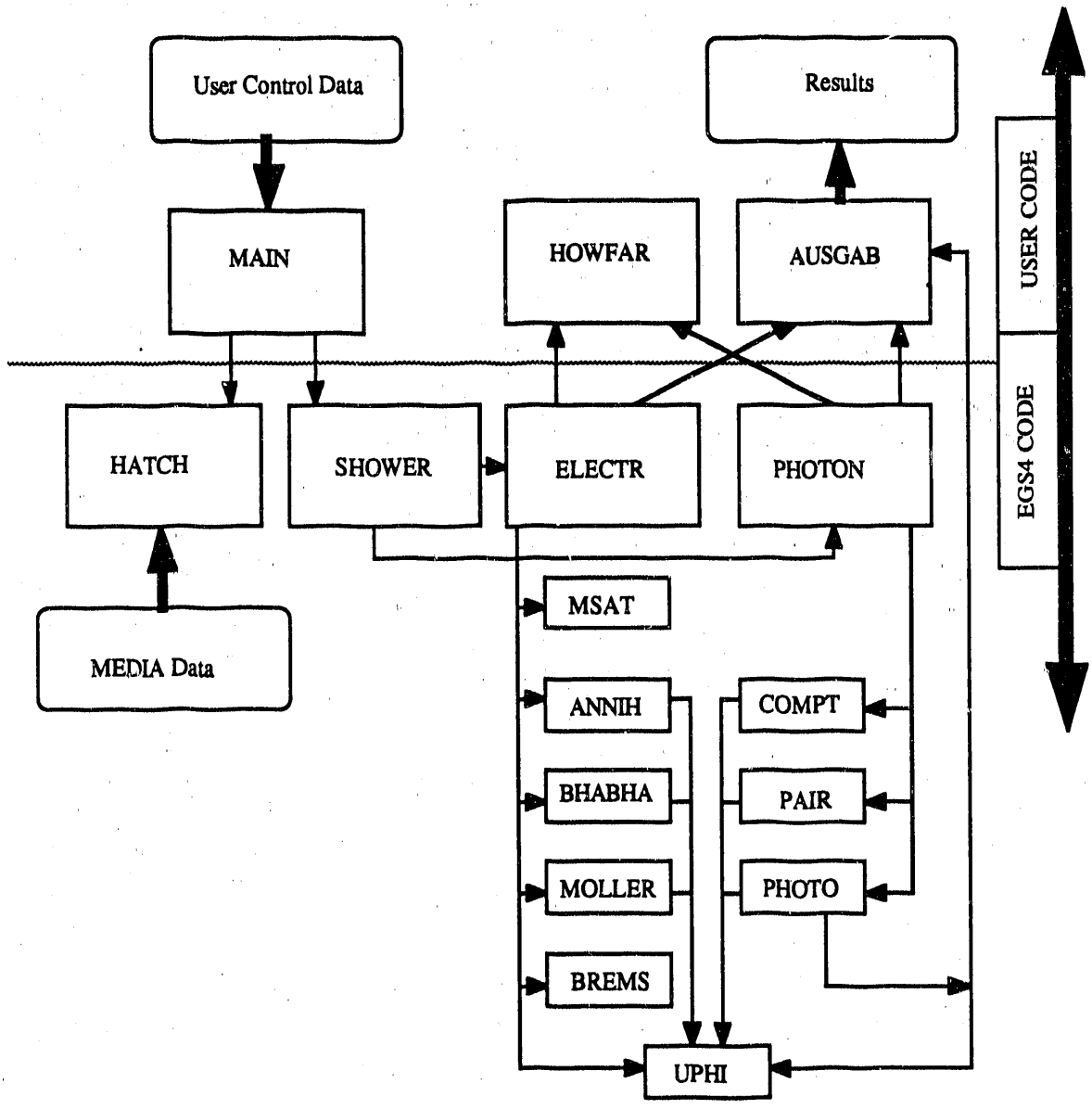

Fig. 2 Flow chart of EGS4 (Adapted from ORNL, 1986)

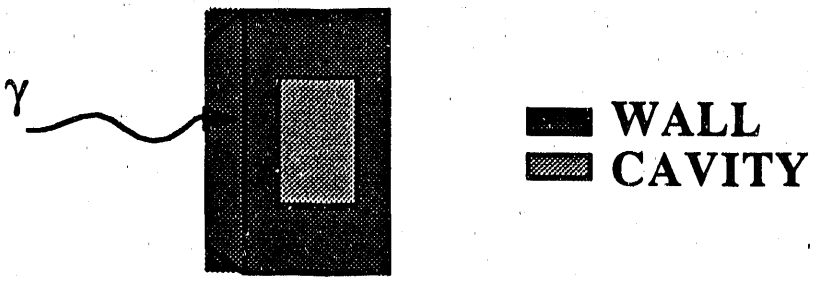

Fig. 3 Cross section of the wall and cavity inside of the Monte Carlo code, EGS4

PROCEDURE

As mentioned above, a cavity and wall were defined in the Monte Carlo code, EGS4, in three dimensions. The parameters for the cavity were the size of a standard Harshaw TLD chip with dimensions 3.1 x 3.1 x 0.89 mm. The cavity was assumed to be composed of LiF, the same composition as the commonly used Harshaw TLD - 100. This cavity was divided into 20 layers and then the layers were divided into 20 x 20 cubes using arrays in the subroutine AUSGAB for purposes of determining the locations of energy deposition. Figure 4 shows a cross section of the geometry inside of EGS4 with the arrays in place. The layers shown were used to determine the average energy deposition in the wall and cavity. The wall boundaries were as thick as the maximum range of the secondary charged particles. A number of steps were taken to arrive at this distance.

First, it was assumed that, at photon energies of ≤ 0.5 MeV, the majority of the interactions were due to the photoelectric effect and thus the maximum kinetic energy, T_{max}, of the resulting electron could be the same as the original photon. For photons ≥ 1 MeV, Compton scattering was assumed to be the main contributor, and thus the

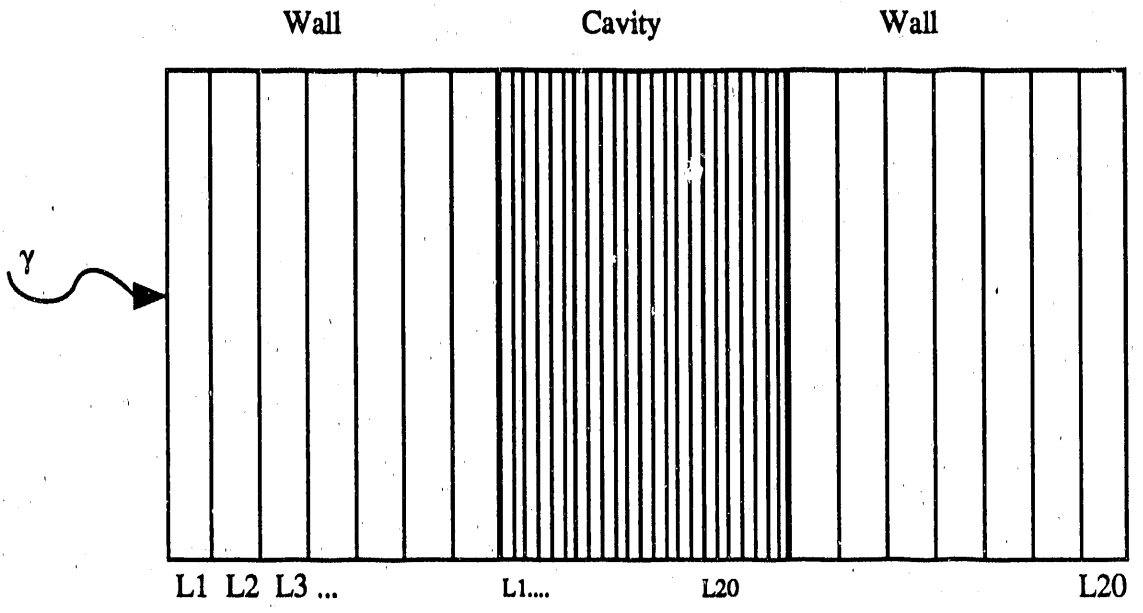

Fig. 4 Two dimensional view of the layers created by geometric arrays used by EGS4.

maximum kinetic energy, T_{max}, of the resulting electron can be obtained from Eq. 3.1 (Attix, 1986):

$$T_{max} = \frac{2\,(h\nu)^2}{2\,h\nu + 0.511\ (MeV)} \quad . \qquad \text{Eq. 3.1}$$

Using T_{max}, the continuous slowing down approximation ranges (R_{CSDA}) were found for the corresponding materials and energies (Attix, 1986). At this point, these ranges were converted into the maximum penetration depth, t_{max}, which is the distance beyond which no particles are observed to penetrate, using values calculated by Spencer (Attix, 1986). For the purposes described here, this distance is the maximum range of the secondary charged particles. Since there were no correction factors available for A-150 plastic, the R_{CSDA} was used in place of t_{max}. Since A-150 has a low effective atomic number, t_{max} is

comparable to R_{CSDA} (Attix, 1986). Table 1 shows the results of the above steps for the energies and materials used in this study. These parameters also were entered into the

Table 1 Maximum Penetration Depth, t_{max}, of Different Materials for Photon Energies 0.5 to 1.5 MeV

(MeV)		t max (cm)				
Photon Energy	T max	Al	C	Cu	Pb	A-150
0.50	0.500	0.0731	0.0902	0.0219	0.0178	0.1757
1.00	0.800	0.1360	0.1694	0.0412	0.0294	0.3300
1.25	1.038	0.1876	0.2352	0.0573	0.0411	0.4066
1.50	1.282	0.2436	0.3034	0.0734	0.0520	0.5915

main program, MAINEGS4, and the surrounding wall, as with the cavity, was described in 20 layers and further by a 20 x 20 per layer array which formed cubes , for precise energy deposition tracking (see Fig. 4).

One hundred thousand (100,000) photon histories were followed in each case to achieve high statistical accuracy. The energy deposited in every cube for all 100,000 photons was printed out along with a layer by layer energy deposition summary at the end of each case. It should be noted that because photons are being used here with relatively small thicknesses, part of the energy was carried through the configuration and escaped without depositing significant amounts of energy. In a real exposure, a similar loss of total energy would occur and, therefore, this result was expected. The absorbed dose is defined as energy deposited per unit mass, so the energy deposited in each region was divided by the product of the cubical dimension, in cm^3, and the respective material density, in g/cm^3, to obtain the absorbed doses (in units of MeV/g).

The resulting values were plotted as a function of thickness to give a "dose profile" through the material representing the wall and the LiF chip (the cavity). These profiles are shown in Figures 5 - 9 for monoenergetic photons with initial energy of 1.25 MeV. In all cases, the cavity is represented by a standard LiF TLD chip and the wall materials are aluminum, carbon, A-150 tissue equivalent plastic, copper, and lead, respectively. In these p s, it is assumed that the photons are incident on the wall from the left side of the figure. These figures are typical for all four photon energies investigated. Each figure was normalized to unity based on the highest dose in the front wall. That is, the highest dose , in the front wall, was obtianed and all other values in the dose profile were normalized to this value. Calculated values are tabulated for 0.5, 1.0, 1.25, and 1.5 MeV monoenergetic photons, for all four wall materials, in Appendix A.

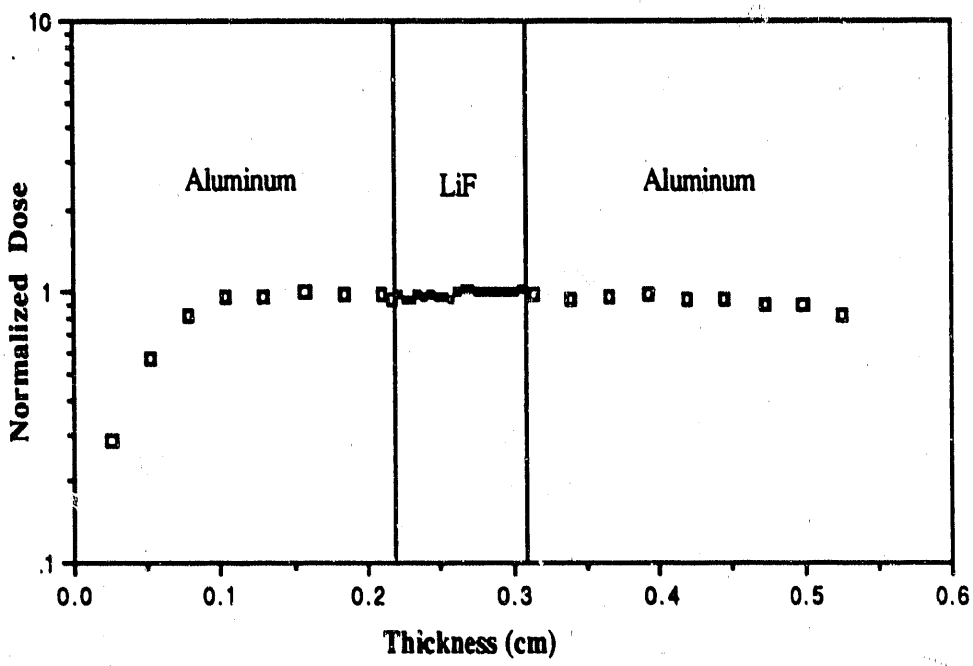

Fig. 5 Dose profile, or energy depositon profile, in an Al - LiF - Al configuration with the photons entering from the left side of the figure (1.25 MeV photons)

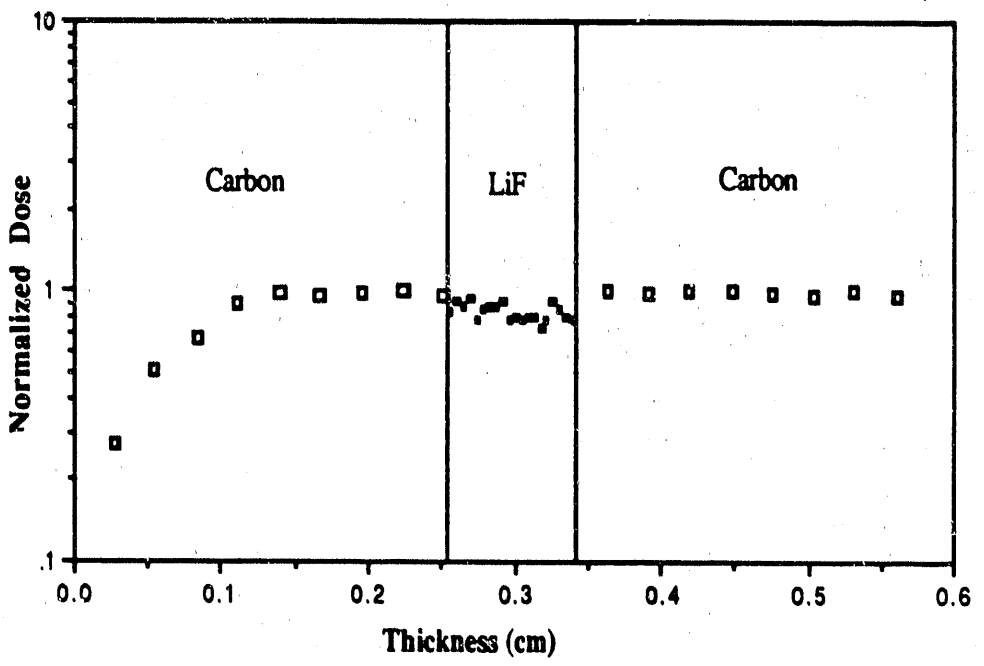

Fig. 6 Dose profile, or energy depositon profile, in a C - LiF - C configuration with the photons entering from the left side of the figure (1.25 MeV photons)

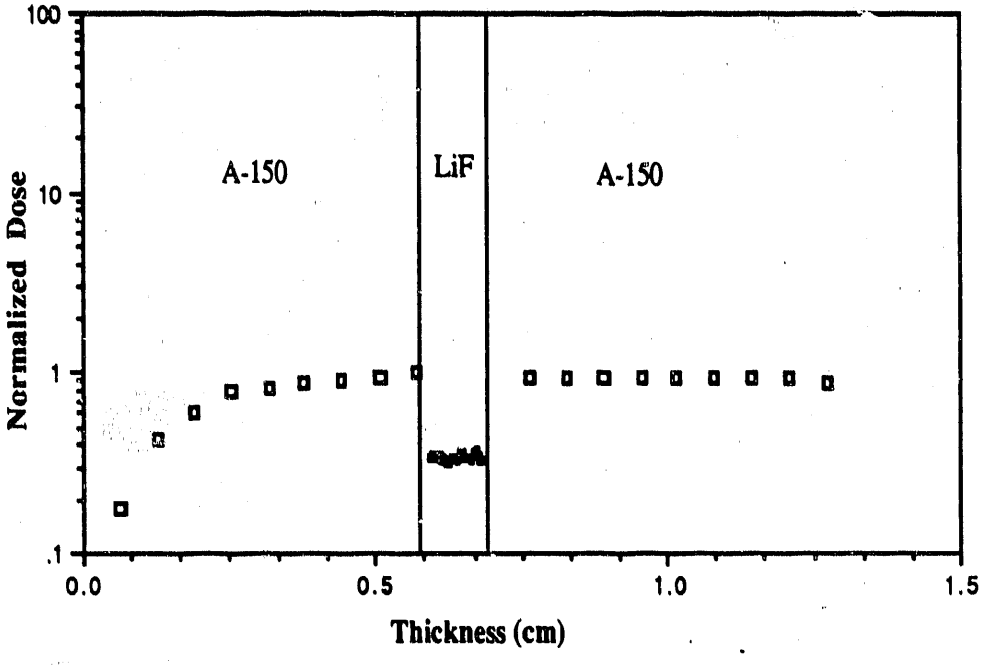

Fig. 7 Dose profile, or energy depositon profile, in an A-150 - LiF - A-150 configuration with the photons entering from the left side of the figure (1.25 MeV photons)

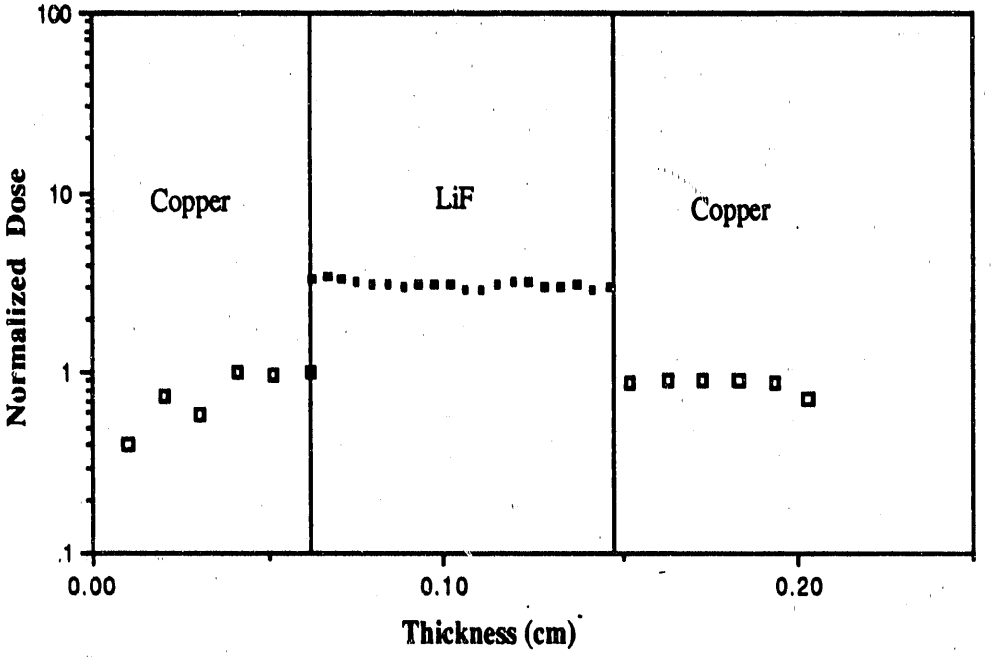

Fig. 8 Dose profile, or energy depositon profile, in a Cu - LiF - Cu configuration with the photons entering from the left side of the figure (1.25 MeV photons)

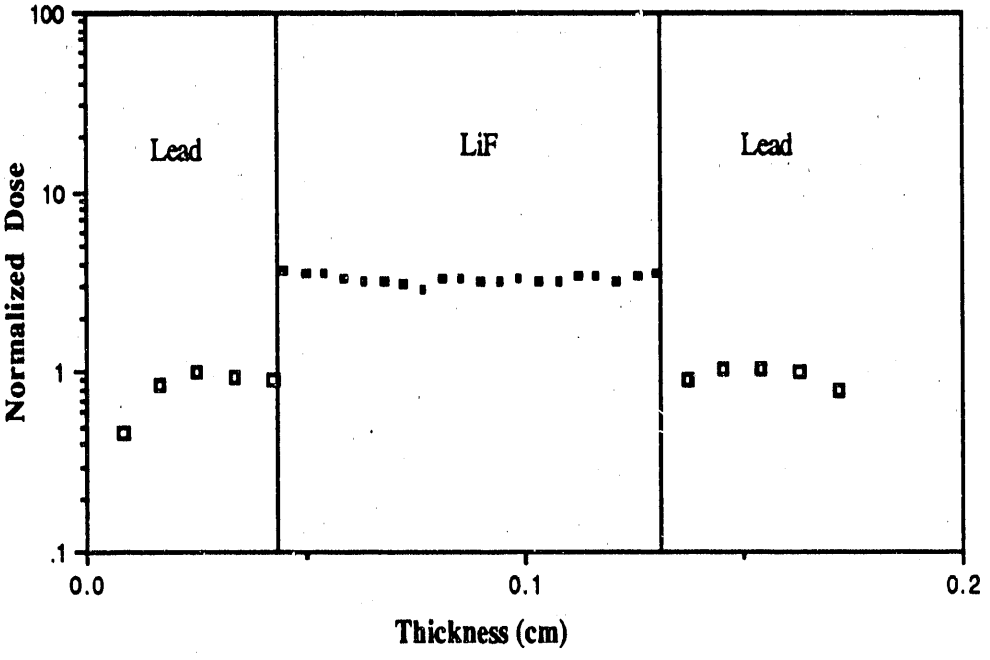

Fig. 9 Dose profile, or energy depositon profile, in a Pb - LiF - Pb configuration with the photons entering from the left side of the figure (1.25 MeV photons)

RESULTS

The Monte Carlo results were used to calculate values of f as defined in equation 1. These results were compared to theorteical values of f which were calculated as part of this investigation.. First, equation 2 was used to calculate the parameter d. In this calculation values of the parameters L and β were needed. For convex cavities and isotropic electron fields, the mean chord length, L, is equal to 4 times the volume divided by the surface area of the cavity. Values of β were be obtained using equation 5. Values of the mass collision stopping powers and the mass energy-absorption coefficients were obtained by interpolation from tables for the appropriate energies (Attix, 1986). A comparison of the Monte Carlo and theoretical values of f is shown in Table 1.

Table 1 Quantitative Comparison of f Values for various media; Monte Carlo vs. Theory

	f Values									
Photon	Aluminum		Carbon		Copper		Lead		A - 150	
E (MeV)	Theory	M.C.	Theory	M.C.	Theory	M.C.	Theory	M.C.	Theory	M.C.
0.50	0.984	0.96	0.926	0.87	1.00	3.3	0.856	3.5	0.834	0.48
1.00	0.987	0.99	0.923	0.93	1.08	3.3	1.270	3.5	0.823	0.56
1.25	0.990	0.99	0.923	0.92	1.09	3.1	1.280	3.5	0.826	0.66
1.50	0.992	0.99	0.924	0.89	1.11	3.3	1.280	3.6	0.826	0.82

The results in the table above show some agreement with the predicted values, e.g., the values for aluminum correlate with theory. The slight variations fall well within the range for possible statistical differences. For the low Z materials, however, it was observed that, at low energies, Monte Carlo values had a slightly wider variation on the low side; for A - 150 plastic this variation is exaggerated. The f-values for carbon also

show some agreement with the theoretical calculations. These materials have relatively low Z numbers and densities. However, for higher density and higher Z materails, the Monte Carlo values are significantly higher (about a factor of 3, for copper) than the predicted values. Similar statements can be made for the lead wall. These differences are believed to be caused by the much higher backscatter from the wall into the cavity associated with the denser, heavier elements. Figure 10 shows the backscatter of Co - 60 photons in an Al - LiF - Al configuration. This is represented by the small diagonal line at the bottom, right portion of the LiF cavity. Compare this to the much larger backscatter curve in Fig. 11, which represents a Pb - LiF - Pb configuration. This extra energy deposition would significantly increase the absorbed dose in the cavity, thus making the f value higher.

CONCLUSIONS

The goals of this project were to produce a Monte Carlo computer code with suitable geometries, run a sufficient number of photon histories for statistical significance, track energy depositions throughout the cavity and wall, and analyze the results and compare to theory. The first of these goals was accomplished by modifying an existing code, called EGS4. This code was developed at the Stanford Linear Accelerator Center (SLAC) and incorporates Monte Carlo techniques to transport and track photons and electrons. The code can be used to follow detailed photon and electron interactions, including Bremsstrahlung production, positron annihilation, Moliere multiple scattering, Moller ($e^- e^-$) and Bhabha ($e^+ e^+$) scattering, continuous energy loss applied to charged particle tracks between discrete interactions, along with pair production, Compton and Rayleigh

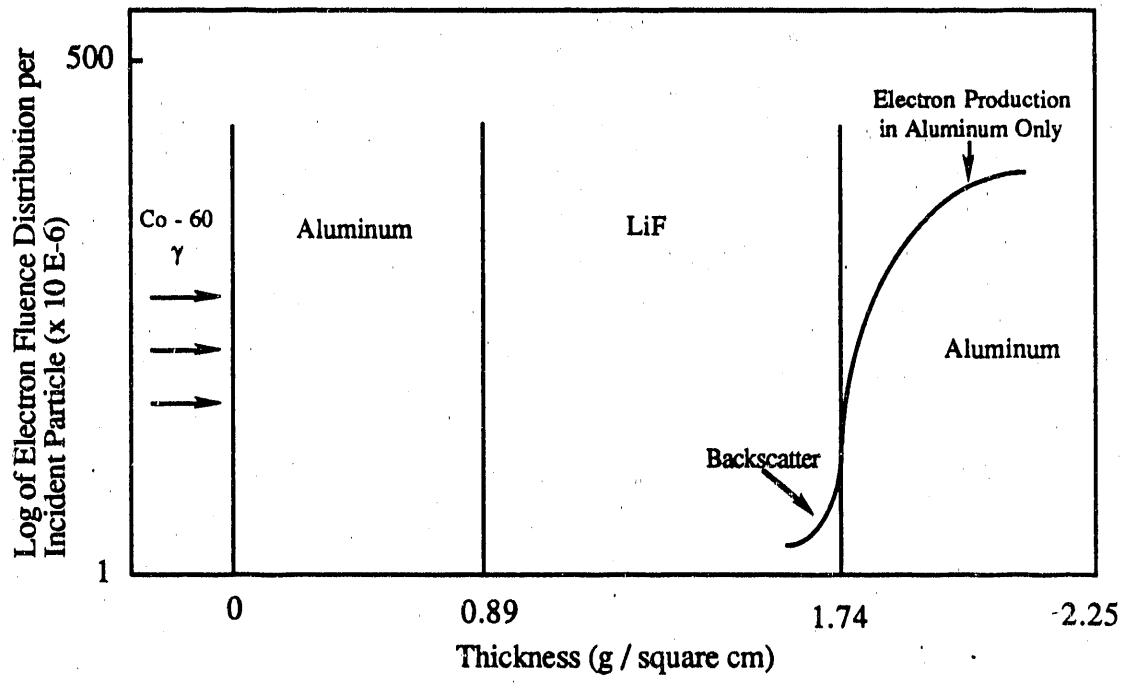

Fig. 10 Representation of backscatter in an Al - LiF - Al configuration (Adapted from Horowitz, 1986).

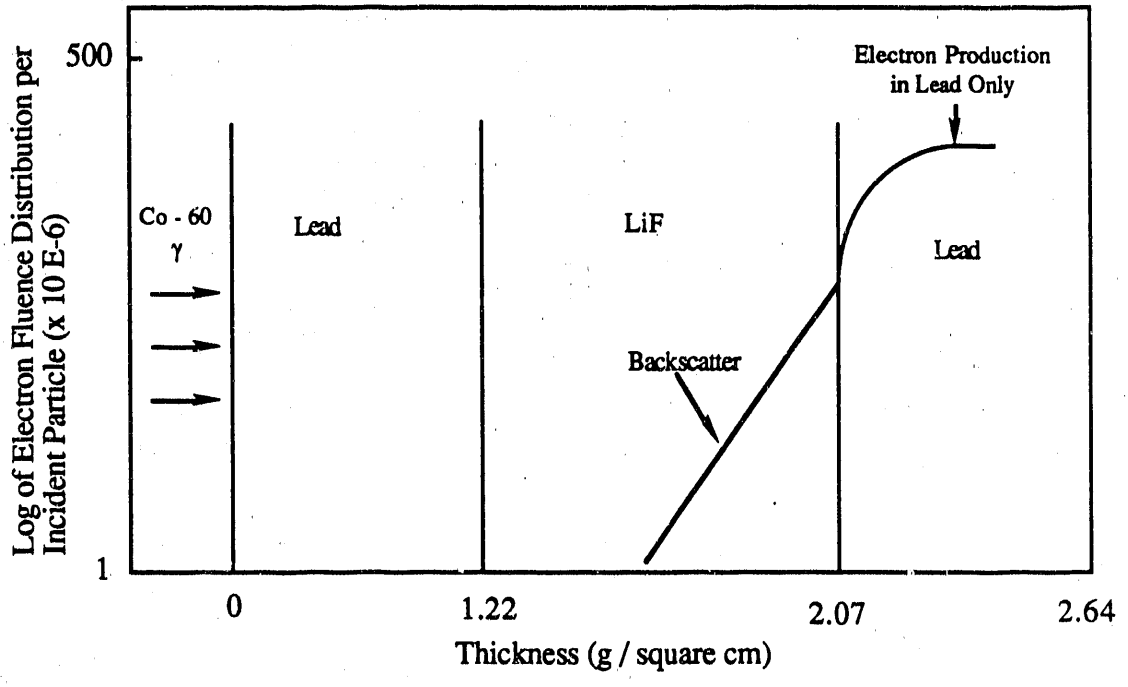

Fig. 11 Representation of backscatter in a Pb - LiF - Pb configuration (Adapted from Horowitz, 1986).

scattering, and the photoelectric effect. A subroutine, HOWFAR, was written which defined a three-dimensional cube and a three-dimensional cavity inside of the cube. The cavity was the size of a standard TLD chip and was defined as LiF. The cube, or wall, was redefined for five different materials including aluminum, carbon, A - 150 tissue equivalent plastic, copper, and lead. The wall thickness for each material was defined as the maximum secondary charged particle range for reasons explained in the text.

One hundred thousand photon histories were run for each case ensuring good statistics. These photons were tracked using a user written subroutine called AUSGAB. In this subroutine, the geometries, wall and cavity, were both broken down into 20 x 20 x 20 arrays. This was done for precise tracking of the energy deposition in both regions. The energy depositions were printed out for each material over a range of energies from 0.5 to 1.5 MeV.

These energy depositions were divided by the respective masses to obtain doses which could be compared to the theoretical absorbed dose values. The absorbed doses were actually compared to theory by using a ratio of cavity dose to wall dose represented by the parameter f. It was found that for low Z materials, cavity theory yielded reasonably accurate doses, however, for higher Z materials, cavity theory overestimated the absorbed doses. By using the results found here, other studies could be initiated defining the relationship between severely mismatched media.

The Burlin theory, as mentioned earlier, does not take into consideration any electron scattering. This as yet unknown exponential backscatter coefficient, b(t), will have to be explored for better interpretations of cavity doses (Horowitz et al., 1986). The Burlin expression should be considered reasonably accurate only in the case of moderately mismatched cavity/medium interfaces where backscattering and other interface effects

play a relatively insignificant role (Horowitz et al., 1986).

The much higher backscatter in the heavier elements and the lack of consideration for this factor in the theory, would seem to lend confidence to the hypothesis proposed herein. That is, the reason for the significant differences in f values for heavy elements is due to backscatter. This, however, has not been proven and deserves further study. It is the opinion of this author that Burlin cavity theory, and its subsequent modifications, be used with caution when estimating a dose in a material with a severely different media than that of the sensitive volume inside the dosimeter. In light of the results and probable explanation found and described in this report, it is felt that this study has been a complete success which will prompt new investigations leading to the development of a system which will interpret doses in any media for any energy with minimal error.

REFERENCES

Attix, F. H. Introduction to radiological physics and radiation dosimetry. John Wiley & Sons, Inc. ; 1986.

Bragg, W. H. Studies in Radioactivity. New York: MacMillian; 1910.

Burlin, T.E. A general theory of cavity ionisation. Br. J. Radiol. 39: 727; 1966.

Burlin, T.E. Cavity - chamber theory. In: Attix, F.H.; Roesch, W.C., ed. Radiation dosimetry. New York and London: Academic Press; 1968.

Burlin, T.E.; Chan, F.K. The energy - size dependence of the response of thermoluminescent dosimeters to photon irradiation. Health Phys. 18: 325; 1969.

Gray, L.H. The absorption of penetrating radiation. Proc. Roy. Soc. A122: 647; 1929.

Gray, L.H. An ionization method for the absolute measurement of γ - ray energy. Proc. Roy. Soc. A156: 578; 1936.

Harshaw / Filtrol. Performance specifications. Harshaw / Filtrol Partnership. Solon, Ohio; 1988.

Horowitz, Y.S.; Moscovitch, M.; Mack J.M.; Hsu H.; Kearsley E. Incorporation of Monte Carlo electron interface studies into photon general cavity theory. Nuclear Science and Engineering. 94: 233; 1986.

Kearsley, E. A new general cavity theory. Phys. Med. Biol. 29: 1179; 1984.

Nelson, W.R.; Hirayama, H.; Rogers, D. W. O. The EGS4 code system. Stanford Linear Accelerator Center, Report 265; 1985.

Oak Ridge National Laboratory, EGS4 A code system for the Monte Carlo simulation of electromagnetic cascade showers. Stanford Linear Accelerator Center. RSIC Computer Code Collection, CCC - 331; 1986.

Ogunleye, O.T.; Attix, F.H.; Paliwal, B.R. Comparison of Burlin cavity theory with LiF TLD measurements for cobalt - 60 gamma rays. Phys. Med. Biol. 25: 203; 1980.

Paliwal, B.R.; Almond, P.R. Applications of cavity theories for electrons to LiF dosemeters. Phys. Med. Biol. 20: 547; 1975.

Spencer, L.V.; Attix, F.H. A theory of cavity ionization. Radiation Research. 3: 239; 1955.

APPENDIX A

DOSE PROFILES FOR MONOENERGETIC PHOTONS

ALUMINUM:

0.5 MeV:

Wall Layer	Energy Deposited (MeV)	Cavity Layer	Energy Deposited (MeV)
1	22.00	1	16.87
2	45.65	2	17.43
3	51.86	3	15.94
4	49.23	4	13.28
5	42.42	5	15.44
6	44.62	6	16.71
7	9.44	7	17.27
8	0.07	8	16.42
9	0.02	9	17.99
10	0.25	10	19.81
11	0.16	11	16.44
12	0.19	12	16.76
13	0.17	13	17.07
14	8.90	14	16.96
15	44.14	15	16.92
16	42.61	16	15.72
17	41.93	17	14.44
18	43.85	18	15.88
19	43.52	19	14.57
20	41.78	20	16.33

1 MeV:

1	33.47	1	32.79
2	71.00	2	28.90
3	96.66	3	27.93
4	112.04	4	31.41
5	115.08	5	30.36
6	119.20	6	33.12
7	132.64	7	33.66
8	69.56	8	34.44
9	0.57	9	30.39
10	0.53	10	33.92
11	0.42	11	34.37
12	0.88	12	31.40
13	65.77	13	33.39
14	123.62	14	29.29
15	121.11	15	29.22
16	125.52	16	30.09
17	130.10	17	31.50
18	125.29	18	31.88
19	120.90	19	30.63
20	97.21	20	30.98

1.25 MeV:				
	1	47.46	1	41.24
	2	102.15	2	39.14
	3	152.08	3	39.59
	4	177.94	4	36.21
	5	197.60	5	38.32
	6	206.19	6	38.47
	7	202.18	7	40.51
	8	209.55	8	39.42
	9	16.89	9	35.96
	10	0.97	10	37.91
	11	1.79	11	36.68
	12	16.50	12	37.39
	13	191.03	13	35.07
	14	184.60	14	34.44
	15	188.30	15	35.96
	16	208.19	16	36.13
	17	199.03	17	36.28
	18	196.75	18	36.98
	19	188.12	19	36.66
	20	152.74	20	36.72
1.5 MeV:				
	1	57.81	1	43.23
	2	140.49	2	42.73
	3	206.25	3	43.82
	4	249.27	4	42.96
	5	286.60	5	45.67
	6	293.55	6	44.84
	7	294.14	7	43.45
	8	276.55	8	41.67
	9	128.93	9	41.71
	10	3.21	10	42.28
	11	3.68	11	40.84
	12	137.68	12	42.11
	13	290.95	13	41.59
	14	273.23	14	40.44
	15	286.51	15	40.70
	16	278.26	16	40.47
	17	253.24	17	45.61
	18	253.48	18	41.66
	19	247.91	19	42.68
	20	234.70	20	44.71

CARBON

0.5 MeV:

1	21.58	1	13.91
2	39.82	2	13.58
3	42.16	3	16.39
4	43.91	4	17.17
5	48.65	5	15.32
6	47.03	6	15.00
7	34.46	7	15.45
8	0.10	8	15.60
9	0.08	9	14.17
10	0.06	10	13.71
11	0.21	11	14.54
12	0.29	12	14.60
13	0.44	13	15.76
14	29.92	14	15.09
15	41.89	15	14.74
16	38.86	16	15.51
17	42.26	17	15.51
18	44.76	18	15.43
19	43.64	19	13.84
20	42.31	20	12.48

1 MeV:

1	41.87	1	28.26
2	76.34	2	29.70
3	104.26	3	26.30
4	128.87	4	25.96
5	126.25	5	25.40
6	133.29	6	30.47
7	134.14	7	28.35
8	123.90	8	28.29
9	0.88	9	30.03
10	0.18	10	30.88
11	0.66	11	29.64
12	1.52	12	29.50
13	123.84	13	29.12
14	138.31	14	30.12
15	134.62	15	27.62
16	131.78	16	28.39
17	138.45	17	28.44
18	133.27	18	26.56
19	127.54	19	26.90
20	111.16	20	25.15

1.25 MeV:				
	1	56.28	1	32.00
	2	106.88	2	35.04
	3	139.87	3	33.90
	4	189.89	4	35.84
	5	207.99	5	30.43
	6	203.00	6	33.37
	7	204.87	7	33.49
	8	208.65	8	34.13
	9	83.12	9	35.27
	10	1.88	10	29.98
	11	2.26	11	30.71
	12	93.48	12	30.15
	13	211.32	13	30.54
	14	205.10	14	31.20
	15	212.01	15	28.04
	16	213.51	16	30.08
	17	205.74	17	34.84
	18	203.31	18	32.67
	19	211.45	19	30.93
	20	203.55	20	30.02
1.5 MeV:				
	1	73.94	1	39.15
	2	147.26	2	37.08
	3	201.35	3	36.46
	4	258.69	4	36.54
	5	268.21	5	35.57
	6	300.07	6	36.38
	7	298.27	7	33.92
	8	295.06	8	32.08
	9	216.81	9	38.47
	10	3.38	10	35.57
	11	4.22	11	37.60
	12	205.50	12	33.44
	13	279.70	13	35.80
	14	317.73	14	32.91
	15	298.71	15	38.04
	16	280.60	16	34.03
	17	285.09	17	35.08
	18	287.79	18	32.27
	19	294.72	19	32.00
	20	271.34	20	37.95

A - 150:

0.5 MeV:

1	16.31	1	7.75
2	31.47	2	7.74
3	35.53	3	9.07
4	41.88	4	8.12
5	38.71	5	7.69
6	42.53	6	8.67
7	45.66	7	7.83
8	39.57	8	7.48
9	0.23	9	8.58
10	0.35	10	9.12
11	0.37	11	8.17
12	0.09	12	7.89
13	39.02	13	7.62
14	41.08	14	7.46
15	39.34	15	7.16
16	40.30	16	7.68
17	38.75	17	8.34
18	37.66	18	9.11
19	41.33	19	9.02
20	41.22	20	8.26

1 MeV:

1	22.64	1	14.10
2	62.66	2	13.19
3	87.43	3	14.17
4	111.75	4	12.69
5	116.34	5	14.24
6	119.95	6	13.41
7	115.35	7	13.85
8	122.84	8	14.47
9	98.43	9	14.69
10	1.97	10	13.92
11	1.97	11	15.15
12	105.54	12	14.40
13	128.16	13	15.70
14	121.90	14	14.94
15	123.90	15	14.66
16	118.86	16	15.65
17	126.82	17	14.74
18	122.56	18	14.59
19	125.19	19	14.51
20	127.28	20	14.89

1.25 MeV:

1	33.07	1	17.89
2	87.27	2	18.81
3	126.16	3	18.44
4	147.66	4	19.31
5	164.49	5	17.96
6	182.61	6	18.93
7	179.50	7	17.92
8	185.87	8	17.73
9	188.07	9	16.52
10	13.88	10	18.78
11	12.99	11	16.66
12	185.15	12	16.58
13	177.42	13	18.64
14	187.20	14	17.30
15	186.73	15	17.50
16	192.19	16	18.47
17	180.45	17	16.50
18	187.65	18	17.01
19	179.52	19	16.87
20	161.74	20	17.64

1.5 Mev:

1	55.53	1	17.39
2	131.33	2	17.67
3	185.13	3	16.97
4	241.98	4	17.76
5	256.20	5	16.76
6	273.23	6	17.28
7	285.40	7	16.65
8	292.74	8	15.93
9	307.26	9	16.98
10	115.70	10	17.34
11	121.94	11	16.58
12	288.73	12	17.88
13	289.21	13	18.55
14	295.37	14	16.95
15	290.92	15	16.82
16	295.01	16	16.73
17	287.91	17	18.41
18	287.82	18	19.23
19	292.90	19	17.75
20	273.56	20	16.53

COPPER:

0.5 MeV:

	1	66.35	1	54.80
	2	87.63	2	58.85
	3	86.89	3	57.68
	4	27.32	4	56.92
	5	0.50	5	60.07
	6	0.27	6	57.33
	7	0.18	7	60.17
	8	0.34	8	55.62
	9	0.32	9	59.50
	10	0.22	10	58.41
	11	0.24	11	60.13
	12	0.32	12	60.37
	13	0.45	13	60.78
	14	0.58	14	58.39
	15	0.19	15	55.65
	16	0.52	16	60.66
	17	25.16	17	56.91
	18	89.70	18	54.53
	19	95.41	19	56.82
	20	86.53	20	54.98

1 MeV:

	1	91.29	1	99.86
	2	169.94	2	104.60
	3	182.24	3	103.18
	4	196.30	4	98.80
	5	170.79	5	95.50
	6	0.20	6	100.62
	7	0.77	7	108.72
	8	1.07	8	100.74
	9	0.22	9	98.62
	10	0.39	10	104.78
	11	0.94	11	102.40
	12	0.69	12	99.49
	13	0.58	13	108.75
	14	1.19	14	110.44
	15	1.00	15	105.79
	16	164.43	16	101.10
	17	197.60	17	109.68
	18	198.77	18	108.00
	19	191.50	19	103.70
	20	166.66	20	98.19

1.25 MeV:

1	119.28	1	129.78
2	225.64	2	133.29
3	265.70	3	129.82
4	297.80	4	122.13
5	294.10	5	120.63
6	187.11	6	117.68
7	0.97	7	116.93
8	1.60	8	120.46
9	0.70	9	120.19
10	1.32	10	118.19
11	0.76	11	113.39
12	0.90	12	111.27
13	1.11	13	119.01
14	2.27	14	123.67
15	166.89	15	124.09
16	273.49	16	113.63
17	275.72	17	117.10
18	274.61	18	118.19
19	266.52	19	113.12
20	212.00	20	117.29

1.5 MeV:

1	132.25	1	143.70
2	279.47	2	139.59
3	347.01	3	143.49
4	375.07	4	136.01
5	370.62	5	132.47
6	377.63	6	145.48
7	87.12	7	141.58
8	1.80	8	143.52
9	1.35	9	141.80
10	1.68	10	139.98
11	2.21	11	135.75
12	1.71	12	141.72
13	3.07	13	127.13
14	74.66	14	129.38
15	359.21	15	126.86
16	373.27	16	142.85
17	385.30	17	139.61
18	350.73	18	146.12
19	333.66	19	139.78
20	298.84	20	130.26

LEAD:

0.5 MeV:

1	298.67	1	192.78
2	401.66	2	145.72
3	340.86	3	153.12
4	1.05	4	172.39
5	0.96	5	196.05
6	0.61	6	218.28
7	1.40	7	230.61
8	1.40	8	249.24
9	0.19	9	260.31
10	0.34	10	269.47
11	0.81	11	269.37
12	0.92	12	264.41
13	0.88	13	274.64
14	1.34	14	261.06
15	1.73	15	253.04
16	2.26	16	263.59
17	0.85	17	261.56
18	415.36	18	261.51
19	502.58	19	258.48
20	410.28	20	271.38

1 MeV:

1	193.92	1	190.04
2	295.58	2	177.50
3	326.14	3	153.10
4	325.37	4	164.56
5	3.73	5	149.73
6	1.98	6	136.92
7	2.41	7	137.41
8	1.91	8	149.74
9	1.57	9	156.76
10	1.81	10	154.15
11	1.64	11	160.38
12	3.14	12	168.59
13	1.25	13	154.52
14	0.81	14	161.77
15	1.89	15	165.55
16	2.23	16	174.12
17	349.31	17	176.32
18	410.67	18	181.15
19	411.85	19	186.44
20	320.25	20	186.21

1.25 MeV:				
	1	194.32	1	183.86
	2	350.98	2	180.16
	3	415.89	3	178.84
	4	394.08	4	168.05
	5	299.83	5	163.67
	6	3.82	6	163.95
	7	2.91	7	154.75
	8	4.89	8	148.17
	9	3.40	9	164.94
	10	3.65	10	166.02
	11	3.91	11	162.45
	12	6.00	12	161.04
	13	4.08	13	167.21
	14	4.13	14	163.38
	15	2.97	15	160.60
	16	305.90	16	175.14
	17	437.64	17	170.97
	18	435.57	18	163.08
	19	415.55	19	172.00
	20	334.52	20	178.14
1.5 MeV:				
	1	220.65	1	211.67
	2	425.32	2	206.26
	3	484.18	3	197.98
	4	490.87	4	186.24
	5	487.50	5	168.41
	6	186.01	6	160.41
	7	5.21	7	165.36
	8	5.51	8	175.75
	9	6.17	9	168.82
	10	4.69	10	183.67
	11	6.62	11	204.51
	12	8.39	12	202.21
	13	7.71	13	197.94
	14	5.36	14	198.91
	15	167.89	15	185.87
	16	435.53	16	194.87
	17	484.81	17	187.34
	18	499.08	18	198.09
	19	522.47	19	182.49
	20	371.89	20	177.44

Small - Scale Dosimetry Calculation
for
Internally Deposited Radionuclides

INTRODUCTION

Electron radiations, administrated both internally and externally, have become increasingly popular for use in radiation treatment of cancer. Beta emitting nuclides are often used in medicine for therapeutic purpose. The nuclides can be injected into a patient in the form of labeled compounds or can be used as applicators. Uses of electrons or beta-emitting radionuclides is preferred because these radiations exhibit a rapid dose fall-off distal to the treatment volume, thus providing protection to vital healthy tissue. The delivery of radioactive materials to tumor sites using radiolabeled monoclonal antibodies is currently being considered for the treatment of malignant tumors. Beta-emitting radioisotopes can now be attached to proteins that can, with great specificity, bind to tumor cell surfaces. Therefore, a new dimension of therapeutic application of beta emitting nuclides is under development, which necessitate a precise and fast dose calculation. Thus, it is now especially important to be able to calculate the dose distribution in small regions with embedded beta-ray sources.

As far as homogeneous media are concerned, dose calculations are facilitated by the use of beta dose point kernels (BDPK) for the media. To solve the problems of routine dosimetry for heterogeneous media, it is impractical to employ realistic and, in principle, accurate, but tedious Monte Carlo methods. Simpler empirical or semiempirical methods, providing rather fast estimates but of limited accuracy, may be acceptable. Small scale dosimetry, utilizing the results from Monte Carlo calculations and performing straightforward dose calculation, is able to provide rapid estimates of absorbed dose with appropriate accuracy.

In many instances, internal dose assessment has resorted to Monte Carlo calculations to analyze the details of source-target relations and radiation dose. However, such an approach is not always practical, which can be time-consuming and wasteful of computer resources, especially in implementing the approximation encountered in medical internal dosimetry. Considering the feasibility of realistic treatments of beta and electron interactions within tissue, a different approach should be investigated. Small Scale Dosimetry, which incorporates the "once-through" Monte Carlo approach, can be used to analyze the energy deposition in the neighborhood of isotropic point sources, and to make straightforward analytical calculations of absorbed dose. This method makes it possible to calculate absorbed-dose distributions for either homogeneous or inhomogeneous sources by doing simple integrals over point-source distributions. Several computer codes have

been developed to process the data base of energy deposition histories and to implement the absorbed dose calculations by using point kernel algorithm. Conceivably, the Small Scale Dosimetry approach may be extended to be applicable for heterogeneous target tissue compositions, as long as the biological data and physiological information of that organ or tissue are well understood.

METHODOLOGY

There are three major steps in the assessment of radiation absorbed doses to small volumes or regions of the body. First, it is necessary to establish the fundamental understanding of interactions between beta radiation and human tissue. The energy deposition in concentric tissue rings is studied. As shown in Fig.1 is the target tissue domain used for energy deposition study, which has radius equal to 1.2 times the R_{csda} (Continuous Slowing Down Approximation Range) and subdivided into 100 concentric shells. A Monte Carlo transport code EGS-4 (Electron Gamma Shower) is used to trace the electron histories and score the energy deposition in each shell. The calculation of Absorbed Fraction (AF), Specific Absorbed Fraction (SAF) and Scaled Dose Kernel (F(r/R)) are performed following Eq. 1, 2 and 3 to establish the data base of monoenergetic electrons, which will be applied for subsequent absorbed dose calculations.

$$AF = \frac{\text{energy deposited in target region}}{\text{energy emitted in source region}} \qquad \text{Eq.1}$$

$$SAF = \Phi = \frac{AF}{\text{mass of target}} \qquad \text{Eq.2}$$

$$F(r/R_{csda}) = \frac{\delta E(r)/E_0}{\delta r/R_{csda}} \qquad \text{Eq.3}$$

where

$\delta E(r)$ is the energy deposition in a shell with distance r from the center of sphere;

E_0 is the average energy of electron or beta-particle;

dr is the thickness of each concentric ring; and

R_{csda} is the Continuous Slowing Down Approximation range.

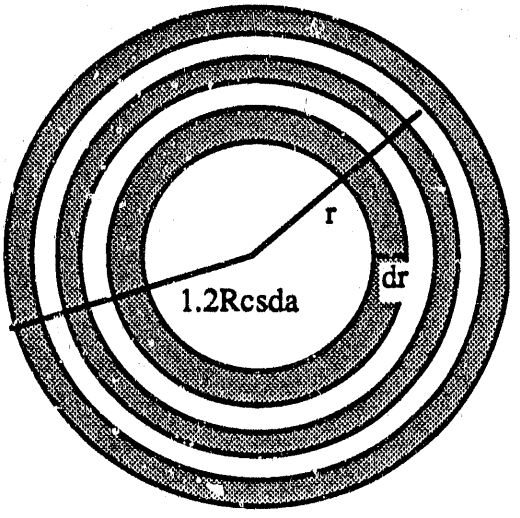

Fig. 1. The tissue sphere with 100 concentric rings used in the energy deposition study. Monte Carlo method is used to trace the electron transportation in each skeletal muscle shell.

Secondly, the advent of radiolabeled monoclonal antibodies (MAB's) has elicited much interest in the possibility of developing cancer cell specific radiopharmaceuticals for therapeutic purpose. In the context of radioimmunotherapy of cancer, there is a need for continued improvement of dosimetry of radionuclides localized in tumors. Therefore, instead of using monoenergetic electrons as the sources, beta radiations from radionuclides with spectral energy emission will be the focus of study. Composite scaled dose kernel, F(r/R), will be generated for the following radionuclides: P-32, Y-90, Cu-67 and I-131, which are the potential candidates for tumor treatment. Dose profile for each radionuclides will be performed to study the therapeutic effect of administration of these radionuclides.

At last, absorbed dose calculation will be performed by selecting thyroid, ovary and kidney as the target organs and using P-32, Y-90, Cu-67 and I-131 as source radionuclides. Mathematical description of the target organs as used by MIRD Committee (Snyder at el. 1969) is employed to define the target domain. Scaled dose kernels obtained from procedure (3) is utilized to calculate the absorbed dose by administrating of these four radionuclides in the selected organs. Then, the absorbed dose is calculated by the equation

$$\text{Dose} = E_{av} \frac{F(r / R_{csda})}{4 \pi r^2 \rho R_{csda}} \qquad \text{Eq.4}$$

where

$F(r/R_{csda})$	is the scaled dose kernel of that given energy;
r	is the distance from source to target;
ρ	is the density of target material.

The isodose profiles at different plane of interest are plotted to represent the results of absorbed dose calculations.

CURRENT PROGRESS

The proposed procedure discussed above have completely fulfilled. A FORTRAN program has been generated to process the database of monoenergetic electrons and produce scaled dose kernel of anv radionuclide by giving the atomic number, end-point energy and branching ratio of that radionuclide. As shown in Fig.2 and Fig.3 are the scaled dose kernel profiles for P-32 and Y-90 in skeletal muscle (ICRP1975).

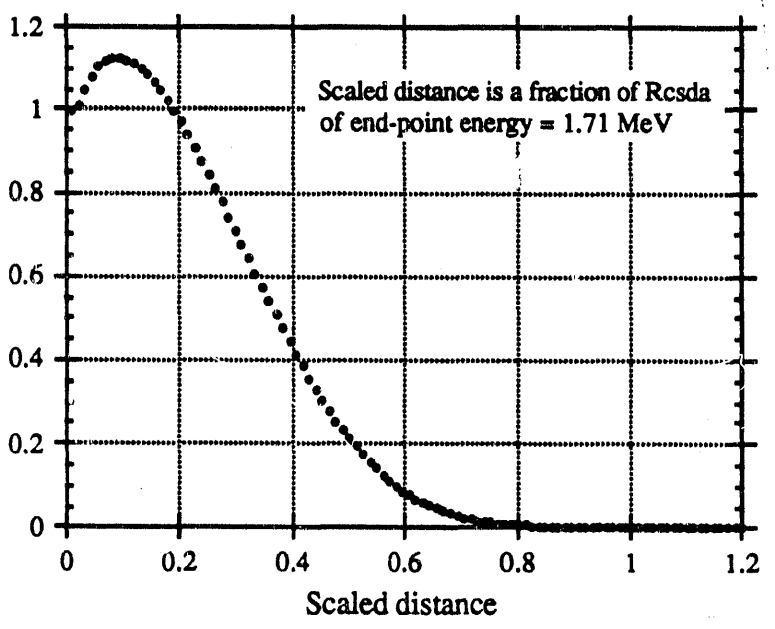

Fig. 2. The scaled dose kernel profile of P-32 in skeletal muscle.The R_{csda} associated with 1.71 MeV electron in skeletal muscle is about 0.794 cm.

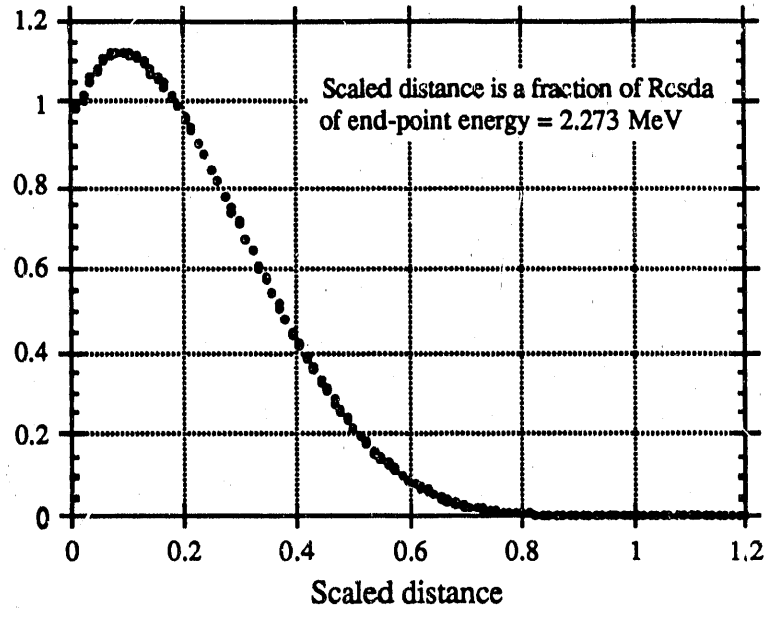

Fig. 3. The scaled dose kernel profile of Y-90 in skeletal muscle.The R_{csda} associated with 2.273 MeV electron in skeletal muscle is about 1.107cm.

The absorbed dose distribution in thyroid by uniformly administrating 1 Bq of P-32 is plotted by a series of isodose contour lines, as shown in Fig.4. The 100% dose point or the maximum dose point in this plot is equal to 3.743E-2 MeV/g. From this plot, the capability of small scale dosimetry is clearly stated and the dose calculation algorithm of small scale dosimetry is sufficiently accurate to analyze the dose distribution of human organ when deposited with radionuclide.

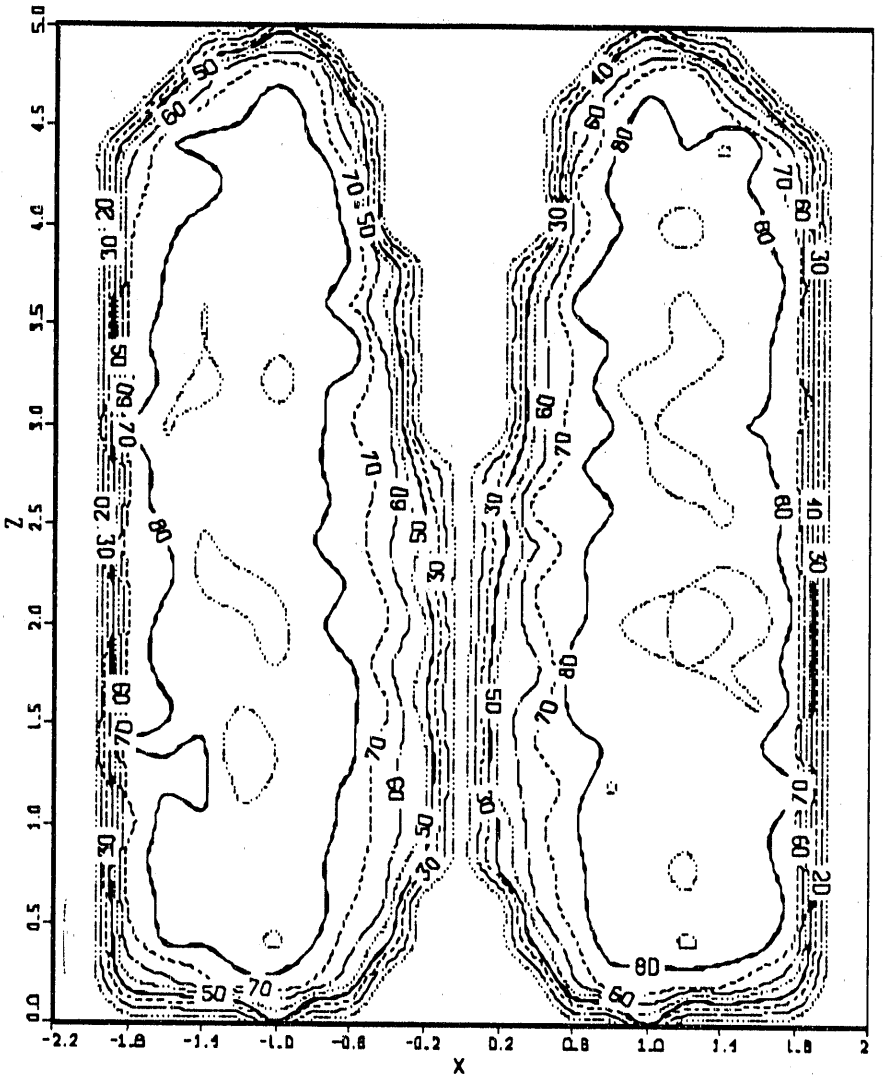

Fig. 4. The isodose contour lines of thyroid by administrating 1 Bq of P-32.

ASSESSMENT OF THE DOSE TO BONE USING A MONTE CARLO TRANSPORT CODE

INTRODUCTION

The study of the toxicity of bone-seeking radionuclides has shown that the soft tissues within spaces in trabecular bone are especially vulnerable to malignant changes induced by radiation. There are three cell populations associated with this soft tissue that are suspect to carcinogenic risk. These are (1) haematopoietic marrow, (2) osteogenic tissue, particularly on the endosteal surfaces, and (3) the reticulo-endothelial tissues in the trabecular spaces (ICRP 1968). Dosimetry for the haematopoietic marrow and the reticulo-endothelial tissues can be considered together since the relevant dose is the mean absorbed dose to the soft tissues in the trabecular cavities. The relevant dose to the osteogenic tissue is the mean dose to a layer of cells of 10 μm thickness lining the marrow cavities (Sissons 1970, Vaughan 1970). Thus, the relevant dose to calculate when considering the effects of radionuclides in bone are the mean absorbed dose to the marrow cavities, and the mean absorbed dose to a 10 μm thick endosteal layer of cells lining the marrow cavities.

Radionuclides that are deposited in the bone ("bone-seekers") are separated into two categories. Radionuclides that are taken up in high concentrations in the bone where active mineralization is taking place are known as "volume seekers". These radionuclides also are distributed diffusely in low concentrations throughout the bone mineral. The ICRP, in their most recent model, assumed uniform concentration of a volume-seeker throughout mineral bone (ICRP 79).

Radionuclides of concern in this situation are calcium, radium, strontium, and barium. These are alkaline earth elements and it was thought originally that they would replace the calcium in the bone mineral. This may be true after a short period of time, but there areimportant differences in how these chemical analogs behave in the skeleton. Their metabolic behavior is different and so is their pattern of distribution. This is seen at least a

short time after the radionuclide reaches the blood stream, such as, for the radionuclide Ca-45. This radionuclide is shown to be taken up immediately after injection and is concentrated on all bone surfaces. Within days after injection it is diffusely distributed throughout mineral bone.

The other category of bone-seekers is known as the "surface-seekers". These are radionuclides that concentrate on bone surfaces, but do not distribute throughout the mineral. The ICRP model assumes these radionuclides remain on the bone surfaces for extended periods (ICRP 79). Radionuclides of concern in this case are plutonium, americium, thorium, cerium, californium, and yttrium. Variations in the way these radionuclides are distributed have important implications for assessment of the radiation dose they will deliver to the sensitive tissues. All of these are surface seekers, but do not distribute themselves on the surfaces in the same manner. Of these radionuclides, plutonium and americium present the greatest practical hazard in the workplace.

Many approaches have been made to the assessment of dose to bone and its radiosensitive cells. All theoretical approaches involve physical assumptions and approximations which are necessary to obtain expressions capable of numerical solution.

BACKGROUND

Two types of structures are found in the skeleton: (1) hard cortical bone found in the shafts of long bones and the plates of flat bones, and (2) trabecular, spongy or cancellous bone contained in the ends of long bones, in the thin-walled vertebrae and between the plates of the flat bones. Three types of bone cells are recognized: osteoblasts, osteocytes, and osteoclasts. These cells perform five functions in the bone. They produce the protein in the bone, stimulate the mineralization of the protein in bone, maintain the bone tissue, resorb bone, and play an active role in mineral physiology. The bone itself serves at least four functions: (1) facilitates mobility and stability, due to muscular attachments, (2) protects vital organs - central nervous system, heart, lungs, liver, and to some extent the female genital system, (3) serves as a storehouse for essesential minerals, such as calcium, and wastes such as lead and plutonium, (4) encloses heamatopoitic tissue, bone marrow.

Cortical bone consists of a mineralized matrix made up of a mosaic of small units called osteons. These are from 200 to 400 μm in diameter and through them run the Haversian canals carrying nutrients from the arteries. These arteries feed the bone cells, the osteocytes, that reside in small lacunae in the surrounding matrix, connected to the nutrient artery and to each other by extremely fine canaliculi. The Haversian canals are from 20 to 100 μm in diameter and are themselves lined with cells, the osteoblasts and the osteoclasts, which can build up or resorb the bone matrix, respectively. These cells, the nutrient arteries and the osteocytes together are the soft tissue component of cortical bone; they maintain the bone and damage to them may result in bone death.

Trabecular bone consists of a fine network of interlacing thin lamella of hard bone which forms a system of interconnecting cavities of various sizes and shapes. The lamellae, or trabeculae, include some osteocytes but, having a thickness of only 100 μm, they do not normally need blood vessels to nurture them as in the osteons of cortical bone. The surface of the trabeculae, the endosteal surfaces, are lined with osteoblasts, osteoclasts and their precursors whose function is bone growth and remodeling. Behind them are primitive bone cells, the osteoprogenitor cells, from which the osteoblasts and osteoclasts develop. The cavities in the trabecular network contain the bone marrow consisting of the red and white cells and their precursors and the stromal cells and their precursors.

The detailed structure of bone varies from bone to bone in both man and animals and indeed varies within a single bone. Whereas the trabeculae do not vary greatly in thickness, the marrow cavities often vary greatly from bone to bone.

OBJECTIVES

This proposal describes an approach to dosimetry of the bone using a Monte Carlo transport code. This code can be used to determine effectively the energy deposited in the bone marrow, the trabeculae, and the cells on bone surfaces, the endosteal layer. To accomplish this assessment, a precise model is needed. Because the structure of the trabecular bone is complex, it cannot be described by simple geometric shapes. Previous work done by Chen and Poston (1982) describe a distribution function of the trabeculae throughout a cross section of bone. This distribution function is based on the mean cavity size that contains the red marrow. The objectives of this proposal can be summarized as follows:

1. Generate a bone model using a trabecular distribution function and compare this computer generated picture with that of an actual bone.

2. Effectively use the Monte Carlo computer code Electron Gamma Shower (EGS4) to estimate absorbed fractions of energy deposited in the bone marrow, trabeculae, and the endosteal layer of the bone.

3. Calculate S-factors for several different radionuclides of interest in the dosimetry of bone.

4. Compare the results with other techniques to assess the accuracy of the bone model developed.

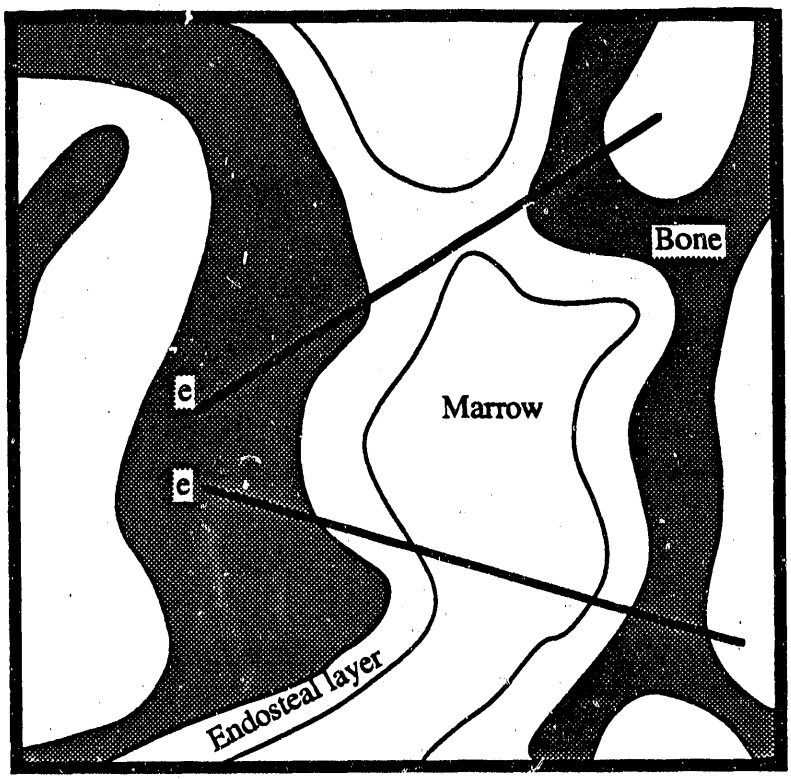

Figure 1. Possible track lengths through a cross section of trabecular bone.

Figure 1 shows a enlarged section of bone for which the paths of the particles will be followed. The path of the particle may traverse the structures as shown, i.e. bone, endosteal layer, marrow, etc. However, this is not the only option. It is also shown that a particle may traverse through the trabeclae and never cross the marrow cavity, thus reducing the dose to that tissue.

METHODOLOGY

The following steps outline the proposed procedure for bone dosimetry using the EGS4 Monte Carlo transport code.

(1) Since the specific absorbed fraction, $\Phi(r,E)$, is an essential element in internal dose estimation, it must be estimated as accuratelyy as possible. This will be done using a Monte Carlo transport code, Electron Gamma Shower (EGS4), to generate the specific absorbed fractions within the tissues of the bone. The database will cover those radionuclides which are bone-seeking β–emitters including P-32, Ca-45, Sr-89, Sr-90, and Y-90.

The EGS4 code system can be used to simulate the coupled transport of electrons and photons in an arbitrary geometry for particles ranging in energy from a few keV to several TeV. EGS4 can be used to follow each particle throughout the tissue of interest. A preliminary evaluation shows that 50,000 histories must be followed to show satisfactory results with acceptable uncertainties.

(2) Table 1 (Chen and Poston 1982) shows the physical characteristics of bone at different locations throughout the skeleton. It is difficult to calculate the absorbed dose in trabeculae, marrow or the endosteal layer without knowing the geometry or location of the marrow cavities. Chen and Poston (1982) introduced a function that describes the distribution of marrow throughout a cross section of bone. The distance traveled by a charged particle through marrow is given by the chord length rather than the cavity size. The chord length distribution function, P(l), may be expressed such that:

$$P(l) = \frac{l}{M^2} \exp - \left(\frac{l}{M}\right)$$

where: M = The most probable chord length which is approximately equal to the mean cavity size divided by two.

l = chord length, $0 < l < l_m$.

Using the data in Table 1, the distribution function given above, and the computer graphics package "DISSPLA", a computer generated picture of the bone will be produced. A comparison between the computer generated picture and a actual picture of a cross-section of bone will demonstrate the accuracy of the distribution function.

(3) Use the Monte Carlo Transport Code (EGS4) to calculate the specific absorbed fractions of energy for monoenergenic electrons over a range of energies.

(4) Using the specific absorbed fractions, calculate S-factors for selected radionuclides.

(5) Verify results of energy deposited, specific absorbed fractions, and S-factor calculations and compare results with other techniques.

The method described will enable more precise calculations of the absorbed dose for particles of any range crossing the irregular and interpenetrating systems of bone trabeculae, marrow cavities, and the endosteal layer. This method may be compared to earlier methods with very simple geometries.

Table 1. Physical characteristics of bone at different location throughout the skeleton.

Bone Region	Red Marrow 1.028 g/cm^3		Bone Mass (g)	Trabecular Mass	Trabeculae 1.92 g/cm^3		Yellow Marrow 0.983 g/cm^3		Mean Cavity Size (mm)
	Mass	Vol			Mass	Vol	Mass	Vol	
Arms:									
Upper	28.5	27.7	474	20	94.8	49.38	9.5	9.7	0.84
Lower			520	15	78	39.27	389	395.7	0.84
Clavicle	24	23.3	49.2	6	2.95	1.54	8	8.1	0.8
Legs:									
Upper	57	55.4	2036	33	671.8	349.94	19	19	0.84
Lower			1588	25	397	206.77	461	469	0.84
Pelvis	543	528.2	177	25	44.25	184.1	181	184.1	0.58
Ribs	153	148.8	688	6	40.25	204.5	201	204.5	0.72
Scalpulae	72	70	206	6	12.36	24.4	24	24.4	0.8
Skull:									
Cranium	178.5	173.6	557	5	27.85	60.5	59.5	60.5	0.72
Mandible	18	17.5	439	5	21.95	6.1	6	6.1	0.72
Spine:									
Upper	51	49.6	130	75	97.5	17.3	17	17.3	0.99
Middle	211.5	205.7	533	75	399.8	71.7	70.5	71.7	0.99
Lower	163.5	159	87.8	66	57.95	55.4	54.4	55.4	0.99

REFERENCES

Chen H. T.; Poston J. W. Estimates of Absorbed Energy in Trabecular Bone Due to β-Particles or Electrons. Health Physics. Vol. 43, No. 5, 647-653; 1982.

ICRP, 1968, A Review of the Radiosensitivity of the Tissues in Bone, Publication II, Oxford: Pergamon.

ICRP, 1979, ICRP Publication 30, Limits for Intakes of Radionuclides by Workers, Part 1, Annals fo the ICRP 2, No.3/4, New York: Pergamon Press.

Loutit, J. F. Construction and Reconstruction of the Bone, Bone and Bone Seeking Radionuclides: Physiology Dosimetry and Effects. Hardwood Academic Publishers, New York, 1980.

Montelius A.; Burlin T.E. The Dosimetry of Bone Incorporating Alpha-emitting Radionuclides. The British Journal of Radiology. Vol. 57, 609-616; 1984.

Montelius A.; Burlin T. E. The Dosimetry of Bone Irradiated by Fast Neutrons. Physics in Medicine & Biology. Vol. 31, No. 9, 955-965.

Prestwich W. V.; Nunes J.; Kwok C.S. Beta Dose Point Kernels for Radionuclides of Potential Use in Radioimmunotherapy. Journal of Nuclear Medicine. Vol. 30 ; 1036-1046, 1989.

Vaughan J. M.; The Effects of Irradiation on the Skeleton. Oxford: Clarendon Press; 1973.

Assessment of the New ICRP Lung Model

INTRODUCTION

Within both the fields of nuclear medicine and radiation protection, there is the need to assess the activity concentration of inhaled radioactive material in the different regions of the respiratory system. So far, it has been shown that the lung, together with the gonads, breast, and red bone marrow, are the more radiosensitive organs within the human body (NCRP 1987). In addition, the lung is one of the more difficult organs to model in that its dynamic behavior requires simultaneous simulation of physical, biological, and biochemical processes.

Physical processes account for the deposition of aerosol particles within the irregular diameters and lengths of the tracheobronchial tree. Biological processes include the mechanical clearance and epithelial absorption resulting in the removal of deposited material from the inner regions of the lung to the circulatory system. These occur in a competition with alveolar absorption of inhaled material.

The use of compartmental analysis has shown to be a simple, yet powerful, mathematical tool in assessing the distribution and retention of radioactive material in the different regions of the respiratory system. Therefore, biokinetic assessment of retention functions for inhaled aerosols are commonly used to calculate absorbed doses to target cells at risk following the inhalation of alpha- and beta-emitting radionuclides. Moreover, dynamic modeling of the distribution and retention of inhaled aerosols in the lung might also be applied in assessing lung burdens of other industrial chemical pollutants.

So far, modeling of the lung has been based on an analytic solution of linear chains of compartments representing the main three physiological regions of the respiratory system (ICRP 1979). In this analysis, the transfer rates between compartments are assumed to be constant. This simplified representation of the respiratory system, however, does not take into account the full range of biological processes which govern the translocation of material within the lung. These processes are more correctly represented as time-varying functions involving nonlinear parameters.

At present, a task group of the ICRP has undertaken an extensive revision of the ICRP Lung Model for use in radiation protection guidance. In this new model, new experimental values are considered for clearance rates, solubility rates, and deposition fractions for a variety of inhaled materials. These parameters are time dependent and, as a result, steady-state solutions to the system can be extremely difficult to obtain. As a result, the task group chose to simplify their system by subdividing the main regions of the new lung model into additional compartments. This process results in, once again, a linear

chain of compartments with time-independent transfer rates. Although this approximation does assure a stable system, it does not reflect the real dynamical behavior of the biological and physico-chemical processes of material translocation in the human lung.

In this research task, a detailed assessment of the new ICRP Lung Model will be made in which all transfer rates in the model will be treated, not as constants, but as time-varying parameters. A dynamic simulation of the lung model will be accomplished using the computer code SAAM (Simulation Analysis and Modeling) developed by Berman and Weiss (1978). Comparisons will subsequently be made of both lung and organ committed dose equivalents following the inhalation of radioactive material as given by both the present and the proposed implementation of this new ICRP Lung Model.

THE NEW ICRP LUNG MODEL

Four main factors have to be considered in modeling the lung. These factors include: (1) breathing rates and volumes of inhaled air in the different regions of the lung during complete breathing cycles; (2) the fraction of inhaled aerosols deposited in the different regions of the lung through the physical processes of inertial impaction, sedimentation, and diffusion; (3) biological clearance processes such as mechanical mucociliary transport of inhaled dust in the tracheobronchial tree, and phagocytosis by alveolar macrophages; and (4) the absorption of soluble (and sometimes "insoluble") material to blood from the extrathoracic, tracheobronchial, and pulmonary regions.

Following this approach, a Task Group of the ICRP has proposed a new compartmental distribution to represent the respiratory system as shown in Fig. 1 (Johnson 1989). It consists of three main regions of interest: a extrathoracic region, a fast-clearing thoracic regions, and a slow-clearing thoracic region. The extrathoracic region includes and represents the clearance and deposition of materials in the nose, mouth, pharynx, and larynx. In this region, material is cleared by mucociliary transport, sneezing, nose wiping and blowing, and dissolution (for soluble particles). Most of the information on nasal deposition comes from experimental work. Mathematical modeling of particle deposition is complicated by the irregular geometry of nasal and mouth passageways (Guilmette et. al 1989) and the resulting uncertainties in aerosol flow patterns (Bowes and Yu 1989).

The two thoracic compartments representing the tracheobronchial (T-B) and parenchymal-nodular (P-N) regions are called the fast and slow translocation compartments, respectively. The fast translocation compartment includes airways 0-16 of the tracheobronchial region. In this region, radioactive inhaled material is deposited by the physical processes of impaction, sedimentation, and diffusion (Hoffmann and Martoneen

1989). At the same time, radioactive material is absorbed to the blood and cleared to the gastrointestinal tract by solubility transport of material through the bronchial epithelium, and by mechanical mucociliary transport by the combined action of mucus-secreting cells, and bronchial glands and ciliated cells. These processes are mathematically represented by exponential time-varying functions illustrated as B(t) and $G_f(t)$ in Fig. 1.

In the slow translocation compartment representing airways 17-23 (bronchioles, alveolar sacs, and thoracic lymph nodes), radioactive material is slowly cleared by competitive processes of mechanical transport and solubilization (Cuddihy and Yeh 1988). Mechanical nonabsorptive processes are controlled by alveolar macrophages. These cells move freely on the epithelium and phagocytize, transport, and detoxify deposited material they contact. Solubilization mechanisms involves dissolution. Particles that dissolve in the alveolar fluid can diffuse through the epithelium and interstitium into the lymph or blood, and those translocated and trapped in interstitial sites may be absorbed. Once again, these processes are simulated by the exponential time-varying functions that are represented in Fig. 1 as $G_s(t)$ and B(t).

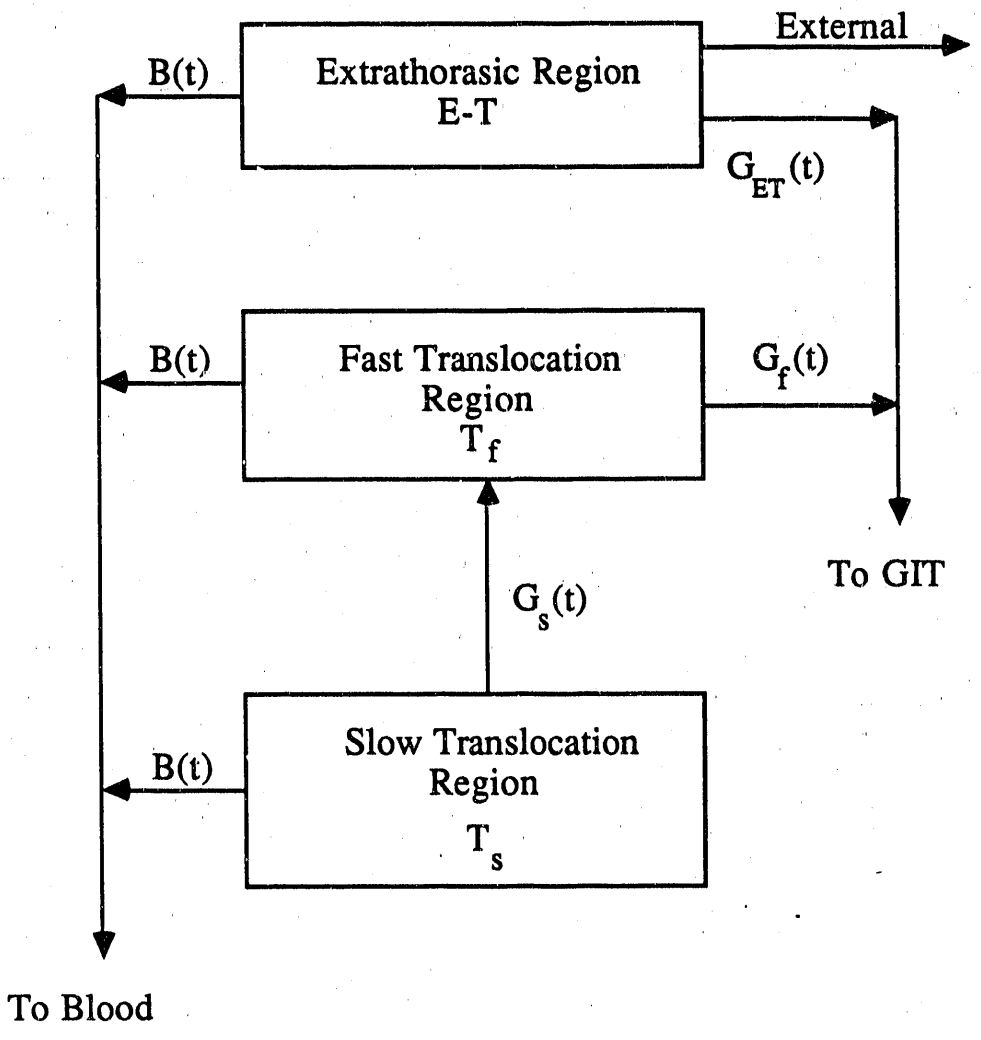

Figure 1. Compartmental distribution of the proposed new ICRP Lung Model.

When all these biological and physicochemical factors are taken into account, the activity of inhaled material distributed in the different lung regions is given by the numerical solution of a mass balance equation describing the compartmental distributions of Fig. 1. Therefore, the concentration of radioactive material in each compartment is given by the solution of a set of coupled, differential equations:

$$\frac{dq_{E\text{-}T}(t)}{dt} = \dot{I}(t)D_{E\text{-}T} - [\,B(t) + G_{E\text{-}T}(t) + \lambda_R\,]q_{E\text{-}T}(t)$$

$$\frac{dq_{T\text{-}B}(t)}{dt} = \dot{I}(t)D_{T\text{-}B} + G_s(t)q_{T\text{-}B}(t) - [\,B(t) + G_f(t) + \lambda_R\,]q_{T\text{-}B}(t) \qquad \text{.....(1)}$$

$$\frac{dq_{P\text{-}N}(t)}{dt} = \dot{I}(t)D_{P\text{-}N} - [\,B(t) + G_s(t) + \lambda_R\,]q_{P\text{-}N}(t)$$

where:

$q_{E\text{-}T}(t)$, $q_{T\text{-}B}(t)$, $q_{P\text{-}N}(t)$ are the activities of an inhaled radionuclide in the different regions of the lung.

$\dot{I}(t)$ = Rate of inhalation of activity of the radionuclide.

$B(t) = \sum_{i=1}^{n} A_i e^{-\lambda_i t}$ with A_i and λ_i constants is a solubility function calculated from experimental fitting processes.

$D_{E\text{-}T}$, $D_{T\text{-}B}$, $D_{P\text{-}N}$ are the total deposition fractions of inhaled material in the different regions of the lung.

$G_s(t)$ = Slow clearance rate function (same form as $B(t)$).

$G_{E\text{-}T}(t)$, $G_f(t)$ = Extrathoracic and fast clearance rates.

CURRENT PROGRESS

Presently, a FORTRAN program is being developed for assessing the total deposition fraction of inhaled and exhaled aerosols of varying aerodynamic diameters for the different regions of the lung. This program will consider values of breathing frequencies and tidal volumes, reported by Hoffman and Martonen (1989), for a 20-year-old at different levels of physical activity. Deposition fractions of inhaled material in the extrathoracic region are assumed for an individual working at a light activity level with a breathing frequency of 15 breath/min and a breathing flow rate of 15 liter/min. Therefore, the fraction of inhaled

material deposited in the nasopharingeal region is first intended to be calculated from the following equation (ICRP 1966):

$$D_{E\text{-}T} = -0.62 + 0.475 \log (D_a^2 Q_a),$$

where

D_a = aerodynamic diameter of the particle

Q_a = breathing flow rate (liter/min).

At the same time, these deposition fractions will be compared with the experimental results of Bowes and Yu (1989) which are represented by the following relationship:

$$DF = 0.153 + 0.0422 \frac{d_a}{(\mu m)},$$

where

DF = deposition fraction

d_a = mass median aerodynamic diameter.

Deposition fractions in the tracheobronchial and pulmonary regions are calculated under the assumption that the solution of the Navier-Stokes equations is in the region of linearity, the settling velocity of an aerosol particle follows Stoke's law. Moreover, it is also assumed that settling velocities are corrected for slip when inertial impaction and sedimentation processes are considered. Therefore, deposition fractions at the different generations of the tracheobronchial and pulmonary regions are calculated as:

$$F = 1 - (1-I)(1-S)(1-D),$$

where

F=Total deposition fraction

I= impaction deposition probability

S= sedimentation deposition probability

D= diffusion deposition probability.

Since values of I, S, and D are dependent upon parameters such as the gravity and branching angles of the airways, as well as the diameters lengths of the airways. Morphometric calculations of the tracheobronchial tree reported by Weibel (1963) have been improved in the design of this program by the substitution of values reported by

Phalen et. al (1985) for generations (0-15) and by Dunnill (1962) for generations (16-22). As a result, the program will be designed accommodate of any change in parameter values.

Concurrent with this program development, the computer code SAAM (Simulation Analysis and Modeling) is being tested in the simulation and acquisition of numerical solutions of the mass balance equations shown in the previous section. At this point, the code has demonstrated excellent agreement between analytical and numerical solutions for the case of linear chains of compartments with constant transfer rates.

The stability of linear dynamical equations like Eq. 1 will depend on the existence of a steady-state solution of the system; this means that if the system is perturbed from the equilibrium state by an impulsive or periodic input function (sudden or periodic inhalation of radioactive material), then the system will return to the same or another equilibrium state as the time tends toward infinity. In attempting to solve the dynamic system of Eq. 1, the steady-state solution becomes important, since the general solution for the time-varying case can always be decomposed into the zero-input response and the zero-state response:

$$\mathbf{q}(t) = \phi\,(t\,;\,t_o\,,\,\mathbf{q}_o\,,\,\mathbf{0}) + \phi\,(t\,;\,t_o\,,\,\mathbf{0}\,,\,\mathbf{u})$$

where $\mathbf{q}(t)$ = is the vector of solutions in the different regions of the lung

$\mathbf{q}_o$ = is the vector of initial conditions of the system

$\mathbf{u}$ = is the vector of inputs of the system.

$\phi\,(t\,;\,t_o\,,\,\mathbf{q}_o\,,\,\mathbf{u})$ = is the transition solution of the system and depends on the temporal integration of the compartmental matrix and the initial conditions.

Since a system's steady-state is a particular solution of the zero-input response, the first step in the numerical solution of a dynamical system like Eq. 1 is to find the steady-state solution of the system to guaranty the stability of the solutions. At this point, SAAM has been tested by calculating the steady-state solution of a two-compartmental distribution representing the metabolism of an arbitrary compound in a turnover study. Simulation of an experiment in the steady-state is carried out by the injection of compound X as a bolus in plasma. Blood samples are collected every hour after injection. The objective is to estimate the steady-state mass distribution among the compartments in a proposed two linear chain of compartments. Figure 5.2 shows a comparison of the simulated solution calculated by SAAM and the experimental blood sample readings. Fitting of the numerical solution with the experimental points was carried out by the use of the optimization and least-squares subroutines of SAAM. The error between the numerical solution and the experimental measures was reduced to be less than 2%. Figures 5.3 and 5.4 show a comparison between the numerical transient solutions calculated from another SAAM

model code and the steady-state solution within the different compartments. They also show how the transient solutions always tend toward the steady-state solution at infinite times, presuming the system remains stable.

REFERENCES

Bair, W. J., "Human Respiratory Tract Model for Radiological Protection: A Revision of the ICRP Dosimetric Model for the Respiratory System," *Health Phys.* **57 Sup.1**, 249-253 (1989).

Bair, W. J., "Overview of the ICRI Respiratory Tract Model," 3rd International Workshop on Respiratory Tract Dosimetry, Albuquerque, New Mexico, July 1-3, 1990.

Berman, M., and M. F. Weiss, SAAM Manual, U. S. Department of Health, Education, and Welfare, Publication No. (NIH) 78-180, 1978.

Bowes, S. M. and C. P. Yu, "Deposition of Inhaled Particles in the Oral Airway during Oronasal Breathing," *Aerosol Sci. Tech.* **11,** 157-167 (1989).

Cuddihy, R. G. and H. C. Yeh,"Respiratory Tract Clearance of Particles and Substances Dissociated from Particles," In: *Inhalation Toxicology,* Springer-Verlag, New York, pp. 169-173, 1988.

Dunnill, M. S., "Postnatal Growth of the Lung," *Thorax* **17**, 329-333 (1962).

Guilmette, R. A., J. D. Wicks, and R. K. Wolff, "Morphometry of Human Nasal Airways in Vivo Using Magnetic Resonance Imaging." *J. of Aerosol Med.* **2** 365-377 (1989).

Hoffmann, W., and T. B. Martoneen, "Predicted Deposition of Nonhygroscopic Aerosols in Human Lung as a Function Subject Age," *J. of Aerosol Med.* **2**, 49-68 (1989).

International Commission on Radiological Protection, "ICRP Task Group in Lung Dynamics: Deposition and Retention Models for Internal Dosimetry of the Human Respiratory Tract," *Health Phys.* **12**, 173-207 (1966).

International Commission on Radiological Protection, " Limits on Intakes of Radionuclides by Workers," ICRP Publication 30. Part 1 *Ann. ICRP* **2** (3/4), Pergamon Press, Oxford, 1979.

Johnson, J. R. and S. Milencoff, "A Comparison of Retention and Excretion between the Current ICRP Lung Model and a Proposed New Model," *Health Phys.* **57 Sup.1**, 263-270 (1989).

Masse, R. and F. T. Cross, "Risk Considerations Related to Lung Modeling," *Health Phys.* **57 Sup. 1**, 283-289 (1989).

National Council in Radiation Protection and Measurements, "Recommendations on Limits for Exposure to Ionizing Radiation," NCRP Report No. 91, Bethesda, 1987.

Phalen, R. F., M. J. Oldham, C. B. Beaucage, T. T. Crocker, and J. D. Mortensen, "Postnatal Enlargement of Human Tracheobronchial Airways and Implications for Particle Deposition," *Anat. Rec.* **212**, 368 (1985).

Weibel, E. R., *Morphometry of the Human Lung*, Academic Press, New York, 1963.

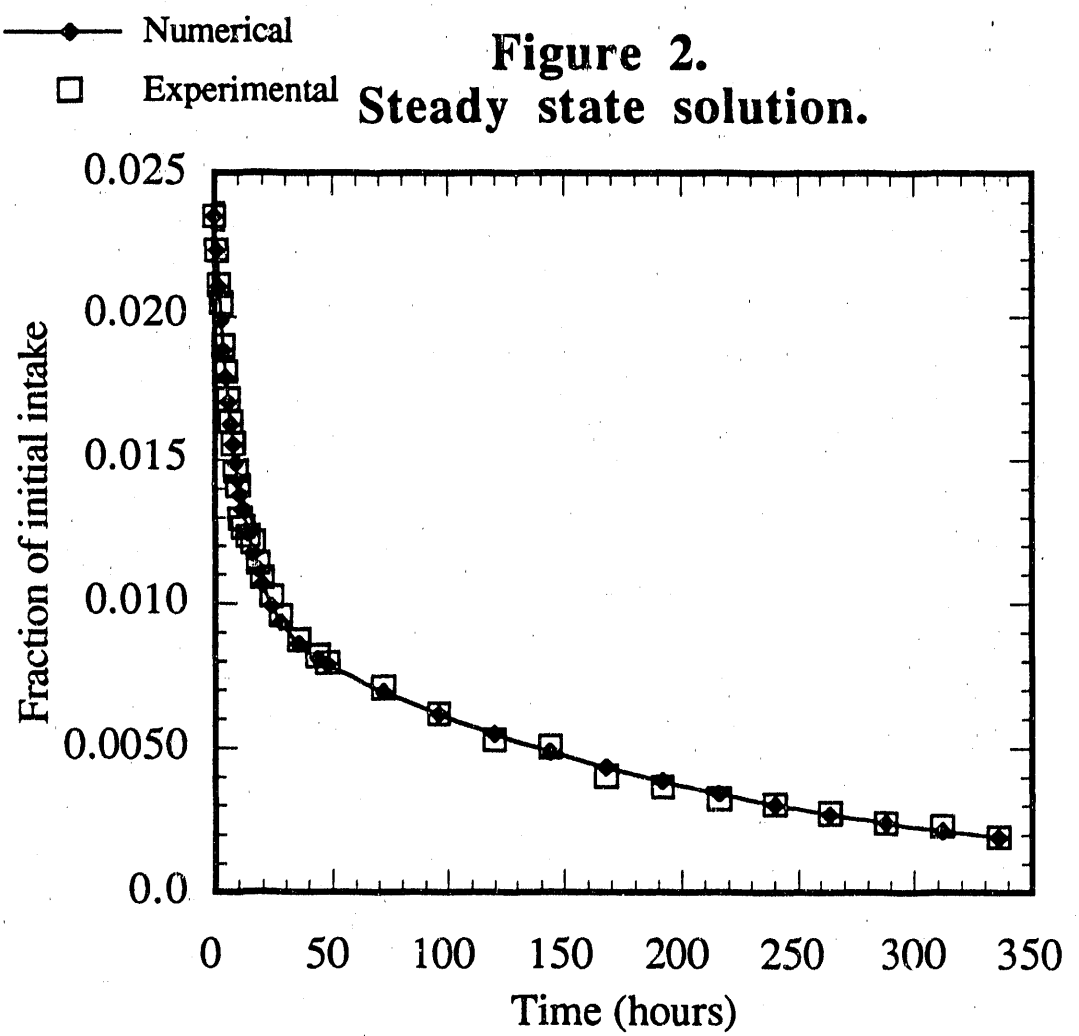

Figure 2.
Steady state solution.

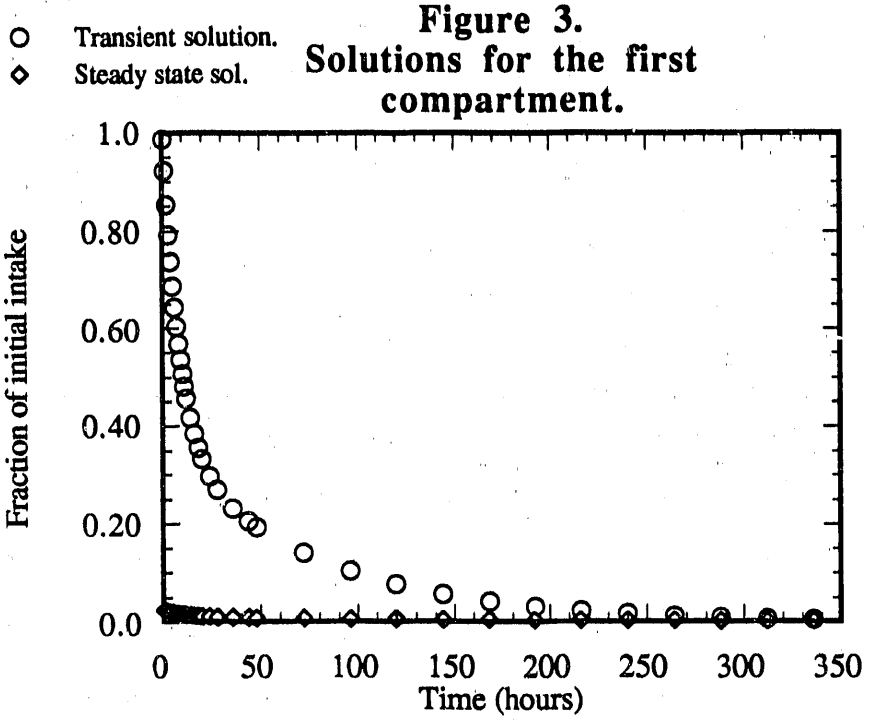

Figure 3.
Solutions for the first compartment.

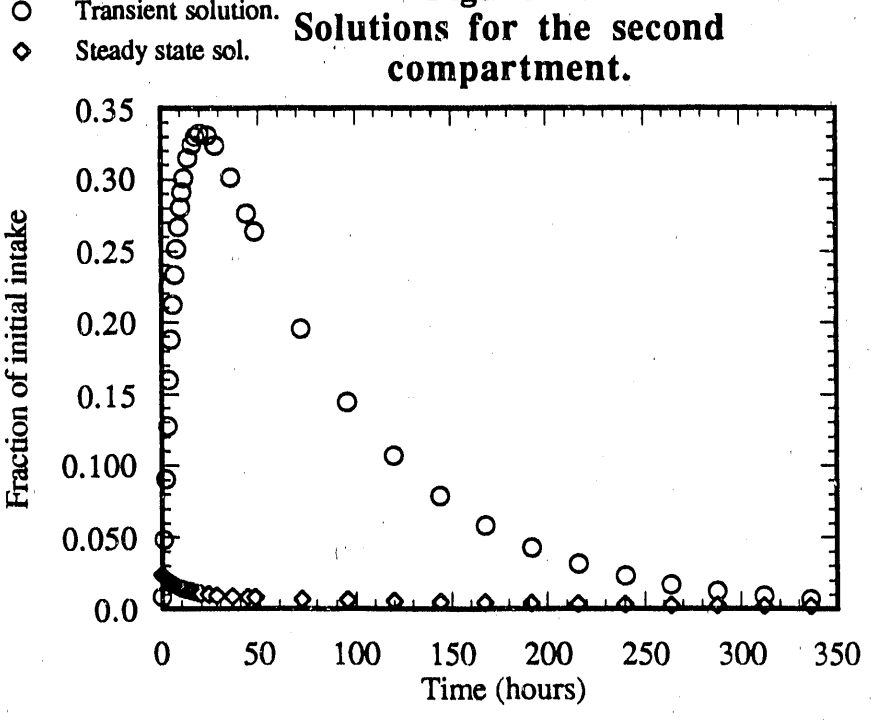

Figure 4.
Solutions for the second compartment.

DEVELOPMENT OF A DIFFERENTIAL VOLUME PHANTOM

INTRODUCTION

In 1964 the Society of Nuclear Medicine formed a committee to fulfill the needs of the nuclear medicine community to determine the radiation absorbed dose to patients who are administered radiopharmaceuticals. The objectives of the Medical Internal Radiation Dose (MIRD) Committee were to provide the best possible estimates of the absorbed dose to the patients resulting from the diagnostic or therapeutic use of internally administered radiopharmaceuticals. Data required to achieve these objectives were:

1) radiological parameters;

2) anatomical and physiological data for patients of various ages and physiognomies, and

3) metabolic distribution data for radiopharmaceuticals.

Uncertainties associated with these data will be propagated in absorbed dose calculations. Although, relevant radiological transformation characteristics of radionuclides are well known, uncertainties in physiological aspects, such as variance in organ morphology and metabolic aspects, e.g., variance in organ uptakes, contribute the greatest sources of errors.

In 1978 a reference heterogeneous phantom was described by MIRD in Pamphlet 5 Revised (Snyder et. al. 1978). This mathematical phantom was used as a model upon which internal absorbed dose calculations were based. The phantom provided an approximately correct anatomical representation of the human body based on ICRP Publication 23 (1975) which described a reference man. The organs in the phantom were described geometrically by mathematical equations. Several revisions and improvements have been made to represent populations of different ages and gender (Cristy et. al. 1987).

New nuclear medicine procedures, such as positron-emission tomography and other imaging techniques, radiation therapy procedures, and blood-flow studies require precise a-priori estimates of absorbed dose to specific organs or precisely defined tissue regions. Consequently, inadequacies in the description of these regions will contribute to errors in absorbed dose calculations. Therefore, certain organs and regions must be more accurately described.

OBJECTIVES

At the present time, a basic variable is used in nuclear medicine procedures to assess the energy per unit mass given to an organ or tissue of the human body for either external beam therapy or internally deposited radionuclides. This variable is the average absorbed dose; which conveys only information concerning the whole tissue or tissues based on a uniform distribution of the radionuclide. However, it does not convey information related to the spatial dose distribution inside a tissue, nor the doses to other healthy tissues near the region of interest. Moreover, the effectiveness of a procedure is not simply based on average absorbed doses but also on the spatial distribution of energy due to different types of radiations (related to the Linear Energy Transfer, LET).

Absorbed dose calculations for internally deposited radionuclides are based on a mathematical phantom which is a gross representation of a reference man. Today's nuclear medicine procedures require better estimates of absorbed doses for the human body. These estimates are of extreme importance due to the sensitivity of certain regions (such as the brain) for the correct planning and delivery of absorbed doses. The correct visualization or representation of regions of the human body will provide a more accurate estimate of the absorbed dose and its distribution throughout an organ or tissue. This representation is based upon improved modeling of an organ or tissue in the human body and also an estimate of the distribution of the radionuclide through the region itself.

Taking the above into consideration, a new differential volume phantom was designed to study the possibilities of generating new information concerning dose volume distributions and radionuclide distribution in the human body (dynamic processes are included). This new phantom is constructed based on physiological, anatomical and metabolic variables obtained from an individual patient which generates a specific phantom that simulates only one specific patient. Such data is obtainable from MRI studies and easily reconstructed to be used as geometrical input for new calculations.

This new phantom required further work to consolidate the concept. A variety of tests were made to assess the feasibility of the original idea.

First Test:

The first step made was to use of the old mathematical phantom described in MIRD Pamphlet 5 Revised and translated into a non-mathematical representation, then the data

was superimposed into a three-dimensional boxel arrangement which provided the location or region of the boxel with respect to an organ or tissue of the body.

Second Test:

This test consisted in extracting information on regions and tissues of the phantom which were defined by the user. The information extracted was the average absorbed dose, isodose curves, the spatial absorbed dose, the dose volume distribution and blood-tissue dose ratio. These variables are not the only ones used but many other can be extracted such as LET spectra distribution (if more than one type of radiation is used.)

Several other tests are now being carried out and results are still not available for commentary and discussion.

METHODOLOGY

The mathematical phantom used in MIRD Pamphlet 5 Revised was reconstructed into a non-mathematical form. Figure 1 shows a representation of cross sections of the mathematical phantom by the planes z = 0, 1, 2, 3, 4, 5, 6, 7, 8, 9, 10 and 11 cm. These non-mathematical representations of a phantom were used to reconstruct a three-dimensional representation of the phantom shown in Figure 2. This anatomical representation was then coupled with the Monte Carlo transport code Electron Gamma Shower (EGS4) to assess energy deposition patterns in different regions of the human body.

The identification of regions or tissues in this new mathematical phantom are left to the user. It is possible to assess the dose volume histogram of any region by selecting in the physical boundaries of the region. As an example, Figure 3 shows the main results of the variance of energy deposition throughout the liver itself containing a uniform distribution of ^{99m}Tc. This pictorial result conveys more information concerning the tissue than just having the average absorbed dose. As an example, Figure 4 shows the isodose contours superimposed with the different organs; the source region was defined as the cortex of the kidney and the radionuclide used was ^{99m}Tc. Similar results were obtained in a three-dimensional representation.

Task 1:

The first task consists of construction of the phantom using MRI images obtained from an specific patient. The images should be processed in such a form that they can be used for Monte Carlo transport. The implementation of such images should require the use of digitizers to locate regions of the body in which the radionuclide is concentrated. This will allow the assessment of the radionuclide distribution inside different organs of the body, as well as calculation of retention times and other metabolic parameters. This process is tedious and requires large blocks of computer time to process; however, once done it is a single step to obtain absorbed doses for the regions of interest in the human body.

Task 2:

The second task consists of the determination of regions of the human body which are of importance for medical procedures (e.g., the brain). Then it is necesssary to determine the different physiological and metabolic parameters to be used in the phantom. The objective is to locate the radionuclide distribution throughout the phantom itself and, therefore, assess the distribution in different regions and tissues of the body. This will allow the correct sampling of the radionuclide distribution rather than just assuming a uniform distribution. Having located and excluded the regions of interest, the code EGS4 will be used to asses energy deposition patterns in the body (as shown in figures 3 and 4). The results obtained will allow a complete state of the art treatment planning for abnormal regions of the human body.

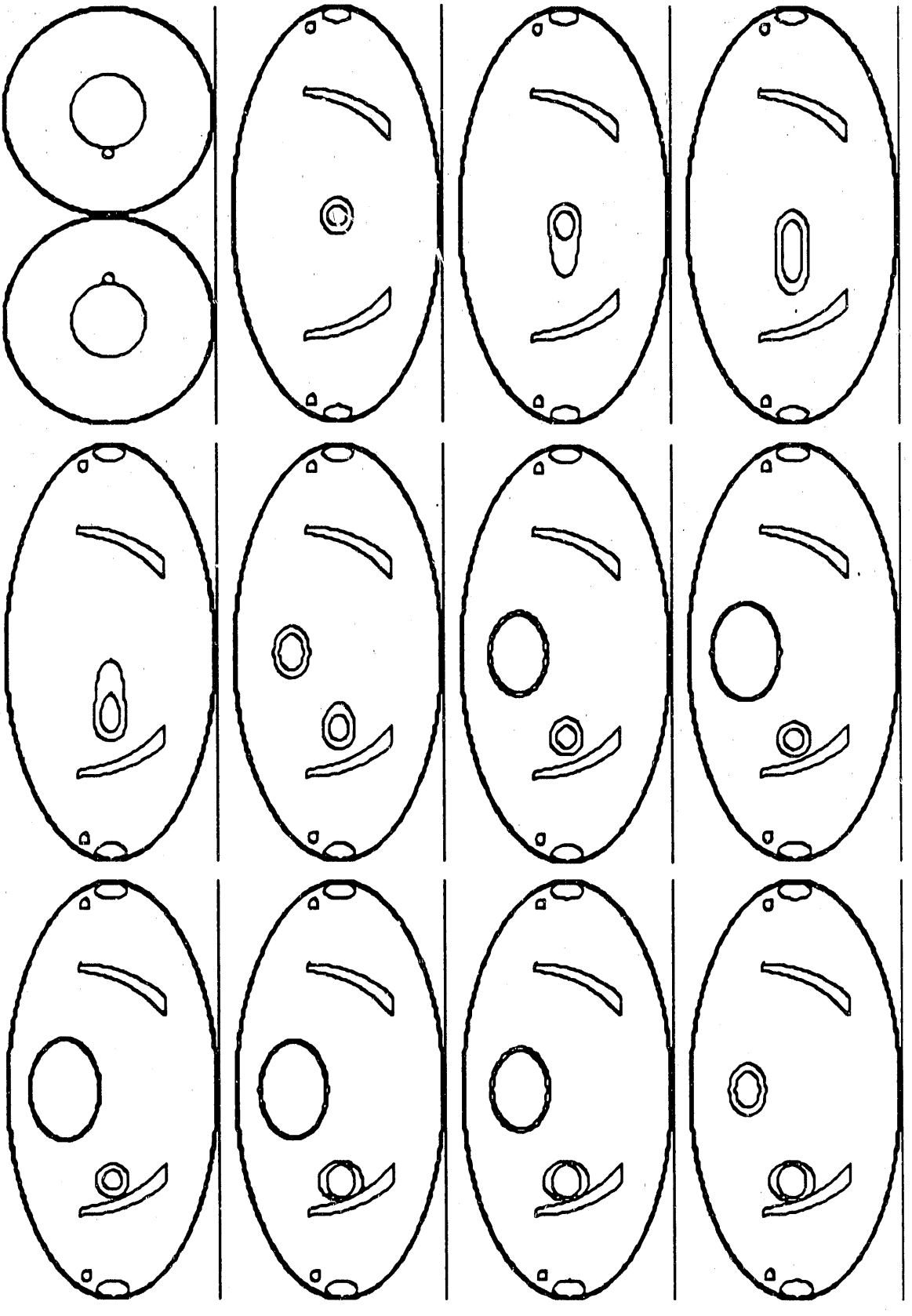

Figure 1. Schematic representation of the mathematical phantom. The cross sections were used to generate a non-mathematical phantom to be used in transport calculations.

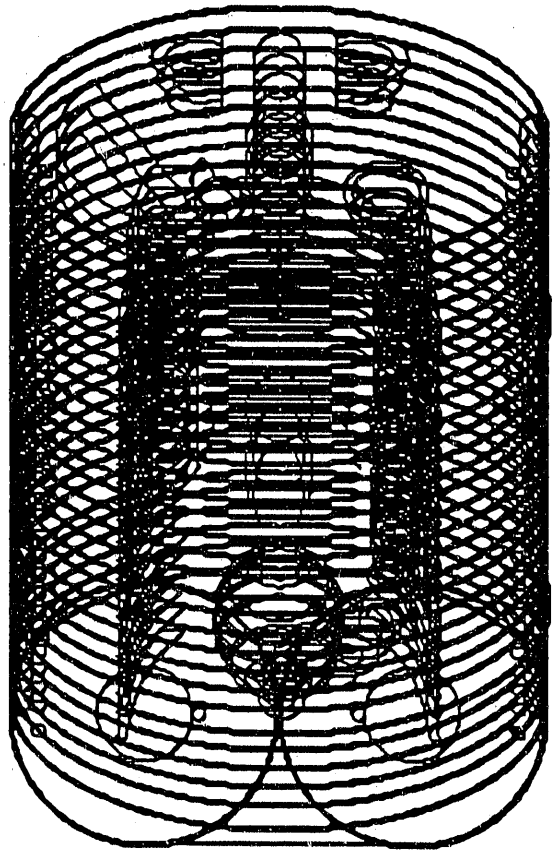

Figure 2. Consolidation of two dimensional cross sections to generate a three dimensional view of the non-mathematical phantom. This configuration was used to obtain information of different regions and tissues of the human body.

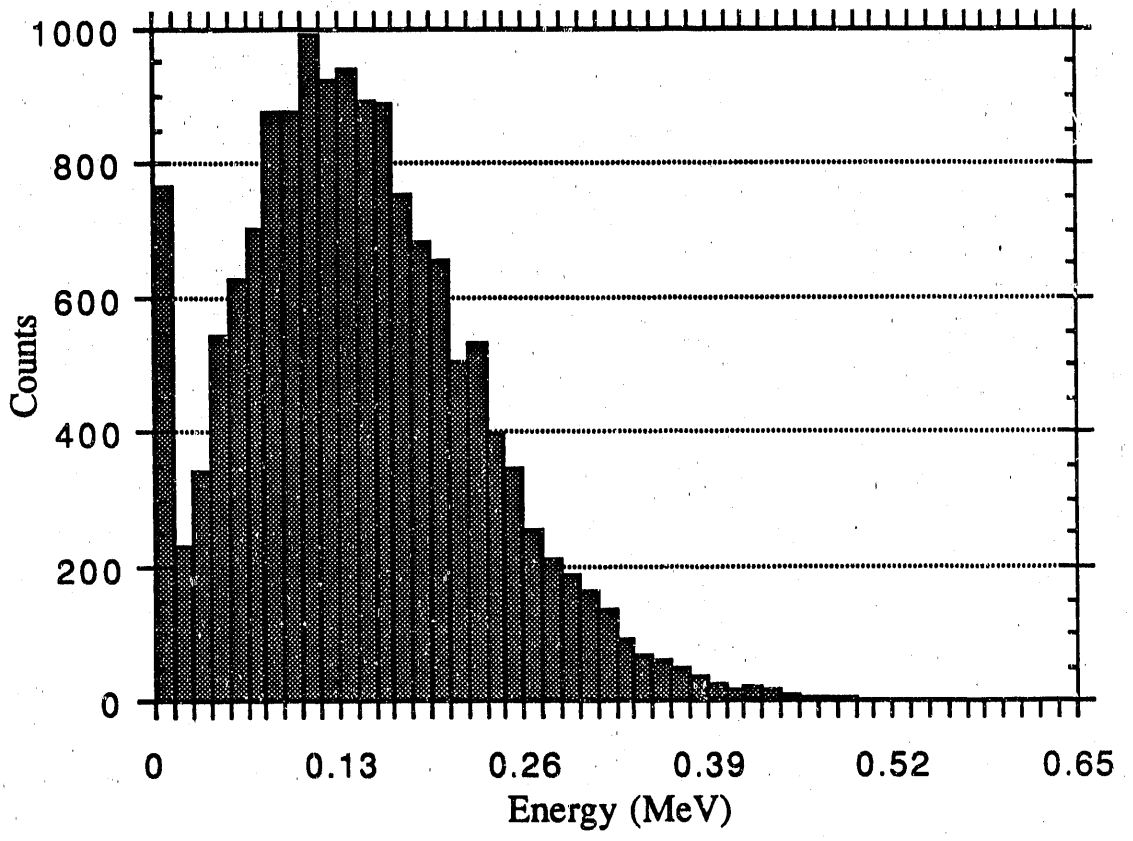

Figure 3. Energy - Volume histogram for the liver for ^{99m}Tc uniformly distributed in the l iver. As can be seen the distribution is wide; the dose-volume distribution will be similar, however, the shape of the distribution will be the same.

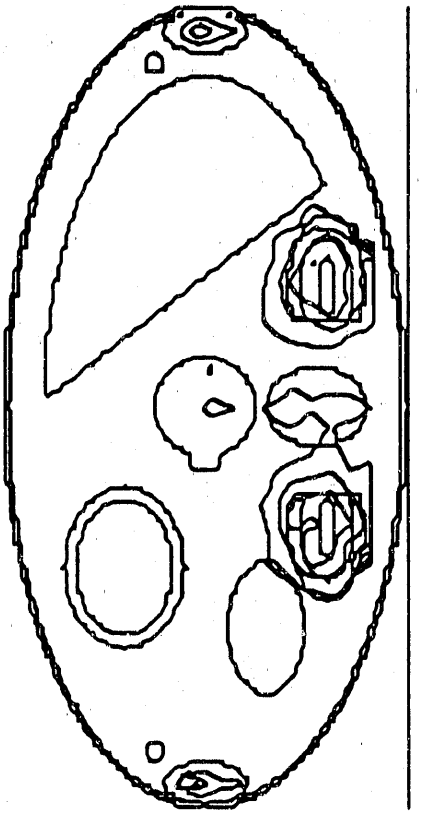

Figure 4. Superposition of a dose contour and a cross section of the phantom at z= 35.0 cm. The source region was the cortex of the kidneys with a uniform distribution of ^{99m}Tc. This plot allows the visualization of the isodose curves superposed with the different regions and organs of the phantom.

END

DATE FILMED

02 / 15 / 91